Fakultät für Informatik
Technische Universität München

Quantifying Hemodynamics in the Aorta with Four-Dimensional Flow Magnetic Resonance Imaging

Judith Zimmermann

Vollständiger Abdruck der von der Fakultät für Informatik der Technischen Universität München zur Erlangung des akademischen Grades einer

Doktorin der Naturwissenschaften (Dr. rer. nat.)

genehmigten Dissertation.

Vorsitzende:
Prof. Dr. Cristina Piazza

Prüfende der Dissertation:
1. Prof. Dr. Bjoern H. Menze
2. Prof. Dr.-Ing. Anja B. Hennemuth
3. Prof. Dr. Susanne Schnell

Die Dissertation wurde am 28.07.2021 bei der Technischen Universität München eingereicht und durch die Fakultät für Informatik am 12.11.2021 angenommen.

QUANTIFYING HEMODYNAMICS IN THE AORTA WITH FOUR-DIMENSIONAL FLOW MAGNETIC RESONANCE IMAGING

JUDITH ZIMMERMANN

Dissertation

July 2021

Judith Zimmermann: *Quantifying Hemodynamics in the Aorta with Four-Dimensional Flow Magnetic Resonance Imaging*, Dissertation, © July 2021

Technical University of Munich
Department of Informatics
Boltzmannstrasse 3
85748 Garching bei München
Germany

Pantha rhei. (Everything flows.)

— Heraclitus

Dedicated to my grandparents.

ABSTRACT

Studying the dynamics of blood flow is a key task for diagnosis, treatment, and monitoring of any diseases affecting the heart and the complex vasculature. With emerging biomedical imaging principles such as four-dimensional flow magnetic resonance imaging (*4D flow MRI*), we can map time-resolved and multi-directional blood velocity distributions in a three-dimensional volume of interest. Using image-based computational methods, the measured high-dimensional velocity data can be leveraged to perform a quantitative analysis of hemodynamic features. Clinical studies on various cohorts have suggested that these features present novel predictive markers that may aid cardiovascular disease management toward better patient outcomes. However, 4D flow MRI is yet to become a default sequence for quantitative flow assessment in the clinical routine. This thesis contributes to a better understanding of the potentials and limitations of quantifying hemodynamics using 4D flow MRI, with a particular focus on its applicability in aortic diseases. We develop and investigate quantitative flow parameters based on (i) *in vivo* MRI data of healthy and diseased aortas, (ii) *in vitro* MRI data, which we acquire with a custom-build physiological flow circuit that allows for highly controlled, model-based, and prolonged (i.e. non-accelerated) imaging studies, and (iii) simulated CFD data that we incorporate for proof-of-principle and comparison at multiple points. Key contributions of the conducted studies are: (i) a description of the impact of data noise, image resolution, and vessel wall motion on wall shear stress estimation; (ii) an investigation of the sensitivity of image-derived pulse wave velocity estimates for changes in aortic wall compliance, as well as confounding effects of temporal sampling; and (iii) novel insights into hemodynamics of aortic dissections, in particular the complex interplay between flow, pressure and wall dynamics, which we compare with CFD simulations using fluid-structure interaction. Results emphasize the versatility and promising potentials of quantitative 4D flow MRI while underlining important current limitations. This should consolidate the role of 4D flow MRI in basic and translational cardiovascular research, and further promote its use in the clinic.

ZUSAMMENFASSUNG

Die Analyse der Blutflussdynamik spielt eine zentrale Rolle in der Diagnose, Behandlung und Überwachung jeglicher Erkrankungen des Herzens und des komplexen Gefäßsystems. Mit Bildgebungsverfahren wie der vierdimensionalen Fluss-Magnetresonanztomographie (*4D-Fluss-MRT*) werden zeitaufgelöste und multidirektionale Blutgeschwindigkeitsverteilungen in einem dreidimensionalen Volumen abgebildet. Weiterhin können mit computergestützter Bildanalyse die gemessenen Daten verarbeitet werden, und eine quantitative Analyse von hämodynamischen Parametern durchgeführt werden. Klinische Studien an einer Vielzahl von Patientenkohorten haben gezeigt, dass diese Parameter neue Biomarker darstellen, die das Management von Herz-Kreislauf-Krankheiten hin zu verbesserter Behandlungsergebnisse unterstützen können. Allerdings ist die 4D-Fluss-MRT noch keine Standardmethode zur Quantifizierung der Hämodynamik in der klinischen Routine. Diese Arbeit trägt zu einem besseren Verständnis der Potenziale und Limitationen der 4D-Fluss-MRT bei; der Fokus liegt dabei auf der Anwendbarkeit zur Quantifizierung hämodynamischer Parameter in der Aorta. Wir untersuchen bildbasierte Metriken mit (i) *in vivo* Daten von gesunden und pathologischen Aorten, (ii) *in vitro* Daten, die wir mit einem maßgeschneiderten physiologischen Strömungskreislauf erfassen, der hochkontrollierte, modellbasierte und verlängerte (d. h. nicht beschleunigte) Bildakquisitionen ermöglicht, und (iii) simulierte Blutflussdaten, die für Proof-of-Principle Experimente und zum multi-modalen Vergleich integriert werden. Die durchgeführten Studien beinhalten unter anderem die folgenden zentralen Beiträge: (i) die Beschreibung des Einflusses von Datenrauschen, Bildauflösung und Gefäßwandbewegung auf die Schätzung der Wandschubspannung; (ii) die Untersuchung der Sensitivität von bildbasierten Kalkulationen der Pulswellengeschwindigkeit für Änderungen der Aortenwand-Compliance; und (iii) neue Einblicke in die Hämodynamik von Aortendissektionen mittels 4D-Fluss-MRT, insbesondere das komplexe Zusammenspiel zwischen Fluss-, Druck- und Wanddynamik, wobei alle gemessenen Parameter mit CFD Simulationen unter Verwendung von Fluid-Struktur-Interaktion (FSI) verglichen werden. Die Ergebnisse unterstreichen die Vielseitigkeit der quantitativen 4D-Fluss-MRT, während gleichzeitig kritische aktuelle Limitationen hervorgehoben werden. Dies sollte die Bedeutung der 4D-Fluss-MRT festigen und ihren Einsatz in der klinischen Routine weiter etablieren.

PUBLICATIONS

This publication-based dissertation comprises original reprints of the following published peer-reviewed articles:

[1] J. Zimmermann et al. "Wall shear stress estimation in the aorta: Impact of wall motion, spatiotemporal resolution, and phase noise." In: *J. Magn. Reson. Imaging* 48.3 (2018), pp. 718–728. DOI: 10.1002/jmri.26007.

[2] J. Zimmermann et al. "On the impact of vessel wall stiffness on quantitative flow dynamics in a synthetic model of the thoracic aorta." In: *Scientific Reports* 11 (2021), p. 6703. DOI: 10.1038/s41598-021-86174-6.

[3] J. Zimmermann et al. "Quantitative Hemodynamics in Aortic Dissection: Comparing in Vitro MRI with FSI Simulation in a Compliant Model." In: *Funct. Imaging Model. Heart. FIMH 2021. Lecture Notes Comput. Science*. Vol. 12738. Springer, Cham, 2021, pp. 575–586. DOI: 10.1007/978-3-030-78710-3_55.

Peer-reviewed conference contributions are not subject to evaluation, but complement the content of the above. The following are reproduced in the appendix:

[1] J. Zimmermann, H. Mirzaee, and A. Hennemuth. "Software Flow Phantoms for Assessing the Image-Based Computation of Hemodynamic Parameters." In: *Eurographics Workshop Visual Comput. Biol. Med.* Bremen, 2017.

[2] J. Zimmermann et al. "Towards wall shear stress computation in the moving aorta: Application of different tracking algorithms." In: *Proc. ISMRM Workshop on Quantitative MR Flow*. San Francisco, CA, 2016.

[3] J. Zimmermann et al. "Advancing quantitative 4D flow MRI: Assessment of manual versus automatic boundary definition in the aorta." In: *Proc. SCMR 20th Scientific Sessions*. Washington D.C., 2017, P99.

[4] J. Zimmermann et al. "Exploring vessel inward normal computation for 4D flow based wall shear stress estimation in complex vessel geometries." In: *Proc. ISMRM 26th Annual Meeting*. Paris, 2018, P3435.

[5] J. Zimmermann et al. "Computational metrics for quantitative characterization of vortical flow patterns based on 3D PC-MRI data." In: *Proc. ISMRM 27th Annual Meeting*. Montreal, 2019, P1967.

[6] J. Zimmermann et al. “Fully dimensional vessel segmentation in non-contrast-enhanced 3D PC-MRI image data.” In: *Proc. ISMRM 27th Annual Meeting*. Montreal, 2019, P1966.

[7] J. Zimmermann et al. “Impact of Vessel Wall Characteristics on Quantitative 4D-Flow Dynamics in Compliant 3D-Printed Thoracic Aorta Models.” In: *Proc. ISMRM 28th Annual Meeting*. Virtual, 2020, P2280.

[8] J. Zimmermann et al. “Evaluating ICOSA6 4D-Flow in a Compliant Aortic Dissection Model with Large Velocity Range and Complex Flow Patterns.” In: *Proc. ISMRM 29th Annual Meeting*. Virtual, 2021, P2093.

[9] J. Zimmermann et al. “In Vitro 4D-Flow and Pressure Mapping in the True and False Lumen of a Type-B Aortic Dissection Model.” In: *Proc. SCMR 24th Scientific Sessions*. Virtual, 2021.

ACKNOWLEDGMENTS

My journey to this day would not have been possible without the support and guidance from many people at several institutions around the world.

Prof. Bjoern Menze, thank you for welcoming me to the IBBM group and advising this dissertation, but also for giving me the freedom and flexibility to explore many collaborations with others.

Prof. Anja Hennemuth, thank you for being an excellent supervisor and mentor throughout. You introduced me to the world of flow image analysis and many exciting software projects, and to a great and fun team both in Bremen and Berlin. I learned so much and I owe you my sincere gratitude for making this journey happen.

Prof. Daniel Ennis, thank you for supporting my move around the world with the great opportunity to work in your lab (again!). You are the person who first sparked my curiosity about cardiovascular MRI and it certainly lasted. At Stanford, you provided terrific guidance and infrastructure, by all means, to a project that at times felt too ambitious and never-ending. I have grown so much, both personally and professionally, and thank you very much for the trust you have placed in me.

I would also like to thank Prof. Susanne Schnell for her kind offer to review this work as an examiner as well as Prof. Cristina Piazza for chairing the examining committee.

From day one, I had the privilege to work with Fraunhofer Institute for Digital Medicine MEVIS both in Bremen and at ICM Charité Berlin — thanks in particular to colleagues Lennart Tautz, Markus Hüllebrand, Christian Schuhmann, Daniel Romberg, Johann Drexl, and Hanieh Mirzaee. I am glad to have been part of your supportive open-door culture and appreciate all of the help I received with development questions.

To the clinical MRI team at the German Heart Center Munich — Christian Meierhofer, Heiko Stern, Heiner Latus, Naira Mkrtchyan, Nereida Shehu — thank you for providing your clinical expertise, for great insights into congenital heart disease and clinical cardiac MRI, and for enabling infrastructure and support for all volunteer scan sessions that we completed at DHM.

To all fellow doctoral students and lab friends at IBBM in Munich, thanks for being great office colleagues during my time at the MSB office in Garching, travel companions to various conferences and summer schools, and for superb biryani and hot pot nights — in particular, Dhritiman Das, Carolin Pirkl, Anjany Sekuboyina, Suprosanna Shit, Bran Li, Yu Zhao, John La Master, and Diana Waldmannstetter.

For the past two years, it has been an absolute joy to work with a wonderful group of individuals at and around the CMR lab at Stanford Radiology and at the VA Palo Alto — Mike Loecher, Tyler Cork, Fikunwa Kolawole, Seraina Dual, Matt Middione, Jessica Martinez, Nyasha Maforo, Kevin Moulin, Julio Oscanoa, Vicky Wang, Alex Wilson, Amanda Tun, and Jackie Velasquez. With endless hours spent at the scanner, most data simply would not have been collected if it wasn't for my lab mates' generous help. (Special thanks to TEC in particular for this!) Also, I was fortunate to mentor several incoming and summer students who not only assisted with my projects but taught me much about how to become a better teacher.

Stanford excels as a highly collaborative community, and my project there would not have happened without several cross-departmental connections. In particular, I would like to thank Kathrin Bäumler and Alison Marsden for all things CFD, Nicole Schiavone for sharing all of her expertise about flow loops, Dominik Fleischmann and CVI folks for numerous fruitful Tuesday night discussions, Kyle Gifford, Chris Le Castillo, Marie-Anne Valiquette, and Shannon Walthers for outstanding work with their 3D printers, as well as Sachin Malik and Payam Massaband for their efforts to enable my experimental studies at the VA site.

To the staff at TUM-GCB and TUM-GS, thanks for your support with all administrative matters and for coordinating many scientific and transferable skills seminars, which I always found very helpful.

Several sources of funding made this work possible (see funding sources listed in publications), but in particular, I want to acknowledge direct grant support that I received over the years from the German Heart Foundation and the German Academic Exchange Services (DAAD).

Most importantly, to my family and dearest friends in Heidelberg, Munich, the Bay Area, and beyond — *Thank you* for bearing with me through everything, for the most genuine friendships at the best and the worst of times, and for always and continuously supporting my life adventures.

Go into the world and do well.
But more importantly, go into the world and do good.

— Minor Myers Jr.

CONTENTS

I INTRODUCTION AND BACKGROUND

1 INTRODUCTION 3
- 1.1 Contributions 4
- 1.2 Outline 5

2 BACKGROUND 7
- 2.1 The cardiovascular system 7
  - 2.1.1 The heart 7
  - 2.1.2 The cardiac cycle 8
  - 2.1.3 Physiology of the aorta 9
  - 2.1.4 Examples of aortic disease 11
- 2.2 Phase contrast magnetic resonance imaging 13
  - 2.2.1 Theory of encoding motion 13
  - 2.2.2 Phase from many things 16
  - 2.2.3 Velocity sensitivity and V_{enc} 17
  - 2.2.4 2D PC MRI sequence 18
  - 2.2.5 k-space segmentation 19
- 2.3 Multi-directional flow encoding (4D-flow MRI) 20
  - 2.3.1 Scan time and acceleration techniques 22
  - 2.3.2 Acquisition and processing pipeline 24
- 2.4 Image-based hemodynamic parameters 27

II CONTRIBUTIONS

3 WALL SHEAR STRESS ESTIMATION IN THE AORTA: IMPACT OF WALL MOTION, SPATIAL RESOLUTION, AND PHASE NOISE 35

4 ON THE IMPACT OF VESSEL WALL STIFFNESS ON QUANTITATIVE FLOW DYNAMICS IN A SYNTHETIC MODEL OF THE THORACIC AORTA 49

5 QUANTITATIVE HEMODYNAMICS IN AORTIC DISSECTION: COMPARING IN VITRO MRI WITH FSI SIMULATION IN A COMPLIANT MODEL 65

III DISCUSSION AND OUTLOOK

6 DISCUSSION OF THE PRESENTED WORKS 81

7 ONGOING AND FUTURE WORK 85

IV APPENDIX

A TOWARDS WALL SHEAR STRESS COMPUTATION IN THE MOVING AORTA: APPLICATION OF DIFFERENT TRACKING ALGORITHMS 89

B ADVANCING QUANTITATIVE 4D FLOW MRI: ASSESSMENT OF MANUAL VERSUS AUTOMATIC BOUNDARY DEFINITION IN THE AORTA. 93
C SOFTWARE FLOW PHANTOMS FOR ASSESSING IMAGE-BASED COMPUTATION OF HEMODYNAMIC PARAMETERS 95
D EXPLORING VESSEL INWARD NORMAL COMPUTATION FOR 4D FLOW BASED WALL SHEAR STRESS ESTIMATION IN COMPLEX VESSEL GEOMETRIES 97
E FULLY DIMENSIONAL VESSEL SEGMENTATION IN NON-CONTRAST-ENHANCED 3D PC-MRI DATA. 103
F COMPUTATIONAL METRICS FOR REPRODUCIBLE CHARACTERIZATION OF COHERENT FLOW PATTERNS IN 3D PC-MRI DATA. 109
G IMPACT OF AORTIC WALL STIFFNESS AND THICKNESS ON QUANTITATIVE 4D FLOW DYNAMICS IN 3D-PRINTED THORACIC AORTA MODELS. 115
H IN VITRO 4D-FLOW AND PRESSURE MAPPING IN THE TRUE AND FALSE LUMEN OF A TYPE-B AORTIC DISSECTION MODEL. 121
I EVALUATING ICOSA6 4D-FLOW IN A COMPLIANT AORTIC DISSECTION MODEL WITH LARGE VELOCITY RANGE AND COMPLEX FLOW PATTERNS. 127

BIBLIOGRAPHY 133

LIST OF FIGURES

Figure 2.1 Human circulatory system and anatomy of the aorta. 8
Figure 2.2 Wiggers diagram showing events of the cardiac cycle. 9
Figure 2.3 Artic wall layers and false lumen formation in aortic dissection. 10
Figure 2.4 Tricuspid versus bicuspid aortic valve and the effect on flow dynamics 11
Figure 2.5 Magnitude and phase image data. 15
Figure 2.6 Gradient versus phase shift relationship. 16
Figure 2.7 Flow compensated and flow encoded (bipolar) gradient waveforms with respective phase shifts of static and moving spins. 16
Figure 2.8 Mapping accrued phase shifts to absolute velocities. 18
Figure 2.9 Pulse sequence diagram for spoiled gradient echo (SPGR) acquisition. 19
Figure 2.10 Pulse sequence diagram for through-plane encoded 2D PC MRI acquisitions using a flow compensated and flow encoded part. 20
Figure 2.11 k-space segmentation principle for time-resolved and cardiac-triggered MRI. 21
Figure 2.12 2D PC magnitude data and phase image data with three-directional velocity encoding. 22
Figure 2.13 Reformatted planar views of the heart with absolute velocity overlay. 23
Figure 2.14 4D flow MRI streamline visualization in congenital defects of the aorta. 24
Figure 2.15 4D flow MRI data acquisition and processing pipeline. 26
Figure 2.16 Shear stress and velocity gradient arising from an applied force deforming a rectangular fluid element. 28
Figure 7.1 Varying morphology of aortic dissection tear size. 86
Figure A.1 Processing pipeline for definition of multi-planar-reformatted (MPR) images. 90
Figure A.2 3D WSS visualization at single timepoint. A time-independent and static surface mesh was used. 91

Figure A.3 Results for Dice index and Hausdorff distance for different contour tracking algorithms. 91
Figure B.1 Dice index and Hausdorff distance results for inter-observer variability, algorithm performance, and algorithm initialization variability. 94
Figure C.1 The influence of V_{enc} choice on noise level in simulated phase data. 96
Figure D.1 Computation of vessel inward normals based with adapted an conventional method. 99
Figure D.2 WSS estimates based on conventional and addapted inward normal computation. 100
Figure D.3 Vessel inward normals in *in vivo* data. 101
Figure D.4 Absolute and relative WSS differences comparing conventional and adapted inward normal computation. 102
Figure D.5 Absolute and relative OSI differences comparing conventional and adapted inward normal computation. 102
Figure E.1 Algorithm workflow for 4D vessel segmentation. 104
Figure E.2 Distribution of cross-sectional manual contours used for 4D vessel segmentation algorithm evaluation. 105
Figure E.3 4D+t segmentation for three *in vivo* cases. 106
Figure E.4 Statistical evaluation of 4D segmentation output when compared to manual contours. 107
Figure F.1 Workflow for quantitative vortical pattern characterization. 109
Figure F.2 Synthetic data with various circulation strength numbers and Gaussian noise levels. 112
Figure F.3 Vortex quantification in three patients with aortic valve stenosis, both pre- and after post-valve replacement. 113
Figure G.1 Aortic wall mesh modelling for 3D printing and definition of landmarks for PWV estimation. 116
Figure G.2 Absolute velocity maps at mid-systole. 117
Figure G.3 PWV estimation along the descending aorta centerline. 118
Figure G.4 Flow rate waveforms and PWV estimates for three aorta models with two HR levels. 119
Figure H.1 TBAD model construction, experimental setup, and pressure mapping points. 123
Figure H.2 4D flow based path lines traces and absolute velocity maps in TBAD model. 124

Figure H.3 2D analysis at cross-sectional landmarks and pressure recordings for TBAD study. 125
Figure I.1 Schematic diagram showing the layout of the developed flow circuit setup. 128
Figure I.2 Phase data and pathline traces for 4D flow MRI data based on conventional 4-point encoding and ICOSA6. 130
Figure I.3 Cross-sectional quantitative results for 4D flow MRI data based on conventional 4-point encoding and ICOSA6. 131

ACRONYMS

2D	Two-dimensional
3D	Three-dimensional
4D	Four-dimensional
AAo	Ascending aorta
BAV	Bicuspid aortic valve
BCT	Brachiocephalic trunk
bSSFP	Balanced steady-state free precession
CMR	Cardiovascular magnetic resonance [imaging]
CS	Compressed sensing
CFD	Computational fluid dynamics
CVD	Cardiovascular disease
DAo	Descending aorta
DL	Deep learning
EPI	Echo planar imaging
FL	False lumen [of TBAD]
FOV	Field of view
FSI	Fluid-structure interaction
GRAPPA	Generalized autocalibrating partial parallel acquisition
HR	Heart rate

IVSD	Intra-voxel standard deviation
LA	Left atrium
LV	Left ventricle
LCC	Left common carotid [artery]
LSA	Left subclavian artery
ML	Machine learning
MDHM	Multi-directional high moment [encoding]
MRI	Magnetic resonance imaging
OSI	Oscillatory shear index
PAT	Parallel acquisition technique
PCMRA	Phase contrast magnetic resonance angiography
PIT	Primary intimal tear [in TBAD]
PWV	Pulse wave velocity
PC	Phase-contrast
RA	Right atrium
RV	Right ventricle
RF	Radiofrequency, also: Regurgitant fraction
RR	R-to-R peak [cardiac] cycle
SD	standard deviation
SPGR	Spoiled gradient echo
T_A	Acquisition time
T_E	Echo time
T_R	Repetition time
TAWSS	Time-averaged wall shear stress
TBAD	Type B aortic dissection
TL	True lumen [in TBAD]
TKE	Turbulent kinetic energy
V_{enc}	Velocity encoding range
VIPR	Vastly undersampled isotropic projection reconstruction
WSS	Wall shear stress

Part I

INTRODUCTION AND BACKGROUND

1 INTRODUCTION

"Cardiology is about flow. The primary purpose of the cardiovascular system is to drive, control, and maintain blood flow to all parts of the body."[1]

The ultimate task of the cardiovascular system is to continuously supply all organs with oxygen and nutrients. Its effective and efficient functioning is inevitable to life. It may not be surprising that the heart, the driving force of blood circulation, is the first functional organ in vertebrate embryos and starts beating (in the human) only five weeks after conception.

Today, mortality associated with cardiovascular diseases (CVD) makes up 32 % of global deaths, representing the number one cause of death worldwide.[2] The burden on health care systems and society as a whole and the associated costs for CVD treatment are immense. CVD include pathologies of the heart itself, but also conditions that affect the complex vasculature, from small cerebrovascular arteries in the brain to large vessels such as the aorta. Some CVD conditions are acquired over lifetime, others present themselves as congenital defects.

As with most diseases, early detection and tailored disease management are of utmost importance to improve patient outcome. To achieve the best possible patient outcome, understanding the complex dynamics of blood flow must be a focus of research: how they describe the underlying pathophysiological condition, how they explain where lesions form, how they dictate disease progression, how they reveal the extent of restauration after an intervention.

Cardiovascular magnetic resonance imaging (MRI) has established itself as a key modality to study CVD. Specifically, phase-contrast MRI allows for the measurement of blood flow velocity with full volumetric coverage [87]. That is, we are able to obtain *in vivo* time-resolved three-directional flow information at millimeter resolution of the whole heart and surrounding great vessels — a technique referred to as *4D flow MRI* — all within one scan session. Recent developments to achieve clinically acceptable scan durations are expected to further push the use of 4D flow MRI as part of the standard imaging protocol for CVD assessment.

The generated 4D flow image data is analyzed using computational methods for both qualitative and quantitative assessment. Qualitatively, we can visualize instantaneous flow patterns and profiles, and render blood particle traces over time. Quantitatively, we can derive

1 Yoram Richter and Elazer R. Edelman, *Cardiology is Flow*, 2006 [112]

2 Estimated percentage for 2019, World Health Organization, `www.who.int`

numerical results for flow rates, net flow, velocity statistics, wall shear stress, pressure gradients, and others.

Over the past 10 to 15 years, these qualitative and quantitative metrics have been utilized in numerous (mostly small-cohort) studies focusing on a broad spectrum of CVD, from diseases of the cerebrovascular system (e.g. intracranial aneurysm, arteriovenous malformation), through complex congenital defects (e.g. tetralogy of Fallot, single-ventricle hearts, septal defects), to heart valve malfunctions (e.g. stenosis, regurgitation).[3] Aortic diseases have been a major focus in the clinical application of 4D flow MRI and the use of image-based predictive flow biomarkers [20]. For example, studies showed: the influence of a bicuspid aortic valve (rather than a tricuspid one) on flow eccentricity, jets, wall shear stress (WSS), and helical flow patterns [6, 15, 61, 62]; the association between 4D flow-based pulse wave velocity (PWV) and wall stiffness [40, 89, 92]; or evidence of a relationship between altered wall shear stress and plaque formation in atherosclerosis [51, 93].

Despite these many reports that show promising clinical applications of 4D flow MRI, the technique is yet to become a default sequence in the clinical routine. While relatively long acquisition times seem to be the obvious (and always listed) bottleneck delaying widespread clinical translation, open questions also remain concerning the robustness and reliability of quantifying hemodynamics with 4D flow MRI. Uncertainties in flow quantification may originate from the various image analysis tasks performed during post-processing, but also from erroneous velocity data owing to limited spatio-temporal resolution, the chosen acquisition parameters, the use of scan acceleration techniques, and/or artifacts due to cardiac and respiratory motion.

The *overall research aim* was to promote 4D flow MRI through expanding our understanding of its potentials and limitations regarding the image-derived computation of quantitative parameters. Findings should support decisions about when and how to include these quantitative parameters in large-cohort studies and further push developments to improve 4D flow MRI acquisitions. In the long term, this should consolidate the use of 4D flow MRI as default quantitative flow imaging sequence in the clinical routine.

1.1 CONTRIBUTIONS

This work's contributions advance the analysis of quantitative hemodynamics with 4D flow MRI. We performed experimental MRI studies, and developed and evaluated image post-processing strategies that quantitatively analyze 4D flow MRI data, including *in vivo* data of

3 Clinical applications are given in a plethora of 4D flow MRI review articles [50, 60, 91, 94, 121, 126, 135].

healthy volunteers and patients with aortic pathologies, as well as *in vitro* 'phantom data'.

Individual technical and scientific contributions comprise the following:

- developing an advanced MRI-compatible flow circuit setup that integrates patient-specific large vessel models under highly-controlled physiological conditions;
- applying novel 3D printing technologies for manufacturing subject-specific compliant aorta models;
- understanding the influences of image noise, image resolution, and vessel wall motion on 4D flow-based wall shear stress (WSS);
- benchmarking the sensitivity of 4D flow-based pulse wave velocity estimates for aortic wall compliance and temporal sampling;
- benchmarking MRI against computational fluid dynamics with fluid-structure interaction (CFD FSI). Here, boundary conditions for tuning the simulation framework were directly informed by measurements from the experimental setup;
- providing novel insights into flow and pressure dynamics in aortic dissections.

1.2 OUTLINE

In part I, the following chapter 2 provides the clinical and technical background and is divided into four sections. Sec. 2.1 gives a concise introduction to anatomy and physiology of the cardiovascular system with a focus on the human aorta. Sec. 2.2.4 reviews the physics principles of phase-contrast MRI. Sec. 2.3 reviews multi-directional and three-dimensional flow encoding (4D flow MRI); and sec. 2.4 defines quantitative hemodynamic parameters in the context of 4D flow MR image analysis.

In part II, Chap. 3 [148], we propose and implement software tools for image-based planar WSS estimation. We analyze the robustness of wall shear stress and oscillatory shear index against vessel wall motion, signal noise, and spatial resolution. Quantitative analysis is performed on simulated data with varying noise and spatial resolution levels, as well as *in vivo* 4D flow MRI data of patients with aortic valve defects and healthy volunteers.

In Chap. 4 [154], we develop a custom-build *in vitro* physiological flow circuit setup that embeds subject-specific and compliant 3D printed aorta models. This publication presents (1) a detailed description of the technical aspects of the flow circuit and (2) deploys the setup to investigate the relationship of aortic wall stiffness on

image-based quantitative hemodynamics. A particular focus is on the computation of flow-waveform-derived pulse wave velocity and confounding effects of temporal sampling.

In Chap. 5 [155], we advance our prior developments by integrating a patient specific model of a dissected aorta to study luminal flow and pressure dynamics in the true and false lumen. Furthermore, we perform CFD FSI simulations with a deformable structural domain (aortic wall), which are informed by measured flow and pressure boundary conditions. Qualitative and quantitative analyses regarding flow patterns, net flow splits, and pressure are presented, focusing on the similarities and differences between measured (MRI) and simulated (CFD FSI) data.

In part III, Chap. 6, the overall contributions of this dissertation are discussed and important limitations, which shall be the focus of follow-up work, are revisited. Chap. 7 gives an outlook for ongoing and future work.

In part IV, the appendix includes all relevant conference abstracts. Although these shall not contribute to the evaluation of this publication-based dissertation, they are reproduced as they complement the content.

2 BACKGROUND

2.1 THE CARDIOVASCULAR SYSTEM

The cardiovascular system is an organ system with the task to circulate blood and nutrients around the human body. It comprises the heart as the central pump and vasculature, with large and small vessels (Fig. 2.1, left). Per definition, the systemic circulation transports oxygenated blood from the pumping heart to all organs, and deoxygenated blood from the same organs back to the heart. The pulmonary circulation connects the heart with the lungs where blood is reoxygenated as we breath in and out. We refer to arteries as all vasculature transporting blood away from the heart, and to veins as all vasculature reaching back to the heart.

The following gives a brief introduction to the anatomy and physiology of the heart and the aorta, which is the vessel of interest of much of the work presented in this dissertation. For a comprehensive description of cardiovascular mechanics, it is worthwile looking into 'The Mechanics of the Circulation' by Caro et al. [26].

2.1.1 *The heart*

The (healthy) heart itself has a left and a right side, each of which comprise one atria (LA: left atria, RA: right atria) and one ventricle (LV: left ventricle, RV: right ventricle). LA receives oxygenated blood via the pulmonary veins from the lungs, sends it through the mitral valve into the LV, which then pumps it out through the aortic valve into the aorta and further to all organs. RA receives deoxygenated blood via the vena cava from all organs, sends it through the tricuspid valve into the RV, which then pumps it out through the pulmonary valve into the pulmonary artery, which connects back to the lungs.

The cardiac output (CO, in L/min) is defined by the stroke volume (SV, in mL) times the heart rate (HR, in min^{-1}):

$$\mathrm{CO} = \mathrm{SV} \cdot \mathrm{HR}. \tag{2.1}$$

At rest, the adult human heart pumps around 5 L of blood per minute, at a rate of 60–90 beats per minute, depending on age and physical condition, which leads to an average SV of 70 mL. However, the heart has excellent capabilities to adapt and a well-trained athlete may output up to 30 L/min by increasing both SV and HR during exercise.

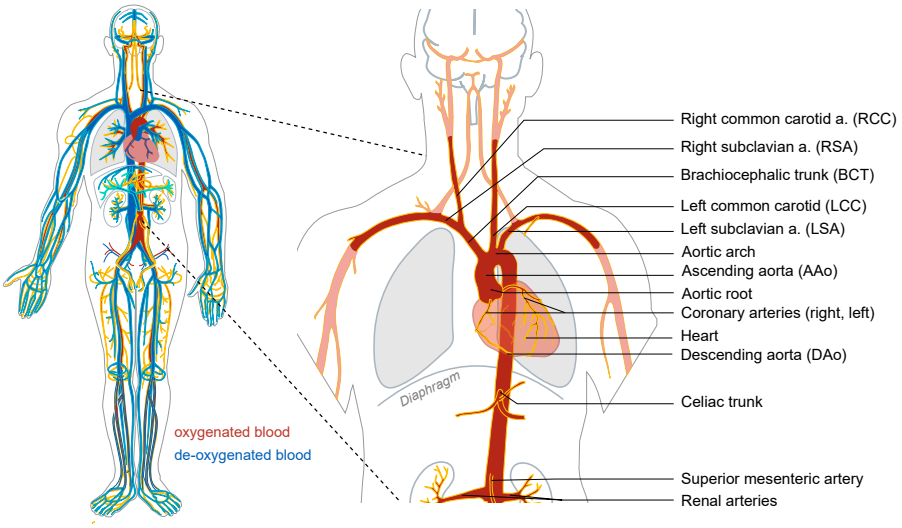

Figure 2.1: The complex circulatory system of the human body (left) and the thoracic (above diaphragm) and abdomial (below diaphragm) aorta with major branching vessels (right). (Adapted based on originals by Mikael Häggström and Mariana Ruiz Villarreal, CC-BY-3.0)

2.1.2 *The cardiac cycle*

Events of the cardiac cycle are illustrated in the so-called Wigger's diagram (Fig. 2.2). It includes time-dependent pressure waveforms in the LA, LV, and aorta, blood volume in the LV, the electrocardiagram (ECG) signal originating from the heart, and a phonocardiogram, which presents the typical sounds that accompany certain events.

Overall, the duration of heart contraction is referred to as systole, while the relaxation of the heart is referred to as diastole.

Systolic phase. The contraction of the heart is initiated by an electrical impulse which spreads to the ventricles through a conduction system. This stimulus is observed in the ECG signal as the QRS complex and marks the beginning of the cardiac cycle. The left ventricle contracts under constant blood volume. LV pressure rises until it hits the luminal pressure level of the aorta, which causes the aortic valve to open. Consequently, blood is ejected. During the ejection phase, LV volume decreases gradually, followed by a decrease of LV pressure, and eventually closure of the aortic valve.

Diastolic phase. Following aortic valve closure, the LV starts to relax under constant blood volume (as both valves are closed). LV pressure drops rapidly until it falls below LA pressure, which initiates the opening of the mitral valve, and blood to flow from the LA into the LV. LV fills up steadily until the mitral valve closes again, which is essential to prevent blood from flowing back into the LA during the subsequent next contraction event. We should add that the closure of the mitral valve is supported by the so-called papillary muscles which

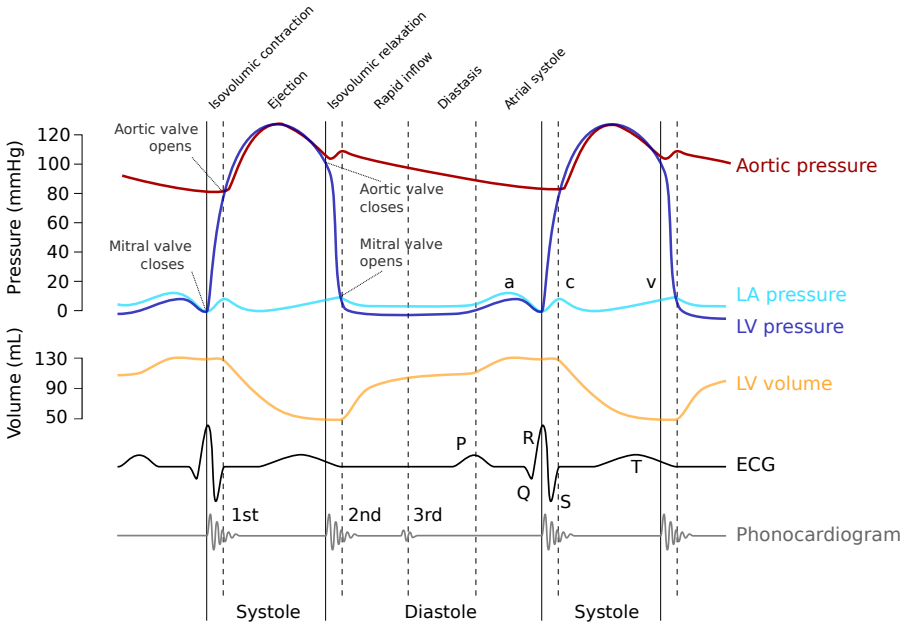

Figure 2.2: Wiggers diagram showing events of the cardiac cycle. (Adapted based on original by Daniel Cheng, CC-BY-4.0)

connect to the mitral valve leaflets on one end and the ventricular wall on the other end.

Events on the right hand side of the heart (RV, RA) are very similar to the events described above and thus not mentioned here. The 'lub-dub' heart sounds (see phonocardiogram) are associated with the closing of the valves at the beginning of systole and diastole, respectively.

2.1.3 *Physiology of the aorta*

The aorta is the largest vessel of the vasculature carrying around 200 million liters of blood in an average lifetime, and the aortic valve is its 'Golden Gate' if you will.

ANATOMY The aorta is divided into the thoracic aorta (above diaphragm level) and the abdomial aorta (below diaphram level) and has several major branching vessels (Fig. 2.1, right). The thoracic aorta starts with the aortic root from which the coronary arteries branch off. It follows the ascending aorta (AAo), the aortic arch — from which the left and right subclavian arteries and the left and right common carotid arteries branch off —, and the descending aorta (DAo). The aorta breaks through the diaphragm and other major branching points follow further distally (celiac trunk, mesentric artery, renal arteries, etc.) supplying blood to abdomial organs. The distal end of the (abdomial) aorta is the branching point of the iliac arteries, which sits approximately at navel height. The diameter of the aorta measures 20–30 mm at the root and tapers down toward its distal end.

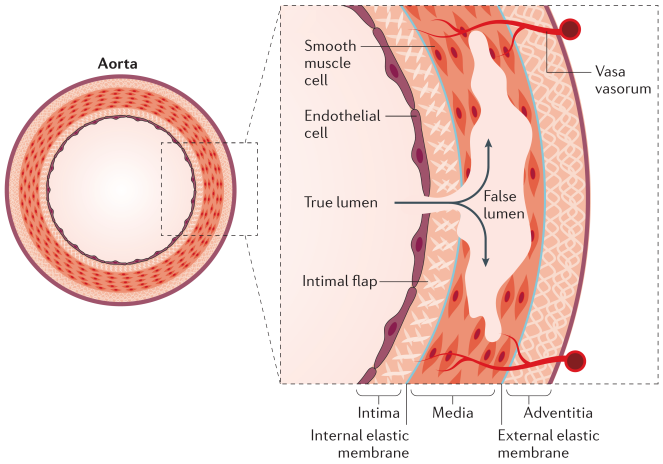

Figure 2.3: Layers of the aortic wall and dissection of the wall with formation of a secondary ('false') lumen. Image courtesy of Nienaber et al. [102]

AORTIC WALL The aortic wall has an average thickness of 2–3 mm and is composed of multiple layers: the (outer) adventitia, (middle) media, and (inner) intima layer (Fig. 2.3).

The adventitia contains the blood vessels supplying the aortic wall (vasa vasorum) and nerves. Owing to a rich collagen content, the tensile strength of the adventitia is the highest among the three layers. The adjacent media layer accounts for up to 80 % of the aortic wall thickness and consists of elastic tissue intertwined with muscle fibers. The intima is the thin inner wall layer, characterized histologically by a basement membrane lined with endothelial cells that are in direct contact with the blood.

The compliant nature of the aortic wall (and the vasculature in general) is key to its function. If it were stiff, pressure would rise significantly during systole, and drop to close to zero in diastole. Moreover, the pressure pulse would be similar in shape and synchronous at any site along the vessel. But, owing to the vessel's compliance, the vessel distends during systole, acting like a capacitor, and recoils during diastole, mimicking a secondary ejection phase. This way, blood flow in peripheral arteries is kept alive during diastole.

FLOW AND PRESSURE In the healthy aorta, peak systolic flow rates (in the AAo) reach 300–450 mL/s and peak velocities are typically at around 150 cm/s. Luminal pressure is at 110–120 mmHg during systole and at 70–80 mmHg during diastole. The pressure waveform (as measured in the AAo) depicts some particular features. The first being the so-called dicrotic notch at the beginning of systole (also shown in Fig. 2.2). This short elevation of pressure is due to sudden closure of the aortic valve. Second, the pressure wave reflects at branching points of the arterial tree, which leads to systolic pulse amplifications,

typically seen as secondary bumps on top of the main pressure lobe. As the pressure pulse travels downstream and into the peripherial arteries, peak pressure increases. In contrary, the flow waveform widens owing to the dampening effects of the compliant aortic wall.

2.1.4 *Examples of aortic disease*

There is a wide spectrum of diseases involving the aorta and/or aortic valve, both congenital and acquired [45]. A few selected examples are briefly introduced in the following.

AORTIC VALVE STENOSIS Aortic valve stenosis occurs when the opening area of the aortic valve is narrowed. Most commonly, a stenotic valve is caused by calcification of the leaflets [76]. A *bicuspid aortic valve* — a congenital defect where there is only two instead of three leaflets — is also associated with aortic stenosis [115]. The narrowed cross-sectional outflow area increases resistance, which leads to increased LV pressure and an increased (negative) pressure gradient across the valve. A flow jet may form during systole, followed by flow turbulences and/or helical flow patterns in the AAo (Fig. 2.4). The severity of the aortic stenosis or BAV can be assessed by quantitatively characterizing these hemodynamic features.

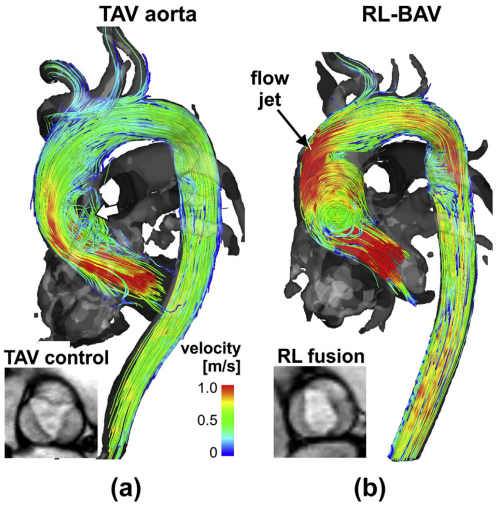

Figure 2.4: 4D flow MRI streamlines in systole in subject with (a) tricuspid aortic valve (TAV) and (b) bicuspid aortic valve (BAV). In the case of BAV, the right and left coronary leaflets are fused thus the label RL-BAV. Image courtesy of Markl et al. [94].

AORTIC INSUFFICIENCY Aortic insufficiency, also known as aortic regurgitation, occurs when there is reverse flow from the aortic root into the LV during ventricular diastole, meaning the valve is not fully closed when it should be. As a consequence, net flow is reduced and

the cardiac muscle has to work harder to provide the same output. The severity of aortic insufficiency can be quantifie, d by measuring the regurgitant flow fraction (RF).

ANEURYSM An aortic aneurysms is a baloon-like dilation in the thoracic or abdomial aorta. An aneurysm poses the risk of partial (i.e., dissected aortic wall) or complete rupture; the latter leads to life-threatening internal bleeding. Aneurysms are typically monitored by measuring size and growth rate (e.g. through repeated imaging sessions), but flow parameters (e.g. wall shear stress) may be additional markers for risk-stratification.

AORTIC DISSECTION In an aortic dissection, layers of the aortic wall tear apart locally at one or multiple points (Fig. 2.3) [102]. Blood will rush in between the separated layers and form a secondary ('false') lumen. An aortic dissections is categorized according to its anatomical location. As per 'Stanford' classification, a type A dissection involves the AAo or AAo + DAo, whereas a type B dissection involves the DAo only. The ultimate risk of an aortic dissection is a complete rupture of the aortic wall. Conventionally, the prognosis and treatment strategy is based on geometric features (e.g. false lumen size and growth rate). But hemodynamic markers (e.g. net flow through the false lumen, pressure distribution) are also of potential interest and may confer added sensitivity for patient-specific treatment planning.

2.2 PHASE CONTRAST MAGNETIC RESONANCE IMAGING

Magnetic resonance imaging (MRI) is a tomographic imaging modality based on the physics principles of nuclear magnetic resonance (NMR). Its versatility, unprecedented soft tissue contrast, and broad spectrum of basic science and clinical applications established MRI as a primary radiological method. MRI was first invented in the 1970s, led by Paul C. Lauterbur and Sir Peter Mansfield [74, 86], and has since grown a large research community.

In a nutshell, with MRI we use a strong static *magnet* (1.5 T or 3 T in the clinical setting) to align magnetic moments of nuclear spin along one spatial direction; radiofrequency (RF) transmit and receive coils to excite these spins (i.e. flipping their moment direction) and to later collect the actual MR signal (i.e. the oscillating *resonance* signal that the spins emit while relaxing back to their original state); several gradient coils to generate time- and spatially varying magnetic fields for three-dimensional spatial encoding of the *image* volume; as well as computer hardware and tailored software to control all processes. The image contrast is achieved as different tissues have different intrinsic relaxation properties (labeled T_1 and T_2) and varying amounts of spin density (ρ). MRI is non-invasive and does not require the injection of an agent or tracer, as opposed to nuclear medicine techniques. It also does not use ionizing radiation, as opposed to for example X-ray or computed tomography.

While conventional MRI methods generate data of qualitative nature and the image intensity represents a weighted combination of the intrinsic tissue properties, a subgroup of MRI acquisition protocols provides quantitative data. One quantitative technique is phase contrast MRI (PC MRI), which encodes the velocity of moving spins into the phase component of the complex valued MRI signal [19, 99–101, 106, 107]. In other words, we can reconstruct two- or three-dimensional image matrices for which each element is a one- or multi-directional vector describing blood flow velocity in the three-dimensional space.

The following should provide necessary background information on PC MRI, from the general theory of sensitizing velocity of moving spins, velocity encoding strength, cardiac motion controlling, to multi-directional and three-dimensional velocity mapping. For a detailed mathematical description of the MR imaging physics, I would like to direct the reader to — my personal favorite — Bernstein et al. [11] or Brown et al. [18].

2.2.1 *Theory of encoding motion*

To understand the mechanism of encoding spin velocity into MRI signal phase, we should introduce the linear relationship between the

magnetic field and the rotating frequency of magnetic moments that experience it, also known as Lamor equation:

$$\omega = \gamma B, \tag{2.2}$$

where B is the magnetic field, ω is the so-called Lamor frequency, and γ is the gyromagnetic ratio — a specific constant for every given nuclei. (For MRI targeting hydrogen-1 nuclei $\gamma_{1H} = 42.57\,\mathrm{MHz\,T^{-1}}$.) The present magnetic field B originates from multiple sources, and for now we will consider B as:

$$B(\vec{r}, t) = B_0 + \Delta B + \vec{G}(t) \cdot \vec{r}(t), \tag{2.3}$$

where B_0 is the strong main (static) magnetic field, ΔB is the sum of all local field inhomogeneities, and $\vec{G}(t) \cdot \vec{r}(t)$ is the superimposed and time varying magnetic gradient field. This leads us to

$$\omega(\vec{r}, t) = \gamma B_0 + \gamma \Delta B + \gamma \vec{G}(t) \cdot \vec{r}(t). \tag{2.4}$$

As we typically look at this in the rotating reference frame — precessing with $\omega = \gamma B_0$ — we can drop the first term and write

$$\omega(\vec{r}, t) = \gamma \Delta B + \gamma \vec{G}(t) \cdot \vec{r}(t). \tag{2.5}$$

The MR signal which gets picked up by the radiofrequency coil is complex valued, which means every image consists of a magnitude and a phase component

$$I(\vec{r}, \rho, T_1, T_2) = |I(\vec{r}, \rho, T_1, T_2)| e^{i\phi}. \tag{2.6}$$

The image intensity is a function of space ($\vec{r}$), hydrogen-1 density (ρ), and intrinsic tissue relaxation times T_1 and T_2. Fig. 2.5 shows an example for both a magnitude and phase image slice. As illustrated in Fig. 2.6 signal phase adds up as the gradients are played out and the stronger the gradient amplitude and the longer they are turned on, the more phase accumulates.

Most conventional MRI sequences only make use of the magnitude image data which typically depicts anatomical information. However, in PC MRI, the phase component is used to sensitize velocity of moving spins. To determine the phase that spins at a specific location accrue up until the echo time (T_E), we integrate equation 2.5 over T_E:

$$\phi(\vec{r}, t) = \gamma \Delta B T_E + \gamma \int_0^{T_E} \vec{G}(t) \cdot \vec{r}(t). \tag{2.7}$$

$\gamma \Delta B T_E$ is referred to as the phase offset ϕ_0. To describe the position of any spin, we expand $\vec{r}(t)$ with its Taylor series expansion

$$\vec{r}(t) = \vec{r}_0 + \vec{v}t + \frac{1}{2}\vec{a}t^2 + \dots \tag{2.8}$$

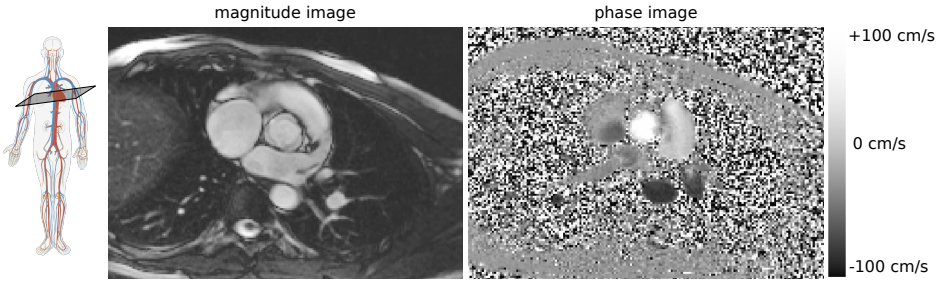

Figure 2.5: Magnitude (from cine bSSFP sequence) and phase (from PC MRI sequence) image data. The 2D slice was prescribed such that it cuts through the base of the heart and the aortic valve. Image acqisiton was triggered to peak systole to capture the open aortic valve.

For the purpose of describing the coherent motion blood elements we may neglect any second or higher order term in Eq. 2.8, thus the phase that is accrued while playing the magnetic gradient is

$$\phi(\vec{r},t) = \phi_0 + \gamma\vec{r}_0 \int_0^{T_E} \vec{G}(t)dt + \gamma\vec{v} \int_0^{T_E} \vec{G}(t)tdt. \tag{2.9}$$

Following the phase offset term ϕ_0 we can now see what is called the 0th and 1st moment of the gradient:

$$M_0 = \int_0^{T_E} \vec{G}(t)dt \qquad \text{and} \qquad M_1 = \int_0^{T_E} \vec{G}(t)tdt. \tag{2.10}$$

Equation 2.9 already hints at the relationship between the velocity $\vec{v}$ of moving spins and the accumulated phase. The key for generating phase data that directly describe the velocity of moving spins is to play gradients which effectively null M_0, and for which M_1 is nonzero. (Additionally, we need to cancel out the ϕ_0 term, as described in sec. 2.2.2). If this condition for gradient moments holds true, the relationship between the acquired phase and velocity of spins moving along the gradient direction can be described as

$$\phi(\vec{r},t) = \gamma\vec{v}M_1. \tag{2.11}$$

In practice, to achieve $M_0 = 0$ and $M_1 \neq 0$, we utilize so-called bipolar gradients (Fig. 2.7, bottom), for which the net phase after τ is zero for static spins but nonzero for moving spins. Other MR imaging sequences for which accumulated phase is unwanted as phase offsets lead to a number of phase-related artifacts (e.g. flow artifacts) need to be designed such that M_1 is nulled, too. This principle is then referred to as a flow or motion compensated gradient waveforms (Fig. 2.7, top) and will come in handy for canceling out the ϕ_0 term.

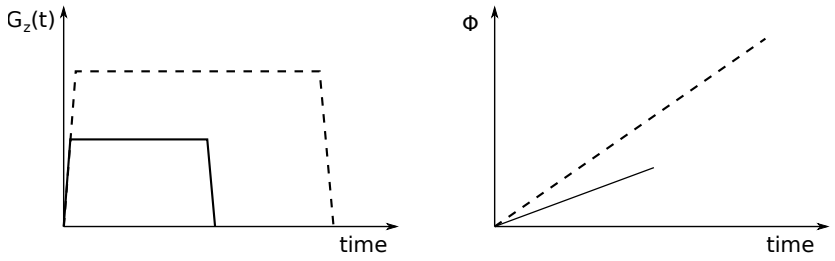

Figure 2.6: Relationship between played gradient $G_z(t)$ and accrued phase ϕ for a static spin.

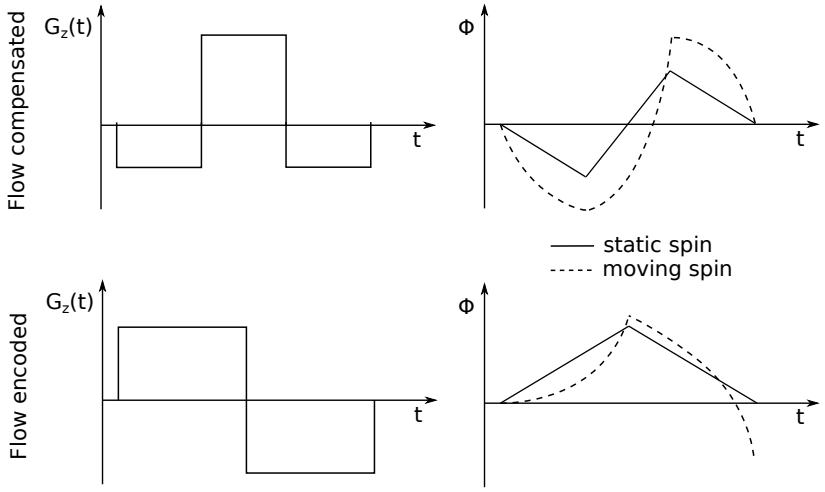

Figure 2.7: Flow compensating (top) and flow encoded (i.e. bipolar, bottom) gradient waveforms and accrued phase for static and moving spins. In PC-MRI we make use of both gradient waveforms to sensitize first order blood flow velocity. Note that the second and higher order velocity terms are negligible for our purposes an not displayed here.

2.2.2 *Phase from many things*

Before moving on to introducing the complete pulse sequence used in PC MRI, it is important to understand that phase in the complex valued MR signal originates from many things besides motion. Needless to say, we intentionally induce phase shifts while playing out gradients to spatially encode the MR signal in the second dimension of k-space ('phase-encode direction', k_y). But phase offsets also originate from (i) B_0 field inhomogeneity and susceptibility effects (referred to as off resonance effects, ϕ_0), (ii) chemical shift effects (ϕ_{cs}), (iii) Maxwell terms ($\phi_{maxwell}$), also known as concomitant fields, and (iv) eddy currents (ϕ_{eddy}).

To correct for (i) ϕ_0 (as given in equation 2.9), one widely adapted approach is to run one flow compensated pulse sequence with M_0 and M_1 nulled, followed by a flow encoded pulse sequence with M_0 nulled and M_1 nonzero. As both data should have identical ϕ_0, we

then reconstruct a phase difference map to cancel out the unwanted phase offset and end up with the phase difference:

$$\Delta\phi = \gamma\vec{v}\Delta M_1. \tag{2.12}$$

Note that in practice, we do not run this subtraction on the final pixel-by-pixel velocity maps, but perform multiplication of the complex flow compensated data with the complex conjugate of the flow encoded data [10].

Other sources of phase offsets (ii – iv) would lead to substantially inaccurate velocity maps and perturbed quantitative flow parameters if not corrected for. These effects and methods for correction are described in detail elsewhere [12, 28, 53, 59].

To summarize, ϕ_{cs} can be mitigated by selecting a mid to high RF bandwidth, though we trade off SNR by doing so; $\phi_{maxwell}$ can be corrected for analytically; and ϕ_{eddy} can be minimized by estimating a phase difference offset map for each scan and subtracting this offset map from the final phase difference volume. This map can be generated by either fitting a polynamial through (known) stationary tissue, or by running an additional PC MRI scan using a static phantom for which the image output directly depicts the offset map. While the former is dependent on having sufficient static tissue within the FOV [21], latter adds an additional phantom scan and thus is typically not done as part of the clinical routine.

To complete the list of necessary PC MRI correction steps: distortion effects in both magnitude and phase data owing to (imperfect) nonlinear gradients are system-specific and can (must) be corrected for, e.g. as proposed by Markl et al. [87].

2.2.3 *Velocity sensitivity and V_{enc}*

The net gradient moment ΔM_1 in the phase difference term (Eq. 2.12) gives rise to the proportionality between the spin velocity and the reconstructed phase difference $\Delta\phi$.

$$\vec{v} = \frac{\Delta\phi}{\gamma\Delta M_1}. \tag{2.13}$$

The maximum phase that we can measure is $\pm\pi$ which leads us to the so-called velocity encoding strength (V_{enc}), that is the velocity which gets mapped to a phase shift $\pm\pi$:

$$\pm V_{enc} = \frac{\pm\pi}{\gamma\,|\Delta M_1|}. \tag{2.14}$$

All other velocities smaller than $|V_{enc}|$ are mapped to a phase number between 0 and $\pm\pi$ as illustrated in Fig. 2.8. V_{enc} is one of the

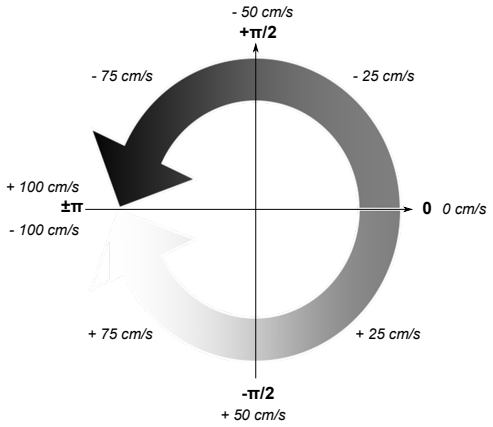

Figure 2.8: Mapping accrued phase shifts to absolute velocities with V_{enc} = 100 cm/s.

important parameters to define prior to the PC MRI acquisition and should be chosen such that peak velocities within the region of interested are captured. However, we trade-off low velocity noise (σ_v) when setting a higher V_{enc}, according to this linear relationship:

$$\sigma_v = \frac{\sqrt{2}}{\pi} \frac{V_{enc}}{SNR}, \tag{2.15}$$

where SNR is the signal-to-noise-ratio of the MRI signal magnitude.

Velocities higher than the chosen V_{enc} will induce phase wrap-around artifacts. For example, if V_{enc} = 100 cm/s, a velocity vector with $|\vec{v}|$ = 110 cm/s will map to $|\vec{v}|$ = 90 cm/s with swapped sign. This phenomenon is also referred to as *aliasing* and can — to a certain extend — be corrected for with image post-processing [66, 79].

2.2.4 *2D PC MRI sequence*

We use a spoiled gradient echo (SPGR) pulse sequence as base to develop our flow encoding PC MRI pulse sequence (Fig. 2.9). An SPGR consists of an RF excitation pulse played together with the slice-select gradient (G_{slice}), followed by a phase-encoding gradient (G_{phase}), followed by a readout gradient (G_{read}) during which the MR signal (echo) is collected, followed by a spoiler gradient to crush remaining transverse magnetization before the next RF excitation and T_R interval. To generate a 2D image with N lines along phase-encode direction, this pulse sequence needs to be repeated N times to fill in a fully sampled k-space.

To modify the SPGR sequence toward a PC MRI acquisition, we need to add necessary gradient lobes for flow compensation and flow encoding (Fig. 2.10). The flow compensated part includes the M_0 and M_1 nulled gradients, shifting the readout section in time. It is followed by the flow encoded part which includes the bipolar gradient lobes.

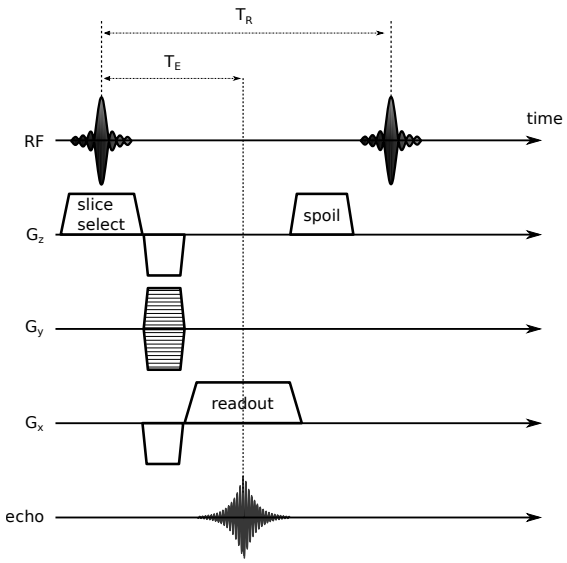

Figure 2.9: Pulse sequence diagram for spoiled gradient echo (SPGR) acquisition. Note that this sequence is neither M_0 nor M_1 nulled and phase will accumulate over time.

Again, this line of gradient waveforms needs to be repeated for every phase encoding step. We can already see that encoding velocity into phase requires additional time compared to a conventional SPGR ($> 2T_R$).

2.2.5 *k-space segmentation*

In cardiovascular motion and flow imaging, we typically are interested in temporally resolved data (labeled *cine* in MRI jargon). In this context, a widely established concept is *k-space segmentation*, as illustrated in Fig. 2.11.

An electrocardiogram (ECG) provides a trigger signal at the time of the QRS complex which initiates data acquisition at the beginning of the cardiac cycle. The cardiac cycle gets divided up into N temporal frames, also referred to as cardiac frames, and for each frame only a segment of k-space is filled in. The segment size — i.e. the number of k-lines — can vary, but ultimately it influences the effective temporal resolution or cardiac frame length. During the first RR cycle, we fill in segment 1 for each cardiac frame, during the second RR cycle, we fill in segment 2 of each frame, etc. The acquisition is complete once all segments are filled in and after reconstruction we end up with a stack of N images representing one cardiac cycle that in fact were stitched together over multiple heart beats.

The performance and efficiency of k-space segmentation is dependent on a 'clean' ECG signal and (ideally) constant HR without much variation over the duration of the scan. For example, patients with cardiac arrhythmia pose a challenge for efficient k-space segmentation.

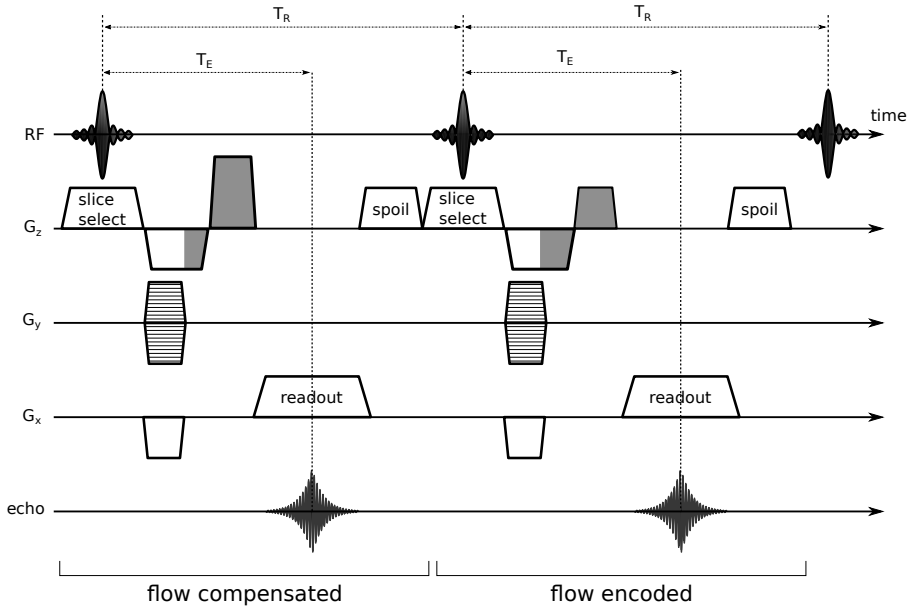

Figure 2.10: Pulse sequence diagram for through-plane encoded 2D PC MRI acquisitions using a flow compensated and flow encoded part. The gradient lobes nulling M_0 and M_1 (flow compensated part) and nulling M_0 only (with $M_1 \neq 0$) (flow encoded part with bipolars) are shaded in gray. The effective temporal resolution decreases by a factor of 2 as two TR cycles (or two echos) are needed.

To give a simple example for sequence run time: A 2D PC MRI single-direction encoded acquisition to generate an image with matrix size 256×160 (i.e. 160 k_y lines), with $T_R = 5\,\text{ms}$, single averaging, five k_y lines per segment, no acceleration technique applied, and a given cardiac cycle length of 1000 ms (HR = 60 min^{-1}) provides spatial resolution of $1.5 \times 1.5\ \text{mm}^2$, temporal resolution of 50 ms (or 20 image frames) and it would take 40 heart beats (40 s) to acquire k-space. Note that image frame length is a product of T_R, number of lines per segment, and the factor 2, as we need to acquire the flow compensated and flow encoded part.

2.3 MULTI-DIRECTIONAL FLOW ENCODING (4D-FLOW MRI)

So far, we have reviewed 2D PC MRI, which generates a 2D time-resolved tomographic magnitude and phase-contrast image where the velocity of moving spins along a selected direction (e.g. through-plane) is encoded into phase. This acquisition technique can be extended to encode velocity in all three spatial directions (Fig. 2.12), then referred to as 2D PC MRI with 3-directional velocity encoding.

To enable velocity encoding in x, y, and z direction, we need to play nonzero M_1 bipolar gradients in all three encoding directions (two in-plane, one through-plane). Here, one widely established approach

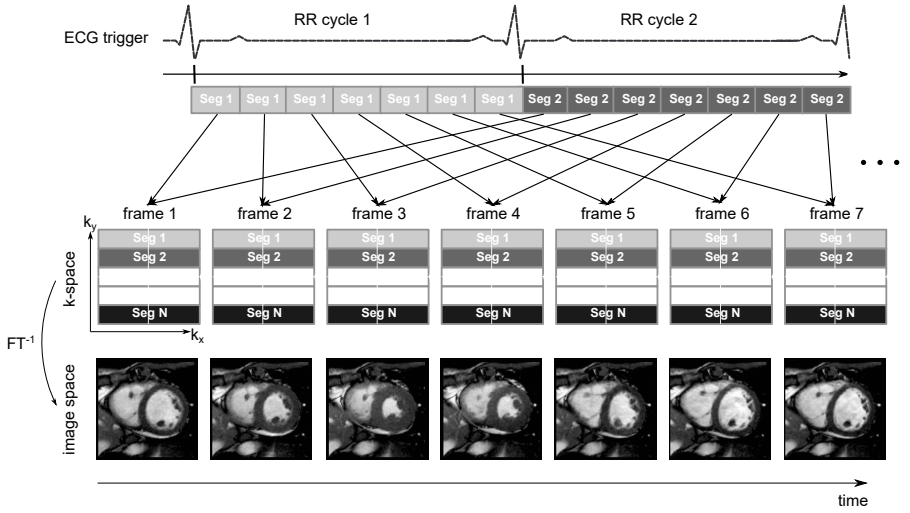

Figure 2.11: k-space segmentation with an electrocardiogram (ECG) trigger to acquire cine data of the beating heart. (Image courtesy of Daniel B. Ennis, with adaptations)

is the 4-point method. That means we run one flow compensated reference scan with a nulled M_0 and M_1, followed by three flow encoded scans, one for each encoding direction, each with a bipolar gradient in the respective direction. The flow compensated data serves as reference for correcting for ϕ_0 in all three flow encoded scans. Besides the 4-point method, there are several other velocity encoding techniques, which will not be described here [29, 39, 67, 105].

We can move to even higher dimensions by acquiring a cine 3D slab rather than a single cine slice. This sequence is referred to as cine 3D PC MRI with 3-directional velocity encoding, or short, *4D flow MRI* [88].

The development of 4D flow MRI opened up new possibilities for studying hemodynamics with several advantages over conventional 2D PC MRI. Given a fully dimensional velocity vector map, we can perform retrospective multi-planar reformatting in arbitrary orientation (Fig. 2.13). Contrary to cine 2D PC MRI, there is no need to manually choose a specific image plane that cuts through the cross-section of interest (e.g. heart valve) prior to running the scan, which is necessary for 2D PC MRI. Further, 3D visualization techniques can be used to qualitative assess flow patterns and velocity distribution with streamlines, or trace particles through one or more cardiac cycles given the time-resolved underlying velocity vector field. On the quantitative side, we can retrieve a number of hemodynamic parameters that will be described in detail in sec. 2.4.

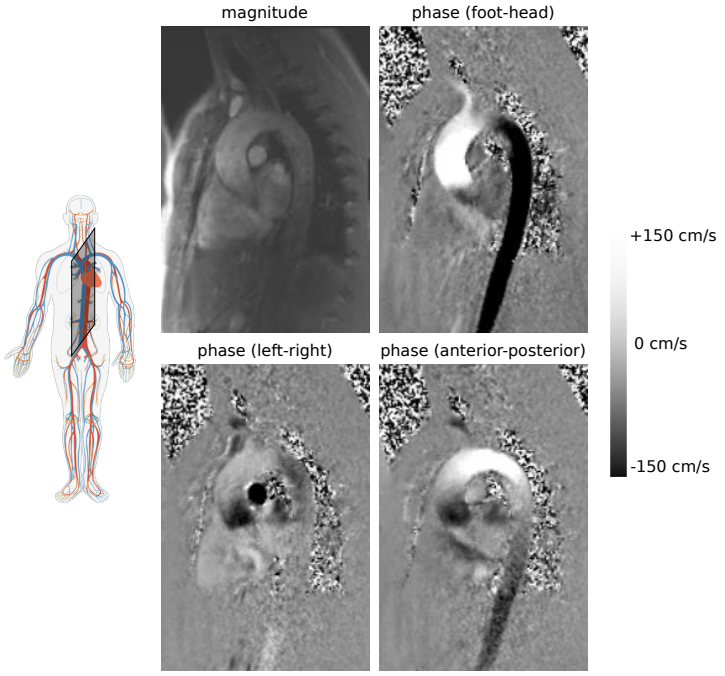

Figure 2.12: 2D PC magnitude and three-directional phase image data with the 2D slice prescribed in sagittal orientation cutting through the aorta ('candy cane view'). The peak systolic frame is shown.

2.3.1 *Scan time and acceleration techniques*

The key challenge with 4D flow MRI is scan time, in particular when it comes to deploying it as part of the clincial routine. In comparison to 2D PC MRI, it is obvious that more time is spent to acquire this high-dimensional dataset. In fact, if we were to run a a whole heart 4D flow MRI scan in the most conventional way with 3 mm through-plane resolution (i.e. at least 40 slices needed to cover most of the heart), in-plane acquisition matrix 256×160, $T_R = 5$ ms, single averaging, two k_y lines per segment, and a given cardiac cycle length of 1000 ms (HR = 60 min), we would scan over 3200 heartbeats (> 53 min) at a temporal resolution of 40 ms. This time increases even further as we apply a motion-controlling breathing navigator which may reduce scan efficiency down to approximately 60 %; that is, the actual data acquisition only takes place during 60 % of the scan duration, and total scan time becomes well over 1 h.

Therefore, acceleration techniques are inevitable for *in vivo* cardiovascular 4D flow MRI. Many concepts for acceleration exist, but the most important are listed below.

PARALLEL IMAGING With parallel imaging (or parallel acquisiton technique, PAT) we purposefully undersample k-space and leverage the spatial information of the multiple elements in the RF coil arrays to reconstruct an image free of aliasing artifacts [33, 55, 111]. Parallel

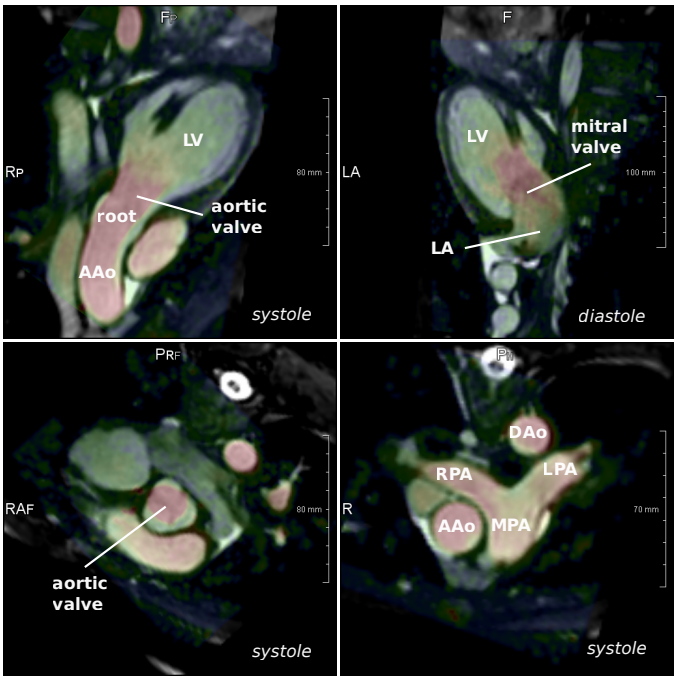

Figure 2.13: Reformatted planar views of the heart (based on 3D SPGR sequence) with absolute velocity overlay (based on 4D flow sequence). AAo: ascending aorta, DAo: descending aorta, LV: left ventricle, LA: left atria, MPA: main pulmonary artery, RPA: right pulmonary artery, LPA: left pulmonary artery.

imaging techniques and its many derivatives (e.g. multidimensional PAT as in k-t GRAPPA) are often used techniques to accelerate 4D flow MRI [5, 17, 68, 117, 118, 127].

COMPRESSED SENSING Compressed sensing (CS) [83, 84] uses incoherent (randomized) k-space undersampling, sparsity transformation, and an iterative optimization process during reconstruction, and in recent years has shown promising results for highly accelerated 4D flow MRI [85, 104, 134]. As per limitations, CS requires longer reconstruction times and may introduce CS-related artifacts, such as blurring of fine details or global ringing.

NON-CARTESIAN SAMPLING As an alternative to sampling k-space on a conventional cartesian grid, other non-cartesian trajectories (e.g. 3D radial projections as in PC VIPR [56, 98]) have been explored to run highly-accelerated 4D flow MRI. Here, acceleration is achieved by shortening the time that is spent to traverse k-space, combined with inherent k-space undersampling.

ECHO PLANAR IMAGING Advances in gradient hardware (i.e. very fast slewing) paved the way to establish echo planar imaging (EPI) [128] techniques that aim to acquire k-space during a single or only a few

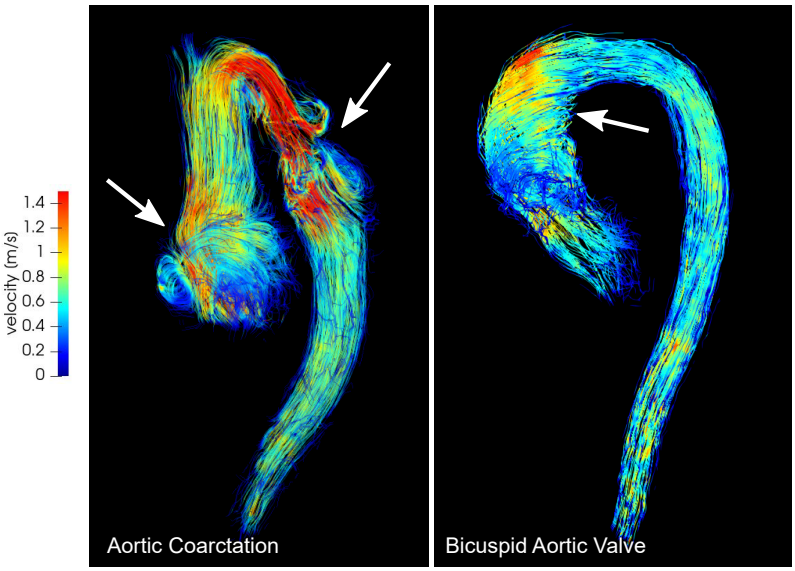

Figure 2.14: 4D flow MRI streamline visualization in congenital defects of the aorta: (left) coarctation of DAo with increased flow velocity through stenotic region, and dilated aortic root with strong flow vortices at cusps; (right) bicuspid aortic valve that mediates helical flow in AAo.

RF excitation events. Multiple studies of recent years reported to have deployed EPI with 4D flow MRI [23, 38, 44].

Nowadays, by making use of these acceleration concepts, a whole heart 4D flow MRI scan with adequate spatio-temporal resolution (e.g. $2.5 \times 2.5 \times 2.5$ mm^3 voxel size, 40 ms cardiac frame length) may take no more than 10 minutes. While this is great news for establishing 4D flow MRI as part of the standard clinical imaging protocol[1], one also needs to acknowledge the possible negative effects on quantitative image quality due to acceleration. For example, Dillinger et al. showed considerable velocity misregistration and degradation of resolution in high velocity regimes when using EPI readout [34]. Schnell et al. [118] show significant differences in peak and mean WSS when using k-t-GRAPPA with acceleration factor R=5.

2.3.2 *Acquisition and processing pipeline*

After data acquisition, several processing steps must be performed to prepare image data for qualitative and quantitative assessment. Fig. 2.15 outlines a typical 4D flow MRI acquisition and processing pipeline and hints at the many steps that need to be performed towards obtaining quantitative hemodynamic parameters.

1 For the application of 4D flow MRI in the clinical setting, the 4D flow MRI consensus statement provides a good reference for setting up sequence parameter [43].

Raw data (i.e. multi-dimensional k-space) will either be reconstructed online (at the MRI scanner workstation) or offline, in case the necessary reconstruction software framework is not available online. Latter typically applies to in-house developed 4D flow sequences with advanced reconstruction requirements. Raw data size may be well over 20 GB for a whole heart imaging volume. Data correction (i.e. compensating for phase offsets, distortion control, etc.) is either done in the Fourier domain (k-space) or the image domain.

Before running qualitative and quantitative flow assessment, several (3D+t) segmentation and/or registration tasks are required. For example, a 3D (or 3D+t) segmentation of the vessel of interest can be used to mask the 3D+t velocity vector field for optimized flow rendering; and cross-sectional lumen contours that are tracked over time are essential to calculate through plane net flow. The magnitude image component displays anatomical information and can be used for these pre-analysis tasks. Other anatomical MRI data that were acquired as part of the exam may also be used. Unless patient bulk motion occurred, all images should be co-registered and 'live' in the same reference frame.

Finally, data is ready to be processed for qualitative visualization and/or quantitiative hemodynamics analysis. Quantitative parameters will be defined in more detail in the following sec. 2.4. A comprehensive survey of 4d flow MRI qualitative and quantitative post-processing was published by Köhler et al. [71].

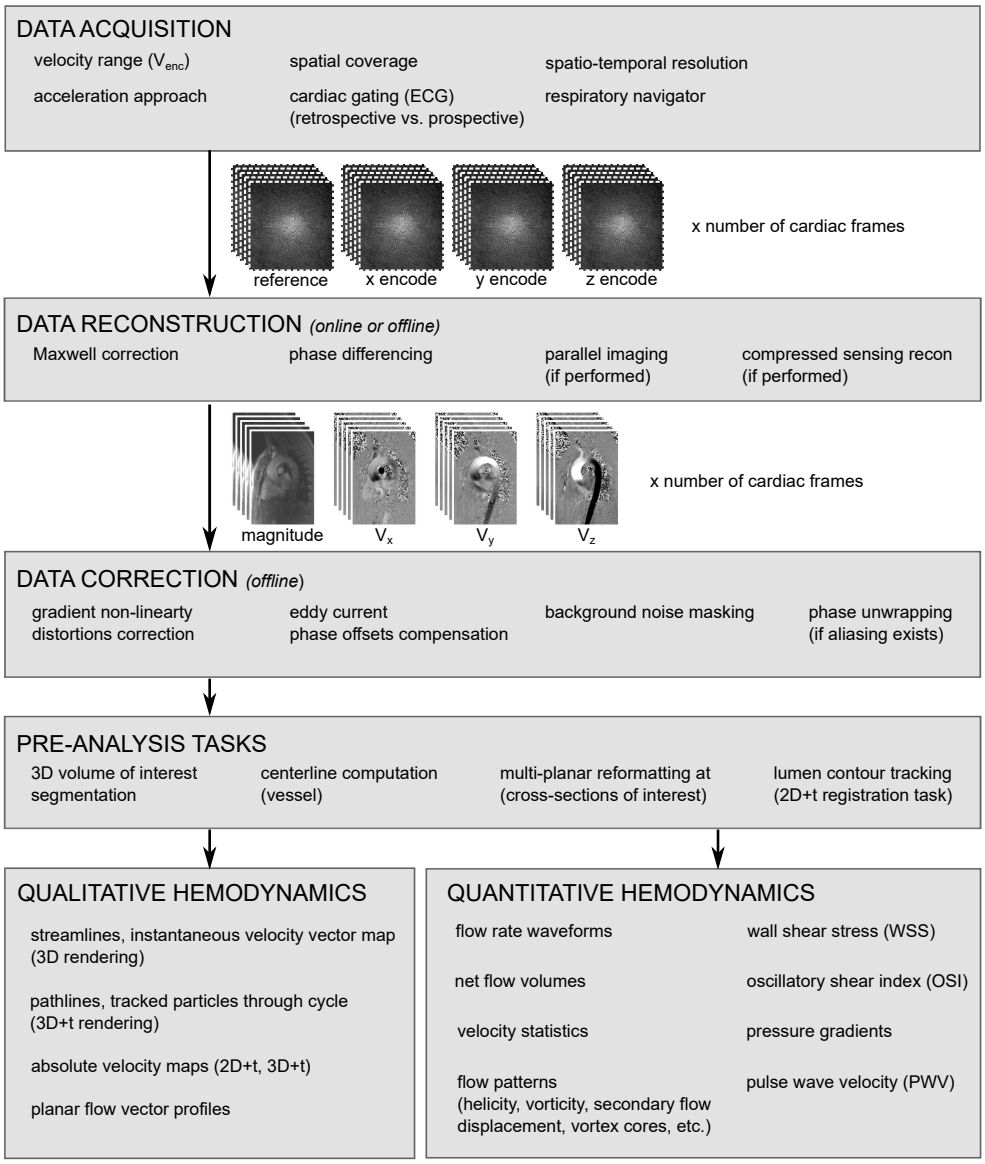

Figure 2.15: 4D flow MRI acquisition and processing pipeline. Data acquisition lists the most important parameters which need to be confirmed (case-by-case) prior to sequence run. For qualitative assessment, a variety of visualization can be done, only a few examples are listed here. For definition of quantitative parameters, see sec. 2.4.

2.4 IMAGE-BASED HEMODYNAMIC PARAMETERS

Given a 3D and time-resolved velocity vector field many quantitative hemodynamic parameters can be derived. The following should list most of those that have been applied in the context of quantitative 4D flow MRI analysis, but certainly include all of which that were studied in this dissertation.

FLOW The time-dependent volumetric *flow rate* (in mL/s) through an arbitrarily oriented cross-section c is defined as the surface integral

$$Q_c[t] = \iint_{A_c} \langle \boldsymbol{v}[\boldsymbol{x}, t], \boldsymbol{n}_c \rangle dA_c, \tag{2.16}$$

where $\boldsymbol{v}[\boldsymbol{x}, t] \in \mathbb{R}^3$ is a time-dependent 3D velocity vector at position $\boldsymbol{x} \in \mathbb{R}^3$, A_c is the cross-sectional area, and $\boldsymbol{n}_c \in \mathbb{R}^3$ is the plane normal defining A_c. Given a planar-reformatted discrete image, in order to calculate the volumetric flow rate, we implement

$$Q_c[t] = \sum_i \langle \boldsymbol{v}_i[t], \boldsymbol{n}_c \rangle \Delta A_c, \tag{2.17}$$

where i presents indices of all pixels that lay within the closed contour and ΔA is the pixel area size. (Note that the definition for an 'enclosed pixel' may vary between implementations for flow rate which adversely affects contour-based quantification.)

Net flow (positive or negative valued, in mL [per cycle]) is then calculated as

$$V_{cycle} = \sum_{t=0}^{N-1} Q_c[t] \Delta t, \tag{2.18}$$

where N is the number of temporal (cardiac) frames and Δt is the frame length.

As the notation of flow rate accounts for the plane normal direction, the *forward flow volume* (FFV, in mL [per cycle]) and *backward flow volume* (BFV, mL [per cycle]) are defined as the area above and below $Q_c[t] = 0$. Consequently, we define the *regurgitant fraction* (RF, in %) through a cross-section as

$$RF = \frac{BFV}{FFV + BFV} \cdot 100. \tag{2.19}$$

Lastly, *peak flow rate* (in mL/s) is defined as

$$Q_{max} = \max_t Q_c[t] \tag{2.20}$$

and may be used to define the *peak systolic* frame (t_{sys})

$$t_{sys} = \arg\max_t Q_c[t]. \tag{2.21}$$

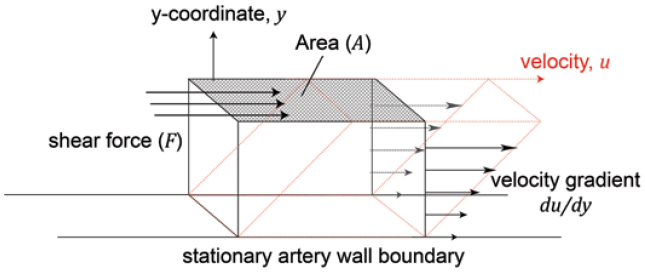

Figure 2.16: Shear stress and velocity gradient arising from an applied force deforming a rectangular fluid element. (Image courtesy of Tu et al. [132])

VELOCITY STATISTICS Time-dependent velocity statistics (in cm/s) are computed either on a 2D reformatted cross-section or a 3D (sub-) volume of interest. We define the *maximum*, *minimum*, and *mean velocity* across all pixels/voxels i as

$$\begin{aligned} v_{max}[t] &= \max_i \|\boldsymbol{v}_i[t]\|,\ v_{min}[t] = \min_i \|\boldsymbol{v}_i[t]\|, \text{ and} \\ v_{mean}[t] &= \frac{1}{M}\sum_i \|\boldsymbol{v}_i[t]\| \end{aligned} \tag{2.22}$$

with M being the number of enclosed pixels/voxels as defined by the contour (in 2D) or surface mesh (in 3D). The magnitude of each velocity vector is defined by the euclidean norm:

$$\|\boldsymbol{v}_i[t]\| = \sqrt{v_{1,i}^2 + v_{2,i}^2 + v_{3,i}^2}. \tag{2.23}$$

WALL SHEAR STRESS Fluid rushing along a boundary layer at which velocities are assumed to be zero ('no-slip-condition') will incur shear stress at that boundary (Fig. 2.16). For an incompressible, Newtonian fluid and assuming a 1D scenario with velocity $v \in \mathbb{R}^1$ (for simplicity) and dynamic fluid viscosity μ we define shear stress as

$$\tau(y) = \mu\frac{\delta v}{\delta y} \tag{2.24}$$

where y is the height above the boundary layer. More specific, *wall shear stress* (WSS, in N/m^2) refers to shear stress at a solid structure (here also in 1D):

$$\tau_w(y) = \tau(y=0) = \mu\frac{\delta v}{\delta y}\Big|_{y=0}. \tag{2.25}$$

In the case of a 3-directional flow field ($\vec{v} = (v_1, v_2, v_3)^T$) defined in 3D space ($\vec{x} = (x_1, x_2, x_3)^T$) this notation becomes more complex and requires the 3D derivative of the velocity vector field:

$$\vec{\tau}_w = \mu \cdot \begin{pmatrix} 2n_1\frac{\delta v_1}{\delta x_1} + n_2(\frac{\delta v_1}{\delta x_2} + \frac{\delta v_2}{\delta x_1}) + n_3(\frac{\delta v_1}{\delta x_3} + \frac{\delta v_3}{\delta x_1}) \\ n_1(\frac{\delta v_1}{\delta x_2} + \frac{\delta v_2}{\delta x_1}) + 2n_2\frac{\delta v_2}{\delta x_2} + n_3(\frac{\delta v_2}{\delta x_3} + \frac{\delta v_3}{\delta x_2}) \\ n_1(\frac{\delta v_1}{\delta x_3} + \frac{\delta v_3}{\delta x_1}) + n_2(\frac{\delta v_2}{\delta x_3} + \frac{\delta v_3}{\delta x_2}) + 2n_3\frac{\delta v_3}{\delta x_3} \end{pmatrix}. \quad (2.26)$$

The WSS vector $\vec{\tau}_w \in \mathbb{R}^3$ at each wall point is three-dimensional and time-dependent. $\vec{\tau}_w$ can be projected onto the vessel's tangent plane at the evaluated wall point ($\vec{\tau}_{w,tang}$), and further be decomposed into its axial ($\vec{\tau}_{w,axial}$) — i.e. parallel to the vessel centerline — and circumferential ($\vec{\tau}_{w,circ}$) — i.e. tangential to a cross-sectional contour in 2D — vector component. For each component, we typically report the vector length, e.g. $\|\vec{\tau}_{w,tang}\|$.

If we wish to estimate WSS along wall contour points on a reformatted cross-sectional plane, we then have $\vec{n} = (n_1, n_2, 0)^T$, and with the assumption of no flow through the vessel boundary — i.e. $\langle \vec{n}, \vec{v} \rangle = 0$ — we can imply

$$\vec{n} \cdot \frac{\delta \vec{v}}{\delta x_3} = n_1\frac{\delta v_1}{\delta x_3} + n_3\frac{\delta v_2}{\delta x3} = 0 \quad (2.27)$$

and equation 2.26 is reduced to

$$\vec{\tau}_w = \mu \begin{pmatrix} 2n_1\frac{\delta v_1}{\delta x_1} + n_2(\frac{\delta v_1}{\delta x_2} + \frac{\delta v_2}{\delta x_1}) \\ n_1(\frac{\delta v_1}{\delta x_2} + \frac{\delta v_2}{\delta x_1}) + 2n_2\frac{\delta v_2}{\delta x_2} \\ n_1\frac{\delta v_3}{\delta x_1} + n_2\frac{\delta v_3}{\delta x_2} \end{pmatrix}. \quad (2.28)$$

In practice, given a discrete velocity map that is sampled on a rasterized image grid, there are several ways to implement spatial derivatives for WSS estimation. Each of which may affect the final WSS output. More details on this were described by Petersson et al. [108].

Besides time-resolved WSS, we define the *time-averaged WSS* as

$$\text{TAWSS} = \frac{1}{N}\sum_{t=0}^{N-1} |\vec{\tau}_w| \quad (2.29)$$

where N is the number of acquired time frames. Further, the *oscillatory shear index* (OSI, unitless $\in [0..0.5]$) describes the fluctuation of the WSS vector direction over time

$$\text{OSI} = \frac{1}{2}\left(1 - \frac{\left|\int_0^T \vec{\tau}_w dt\right|}{\int_0^T |\vec{\tau}_w|\, dt}\right). \quad (2.30)$$

It should be noted that all WSS-related metrics are defined for any wall point on the 2D vessel contour or 3D vessel surface. Binning these wall points into circular segments is useful to ease presentation and analysis of quantitative results and to enable intra- and inter-case comparisons. An example for how to present all WSS-related statistics using wall point correspondence and arc segments is presented in [147].

FLOW DISPLACEMENT The *normalized flow displacement* (NFD, unitless $\in [0..1]$) [122] describes the eccentricity of a cross-sectional non-parabolic flow profile. NFD is defined as the distance of 'center of velocity' (c_v) from the lumen center, normalized to the lumen radius, where

$$c_v = \frac{\sum_i r_i \|\boldsymbol{v}_i\|}{\sum_i \|\boldsymbol{v}_i\|}. \tag{2.31}$$

and $r_i \in \mathbb{R}^3$ is the pixel center position of lumen pixel i.

SECONDARY FLOW We can decompose the velocity vector into a through-plane ($\vec{v}_{tp}$) and in-plane ($\vec{v}_{ip}$) component. The in-plane component is referred to as secondary flow. We can then define a *secondary flow index* (SFI, $\in [0..1]$) to describe the relative amount of in-plane flow as:

$$\text{SFI} = \frac{\|v_{ip}\|}{\|v_{tp}\| + \|v_{ip}\|}. \tag{2.32}$$

SWIRLING FLOW With regard to describing swirling flow patterns, the term *vortex* describes in-plane swirling motion with negligible forward motion in the centerline direction; other swirling motion patterns are termed *helix*.

In this context, the mathematical notation of *vorticity*, or *curl*, of a 3D vector field defined on $\boldsymbol{x} = (x_1, x_2, x_3)^T$ is calculated as

$$\vec{\omega} = \nabla \times \vec{v} = \begin{pmatrix} \frac{\delta v_3}{\delta x_2} - \frac{\delta v_2}{\delta x_3} \\ \frac{\delta v_1}{\delta x_3} - \frac{\delta v_3}{\delta x_1} \\ \frac{\delta v_2}{\delta x_1} - \frac{\delta v_1}{\delta x_2} \end{pmatrix}. \tag{2.33}$$

Vorticity (in s^{-1}) is vector valued and defined per voxel; its norm describes the strength of the local spinning motion at that position, while its direction describes the rotational axis per right-hand-rule.

Intuitively, velocity-based vorticity maps (e.g. displayed as voxel-by-voxel heat maps) can be used as visual indicator of swirling flow [136].

(However, keep in mind that $\vec{\omega} \neq 0$ at the vessel boundary, too, or in general any location with spatial velocity gradient.)

Based on the notation of vorticity, Lorenz et al. [81] utilized *helicity density* H_d and *relative helicity* H_r — both defined voxel-by-voxel — to characterize helical flow in the thoracic aorta:

$$H_d = \vec{\omega} \cdot \vec{v} \qquad \text{and} \qquad H_r = \frac{H_d}{\|\vec{\omega}\| \|\vec{v}\|} \tag{2.34}$$

To get a more explicit description of the core location in 3D vessel space, Spiczak et al. [136] proposed to combine the prediction-correction method with the λ_2 criterium [64] to define a core line; and Drexl et al. [37] combined vorticity maps with a vector pattern matching (VPM) approach, as propsed by Heiberg et al. [58].

Based on a detected core, we can characterize the core and its surrounding swirling pattern by quantitative metrics. These metrics of interest include elongation of the core, size with respect to cross-sectional lumen area, velocity statistics of the swirling velocity field, swirling direction (left or right handed), or the temporal occurrence and duration within cardiac cycle.

PULSE WAVE VELOCITY The pulse wave velocity (PWV, in m/s) of pulsatile flow is a descriptor of arterial stiffness, as defined by the Moens-Korteweg equation:

$$\text{PWV} = \sqrt{\frac{Eh}{2\rho r}} \tag{2.35}$$

where E is the vessel wall's elastic modulus, h the wall thickness, r the vessel radius, and ρ the fluid density.

For image-based PWV estimation, we analyze the relative time shift of derived flow rate waveforms (Eq. 2.16) at two or more cross-section along the vessel's centerline [48, 89, 92, 138]. PWV is then estimated as distance-over-time

$$\text{PWV} = \frac{\triangle d}{\triangle t} \tag{2.36}$$

where $\triangle d$ is a fixed distance along the centerline and $\triangle t$ is the relative temporal offset of flow rate waveforms obtained at sections along the centerline. The temporal offset can be obtained in multiple ways — e.g. time-to-foot (TTF), time-to-peak (TTP), or time-to-half-max (TT50) [138].

With 4D flow MRI we can generate an arbitrary number of reformatted cross-sectional planes p_i and thus an arbitrary number of ($\triangle d_{p,i}$, $\triangle t_{p,i}$) value pairs. The final value for PWV is then defined as the inverse slope of a linear regression line fitted to all ($\triangle d_{p,i}$, $\triangle t_{p,i}$) data points. 4D-flow based PWV estimation is dependent on accurate flow rate curves and sufficient temporal resolution to resolve temporal waveform shifts.

PRESSURE The Navier-Stokes equations describe the motion of incompressible Newtonian fluid. They form the basis to recover *relative* — i.e. with respect to an arbitrary reference point in the volume of interest — time-resolved 3D pressure maps $p(\boldsymbol{x}, t)$ (in mmHg) from 4D flow MRI data:

$$\rho(\frac{\delta \boldsymbol{v}}{\delta t} + \boldsymbol{v} \times \nabla \boldsymbol{v}) - \mu \nabla^2 \boldsymbol{v} + \nabla p = 0, \qquad \nabla \times \boldsymbol{v} = 0. \tag{2.37}$$

where $\boldsymbol{v}$: velocity, ρ: fluid density, and μ: dynamic viscosity.

This partial differential equation (PDE) constrained optimization problem can be solved iteratively. $p(\boldsymbol{x}, t)$ results can then be visualized as time-resolved pressure point clouds in a 3D scene and pressure differentials between any two points of interest (e.g. pre- and post-valve, pre- and post-stenosis) can be studied, which has been reported for phantom and *in vivo* studies [16, 47, 82, 95, 113, 133].

TURBULENT KINETIC ENERGY Turbulent kinetic energy (TKE, in $\mathrm{J\,m^{-3}}$) is a descriptor of energy loss in turbulent (i.e. non-laminar) flow regimes, as most of TKE is dissipated into heat. Potential clinical applications of TKE assessment include studying valve performance (e.g. in aortic stenosis) [14, 42].

PC MRI velocity maps represent the averaged velocity of all spins within a voxel, and we can directly derive mean kinetic energy (MKE). Moreover, as described in [41], TKE is defined based on the velocity fluctuation within each voxel:

$$\mathrm{TKE} = \frac{\rho}{2} \sum_{i=1}^{3} \sigma_i^2, \tag{2.38}$$

where σ_i is the variance for *intra-voxel velocity fluctuation*, or intra-voxel standard deviation (IVSD), in encoding direction i and ρ is fluid density.

In contrast to the 4D flow MRI acquisition scheme with flow compensated and flow encoded part, as introduced in sec. 2.3, IVSD mapping requires two flow encoded parts with different first order gradient moments. For each encoding direction, IVSD maps for are then calculated in k-space by combining the PC-MRI signals of these two different first order moments, as described by Dyverfeldt et al. [41].

Part II

CONTRIBUTIONS

3

WALL SHEAR STRESS ESTIMATION IN THE AORTA: IMPACT OF WALL MOTION, SPATIAL RESOLUTION, AND PHASE NOISE

Authors: **Judith Zimmermann**, Daniel Demedts, Hanieh Mirzaee, Peter Ewert, Heiko Stern, Christian Meierhofer, Bjoern Menze, Anja Hennemuth.

In: Journal of Magnetic Resonance Imaging 2018;48(3):718-728 [148]

Abstract: Purpose. To investigate the robustness of wall shear stress (WSS) and oscillatory shear index (OSI) estimation based on 4D flow magnetic resonance imaging (MRI) against vessel wall motion in the ascending aorta (AAo) throughout the cardiac cycle. Also, to compare these sources of error with inaccuracies induced by spatio-temporal resolution and velocity encoding (V_{enc}). *Methods.* Synthetic 4D flow MRI data of the aorta was simulated using the Lattice-Boltzmann method, and was used to vary spatio-temporal and V_{enc} dependent phase noise. 4D flow MRI of the ascending aorta was performed in healthy volunteers (N=11) and patients with congenital heart defects (N=17). Based on three-dimensional cubic B-splines interpolation of the velocity field, WSS was numerically estimated in mid-systole, early-diastole, and late-diastole. As for synthetic data, we studied the impact of spatio-temporal resolution and phase noise. As for *in vivo* data, we quantitatively compared shear stress results based on tracked (using Morphon deformable registration) and static vessel wall location. *Results.* Synthetic data results show systematic over-/underestimation of WSS when different spatial resolution (mean$\pm$1.96SD up to -0.24 ± 0.40 N/m^2 and 0.50 ± 1.38 N/m^2 for 8-fold and 27-fold voxel size, resp.) and V_{enc}-depending phase noise (mean$\pm$1.96SD up to 0.31 ± 0.12 N/m^2 and 0.94 ± 0.28 N/m^2 for 2-fold and 4-fold V_{enc} increase, resp.) are given. Neglecting wall motion when defining the vessel wall perturbs WSS estimates to a considerable extent (1.96SD up to 1.21 N/m^2) without systematic over-/underestimation (Bland-Altman mean ranging from -0.06 N/m^2–0.05 N/m^2). *Conclusion.* In addition to sufficient spatial resolution and velocity to noise ratio, accurate tracking of the vessel wall is essential for reliable image-based WSS estimation and should not be neglected if wall motion is present.

Contributions of J.Z.: study conceptualization, algorithm development and implementation, image acquisition, image data analysis and interpretation, writing and editing of manuscript.

ORIGINAL RESEARCH

Wall Shear Stress Estimation in the Aorta: Impact of Wall Motion, Spatiotemporal Resolution, and Phase Noise

Judith Zimmermann, MS,[1,2]* Daniel Demedts, MS,[3] Hanieh Mirzaee, PhD,[3,4] Peter Ewert, MD,[2] Heiko Stern, MD,[2] Christian Meierhofer, MD,[2] Bjoern Menze, PhD,[1] and Anja Hennemuth, PhD[3,4]

Background: Wall shear stress (WSS) presents an important parameter for assessing blood flow characteristics and evaluating flow-mediated lesions in the aorta.
Purpose: To investigate the robustness of WSS and oscillatory shear index (OSI) estimation based on 4D flow MRI against vessel wall motion, spatiotemporal resolution, and velocity encoding (VENC).
Study Type: Simulated and prospective.
Population: Synthetic 4D flow MRI data of the aorta, simulated using the Lattice-Boltzmann method; in vivo 4D flow MRI data of the aorta from healthy volunteers ($n = 11$) and patients with congenital heart defects ($n = 17$).
Field Strength/Sequence: 1.5T; 4D flow MRI with PEAK-GRAPPA acceleration and prospective electrocardiogram triggering.
Assessment: Predicated upon 3D cubic B-splines interpolation of the image velocity field, WSS was estimated in mid-systole, early-diastole, and late-diastole and OSI was derived. We assessed the impact of spatiotemporal resolution and phase noise, and compared results based on tracked—using deformable registration—and static vessel wall location.
Statistical Tests: Bland–Altman analysis to assess WSS/OSI differences; Hausdorff distance (HD) to assess wall motion; and Pearson's correlation coefficient (PCC) to assess correlation of HD with WSS.
Results: Synthetic data results show systematic over-/underestimation of WSS when different spatial resolution (mean $\pm$ 1.96 SD up to $-0.24 \pm 0.40\,N/m^2$ and $0.5 \pm 1.38\,N/m^2$ for 8-fold and 27-fold voxel size, respectively) and VENC-depending phase noise (mean $\pm$ 1.96 SD up to $0.31 \pm 0.12\,N/m^2$ and $0.94 \pm 0.28\,N/m^2$ for 2-fold and 4-fold VENC increase, respectively) are given. Neglecting wall motion when defining the vessel wall perturbs WSS estimates to a considerable extent (1.96 SD up to $1.21\,N/m^2$) without systematic over-/underestimation (Bland–Altman mean range –0.06 to 0.05).
Data Conclusion: In addition to sufficient spatial resolution and velocity to noise ratio, accurate tracking of the vessel wall is essential for reliable image-based WSS estimation and should not be neglected if wall motion is present.
Level of Evidence: 2
Technical Efficacy: Stage 2

J. MAGN. RESON. IMAGING 2018;48:718–728.

Assessing features of blood flow through the cardiovascular system is considered a major task in understanding the development and progression of flow-mediated lesions.[1] Among other valuable hemodynamic parameters, wall shear stress (WSS) is the frictional force of the flowing blood exerted on the vessel wall.[2] Various studies support the hypothesis that changes in WSS are associated with endothelial function,[3–6] valvular diseases,[7–9] vessel malformations,[10] kinetic energy loss,[11] and abnormal wall stiffness.[12] Therefore, WSS is an important clinical parameter for risk stratification of altered hemodynamics and vessel wall characteristics.

View this article online at wileyonlinelibrary.com. DOI: 10.1002/jmri.26007

Received Jan 18, 2018, Accepted for publication Feb 24, 2018.

*Address reprint requests to: J.Z., German Heart Center Munich, Lazarettstrasse 36, 80636 Munich, Germany. E-mail: judith.zimmermann@tum.de

From the [1]Department of Computer Science, Technical University of Munich, Munich, Germany; [2]Department of Pediatric Cardiology and Congenital Heart Defects, German Heart Center at Technical University of Munich, Munich, Germany; [3]Fraunhofer MEVIS Institute for Medical Image Computing, Bremen, Germany; and [4]Institute for Computational and Imaging Science in Cardiovascular Medicine, Charité Universitätsmedizin, Berlin, Germany

Additional supporting information may be found in the online version of this article.

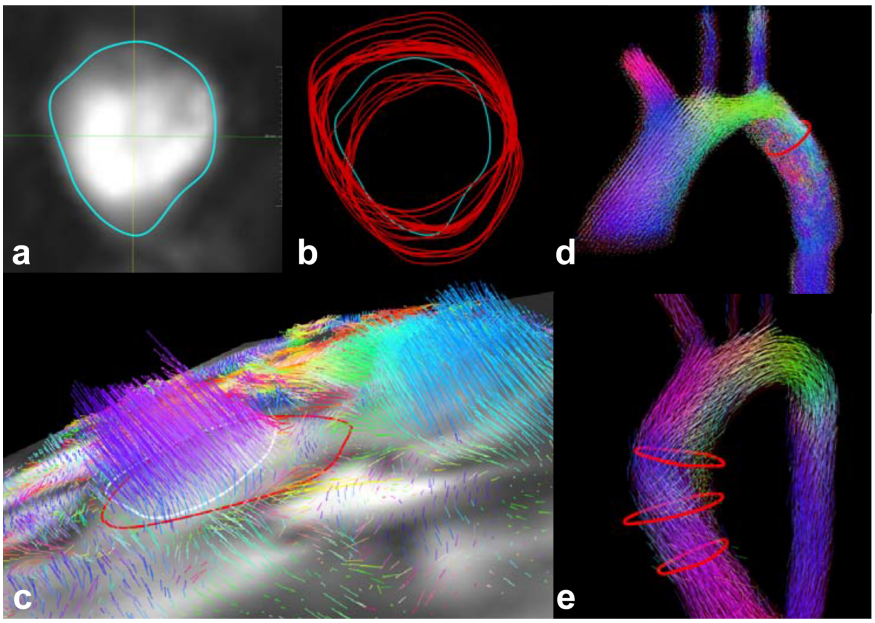

FIGURE 1: A: Reformatted PC-MRA image slice with static contour (blue) based on 3D watershed-based segmentation. B: Wall contours tracked through all cardiac frames (red) based on the deformable registration of subsequent magnitude images. C: Planar velocity field at instantaneous timeframe with tracked contour (red) and static contour (white). Note that A–C depict the identical reformatted image slice. D: Synthetic data with delineated wall contour (red) used for all synthetic data experiments. E: Exemplary in vivo data with three equidistantly spaced wall contours (red) used for in vivo experiments. Vectors are color-coded based on 3D vector direction.

4D flow magnetic resonance imaging (MRI) conveys information on the direction and magnitude of blood flow velocity in all three spatial dimensions. Basic and advanced image analysis paired with intelligent deployment of visualization techniques allow for the assessment of quantitative hemodynamic features. In this context, previous studies presented and evaluated technical developments in order to estimate WSS from 4D flow image data.[10,13,14] Based on the principles of fluid dynamics, WSS (expressed in N/m^2) is linearly dependent on the local velocity gradient along the inward normal of the vessel surface. For incompressible Newtonian fluids, WSS (if a 1D case is considered) is defined as:

$$\vec{\tau} = \eta \left(\frac{\partial \vec{u}}{\partial x} \right)_{x=0} \quad (1)$$

where η: dynamic viscosity of the fluid, u: three-directional fluid velocity, and x: distance from the wall in an inward normal direction.[2] In order to derive the local WSS vector for each imaged timeframe of the cardiac cycle, accurate tracking of the vessel wall points is essential in the first place.

The majority of prior studies considered WSS estimates in peak systole only. Here, a method widely adopted is to segment the vessel of interest based on the time-averaged phase contrast magnetic resonance angiography (PC-MRA) image volume.[10,15–18] However, the resulting surface mesh only represents an approximation of the vessel wall location, as it lacks the dynamics through the cardiac cycle. As the surface mesh based on the PC-MRA image most likely represents the wall location in systole, this approach may be sufficient for assessing systolic WSS. With respect to diastolic timeframes, however, this representation may limit the reliable estimation of WSS. In addition, computing the oscillatory shear index (OSI)—a measure of WSS vector oscillation over time—requires accurate WSS estimates throughout the entire cardiac cycle. To illustrate, Fig. 1A–C depicts the challenges of delineating the wall in a reformatted plane of a 4D flow dataset of the aorta. Here, systolic flow is limited to a certain area of the lumen (captured well by the PC-MRA representation), whereas the true vessel wall strongly deviates from the boundary of systolic flow when tracked throughout the cardiac cycle.

Previous studies assessed the influence of MRI acquisition parameters on shear stress estimates.[13,15,19,20] Particularly, a thorough study by Petersson et al[19] using synthetic data found that image-based WSS estimates are impacted by velocity encoding, velocity resolution, and spatial resolution to a considerable extent. In contrast, an in vivo study by Schnell et al[20] revealed robustness of WSS estimates against higher parallel imaging acceleration factors, which are state-of-the-art for speeding up 4D flow imaging. Moreover, van Ooij et al[21] reported on the reproducibility of systolic velocity and wall shear stress estimation in the healthy aorta.

The purpose of this study was twofold: first, to investigate the impact of vessel wall tracking on 4D flow-based

Journal of Magnetic Resonance Imaging

TABLE 1. Synthetic Datasets Used for Spatiotemporal Resolution and Phase Noise Evaluation

Dataset	Voxel size [mm^3]	VENC [m/s]	Noise factor (rel. to A)	Number of frames per cycle (frame length)
A	$1 \times 1 \times 1$	1	1	25 (32 msec)
B	$1 \times 1 \times 1$	1	1	20 (40 msec)
C	$1 \times 1 \times 1$	1	1	15 (53 msec)
D	$2 \times 2 \times 2$	1	1/8	25 (32 msec)
E	$3 \times 3 \times 3$	1	1/27	25 (32 msec)
F	$1 \times 1 \times 1$	2	2	25 (32 msec)
G	$1 \times 1 \times 1$	4	4	25 (32 msec)

WSS estimates in contrast to approximating the vessel wall by a static surface mesh; second, to compare these findings with inaccuracies implied by spatiotemporal resolution and velocity encoding (VENC)-dependent phase noise in order to put these two sources of error (wall motion and acquisition parameters) into perspective. This work used in vivo volunteer and patient data of the ascending aorta as well as synthetic flow data through the aortic arch.

Material and Methods

Synthetic Data

To assess the impact of varying acquisition parameters, flow through the aorta was simulated on a high-resolution $1 \times 1 \times 1\,\text{mm}^3$ grid using the Lattice-Boltzmann method (LBM).[22] Simulated 3D+t magnitude and phase image volumes were then modified as follows (Table 1): 1) spatial resampling using linear interpolation to create image volumes with $1 \times 1 \times 1\,\text{mm}^3$, $2 \times 2 \times 2\,\text{mm}^3$, and $3 \times 3 \times 3\,\text{mm}^3$ spatial resolution. Phase noise was added in inverse linear relationship with voxel volume; 2) temporal resampling using a cubic B-spline image function and subsequent sampling to generate 15, 20, and 25 frames over the full cardiac cycle (cycle length = 0.8s); 3) adding velocity noise as a linear function of the VENC number as described by Lee et al[23]:

$$\sigma_\phi = \frac{\sqrt{2}}{\pi} \frac{VENC}{SNR} \qquad (2)$$

with SNR = signal-to-noise ratio in magnitude images. Three VENC settings were selected for evaluations (VENC = 1/2/3 m/s). Neither phase offset nor synthetic aliasing was included in the synthetic data. WSS and OSI estimates (see computational method described below) were analyzed at a single location in the descending aorta using an identical delineation of the contour wall (Fig. 1D). In the region of interest flow velocity (mean/min/max) is 0.81/0.06/2.46 m/s and flow rate is 148 ml/s, in peak systole. Note that the synthetic dataset did not exhibit any vessel wall motion.

In Vivo Data

The study was approved by the Institutional Ethics Committee and written consent was obtained from all subjects. The study population included 17 patients with congenital heart defects (bicuspid aortic valve [$n = 15$], atrial septal defect [$n = 1$], and Marfan's syndrome [$n = 1$]), as well as 11 healthy volunteers without any history of cardiovascular disease. All subjects were examined using a 1.5T Magnetom Avanto MRI system (Siemens, Erlangen, Germany) to acquire 4D flow MRI data in a parasagittal view covering the thoracic aorta. No contrast agent was injected prior to the scan. Pulse sequence parameters were as follows: spatial resolution = $2.0–3.0 \times 1.7–2.3 \times 2.3–2.5\,\text{mm}^3$; field of view = $320–400 \times 240–340 \times 64–90\,\text{mm}^3$; temporal resolution = 40 msec (16–24 frames); repetition time / echo time (TE/TR) = 2.7/5.0 msec; flip angle = 7–8°; VENC = 150 cm/s (healthy volunteers) and 150–230 cm/s (patients). Prospective electrocardiogram (ECG) triggering and navigator gating was applied in all acquisitions. PEAK-GRAPPA[24] with an acceleration factor R = 5 and 24 reference lines was applied in all acquisitions excluding the patients with bicuspid aortic valve (not yet available at that time).

Data Preprocessing

Preprocessing steps of in vivo data included: 1) image-based phase offset correction by manually selecting a phase deviation threshold to determine static tissue regions followed by fitting a polynomial to subtract the phase offset; 2) noise masking to exclude phase noise in image background regions; and 3)—if necessary—fully automated phase unwrapping using PRELUDE.[25] None of the above steps was performed on synthetic data, as systematic errors were not included in the simulation. A time-averaged 3D PC-MRA image was then generated to be used for watershed-based segmentation of the entire aorta. Subsequently, a centerline was computed for each aorta segmentation mask and smoothed using Laplacian smoothing.

Vessel Wall Definition

Based on the centerline, three positions in the ascending aorta (equidistant plane spacing = 20 mm) were defined and the image volumes were reformatted to generate three planes oriented perpendicular to the centerline (Fig. 1E). We then generated two contour groups for each plane: 1) Moving contours: for each plane, the vessel wall was manually contoured in a single magnitude image frame in peak systole by placing several knots along the vessel boundary. Morphon deformable registration[26] was applied to calculate 2D deformation fields between neighboring magnitude image frames, which were then used for propagating the knot points through all frames. Spline

interpolation was used to generate a closed contour for each frame. 2) Static contours: static contours for all three positions were defined as the cross-section border of the 3D aortic segmentation at the reformatted 2D plane. Laplacian smoothing (factor = 0.2, number of passes = 100) was applied to all static contours to compensate for possible rough borders of the 3D aortic segmentation.

Both static and moving contours were represented explicitly by a set of path points (~150–200 per contour per frame, depending on contour diameter). WSS estimates were then computed at each path point.

Shear Stress Estimation

WSS was estimated based on the approach described by Stalder et al.[13] In brief, the WSS vector $\vec{\tau}$ is derived for each path point in each timeframe considering:

$$\vec{\tau} = \eta(\dot{\epsilon} \cdot \vec{n}) \tag{3}$$

with η = dynamic viscosity $(0.0032\ Pa \cdot s)$, $\dot{\epsilon}$ = velocity deformation tensor, and $\vec{n}$ = unit surface inward normal at the evaluated path point. $\dot{\epsilon}$ is directly related to the velocity derivatives at the vessel wall and thus requires computation of 3D local derivatives of the velocity field. To cope with the limited spatial resolution of 4D flow MRI data, the applied algorithm performs cubic B-spline interpolation to generate a continuous image function of the 3D and three-directional velocity field.

As opposed to the implementation described by Stalder et al,[13] our work presents two major adaptations. First of all, we considered the full 3D (rather than the planar-only) velocity vector field to generate a 3D image function, which was then used to compute local derivatives at each path point. This way we ensured that both in-plane and longitudinal velocity gradients are taken into account. Second, we integrated the 3D Gauss gradient field $\boldsymbol{G}$ of the segmented vessel mask (with σ set to the average voxel side length) to define the unit surface inward normal $\vec{n}$ at each contour point $\boldsymbol{x}$ as follows:

$$\vec{n}_{\boldsymbol{x}} = \vec{a}_{\boldsymbol{x}} + \vec{g}_{\boldsymbol{x},p} \tag{4}$$

where

$$\vec{g}_{\boldsymbol{x},p} = (\boldsymbol{G}_{\boldsymbol{x}} \cdot \vec{p})\vec{p} \tag{5}$$

is the projection of the local Gauss gradient vector at $\boldsymbol{x}$ onto the plane normal $\vec{p}$ (vessel centerline direction); and $\vec{a}_{\boldsymbol{x}}$ is the inward normal lying on the 2D contour plane, defined by the cross product of the local plane normal and the tangent vector at $\boldsymbol{x}$. Note that $\vec{n}$ is not required to lie within the analysis plane, but adapts to possibly complex (i.e., nonparallel) vessel courses. All WSS vectors were projected onto the local vessel surface tangent plane.

In this work, we used the definition proposed by He and Ku[27] to compute the oscillatory shear index (OSI):

$$OSI = \frac{1}{2}\left(1 - \frac{\left|\int_0^T \vec{\tau}\,dt\right|}{\int_0^T |\vec{\tau}|\,dt}\right) \tag{6}$$

Here, integrals were interpreted as sums with no further temporal resampling. Note that OSI is a unitless index that measures WSS vector oscillation over the entire cycle length, and is thus timeframe-independent.

As the number of existing path points per contour may vary between timeframes (depending on the contour circumference), we sampled each path point ensemble representing the wall contour at a specific timepoint with a fixed equidistant radial pattern (number of rays = 120), using nearest neighbor interpolation. The sampled path points were also used as a means to establish point correspondences between timeframes, which allow for a standardized computation of OSI and WSS statistics (min/max/mean) over time. A 12 angular segment model was then applied to bin WSS and OSI numbers with segment statistics given in mean ±SD. Multiple segment models within the same analysis plane were aligned automatically to ensure that the same index segments correspond to each other. To this end, our implementation used the vessel's center of gravity as an alignment point. All preprocessing steps, image analysis methods, and visualizations were implemented using the MevisLab medical image computing framework.[28]

Statistical Evaluation

To quantitatively grade the motion of the wall over the course of the cardiac cycle, we computed the Hausdorff distance (HD, given in mm) for each static versus moving contour pair. Here, HD depicts the deviation of the tracked contour from the static (ie, averaged) vessel wall location.

For synthetic data, we compared shear stress estimates with regard to varying spatial resolution, VENC setting, and temporal resolution both segment-wise and over time (choosing the segment depicting maximum WSS). In addition, we assessed the impact of dilated and shrunken contours on WSS estimates using the synthetic dataset. For in vivo data, we analyzed absolute differences in WSS and OSI per segment, based on moving versus static contours. In both synthetic and in vivo data we chose to evaluate WSS differences at three distinct timepoints: t1, t2, and t3, at 20%, 40%, and 80% of the acquired cardiac cycle length, respectively. We found that these timepoints roughly correspond to the mid-systole, early diastole, and late diastole. To define a single quantitative metric over all segments per case, analysis plane, and timeframe we defined the median of absolute WSS (OSI) difference over all segments. Bland–Altman analyses were used to assess the difference in WSS and OSI estimates based on static versus moving contours; and Pearson's correlation coefficient (PCC) was used to study how deviations in WSS and OSI correlate with HD.

Results

Synthetic Data Analysis

The results in Fig. 2 show that mean WSS and OSI estimates per segment decrease with increased voxel size, while the standard deviation per segment is noticeably reduced with increased voxel size. When comparing isotropic voxel sizes (1 vs. 2 mm and 1 vs. 3 mm) Bland–Altman lines (mean ± 1.96 SD, given in N/m^2) are as follows: In mid-systole (t1) WSS estimates differ by –0.07 ± 1.41 and –0.51 ± 1.38; in early diastole (t2) WSS estimates differ by –0.24 ± 0.40 and –0.35 ± 0.37; and in late diastole (t3)

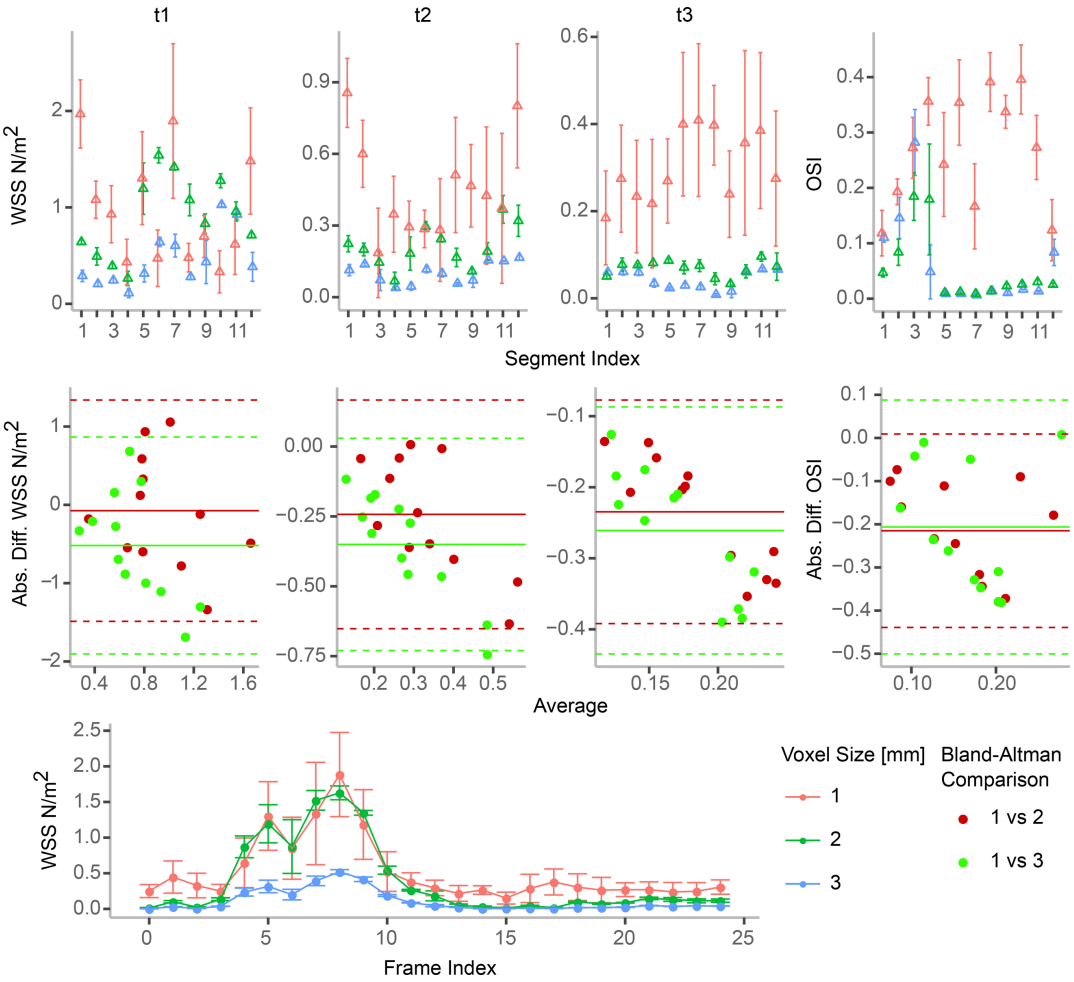

FIGURE 2: Analysis of spatial resolution impact on WSS and OSI in synthetic data. Top: Absolute WSS (mean ± SD) per segment (1–12) for timepoints t1, t2, and t3; absolute OSI value. Middle: Corresponding Bland–Altman plots comparing WSS (OSI) output based on voxel dimension $1 \times 1 \times 1\,mm^3$ vs. $2 \times 2 \times 2\,mm^3$ (red) and $1 \times 1 \times 1\,mm^3$ vs. $3 \times 3 \times 3\,mm^3$ (green). Bottom: WSS time curve in single segment (sampled at 25 timepoints over the course of the cardiac cycle).

WSS estimates differ by –0.23 ± 0.16 and –0.26 ± 0.17. OSI estimates vary by –0.21 ± 0.22 and –0.22 ± 0.29.

The results obtained by varying VENC and thus increasing phase noise are presented in Fig. 3. Overall, we observe that both mean and standard deviation of WSS and OSI per segment is increased with increasing VENC. When comparing VENC settings (1 vs. 2 m/s and 1 vs. 4 m/s) Bland–Altman lines (mean ± 1.96 SD, given in N/m^2) are as follows: In mid-systole (t1) WSS estimates differ by 0.18 ± 0.28 and 0.64 ± 0.70; in early diastole (t2) WSS estimates differ by 0.26 ± 0.31 and 0.87 ± 0.78; and in late diastole (t3) WSS estimates differ by 0.31 ± 0.12 and 0.94 ± 0.28. OSI estimates vary by 0.05 ± 0.06 and 0.09 ± 0.12.

Changes in shear stress estimates due to varying temporal resolution are presented in Fig. 4. Here, OSI estimates (mean ± 1.96 SD) differed by 0.00 ± 0.05 and 0.00 ± 0.04 when comparing temporal resolutions of 32 vs. 40 msec and 32 vs. 53 msec, respectively. Overall, WSS time curves were preserved when changing temporal resolution (Fig. 4, top), although the peak WSS is slightly shifted in time due to lacking temporal precision.

Figure 5 presents the impact of slightly dilated and shrunken wall contours on WSS estimates in synthetic dataset A (highest spatiotemporal resolution, VENC = 1 m/s). Note that zero flow (excluding synthetic noise) was assumed outside the lumen. In segments with increased flow we observe a strong increase in WSS if the contour is defined inside the lumen (inner contour), whereas no typical WSS time curve with peak WSS during systole can be captured if the wall contour is defined beyond (outer contour) the border of the lumen.

In Vivo Data Analysis

Figure 6 (left) shows that wall motion in the aorta was most pronounced at analysis plane 1 (median/min/max HD [mm] at timepoints t1, t2, and t3 was 5.6/2.8/9.1, 5.4/2.6/10.1, and 4.9/3.5/10.1). Also, refer to Supplements 1–3 for

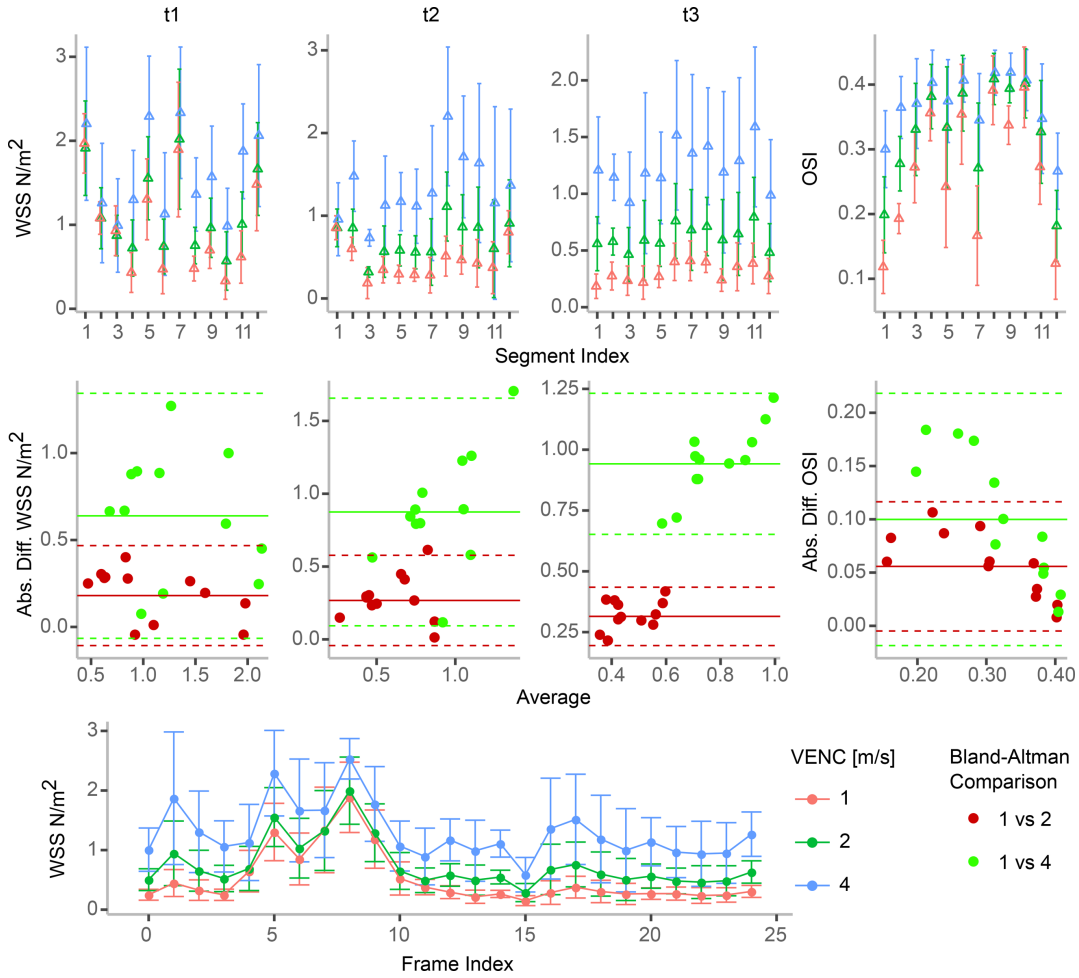

FIGURE 3: Analysis of VENC impact on WSS and OSI in synthetic data. Top: Absolute WSS (mean ± SD) per segment (1–12) for timepoints t1, t2, and t3; absolute OSI value. Middle: Corresponding Bland–Altman plots comparing WSS (OSI) output based on VENC = 1 m/s vs. 2 m/s (red) and 1 m/s vs. 4 m/s (green). Bottom: WSS time curve in single segment (sampled at 25 timepoints over the course of the cardiac cycle).

a visualization of static and moving contours in an exemplary case. Figure 6 (right) plots the computed median absolute difference value per case, plane, and timepoint against the respective HD. PCC values between both variables were: PCC = 0.27 overall; PCC = 0.43/0.09/0.25 for timepoints t1/t2/t3; and PCC = 0.31/0.01/0.06 for planes 1/2/3.

Overall results of in vivo data WSS and OSI estimates based on static versus moving contour definition analyzed at individual planes and timepoints are presented in Fig. 7. Mean absolute differences in WSS estimates appear to be independent of the analysis plane location and point in time with no systematic under-/overestimation (Bland–Altman mean lines ranging from –0.06 to 0.05 N/m^2). Yet the results show strong deviations in absolute WSS differences (±1.96 SD lines (t1/t2/t3) at 1.21/0.82/0.64, 0.72/0.57/0.55, and 0.59/0.70/0.47 for planes 1, 2, and 3, respectively; all numbers given in N/m^2). Moreover, plots suggest that absolute differences between static contour-based and moving contours-based WSS estimates increase with increasing absolute WSS values. Concerning the impact on OSI estimates, the results present no systematic offset between both contouring approaches, but sample points deviate noticeably (±1.96 SD lines at 0.14, 0.15, and 0.16 for planes 1, 2, and 3, respectively).

Figures 8 and 9 show segment-wise WSS evaluation results based on static and moving contour definition that are specific to an exemplary volunteer and patient dataset, respectively. The former case presents with a homogeneous flow profile, while the latter case depicts an altered flow pattern. Both examples present the strong scattering of absolute differences between both approaches with only minor systematic offsets, ie, individual results are in line with the overall results reported above.

Discussion

This work assessed the impact of wall contour position on WSS estimates in the ascending aorta throughout the

Journal of Magnetic Resonance Imaging

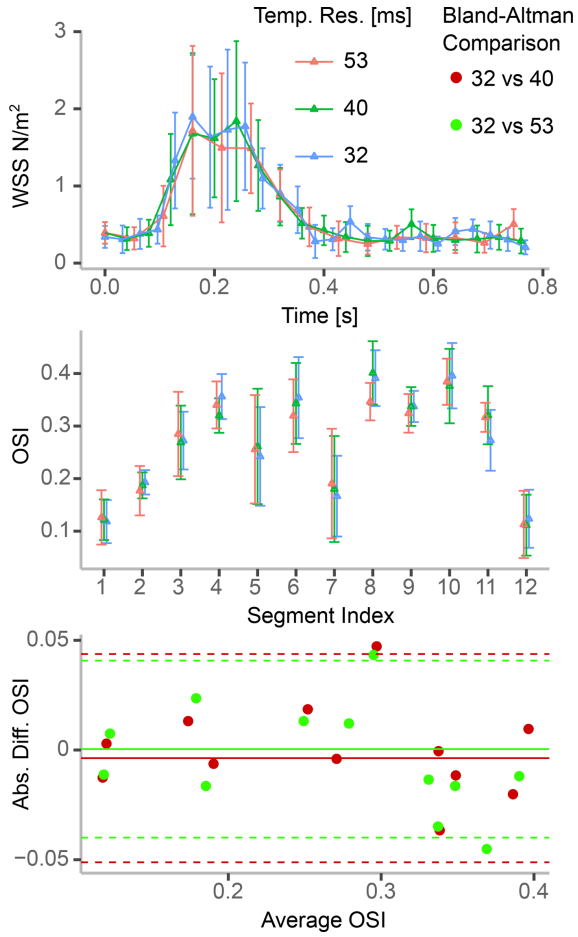

FIGURE 4: Analysis of effect of temporal resolution on WSS and OSI in synthetic data. Top: WSS time curve (mean ± SD) at single segment. Middle: OSI (mean ± SD) per segment. Bottom: Corresponding Bland–Altman plot comparing OSI output based on synthetic frame length = 32 msec vs. 40 msec (red) and 32 msec vs. 53 msec (green).

cardiac cycle. Equally, we evaluated the influence of spatio-temporal resolution and phase noise in synthetic datasets using the identical implementation to estimate shear stress parameters. The latter has already been studied in related works,[13,15,19] although the extent of uncertainties induced by acquisition parameters compared to those induced by imprecise wall tracking had not been reported yet.

As the vessel wall of the ascending aorta exhibits a periodic motion throughout the cardiac cycle that is beyond the typical image resolution, this region was chosen for evaluation. All in vivo acquisitions were performed without the administration of contrast agent (CA), which has been shown to enhance SNR. We chose to only include data scanned without CA to mimic a worst-case scenario regarding SNR and to evaluate the true robustness of estimating shear stress parameters based on 4D flow images. Thus, the results may also be applicable to those subjects who are intolerant to CA administration. The authors want to point out that this study did not seek to compare WSS in subjects with congenital heart defects with WSS in healthy volunteers, which has been covered in previous works.[7–9]

In summary, our results suggest that estimated shear stress parameters strongly depend on where the wall is positioned. Differences in shear stress parameters based on static versus moving (tracked using deformable registration) contours were in the range of those observed when poor spatial resolution and increased phase noise was given.

With respect to spatial resolution, WSS and OSI were greatly influenced by voxel dimensions. Particularly, WSS was underestimated and OSI appeared to be averaged out (ie, the estimation becomes insensitive to WSS vector oscillations) with increasing voxel size. These findings correspond in a qualitative manner to those reported by Stalder et al[13] as well as Petersson et al.[19] According to Stalder et al, WSS drops to 60% of its analytical value for a voxel length of 1 mm and further decreases to above 30% of its analytical value for a voxel length of 10 mm. Equally, Petersson et al show an increasing underestimation of WSS with increasing voxel size and increasing analytical WSS value (ranging from 1 to 20 N/m^2). We note that both referenced works prescribed an idealized parabolic flow profile when synthesizing the underlying image data, whereas the synthetic data presented in this work was generated with MRI-based (ie, measured) inflow boundary conditions. Therefore, we did not attempt to give an analytical WSS value for comparison. Moreover, Petersson et al did not simulate noise with their synthetic data, whereas our approach seeks to model the linear dependency between phase noise, VENC, and spatial resolution.

Regarding VENC dependency, both WSS and OSI increased systematically at higher VENC values (ie, phase noise). We deduce that OSI becomes a measure of phase image noise rather than WSS vector fluctuation if VENC is set to a number greatly exceeding the maximum flow velocity. Besides, assessing shear stress parameters was particularly prone to errors in diastolic timeframes where the velocity-to-noise ratio is decreased. One should take account of this when assessing shear stress in the full cardiac cycle rather than focusing on WSS at peak flow. Here, a dedicated VENC setting focused on analyzing hemodynamics in diastole that is crucial to optimize the velocity-to-noise ratio, and advanced antialiasing techniques[25] are important to compensate for possibly resulting phase-wrapping in systole. With regard to previous works, the results in Petersson et al show only a minor impact of the VENC; however, those results are based on synthetic data excluding noise, which defines one major tradeoff of increased VENC.

Our results suggest that temporal resolution, unlike spatial resolution and phase noise, only has a minor impact on the estimation of WSS and OSI. This partially agrees with findings made by Cibis et al,[15] who reported on a

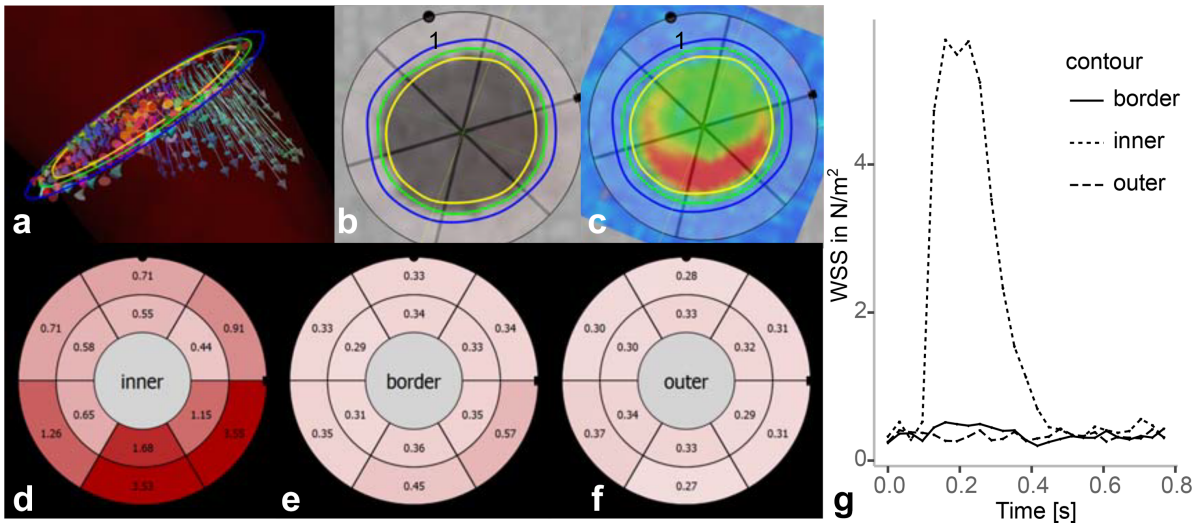

FIGURE 5: Impact of dilated and shrunken wall contours on WSS in synthetic flow data. A: Wall contours at three positions (yellow: inner, green: border, blue: outer) and planar velocity vector field. B,C: Magnitude image and planar velocity field with angular segment model and contour overlay. Segments are indexed clockwise. D–F: WSS estimates for all defined contours presented as bull's-eye plots (BEP). Note that BEPs depict two WSS metrics: Peak systolic WSS (outer BEP values) and mean WSS over time (inner BEP values). G: WSS time curves corresponding to segment 4.

dependence of OSI on temporal resolution. However, in our study, we only examined three resolution settings (32, 40, and 53 msec), whereas Cibis et al lowered it down to 142.9 msec per frame (corresponding to 5–6 frames per cycle at 75 beats per minute). We argue that temporal resolutions at this range are not employed in the clinical setting, and thus did not evaluate the impact to this extreme.

In vivo results showed that inaccurate wall delineation produces WSS and OSI deviations that are considerable. In contrary to the systematic over-/underestimation of shear stress parameters due to poor spatial resolution and phase noise, our results do not suggest any systematic error when the wall contour is falsely positioned. This point is reinforced by the observed weak correlation between the computed HD and the median absolute difference per static-moving contour pair. Although the degree of wall motion is reduced for analysis planes positioned distal to the aortic valve, the measured deviations remain unaffected. Based on the analysis of individual cases, we propose that the extent to which WSS estimates deviate mainly arises from the velocity field in the vicinity of the vessel wall. In our case, small vessels close to the ascending aorta were a major concern. If the true vessel wall is imprecisely captured and neighboring vessels are included, flow through these vessels might become the deciding factor for falsely increased WSS. Therefore, we suggest that the standard deviation of the segment-binned WSS values should act as an indicator for WSS reliability assuming that shear stress should be rather homogeneous within one segment (with appropriately sized segments).

As stated in the introduction, various recent works used the time-averaged PC-MRA image to define a wall contour for peak-systolic WSS estimation. Based on the HD analysis of our work, we claim that this approach is

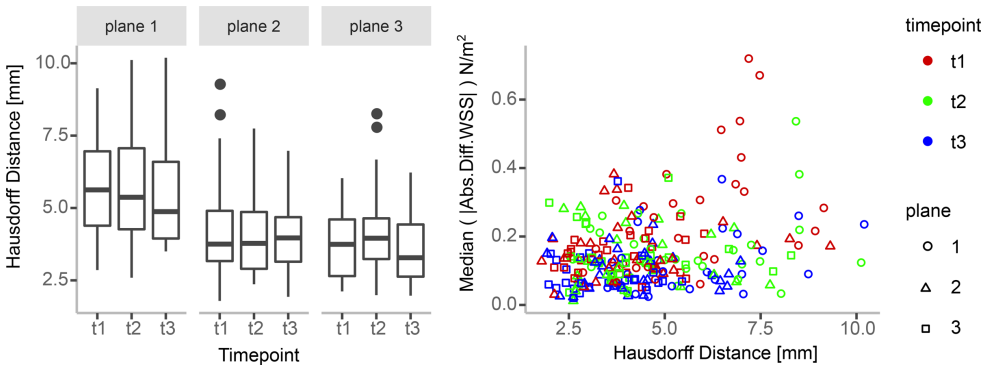

FIGURE 6: HD analysis of static vs. moving wall contours in all in vivo datasets (patients and volunteers). Left: Boxplots of HD per analysis plane and timepoint, with dots depicting outliers. Right: Each scatter point depicts the median (over all segments) of the absolute difference in WSS based on static vs. moving contour against the respective HD.

Journal of Magnetic Resonance Imaging

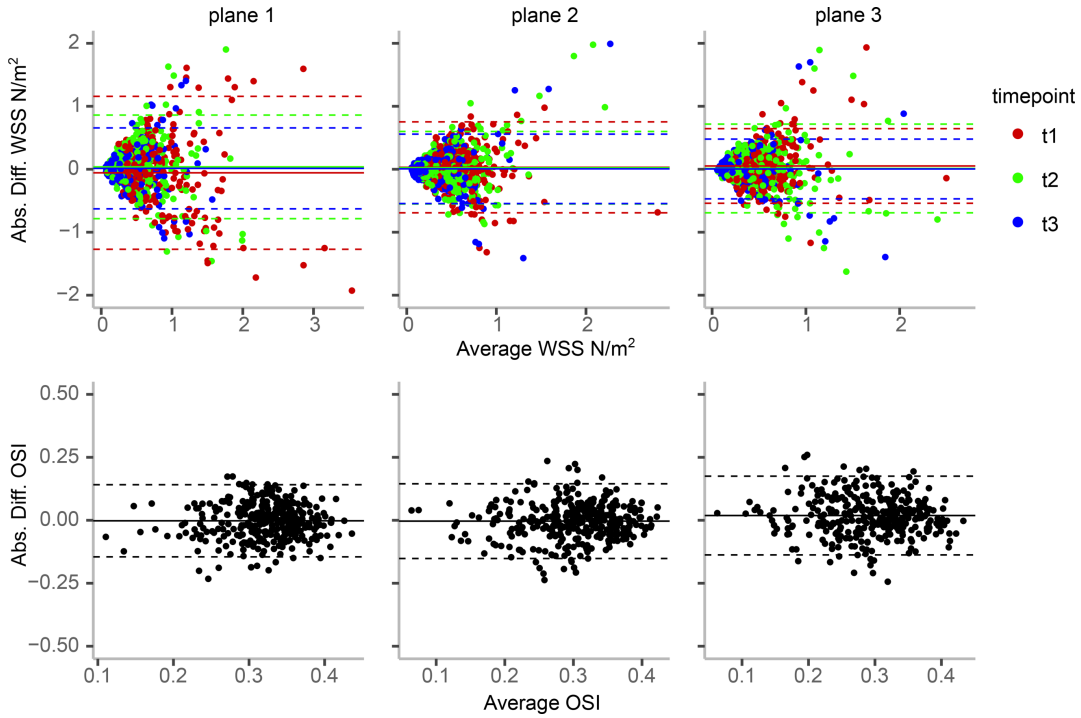

FIGURE 7: Overall results of absolute difference in in vivo WSS (top row) and OSI (bottom row) estimates (patients and volunteers). Bland–Altman plots compare outputs based on moving versus static wall contours. Columns 1–3 depict analysis planes 1–3. Colors depict three different timepoints of the cardiac cycle: mid-systole (t1, red), early diastole (t2, green), and late diastole (t3, blue).

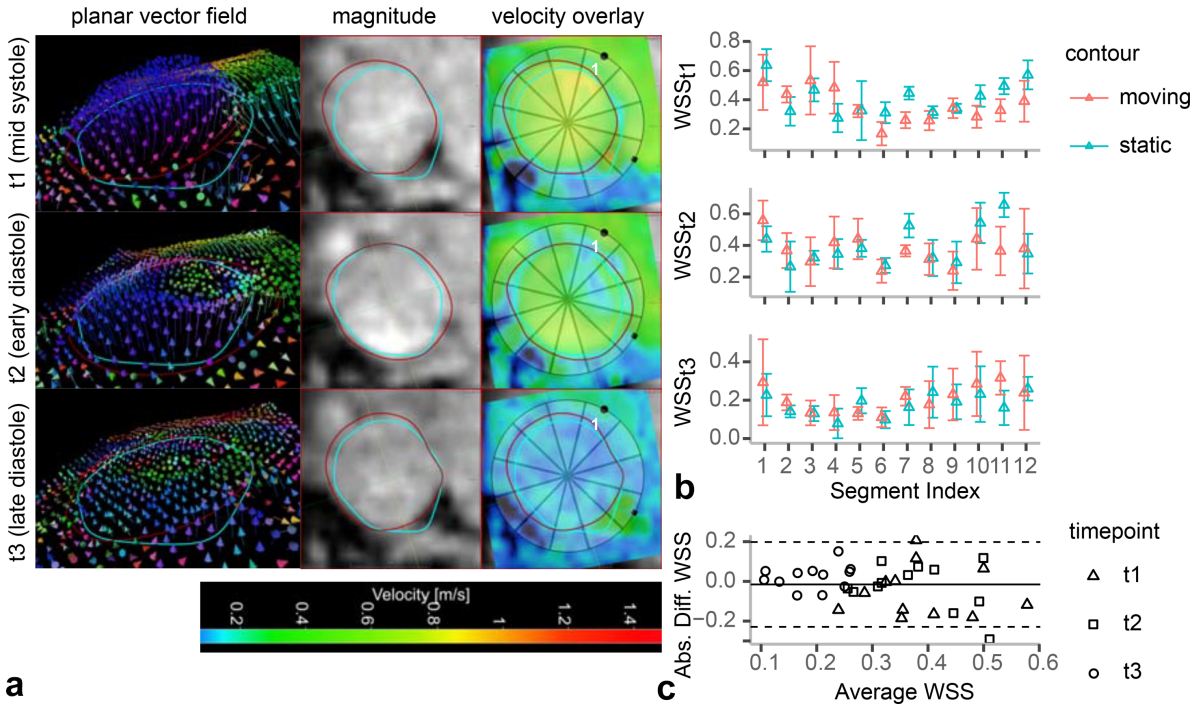

FIGURE 8: WSS analysis of a healthy volunteer dataset. **A:** Visualization of planar velocity vector field (color coding depicts vector direction in 3D), magnitude data, and 2D velocity overlay at timepoints t1–t3. Segments are indexed clockwise (see segment label 1). **B:** Absolute WSS (mean ± SD) per segment comparing WSS output based on moving (red) and static (blue) wall definition. **C:** Corresponding Bland–Altman plot.

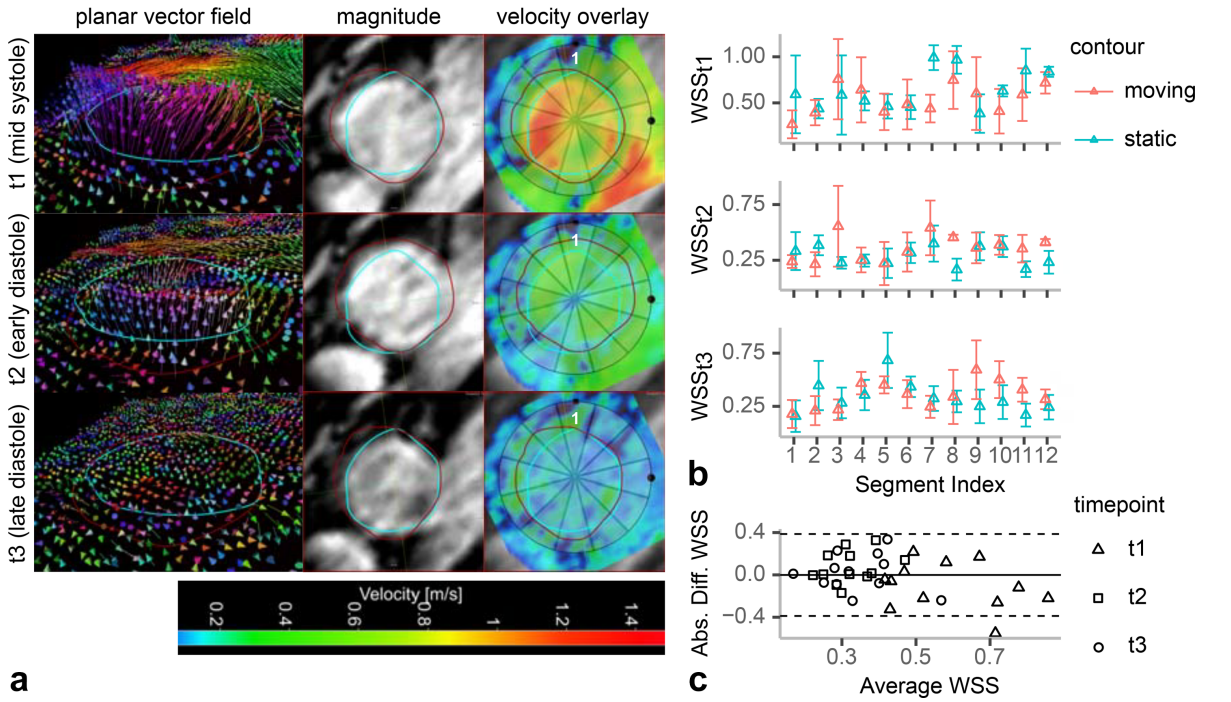

FIGURE 9: WSS analysis of a patient dataset with inhomogeneous cross-section flow profile. A: Visualization of planar velocity vector field (color coding depicts vector direction in 3D), magnitude data, and 2D velocity overlay at timepoints t1–t3. Segments are indexed clockwise (see segment label 1). B: Absolute WSS (mean ± SD) per segment comparing WSS output based on moving (red) and static (blue) wall definition. C: Corresponding Bland–Altman plot.

inaccurate even if merely focused on peak systole. Our results suggest that the tracked contour is not any closer to the static contour in mid-systole than it is in early/late diastole. We propose that this may be explained by inhomogeneous flow that results in misleading PC-MRA, ie, the angiographic representation does not depict the full vessel lumen. This should be taken into account specifically when dealing with flow data exhibiting pathological flow patterns.

Concerning the limitations of the work presented, this study only focused on the ascending aorta, and the study population was vastly comprised of patients with bicuspid aortic valve and of healthy volunteers. We note that other vessels and pathologies should be included to achieve a more representative cohort of all vessels for which shear stress parameters are of clinical interest. Furthermore, in vivo data may comprise all types of errors induced by acquisition parameters. Despite the fact that preprocessing aimed at compensating for phase offsets and possible aliasing, we did not assess to what extent any of the remaining errors perturbed WSS and OSI. Additionally, this work relies on accurate wall tracking and assumes that the moving contour is in line with the true vessel boundary. Although we visually inspected each propagated contour for obvious misregistration, we did not quantitatively evaluate the error propagation due to automated propagation inaccuracies. Here, we also want to point out that deformable registration was only performed in-plane (2D), ie, possible out-of-plane movement of tissue points was neglected. A recent work by Cibis et al[29] proposes time-resolved 3D segmentation of vessels of interest based on 4D flow MRI data.

Regarding numerical WSS computation, our implementation is predicated on Stalder et al[13]; however, other methods exist that have not been considered in this work: Petersson et al[19] compared multiple approaches using numerical simulations; Piatti et al[30] described the use of Sobel derivative filters; and Sotelo et al[18] presented a finite element method. With respect to OSI computation, its definition—as do all other shear stress metrics over time—requires establishing contour point correspondences. Our implementation samples the ensemble of discrete contour points through all timepoints using a static radial pattern to establish the necessary correspondence. This approach only holds true if wall tissue points travel inwards/outwards through the cardiac cycle, and do not rotate around the contour center. Here, any possible errors were not taken into account and should be subject to future works. Lastly, we note that this work is only able to report relative differences in WSS and OSI, since no ground truth was available. Other works sought to validate WSS based on analytical computations.[13,18,19]

In conclusion, the present work suggests that image-based WSS and OSI estimates are considerably sensitive to

where the wall contour is defined. Precise wall tracking should be given particular attention in any image-based shear stress estimation.

Acknowledgements

Contract grant sponsor: Deutsche Herzstiftung e.V., Frankfurt a. M., Germany. Prof. Dr. Anja Hennemuth was supported by Deutsche Forschungsgemeinschaft grant DFG HE 7321/4-1.

We thank Markus Huellebrand, Lennart Tautz, and Christian Schumann for valuable assistance with software development.

References

1. Richter Y, Edelman ER. Cardiology is flow. Circulation 2006;113:2679–2682.
2. Katritsis D, Kaiktsis L, Chaniotis A, Pantos J, Efstathopoulos EP, Marmarelis V. Wall shear stress: Theoretical considerations and methods of measurement. Prog Cardiovasc Dis 2007;49:307–329.
3. Malek AM, Alper SL, Izumo S. Hemodynamic shear stress and its role in atherosclerosis. JAMA 1999;282:2035–2042.
4. Lehoux S, Tedgui A. Cellular mechanics and gene expression in blood vessels. J Biomech 2003;36:631–643.
5. Reneman RS, Arts T, Hoeks APG. Wall shear stress—An important determinant of endothelial cell function and structure—In the arterial system in vivo: Discrepancies with theory. J Vasc Res 2006;43:251–269.
6. Ku DN, Giddens DP, Zarins CK, Glagov S. Pulsatile flow and atherosclerosis in the human carotid bifurcation. Positive correlation between plaque location and low oscillating shear stress. Arterioscler Thromb Vasc Biol 1985;5:293–302.
7. Allen BD, Van Ooij P, Barker AJ, et al. Thoracic aorta 3D hemodynamics in pediatric and young adult patients with bicuspid aortic valve. J Magn Reson Imaging 2015;42:954–963.
8. Hope MD, Sigovan M, Wrenn SJ, Saloner D, Dyverfeldt P. MRI hemodynamic markers of progressive bicuspid aortic valve-related aortic disease. J Magn Reson Imaging 2014;40:140–145.
9. Barker AJ, Markl M, Burk J, et al. Bicuspid aortic valve is associated with altered wall shear stress in the ascending aorta. Circ Cardiovasc Imaging 2012;5:457–466.
10. Bieging ET, Frydrychowicz A, Wentland A, et al. In vivo three-dimensional MR wall shear stress estimation in ascending aortic dilatation. J Magn Reson Imaging 2011;33:589–597.
11. Moyle KR, Mallinson GD, Occleshaw CJ, Cowan BR, Gentles TL. Wall shear stress is the primary mechanism of energy loss in the Fontan connection. Pediatr Cardiol 2006;27:309–315.
12. Kolipaka A, Illapani VSP, Kalra P, et al. Quantification and comparison of 4D-flow MRI-derived wall shear stress and MRE-derived wall stiffness of the abdominal aorta. J Magn Reson Imaging 2017;45:771–778.
13. Stalder AF, Russe MF, Frydrychowicz A, Bock J, Hennig J, Markl M. Quantitative 2D and 3D phase contrast MRI: Optimized analysis of blood flow and vessel wall parameters. Magn Reson Med 2008;60:1218–1231.
14. Potters WV, van Ooij P, Marquering H, Vanbavel E, Nederveen AJ. Volumetric arterial wall shear stress calculation based on cine phase contrast MRI. J Magn Reson Imaging 2015;41:505–516.
15. Cibis M, Potters WV, Gijsen FJ, et al. The effect of spatial and temporal resolution of cine phase contrast MRI on wall shear stress and oscillatory shear index assessment. PLoS One 2016;11:1–15.
16. Harloff A, Berg S, Barker AJ, et al. Wall shear stress distribution at the carotid bifurcation: Influence of eversion carotid endarterectomy. Eur Radiol 2013;23:3361–3369.
17. Van Ooij P, Potters W V., Nederveen AJ, et al. A methodology to detect abnormal relative wall shear stress on the full surface of the thoracic aorta using four-dimensional flow MRI. Magn Reson Med 2015;73:1216–1227.
18. Sotelo J, Urbina J, Valverde I, et al. 3D quantification of wall shear stress and oscillatory shear index using a finite-element method in 3D CINE PC-MRI data of the thoracic aorta. IEEE Trans Med Imaging 2016;35:1475–1487.
19. Petersson S, Dyverfeldt P, Ebbers T. Assessment of the accuracy of MRI wall shear stress estimation using numerical simulations. J Magn Reson Imaging 2012;36:128–138.
20. Schnell S, Markl M, Entezari P, et al. K-t GRAPPA accelerated four-dimensional flow MRI in the aorta: Effect on scan time, image quality, and quantification of flow and wall shear stress. Magn Reson Med 2014;72:522–533.
21. Van Ooij P, Powell AL, Potters WV, Carr JC, Markl M, Barker AAJ. Reproducibility and interobserver variability of systolic blood flow velocity and 3D wall shear stress derived from 4D flow MRI in the healthy aorta. J Magn Reson Imaging 2016;43:236–248.
22. Mirzaee H, Henn T, Krause MJ, et al. MRI-based computational hemodynamics in patients with aortic coarctation using the lattice Boltzmann methods: Clinical validation study. J Magn Reson Imaging 2016;45:139–146.
23. Lee AT, Bruce Pike G, Pelc NJ. Three-point phase-contrast velocity measurements with increased velocity-to-noise ratio. Magn Reson Med 1995;33:122–126.
24. Jung B, Ullmann P, Honal M, Bauer S, Hennig J, Markl M. Parallel MRI with extended and averaged GRAPPA kernels (PEAK-GRAPPA): Optimized spatiotemporal dynamic imaging. J Magn Reson Imaging 2008;28:1226–1232.
25. Jenkinson M. Fast, automated, N-dimensional phase-unwrapping algorithm. Magn Reson Med 2003;49:193–197.
26. Knutsson H, Andersson M. Morphons: Paint on priors and elastic canvas for segmentation and registration. In: Scandinavian Conference on Image Analysis. Lecture Notes in Computer Science. Vol 3540. 2005:292–301.
27. He X, Ku DN. Pulsatile flow in the human left coronary artery bifurcation: average conditions. J Biomech Eng 1996;118:74–82.
28. Ritter F, Boskamp T, Homeyer A, et al. Medical image analysis. IEEE Pulse 2011;2:60–70.
29. Cibis M, Bustamante M, Eriksson J, Carlhäll CJ, Ebbers T. Creating hemodynamic atlases of cardiac 4D flow MRI. J Magn Reson Imaging 2017;46:1389–1399.
30. Piatti F, Pirola S, Bissell M, et al. Towards the improved quantification of in vivo abnormal wall shear stresses in BAV-affected patients from 4D-flow imaging: Benchmarking and application to real data. J Biomech 2017;50:93–101.

4

ON THE IMPACT OF VESSEL WALL STIFFNESS ON QUANTITATIVE FLOW DYNAMICS IN A SYNTHETIC MODEL OF THE THORACIC AORTA

Authors: **Judith Zimmermann**, Michael Loecher, Fikunwa O. Kolawole, Kathrin Baeumler, Kyle Gifford, Seraina Dual, Marc Levenston, Alison L. Marsden, Daniel B. Ennis.

In: Scientific Reports 2021;11:6703 [154]

Abstract: Background. Aortic wall stiffening is a predictive marker for morbidity in hypertensive patients. Arterial pulse wave velocity (PWV) correlates with the level of stiffness and can be derived using non-invasive 4D-flow magnetic resonance imaging (MRI). *Objective.* The objectives of this study were twofold: to develop subject-specific thoracic aorta models embedded into an MRI-compatible flow circuit operating under controlled physiological conditions; and to evaluate how a range of aortic wall stiffness impacts 4D-flow-based quantification of hemodynamics, particularly PWV. *Methods.*Three aorta models were 3D-printed using a novel photopolymer material at two compliant and one nearly rigid stiffnesses and characterized via tensile testing. Luminal pressure and 4D-flow MRI data were acquired for each model and cross-sectional net flow, peak velocities, and PWV were measured. In addition, the confounding effect of temporal resolution on all metrics was evaluated. *Results.* Stiffer models resulted in increased systolic pressures (112, 116, and 133 mmHg), variations in velocity patterns, and increased peak velocities, peak flow rate, and PWV (5.8 to 7.3 m/s). Lower temporal resolution (20 ms down to 62.5 ms per image frame) impacted estimates of peak velocity and PWV (7.31 down to 4.77 m/s). *Conclusion.* Using compliant aorta models is essential to produce realistic flow dynamics and conditions that recapitulated *in vivo* hemodynamics.

Contributions of J.Z.: study conceptualization, design and engineering of experimental setup, image acquisition, image analysis and data interpretation, writing and editing of manuscript.

www.nature.com/scientificreports

scientific reports

Check for updates

OPEN

On the impact of vessel wall stiffness on quantitative flow dynamics in a synthetic model of the thoracic aorta

Judith Zimmermann[1,2]✉, Michael Loecher[1,3], Fikunwa O. Kolawole[4], Kathrin Bäumler[1], Kyle Gifford[1], Seraina A. Dual[1], Marc Levenston[4], Alison L. Marsden[5,6,7] & Daniel B. Ennis[1,3,7]

Aortic wall stiffening is a predictive marker for morbidity in hypertensive patients. Arterial pulse wave velocity (PWV) correlates with the level of stiffness and can be derived using non-invasive 4D-flow magnetic resonance imaging (MRI). The objectives of this study were twofold: to develop subject-specific thoracic aorta models embedded into an MRI-compatible flow circuit operating under controlled physiological conditions; and to evaluate how a range of aortic wall stiffness impacts 4D-flow-based quantification of hemodynamics, particularly PWV. Three aorta models were 3D-printed using a novel photopolymer material at two compliant and one nearly rigid stiffnesses and characterized via tensile testing. Luminal pressure and 4D-flow MRI data were acquired for each model and cross-sectional net flow, peak velocities, and PWV were measured. In addition, the confounding effect of temporal resolution on all metrics was evaluated. Stiffer models resulted in increased systolic pressures (112, 116, and 133 mmHg), variations in velocity patterns, and increased peak velocities, peak flow rate, and PWV (5.8–7.3 m/s). Lower temporal resolution (20 ms down to 62.5 ms per image frame) impacted estimates of peak velocity and PWV (7.31 down to 4.77 m/s). Using compliant aorta models is essential to produce realistic flow dynamics and conditions that recapitulated in vivo hemodynamics.

Aortic wall stiffness is a strong predictor for all-cause and cardiovascular morbidity in patients with systemic arterial hypertension[1–3]. Model-based studies estimate that a total of 1.56 billion people worldwide may be affected by systemic arterial hypertension by 2025[4,5]. Consequently, monitoring aortic wall stiffness has become increasingly important and could guide treatment strategies and prevention of systemic arterial hypertension. Aortic wall stiffening is linked to an increase of pulse wave velocity (PWV) - the velocity at which the blood pressure pulse travels through the circulatory system. For a vessel of constant diameter, this relationship is modeled by the Moens-Korteweg equation:

$$\mathrm{PWV} = \sqrt{\frac{\mathrm{E}h}{2\rho r}} \tag{1}$$

where E is the elasticity modulus, ρ blood density, h wall thickness, and r vessel radius. Several PWV measurement technologies exist, with the carotid-femoral PWV (cfPWV) approach considered the clinical gold-standard[6]. cfPWV is approximated using the foot-to-foot temporal shifts of two signal waveforms (e.g. Doppler) recorded transcutaneously at the common carotid and femoral artery. The technical challenges associated with cfPWV measurements, such as carotid-femoral path length measurement inaccuracies or difficulties in transcutaneous signal recording, have limited broader adoption.

Non-invasive 4D-flow magnetic resonance imaging (MRI) provides three-dimensional (3D) and time-resolved velocity vector maps that serve as basis for image-based quantitative flow characterization[7,8]. In

[1]Department of Radiology, Stanford University, Stanford, CA, USA. [2]Department of Informatics, Technical University of Munich, Garching, Germany. [3]Division of Radiology, Veterans Affairs Health Care System, Palo Alto, CA, USA. [4]Department of Mechanical Engineering, Stanford University, Stanford, CA, USA. [5]Department of Bioengineering, Stanford University, Stanford, CA, USA. [6]Department of Pediatrics, Stanford University, Stanford, CA, USA. [7]Cardiovascular Institute, Stanford University, Stanford, CA, USA. ✉email: juzim@stanford.edu

particular, 4D-flow PWV calculations use a similar transit-time over fixed distance approach as in conventional cfPWV measurements, but in addition exploits the volumetric imaging data[9] and analyzes temporal shifts in flow rate waveforms extracted at numerous cross-sectional image planes along the aorta. This approach enables both regionally specific and more robust PWV estimates compared to two-point methods. In addition, the 3D anatomical image information is used to precisely measure the path length. Previous studies suggest low intra- and inter-observer variability and moderate test-retest performance[10,11]. The same studies affirm that PWV increases with age and in the presence of aortic atherosclerosis.

The otherwise lengthy clinical in vivo 4D-flow MRI scan must be accelerated using parallel imaging, compressed sensing, or fast readout techniques[12–17]. Each of these techniques, however, trades-off spatio-temporal image resolution and signal-to-noise ratio (SNR), both of which impact flow quantification accuracy. 4D-flow MRI sampling requirements to report robust PWV values are missing.

In vitro 4D-flow MRI using subject-specific synthetic aorta models connected to a cardiovascular flow pump enables prolonged imaging, thereby allowing optimal image quality. Moreover, in vitro setups enable studying flow dynamics under controllable conditions. In particular, we can program physiological flow waveforms, tune flow volume splits via outlet resistance control, and tune systemic pulse pressure via integration of capacitor elements. The majority of previous studies simplify their setup using rigid wall materials, which neglects the compliant nature of the human vasculature[18–20]. A limited number of studies embed compliant models, but do not report on how the compliance of the model compares to the human aorta[21,22].

Novel 3D-printing technology permits building models with realistic and varying compliance which we seek to leverage. Herein, this work exploits in vitro 4D-flow MRI with realistic and compliant models of the thoracic aorta to study quantitative flow dynamics. The two objectives of this study were: (1) to demonstrate feasibility of deploying compliant 3D-printed subject-specific aorta models in an MRI-compatible flow circuit setup that matches physiological flow and pressure conditions; and (2) to evaluate the impact of wall stiffness variations on cross-sectional flow metrics and PWV.

Methods

Compliant aorta models. An in vivo chest 4D-flow MRI dataset was acquired from a healthy subject (50 y/o, male) using a protocol that was in accordance with relevant guidelines and regulations, and approved by Stanford University Institutional Review Board. Informed consent was obtained from the subject prior to imaging. The 4D-flow MRI magnitude image was used to generate a subject-specific polygon mesh model of the thoracic aortic wall including the brachiocephalic trunk, left common carotid, and left subclavian artery. The wall domain mesh generation (Fig. 1f) consisted of: (1) binary segmentation of the aortic lumen; (2) polygon surface meshing of lumen mask (edge size = 0.8 mm); (3) extrusion of the mesh nodes in the normal direction to define the outer wall surface mesh; (4) boolean differencing of the outer wall and lumen surface mesh. The resulting wall thickness ($h_{wall} = 2$ mm) was within the reported range of the average wall thickness of the human adult aorta[23]. The mesh model was extended by cylindrical caps (length = 20 mm) at the ascending aorta inlet and at the four outlets to enable connection to customized barbed model-tubing transition elements. These steps were performed using SimVascular[24] and Meshmixer (Autodesk) open software tools.

A photopolymerization 3D printer (J735 PolyJet, Stratasys) with novel printing materials (Agilus30 and Vero-Clear, Stratasys) was used to manufacture two compliant and one nearly rigid model of the subject-specific aorta geometry (referred to as M_{c1}, M_{c2}, and M_r). Printed models were finished with a thin coating (Bectron, Elantas) to prevent fluid absorption (Fig. 1h). To characterize the material stiffness, standardized dumbbell shaped samples (ASTM D412 type A) were 3D-printed in the same batch and using the same material blend as the aorta models.

Uniaxial tensile testing (Instron 5848 Microtester, 10-KN load cell) was performed on three dumbbell samples per material elasticity. Samples were pre-conditioned with five loading and unloading cycles to 10 % peak strain followed by a sixth measurement cycle to 50 % peak strain. Testing was done at ambient conditions with a strain rate of 25%/sec. This rate corresponds to the upper loading rate limit on the aorta models when embedded in the flow circuit, which was assessed by analyzing the dynamic wall circumference in the imaging data. 3D-printing direction anisotropy was evaluated by varying the sample's orientation on the print bed.

Flow circuit setup. An MRI-compatible flow circuit setup (Fig. 1a) was engineered to enable *in vitro* 4D-flow imaging of the aorta models under physiological and controllable flow and pressure conditions. The inlets and outlets of the models were sealed to tubing via custom-fit 3D-printed barbed connectors with tapered transitions and then embedded into a ballistics gel block (Fig. 1b, ClearBallistics). The gel block provided a fixed positioning reference and had a short T1 relaxation time, which facilitated using it as static "tissue" for eddy current induced phase offset correction. Aortic model and gel block were placed inside an enclosed box that connects through five box-mounted flow ports to both the pump unit (CardioFlow 5000 MR, Shelley Medical Imaging Technologies) and to the fluid reservoir which supplies the pump unit via a return flow path.

The subject's previously performed MRI exam included aortic flow measurements from which the flow rate waveform was derived and programmed to the pump unit. To this end, the original waveform was spline-interpolated, down-scaled to meet the pump's peak flow rate limit (300 mL/s), and discretized ($\Delta t = 10$ ms) over a cardiac cycle length of RR = 1000 ms (heart rate 60 bpm). The resulting stroke volume was 71.2 mL and total flow was 4.3 L/min.

Flow volume splits across model outlets were controlled via the ratio of clamping the soft downstream tubing (ID = 12.7 mm) at $R1_{dist}$ and $R2_{dist}$ with adjustable pinch valves. We note that $R1_{prox}$ and $R2_{prox}$ were inherently defined by the model-to-capacitor tubing which should be kept as short as possible to most efficiently leverage the effect of the capacitors (described below). Flow splits were assessed using an ultrasonic flow probe (ME-PXL14, Transonic) that clamped-on at the DAo outlet and was connected to a data acquisition system (DAQ)

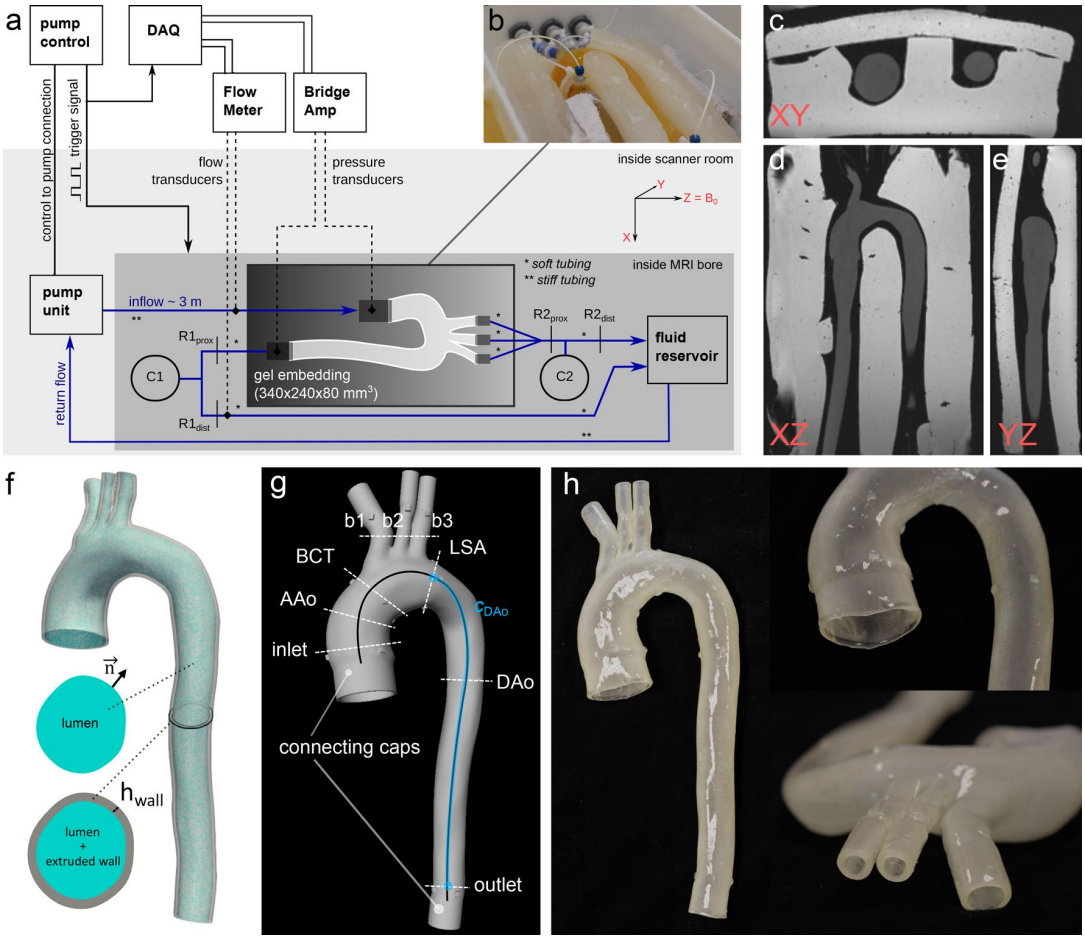

Figure 1. (**a**) Schematic of the MRI-compatible flow circuit setup. The pump unit was positioned at the end of the patient bed; the fluid reservoir was positioned on the patient bed and inside the MRI bore. The pump controller provided a pulse for triggering both image acquisition and DAQ signals. Ultrasonic flow transducers and pressure transducers (dotted lines) were disconnected after tuning and prior to moving the setup to the MRI iso-center. (**b**) Photograph of the model-specific gel block with embedded aorta model and ports (blue) at inlet and outlet to insert pressure transducers. (**c**–**e**) 3D spoiled-gradient echo MRI image data for three reformatted planes (XY, XZ, YZ) depicting the aorta model embedded into the gel. (**f**) Model construction showing lumen mesh (cyan) and extruded wall mesh (gray). (**g**) Final print-ready aortic wall model with defined cross-sectional landmarks, full centerline (black), and descending aorta centerline (blue) that was used for PWV analysis. The original model was extended with cylindrical caps (length = 2 cm) at the inlet and all outlets to accommodate connection to customized barbed connectors that then connect to tubing. (**h**) Photographs of a finished 3D-printed model. Graphics created using Inkscape (v0.92, https://inkscape.org/), SimVascular (release 2020–04, https://simvascular.github.io/), and Meshmixer (v3.5, https://www.meshmixer.com/).

via a flow module (TS410, Transonic). Based on preliminary bench top tests, we targeted a flow volume split of 70/30 for model M_{c1}.

Pulse pressure was controlled using two capacitance elements at the DAo outlet (C1) and at the merged arch branches (C2). The capacitors were designed as cylindrical towers with sealed air compression chambers in which the enclosed air volume (height = 16 cm, diameter = 10.2 cm) dictated the amount of downstream capacitance. Pressure transducers (Micro-Tip SPR-350S, Millar) were inserted at the model inlet and descending aorta outlet, and pressure signal was received at the DAQ through a bridge amplifier front-end (FE224 Quad Bridge, ADInstruments). The mean arterial pressure was elevated by increasing the overall system resistance via the distal pinch valves which—after final tuning—reduced the tubing cross-section to a slit of 1.3–2.3 mm. We defined 110–120 mmHg and 70–80 mmHg as target systolic (P_{sys}) and diastolic (P_{dias}) pressure ranges for model M_{c1}.

For the three models, identical inflow conditions were programmed, whereas pressure and flow split tuning was performed with model M_{c1} only. Subsequently, models M_{c2} and M_r were embedded under the identical periphery without re-tuning system capacitance or resistance. All DAQ data analysis was performed using dedicated DAQ software (LabChart 8, ADInstruments).

	High temp-res	Baseline temp-res	Low temp-res
FoV (mm^3)	360 × 260 × 100	360 × 260 × 100	360 × 260 × 100
Acquisition matrix	144 × 104 × 40	144 × 104 × 40	144 × 104 × 40
Spatial resolution (mm)	2.5 isotropic	2.5 isotropic	2.5 isotropic
Lines per segment	1	2	3
Reconstructed frames	50	25	16
Temporal resolution (ms)	20	40	62.5
TE/TR (ms)	2.8/5.2	2.8/5.2	2.8/5.2
V_{enc} (cm/s)	120	120	120
Flip angle (°)	15	15	15
BW (Hz/px)	451	451	451
Scan time (mm:ss)	42:40	21:20	14:40

Table 1. 4D-flow MRI sequence parameters. Three data sets were acquired with each model, resulting in a total of nine datasets available for analysis. Variations in effective temporal resolution were controlled by the number of acquired k-space lines per segment, and the number of reconstructed cardiac frames was adapted accordingly. *FOV* field of view, *TE* echo time, *TR* repetition time, V_{enc} velocity encoding range, *BW* bandwidth.

Imaging experiments. Imaging experiments were performed using a 3T MRI scanner (Skyra, Siemens Healthineers) with a 32-channel spine and a 18-channel chest coil. We used a total fluid volume of seven liters (glycerol-water mixture with ratio = 40/60) with T_1-shortening contrast agent (ferumoxytol, concentration = 0.75 mL/L) for increased signal-to-noise ratio (SNR). Protocol steps were as follows: (1) set up "fluid-empty" circuit on the MRI scanner table; (2) flush and de-bubble all fluid lines (steady flow); (3) record and tune pressures and flow splits (pulsatile flow); (4) remove pressure and flow transducers before moving setup to MRI isocenter; (5) run high-resolution 3D spoiled gradient echo (SPGR) acquisition (steady flow, 71.2 mL/s, Fig. 1c–e); (5) run 4D-flow acquisitions (three series, all pulsatile flow); (6) run 2D-PC and 2D-cine-GRE at pre-defined landmark slices (14 series, all pulsatile flow). The pump trigger signal was used for retrospective cardiac gating (direct input to scanner) and to later synchronize signals from pressure and ultrasonic recordings (direct input to DAQ). Image acquisition time per model was 1 hour 45 minutes, and total end-to-end experiment time (including setting up and swapping models) was 10 hours.

2D-PC and 2D-cine-GRE MRI. Two-dimensional (2D) imaging through lumen cross-section was performed at the following landmarks (Fig. 1g): ascending aorta inlet ('inlet'), ascending aorta ('AAo'), arch just proximal to brachiocephalic trunk ('BCT'), and distal to left subclavian artery ('LSA'), mid-descending aorta ('DAo'), descending aorta outlet ('outlet'), and three arch branches ('b1', 'b2', 'b3'). 2D MRI sequences included: (1) 2D cine gradient echo (2D-cine-GRE) with in-plane resolution 0.9 × 0.9 mm, slice thickness = 6 mm, FoV = 240 × 150 mm, TE/TR = 3/4.75 ms, flip angle = 7°, averages = 2, retrospective gating, number of temporal frames = 50 (frame length = 20 ms), no parallel imaging acceleration; and (2) 2D phase-contrast (2D-PC) with V_{enc} = 90–120 cm/s, in-plane resolution 1.1 × 1.1 mm, slice thickness = 6 mm, FoV = 220 × 123 mm, TE/TR = 3/21 ms, flip angle = 25°, averages = 2, retrospective gating, number of temporal frames = 50 (frame length = 20 ms), no parallel imaging acceleration.

4D-flow MRI. We used a conventional 4D-flow sequence with Cartesian k-space sampling, a velocity encoding range (V_{enc}) of 120 cm/s, and repeated scans at three temporal resolutions (20 ms, 40 ms, 62.5 ms), leading to a total of nine datasets (Table 1). V_{enc} was chosen to optimize signal-to-noise ratio during systole while avoiding phase-wrapping artifacts, i.e. just above peak systolic velocities as measured by preceding 2D-PC. To minimize phase offsets and to improve geometric fidelity, the image data were corrected for Maxwell terms (during reconstruction), gradient non-linearity, and eddy current (both post-reconstruction). Distortion correction due to gradient non-linearity was implemented as described by Markl et al.[25] 3D phase images were corrected for eddy current effects via linear fitting of 3D offset maps through the ballistics gel image region. No phase unwrapping was required. 4D-flow images were processed using MEVISFlow software solution (v11.2, Fraunhofer Institute for Digital Medicine)[26].

Image analysis. *2D-PC and 2D-cine-GRE analysis.* For all cross-sectional landmarks (Fig. 1g) aorta lumen contours were manually drawn in the first cardiac frame ($t = 0$) of the 2D-cine-GRE slices and tracked through all subsequent frames ($t = 1{-}49$) using a phase-based motion tracking algorithm as described by Tautz et al.[27]. Lumen expansion was assessed by calculating relative contour area change over time. Identical contours were used to assess inflow conditions and net flow splits based on the acquired 2D-PC data.

4D-flow analysis. For each aorta model, we segmented a 3D aorta lumen mask $m[\boldsymbol{x}]$ in the 3D SPGR image data using an automated 3D region growing algorithm, and subsequently derived the lumen centerline (c_{full}) using a skeleton approach[28] on the 3D binary mask. The centerline was used to define cross-sectional planes for 4D-flow

parameter quantification at landmarks identical to those defined as part of the 2D acquisitions (Fig. 1b) and to extract equidistant flow waveforms used for the PWV computation.

Based on the 4D-flow magnitude image output, time-resolved lumen contours were automatically tracked as described above. The following 4D-flow based metrics were computed: flow rate (mL/s), net flow per cycle (mL), and mean/max velocity (cm/s). All metrics were compared for all combinations of model wall stiffness and temporal resolution.

PWV calculation. PWV computation was focused on the descending aorta only (with centerline c_{DAo}, reaching from landmarks 'LSA' to 'outlet'), owing to flow effects at the arch branches that alter flow waveforms and compound the computation. Given the full velocity vector field $\boldsymbol{v}[\boldsymbol{x}, t]$, lumen mask $m[\boldsymbol{x}]$, and c_{DAo}, flow rate curves were computed as follows: (1) define N cross-sectional analysis planes with normal vector $\boldsymbol{n}_k$ with $k = [1, \mathrm{N}]$ at equidistant points c_k along c_{DAo} (spacing = 5 mm) ; (2) retrieve oriented lumen cross-sections A_k at planes defined by $\boldsymbol{n}_k$, c_k, and lumen mask $m[\boldsymbol{x}]$; (3) compute flow rate

$$Q_k[t] = \int \langle \boldsymbol{v}[\boldsymbol{x}, t], \boldsymbol{n}_k \rangle dA_k.$$

$Q_k[t]$ curves were interpolated using cubic-splines and the time-to-foot (TTF) approach (Fig. 7a) was used to calculate PWV[29]. Briefly, $\mathrm{TTF_k}$ for each $Q_k[t]$ curve was defined as the x-intercept of a line fitted through the waveform's upslope points at 20 % and 80 % of the peak flow rate. $\mathrm{TTF_k[c_k]}$ was plotted as function of the centerline location and $\mathbf{PWV_{TTF}}$ was defined as the inverse slope of the linear regression line fitted to $\mathrm{TTF_k[c_k]}$. Linear regression used a conventional least-square-error (LSE) approach as well as a random sampling consensus (RANSAC) algorithm to better handle outlier.

Results

Tensile testing. All material samples exhibited non-linear stress-strain behavior. The incremental Young's moduli were estimated by the tangent modulus (E_t) at nominal stress $\sigma = 0.053$MPa, which was approximated by $\sigma = Pr/h_{wall}$ with P given by the recorded mean pressure $P_{MAP} = 57$mmHg (during pulsatile flow), wall thickness $h_{wall} = 0.002$m, and average lumen radius $r = 0.014$m. E_t for the compliant models $\mathrm{M_{c1}}$ and $\mathrm{M_{c2}}$ were 1.27MPa (ranging 1.23MPa to 1.31MPa) and 4.3MPa (ranging 3.7MPa to 4.88MPa), respectively. As for model $\mathrm{M_r}$, no absolute elasticity estimates could be derived from the given stress-strain data, but differences in $\mathrm{M_r}$ elasticity were approximated to be at least 15-fold ($>$ 15MPa) when compared to model $\mathrm{M_{c1}}$. 3D-printing anisotropy was negligible with differences $<$ 5% within the relevant strain range for all three samples. Stress-strain plots are shown in Supplementary Fig. S1.

Pressure tuning. Pressure recordings were performed on the scanner bed prior to image acquisition. Pressure waveforms (Fig. 2, top row) recorded at the model inlet show increased peak pressures in models $\mathrm{M_{c2}}$ (116mmHg) and $\mathrm{M_r}$ (133mmHg) compared to the most compliant model $\mathrm{M_{c1}}$ (112mmHg). At the model outlet (DAo branch) peak pressures dropped by 7mmHg for both compliant models $\mathrm{M_{c1}}$ and $\mathrm{M_{c2}}$, and by 11mmHg for the nearly rigid model $\mathrm{M_r}$. Diastolic pressure values were between 38mmHg and 40mmHg for all models at the inlet and dropped by 1mmHg at the outlet. All pressure waveforms showed an oscillating behaviour both in systole and diastole, which was most dominant in model $\mathrm{M_r}$.

Flow split tuning. Flow splits between all model outlets were consistent between the three models, with net flows of 48–49 ml measured with the ultrasonic probe at the descending aorta outlet prior to each acquisition (corresponding 68% of the programmed inlet flow). Inlet net flow volumes calculated from 2D-PC flow rate waveforms (Fig. 2, row 2) ranged from 64.6 to 66.4 ml; 2D-PC DAo outlet net flow volumes ranged from 51.6 to 52.7 ml. Adding up 2D-PC measured net flow at all outlets (b1, b2, b3 and DAo) total outflow was 70.0, 70.8, 67.8 ml for $\mathrm{M_{c1}}$, $\mathrm{M_{c2}}$, and $\mathrm{M_r}$, corresponding to relative differences of 1.7, 0.6, and 4.8 % from the programmed inflow (71.2 ml).

Aorta wall expansion. Aortic wall expansion was clearly visible in systole for models $\mathrm{M_{c1}}$ and $\mathrm{M_{c2}}$ and most pronounced in the ascending aorta. The wall expanded non-uniformly for all evaluated landmarks (Fig. 2, row 4, and Supplementary Fig. S2) owing to the posterior constraint provided by the gel block (Fig. 1c). Based on the tracked contours, the calculated cross-sectional area increased by $>$ 5% in models $\mathrm{M_{c1}}$ and $\mathrm{M_{c2}}$, whereas no detectable area change ($<$ 1%) was measured for model $\mathrm{M_r}$ (Fig. 2, row 3). For models $\mathrm{M_{c1}}$ and $\mathrm{M_{c2}}$, relative area change over the cardiac cycle also depicted a small secondary lobe in early diastole which was in phase with the secondary lobes of the pressure and flow rate waveforms.

Velocities at cross-sections. Figure 4 shows a qualitative comparison between model $\mathrm{M_{c1}}$ and model $\mathrm{M_r}$ and their velocity vector profiles for cardiac frames at peak systole and end systole. While profiles in models $\mathrm{M_{c1}}$ and $\mathrm{M_r}$ were similar at peak systole, minor qualitative differences were observed at end systole, particularly at landmarks proximal to the arch branches. Here, the nearly rigid model $\mathrm{M_r}$ showed a more centered cross-sectional velocity profile with less backward flow components and less helical flow tendencies. Velocity profiles at landmarks distal to the arch branches mainly differed with regards to the velocity vector magnitude, with higher velocities in model $\mathrm{M_r}$. Model dependent velocity differences in the descending aorta can also be observed in maps of traced particles, as visualized in Fig. 3.

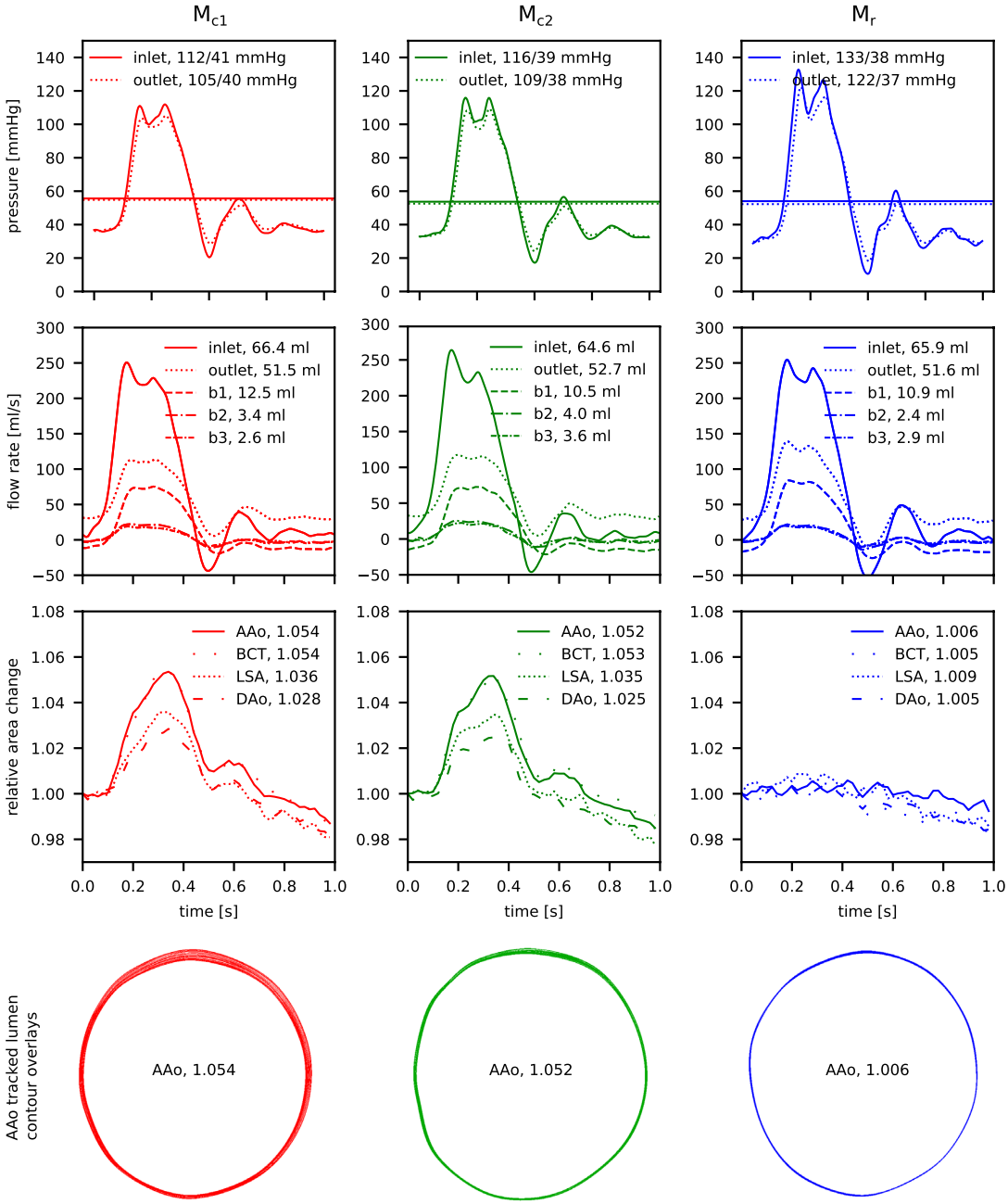

Figure 2. Experimental setup conditions for aorta models M_{c1} (red), M_{c2} (green), and M_r (blue), evaluated at selected landmarks (Fig. 1g). (Row 1) Pressure conditions recorded at inlet (solid) and outlet (dashed). (Row 2) Flow rate waveforms at inlet and all outlets with calculated net flow volumes, based on 2D PC-MRI data. (Row 3) Cross-sectional area change relative to area at cardiac cycle start, based on tracked lumen contours in 2D-cine-GRE data. (Row 4) Overlay of tracked lumen contour at cross-section AAo for all acquired time frames (N = 50). Animated contour tracking results are presented in Supplementary Fig. S2. Plots created using Python (v3.6, https://www.python.org/).

Figure 5 shows mean and maximum velocity analysis results. Maximum velocities at peak systole were highest in model M_r (73.1 cm/s at AAo, 42.5 cm/s at BCT, 39.1 cm/s at LSA, and 43.2 cm/s at DAo) compared to both compliant models M_{c1} (73.0 cm/s at AAo, 38.5 cm/s at BCT, 35.4 cm/s at LSA, and 35.5 cm/s at DAo) and M_{c2} (70.5 cm/s at AAo, 36.6 cm/s at BCT, 35.5 cm/s at LSA, and 39.2 cm/s at DAo). Likewise, cross-sectional mean velocities in systole were higher in model than in the compliant models. Decreasing temporal sampling from 50 frames down to 16 frames showed greatest effects at the AAo landmark for peak velocity which decreased by 16%, 19 %, 14 % for M_{c1}, M_{c2}, and M_r.

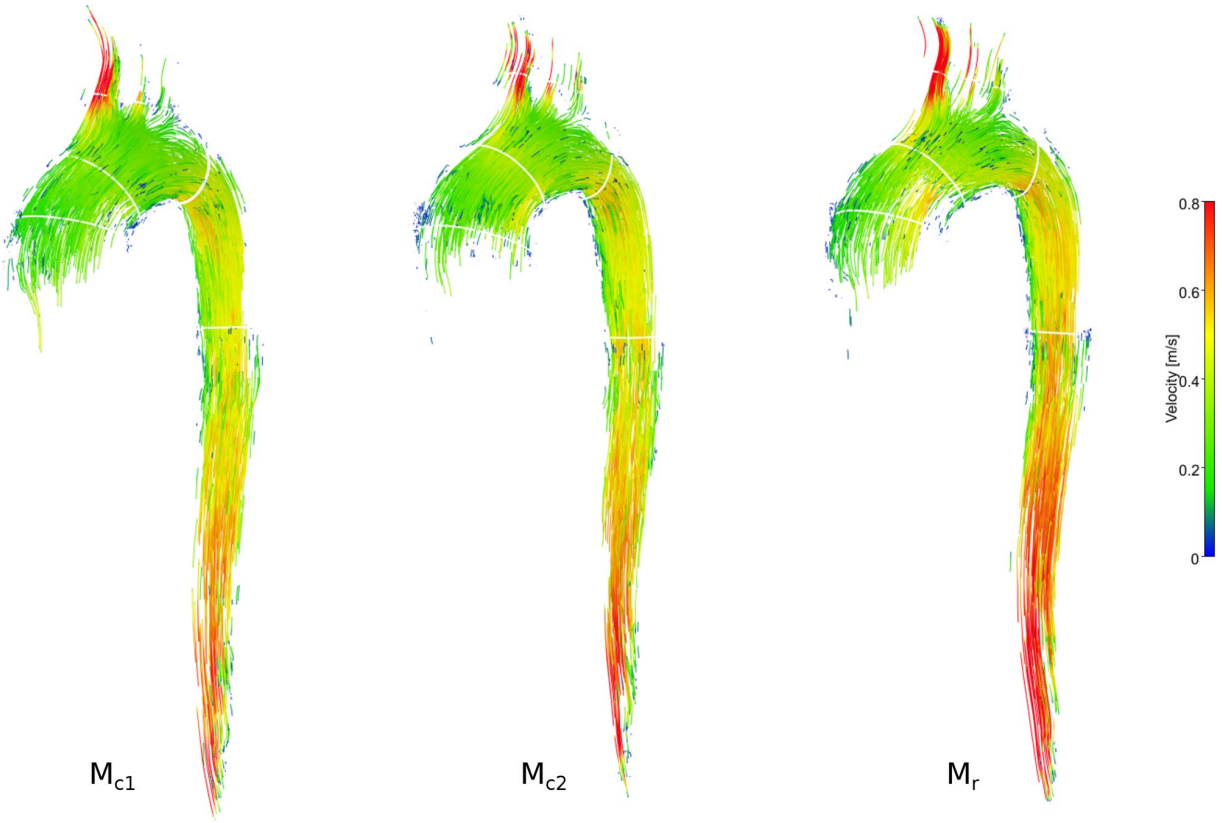

Figure 3. Particle tracing based on 4D-flow MRI data for the three aorta models of identical subject-specific geometry, but different wall stiffness. While particle traces matched among the three models, velocities along the descending aorta—as depicted by the color—were slightly higher in the nearly rigid model M_r. An animated version of traced particles is shown in Supplementary Video S3–5. Graphic created using MevisLab (v3.4a, https://www.mevislab.de/).

Flow at cross-sections. Figure 6 shows flow rate and cumulative net flow results. Results were similar between different models or between 4D-flow data of different temporal sampling rates. Net flow values were 69.6 ± 1.9 ml for AAo, 63.4 ± 1.6 ml for BCT, 47.0 ± 0.7 ml for LSA, and 45.7 ± 1.0 ml for DAo (given as mean ± SD over three models and three temporal sampling rates). Net flow at the landmarks upstream and downstream of the arch branches were within 10% of the programmed pump value (71.2 ml) and the measured ultrasonic value (48.5 ml), respectively.

Flow rate waveforms over the cardiac cycle (Fig. 6, solid lines) showed weaker peak flow rate dampening with increased model wall stiffness. This effect was most pronounced at landmarks further downstream (LSA, DAo). 4D-flow sampled at 50 frames per cycle revealed a double flow rate peak in systole at all cross-sections, which was much less apparent in the dataset sampled at 25 frames per cycle and not apparent in the dataset sampled at 16 frames per cycle. Moreover, a distinct second (t = 0.66 s) and third (t = 0.85 ms) flow rate peak were present in all derived waveforms, irrespective of model stiffness and temporal sampling rate.

PWV. PWV values were estimated from time-to-foot (TTF) delays of flow rate waveforms at equidistantly spaced cross-sectional planes along the descending aorta (Fig. 7b). Based on the datasets with highest temporal sampling (50 frames/cycle), PWV was 6.98 m/s (LSE) and 5.78 m/s (RANSAC) for model M_{c1}, and 7.31 m/s (LSE) and 7.31 m/s (RANSAC) for model M_{c2}. Both for model M_{c1} and M_{c2}, PWV values were lower with datasets sampled at 25 frames/cycle and further decreased for datasets sampled at 16 frames/cycle. The 16 frames/cycle dataset of model M_{c1} included four extreme outlier points posting large negative TTF values. These points were excluded prior to fitting the linear model. No linear relationship between TTF and centerline position was detectable for model M_r irrespective of temporal resolution. Consequently, while PWV was very high, no PWV values could be reported based on the data.

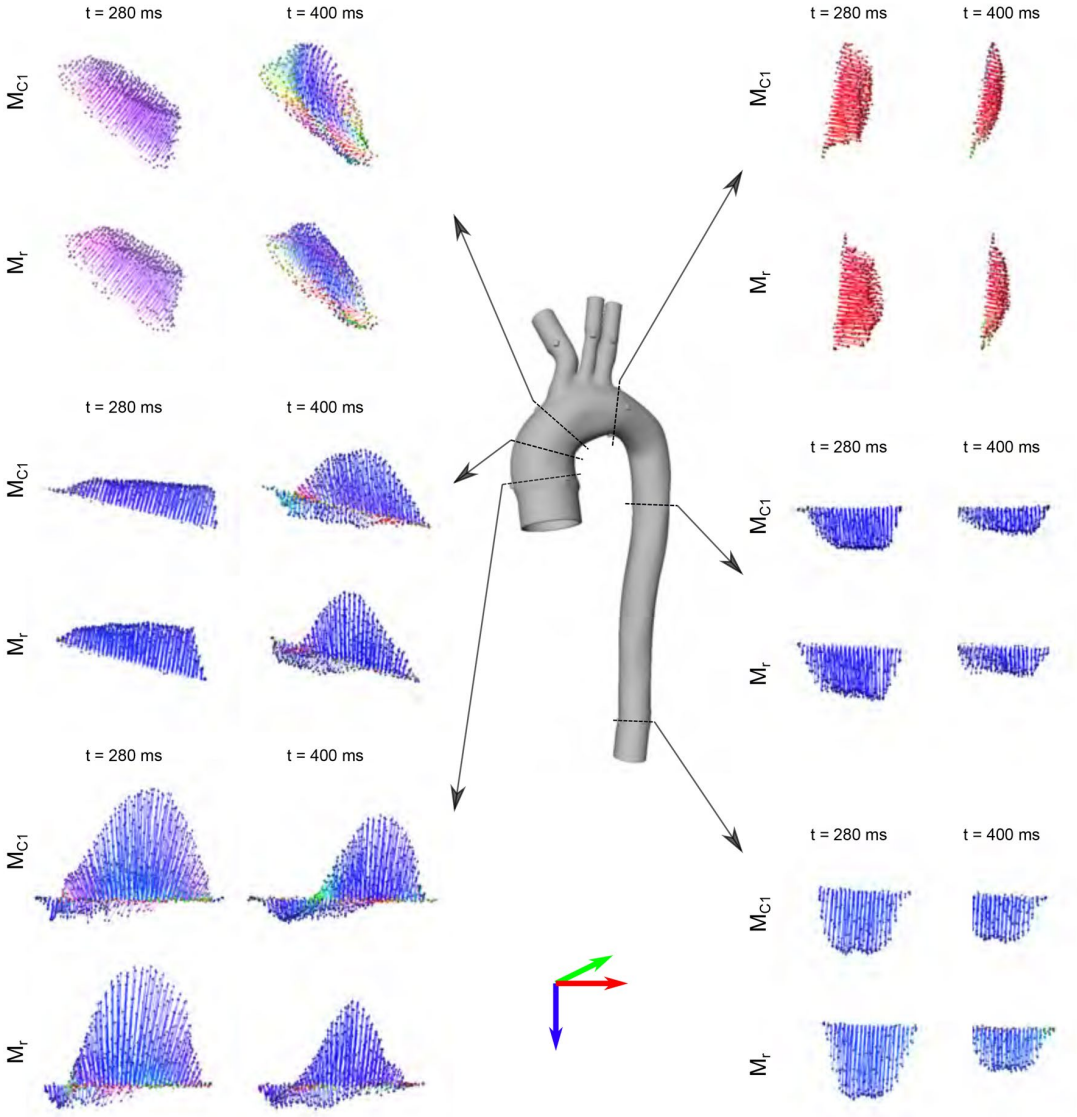

Figure 4. 4D-flow cross-sectional velocity profiles in models M_{c1} (top) and M_r (bottom) at peak-systolic ($t = 280$ ms) and end-systolic ($t = 400$ ms) frames. All profiles are 3D-rendered using the identical camera view and colored according to the 3D direction (red-green-blue arrow legend). Backward flow is visible at cross-sections prior to the arch branches (inlet, AAo, BCT), specifically at end-systole. One can appreciate the different vector profiles for the compliant model M_{c1} when compared to the nearly rigid model M_r. Velocity profiles rendered using MevisLab (v3.4a, https://www.mevislab.de/).

Discussion

This study demonstrated the feasibility of integrating a subject-specific aorta model with varying wall elasticity into an MRI-compatible flow circuit setup that operates under physiological flow and pressure conditions. Utilizing prolonged and highly-controlled in vitro 4D-flow imaging, we showed the influences of aortic wall compliance and temporal sampling rates on both cross-sectional flow parameters and 4D-flow derived PWV.

Stress-strain testing of the compliant 3D-printing material suggested that the derived tangent moduli E_t of models M_{c1} and M_{c2} are in the same range as the incremental Young's moduli that have been reported for a 'young' (more compliant) and 'old' (stiffer) human thoracic aorta, respectively[30]. We did not attempt to report E_t for the non-realistic model M_r due to the material's substantially higher stiffness which challenged reliable tensile testing, but approximated the difference in elasticity to be at least 15-fold when compared to model M_{c1}.

Pressure tuning was performed for model M_{c1} only. Subsequently, model M_{c1} was interchanged with models M_{c2} and M_r, but resistance and downstream capacitance were kept constant. This approach allowed for isolated evaluation of the effect increased wall compliance on pressure and flow. While tuning model M_{c1} to physiological P_{sys} was successful, P_{dias} was below the target range of 70–80 mmHg. Previous work with advanced MRI-compatible flow circuit setups reported similar increased (i.e. > 50mmHg) pulse pressures[21,31,32]. We note that

www.nature.com/scientificreports/

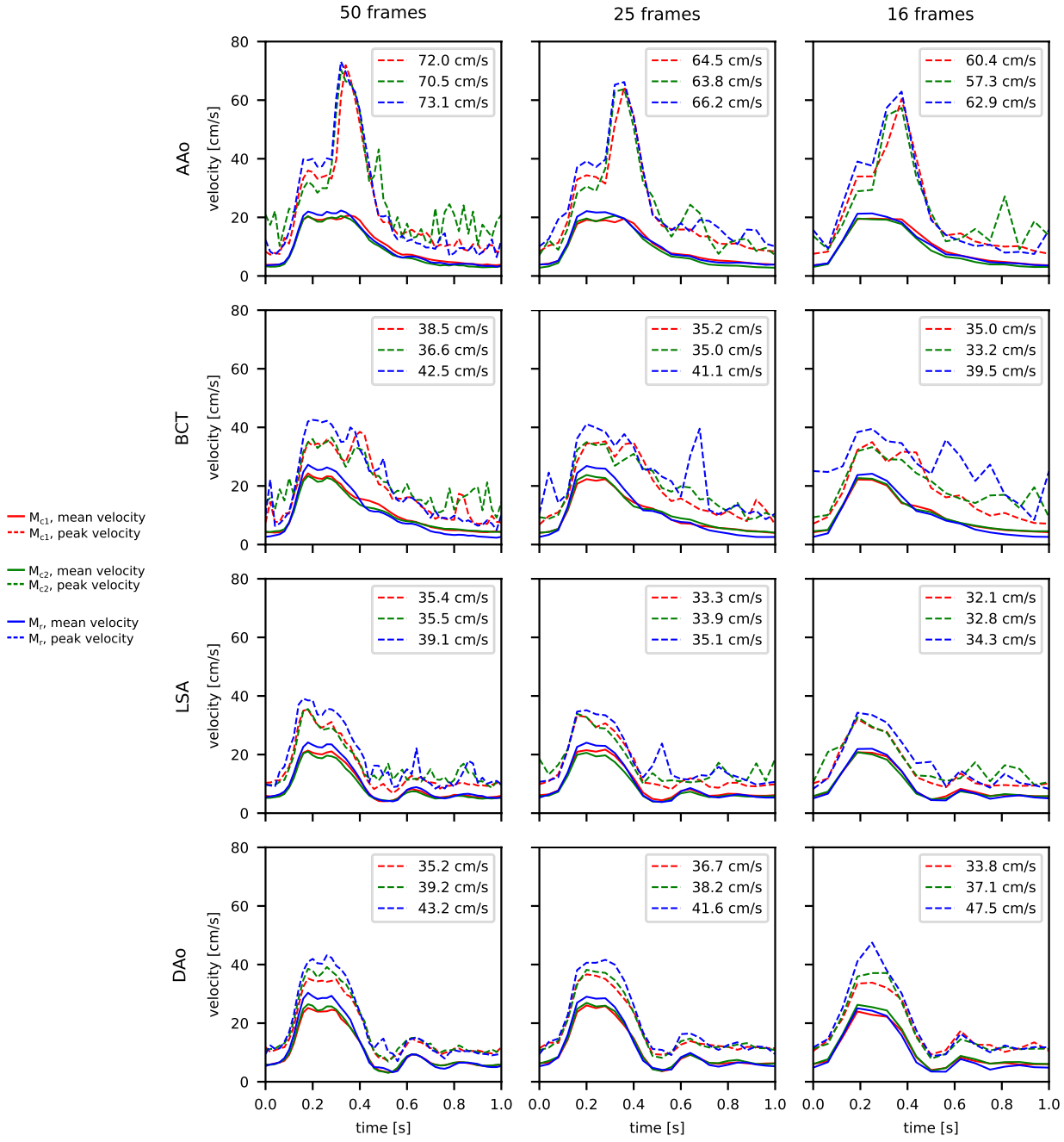

Figure 5. 4D-flow cross-sectional mean (solid) and maximum (dashed) velocity at four landmarks (Fig. 1g) and three different temporal sampling rates. Highest peak-systolic velocities (see values in legends) were measured in model M_r (blue); and inter-model peak-systolic velocity differences were greater at landmarks further downstream. The temporal sampling rate impacted the measurement of peak velocities, which was most pronounced at AAo point. Spikes in diastole were attributed to noise in near-boundary pixels and inaccurate contouring. Plots created using Python (v3.6, https://www.python.org/).

two main factors determine successful pressure tuning: (1) P_{sys} or P_{MAP} can easily be elevated by increasing flow resistance distal to the capacitors for which the pulse pressure remains constant; (2) pulse pressure is governed by the available capacitance, i.e. compressible air volume (C1, C2) and by the ratio of distal to proximal resistance ($R1_{dist}/R1_{prox}$, $R2_{dist}/R2_{prox}$). A greater ratio provides a wider range for tuning pulse pressure. Despite P_{dias} being lower than physiological values, the achieved conditions were found to be sufficient to study the impact wall compliance on flow dynamics. Interchanging models under consistent resistance and capacitance settings led to two effects on pressure: (1) P_{sys} increased in model M_{c2}, and more so in model M_r, but no effects were

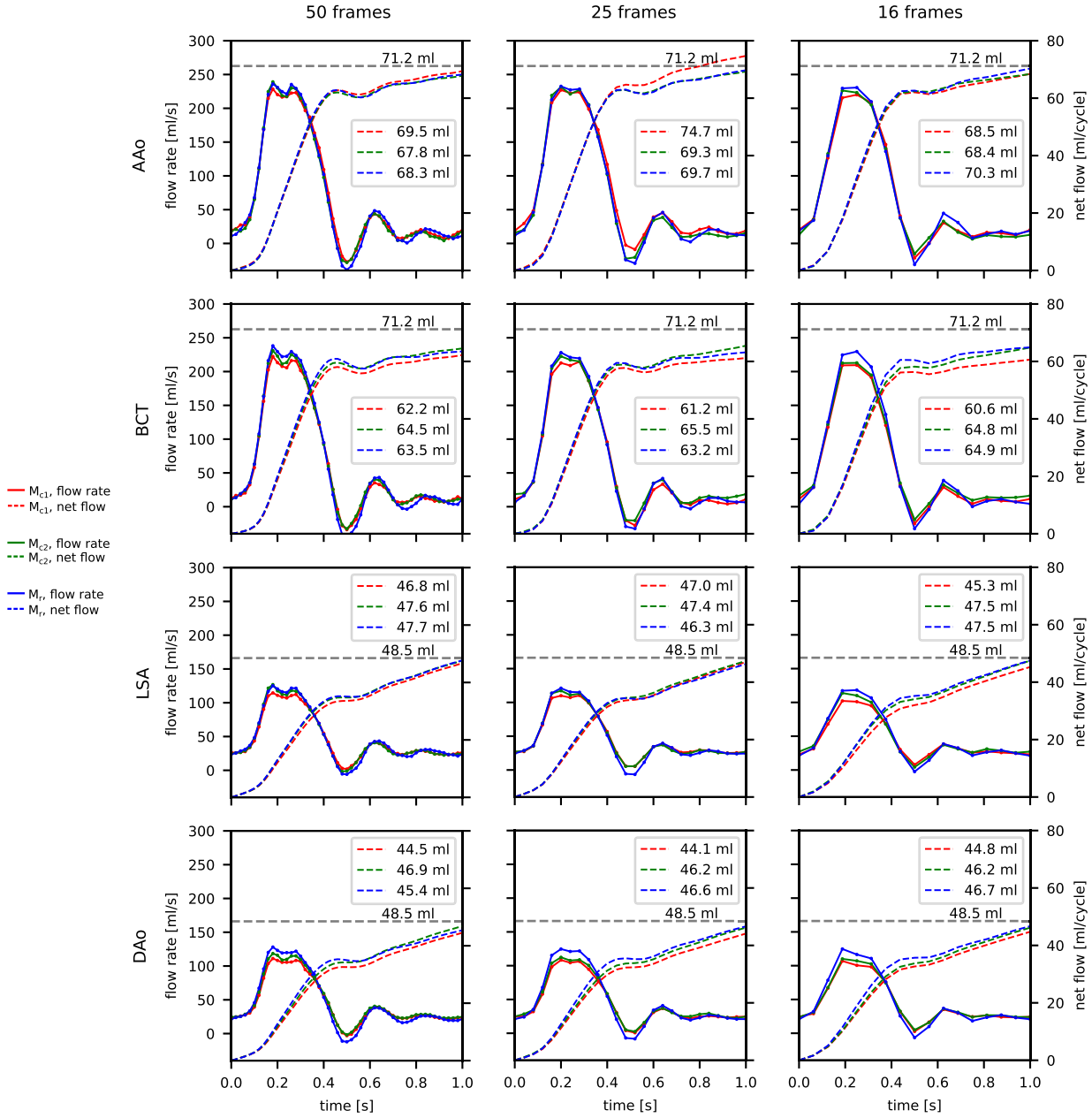

Figure 6. 4D-flow derived flow rate waveforms (left ordinates) and cumulative net flow (right ordinates) at four landmarks (Fig. 1g) and three different temporal sampling rates. Grey horizontal lines show the expected net flow according to the programmed inflow (71.2 mL/cycle) for the AAo and BCT slices, and measured (via ultrasonic transducer during setup tuning) DAo branch outflow (48.5 mL/cycle) for the LSA and DAo slices. Plots created using Python (v3.6, https://www.python.org/).

seen on P_{dias}; (2) inlet to outlet peak pressure differences increased with increasing wall stiffness. Both of these observations were as expected and they affirmed the validity of the setup.

Pressure and flow rate oscillations (Fig. 2) are expected to be caused by wave reflections at several branching points—natural arch branches, rigid flow connectors, flow valves, etc.—and under-damping in the system. Other studies with comparable flow circuit setups showed similar oscillating waveform shapes[21,31,32]. Additional engineering efforts to mitigate this phenomenon may benefit analyses of pressure and flow waveform shapes in multiple vessel geometries and/or under varying boundary conditions.

4D-flow image-based visualizations of vector profiles and traced particles indicated that variations in wall compliance lead to variations in velocity amplitudes and profiles (Figs. 3, 4). The quantitative analyses showed that both mean and maximum velocities decreased for the compliant models when compared to the nearly rigid version. Likewise, flow rate waveform dampening was most pronounced in the most compliant model and

www.nature.com/scientificreports/

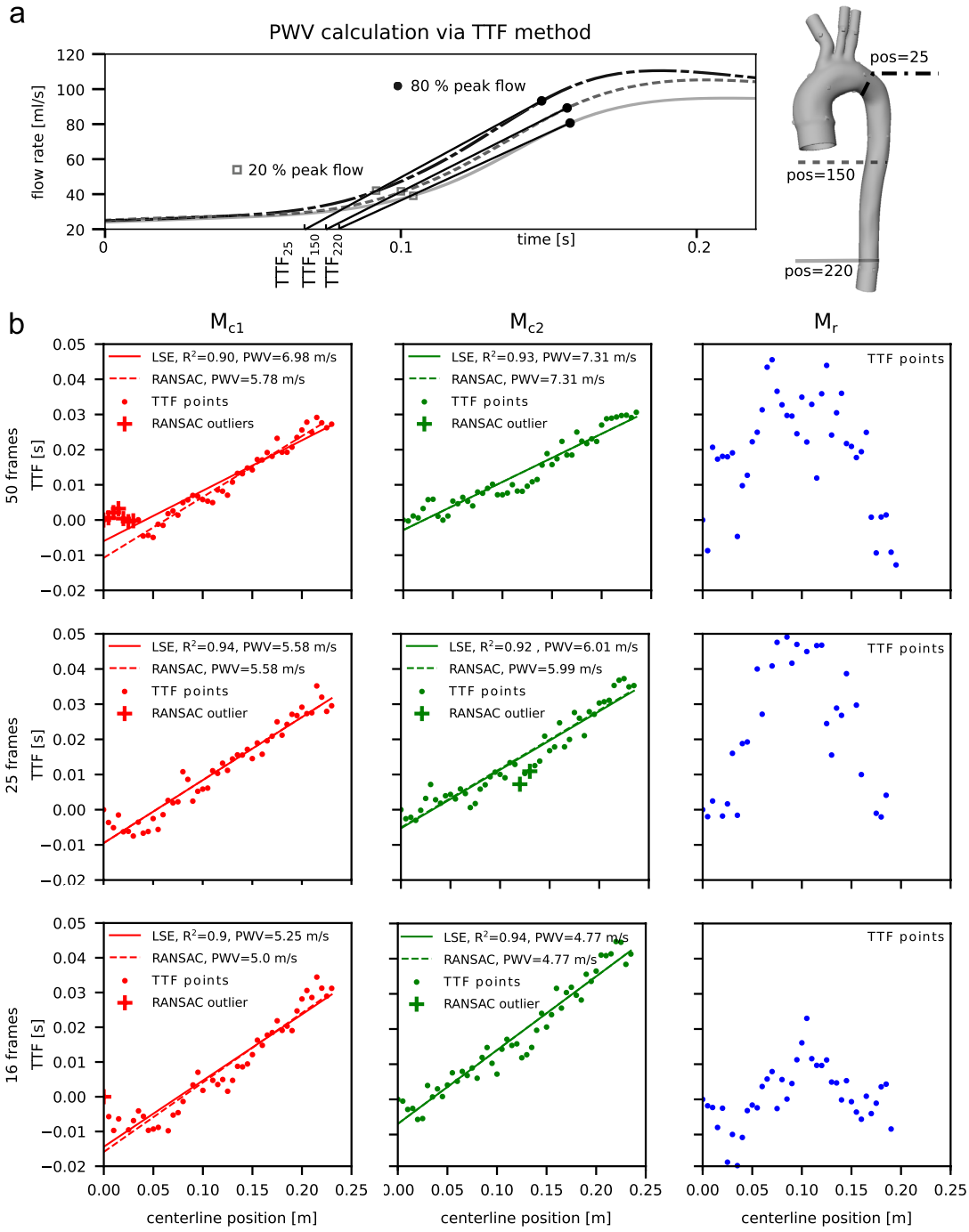

Figure 7. (**a**) Principle of retrieving TTF values at three positions along the descending aorta centerline. (**b**) PWV calculations for models M_{c1} (red), M_{c2} (green), and M_r (blue) for three temporal sampling rates (row 1 through 3). Scattered points depict TTF of flow rate waveforms extracted at equidistantly spaced cross sections along c_{DAo} (Fig. 1f). All TTF values are shown as TTF differences to TTF at centerline position 0. Conventional LSE linear regression (solid line, with R^2 given in legend) and RANSAC (dashed line with assigned outlier marked +) were used to derive PWV values, defined as the inverse slope of the respective line (given in legend). Differences in PWV were observed between models M_{c1} and M_{c2}. However, temporal sampling rates impacted these values, with decreasing PWV estimates for lower temporal resolution. It appears that PWV in model M_r is too fast such that plausible TTF along the centerline cannot be resolved with the 4D-flow based approach. LSE is very sensitive to outlier data which was apparent in data M_{c1} (50 frames) and M_{c1} (16 frames). For the latter one, four TTF points laid outside the displayed y-axis with linear regression deviations >100 × RMSE and were thus excluded prior to fitting the model. TTF, time-to-foot; LSE, least-squared-error; RANSAC, random sampling consensus; RMSE, root-mean-squared-error. Plots created using Python (v3.6, https://www.python.org/).

the further downstream the centerline. Thus, in comparative in vitro to in vivo studies—regardless of efforts to match patient-specific inflow conditions—fully rigid aorta models are likely insufficient for direct comparison.

4D-flow based PWV calculations in compliant models M_{c1} and M_{c2} provided values within the range of PWV values that have been reported in in vivo 4D-flow studies[11,33,34]. PWV in the model M_r was too high to reliably resolve TTF delays along the centerline. Thus, we did not attempt to report a 4D-flow derived PWV for model M_r. The referenced *in vivo* studies included healthy volunteers (young and old) and patients with atherosclerosis. Mean PWV among the respective cohorts ranged from 3.8 to 6.4 m/s. However, they did not include PWV measurements based on multiple 4D-flow datasets with varying temporal resolutions, which ranged from 32–41 ms—a typical temporal resolution in in vivo 4D-flow acquisitions amid scan time limitations. Another previous study utilizing through-plane encoded 2D-PC MRI with higher temporal resolution (6–10 ms), reported PWV values ranging from 4.3 m/s (healthy and young controls) to 6.5 m/s (older patients).

In contrast to the reported in vivo 4D-flow based PWV values, theoretical PWV values based on Moens-Korteweg (Eq. 1) are 8–10.7 m/s for model M_{c1}, 14.9–20 m/s for model M_{c2}, and 31–41 m/s (assuming E_t of model M_r to be 15-fold over model M_{c1}). The given ranges correspond to the change of aortic diameter, which ranges from 36 mm in the ascending aorta to 20 mm in the distal descending aorta. These theoretical values may be debated, as the Moens-Korteweg equations assumes a constant vessel diameter, which is not true of the aorta.

Variations in 4D-flow temporal resolutions affected PWV considerably. Assuming that the presented 4D-flow data at highest temporal resolution ($\Delta t = 20$ ms) generates the most reliable PWV values, the present results suggest that lower temporal sampling rates underestimate absolute PWV (up to 35 %). Specifically, our data shows that the impact of temporal resolution on PWV calculation may be more dominant than the effect of varying wall compliance. One TTF plot (model M_{c1}, 16 frames) included distinct outlier points with negative TTF delay that were removed prior to linear model fitting. This emphasizes that reliable PWV calculations are highly dependent on accurate flow waveforms, particularly when derived from data with low temporal resolution. In that case, using the alternative iterative RANSAC approach for fitting a linear regression showed the effect on PWV while directly excluding these outlier points.

Four key limitations of this study were identified. First, only a single approach for PWV measurement (TTF) was used. In addition to the TTF, others derived PWV by time-to-peak (TTP), time-to-upstroke (TTU), and by correlation analysis of time-shifted flow waveforms (xCorr)[29,34,35]. Wentland et al.[34] analyzed differences in PWV for these four approaches. PWV values were similar for TTF, TTU and xCorr, while TTP results deviated most due to challenges of detecting the true peak flow point in data with mediocre temporal resolution.

Second, synthetic aorta models were manufactured with uniform wall thickness and elasticity which simplifies the in vivo aorta. These local variations of the model may impact calculated PWV values. A subject-specific wall mesh directly built on a vessel wall segmentation—rather than segmenting the lumen and extruding the surface by a pre-defined and uniform wall thickness—may be an alternative approach. To this end, a 3D dark blood MRI protocol is able to provide the necessary image basis for building models with non-uniform wall thickness[36].

Third, potential effects of cardiac motion on aortic hemodynamics cannot be assessed with our setup, as there was no contracting left ventricle and/or moving aortic valve. While PWV analyses were focused on the descending aorta and thus are expected to not be impacted, hemodynamics in the ascending aorta may change.

Fourth, the study design did not assess the effects of heart rate or pressure variations on PWV, which remains a controversial topic according to other previous studies. A pre-clinical study with rats reported a positive HR to PWV correlation, which was further pronounced at higher mean arterial pressures[37]. Clinical studies that paced patients at different heart rates found either a positive HR to PWV correlation[38–41] or no correlation[42,43]. If heart rate to PWV dependencies were to be investigated with the presented in vitro setup, careful considerations need to be made on how to modify the inlet flow rate waveform and whether or not pressures should be regulated with programmed HR changes. Given this open research question, we consider the present flow circuit setup with compliant aorta models to be of high value to further investigate heart rate and pressure variations.

In conclusion, this work demonstrated 3D-printed subject-specific compliant models of the thoracic aorta integrated into a highly-controlled physiological flow circuit for assessment via in vitro MRI. Using compliant rather than rigid models of the aorta is essential to produce realistic flow dynamics and conditions that recapitulate in vivo hemodynamics.

Data availability

The subject-specific thoracic aorta model and custom-build model-specific connectors (.stl files), as well as all acquired MRI DICOM data is publicly available: https://purl.stanford.edu/dz488kx6180.

Received: 23 December 2020; Accepted: 9 March 2021
Published online: 23 March 2021

References

1. Blacher, J. *et al.* Impact of aortic stiffness on survival in end-stage renal disease. *Circulation* **99**, 2434–2439. https://doi.org/10.1161/01.CIR.99.18.2434 (1999).
2. Laurent, S. *et al.* Aortic stiffness is an independent predictor of all-cause and cardiovascular mortality in hypertensive patients. *Hypertension* **37**, 1236–1241. https://doi.org/10.1161/01.HYP.37.5.1236 (2001).
3. Asmar, R., Rudnichi, A., Blacher, J., London, G. M. & Safar, M. E. Pulse pressure and aortic pulse wave are markers of cardiovascular risk in hypertensive populations. *Am. J. Hypertens.* **14**, 91–97. https://doi.org/10.1016/S0895-7061(00)01232-2 (2001).
4. Kearney, P. M. *et al.* Global burden of hypertension: analysis of worldwide data. *Lancet* **365**, 217–223. https://doi.org/10.1016/s0140-6736(05)17741-1 (2005).
5. Zhou, B. *et al.* Worldwide trends in blood pressure from 1975 to 2015: a pooled analysis of 1479 population-based measurement studies with 19·1 million participants. *Lancet* **389**, 37–55. https://doi.org/10.1016/S0140-6736(16)31919-5 (2017).

6. Laurent, S. *et al.* Expert consensus document on arterial stiffness: Methodological issues and clinical applications. *Eur. Heart J.* **27**, 2588–2605https://doi.org/10.1093/eurheartj/ehl254 (2006).
7. Markl, M. *et al.* Time-resolved three-dimensional phase-contrast MRI. *J. Magn. Reson. Imaging* **17**, 499–506. https://doi.org/10.1002/jmri.10272 (2003).
8. van der Geest, R. J. & Gard, P. Advanced analysis techniques for intra-cardiac flow evaluation from 4D flow MRI. *Curr. Radiol. Rep.* **4**, 38. https://doi.org/10.1007/s40134-016-0167-7 (2016).
9. Markl, M. *et al.* In vivo wall shear stress distribution in the carotid artery: effect of bifurcation geometry, internal carotid artery stenosis, and recanalization therapy. *Circul. Cardiovasc. Imaging* **3**, 647–655. https://doi.org/10.1161/circimaging.110.958504 (2010).
10. Markl, M., Frydrychowicz, A., Kozerke, S., Hope, M. & Wieben, O. 4D flow MRI. *J. Magn. Reson. Imaging* **36**, 1015–36. https://doi.org/10.1002/jmri.23632 (2012).
11. Dyverfeldt, P., Ebbers, T. & Länne, T. Pulse wave velocity with 4D flow MRI: systematic differences and age-related regional vascular stiffness. *Magn. Reson. Imaging* **32**, 1266–1271. https://doi.org/10.1016/j.mri.2014.08.021 (2014).
12. Valvano, G. *et al.* Accelerating 4D flow MRI by exploiting low-rank matrix structure and hadamard sparsity. *Magn. Reson. Med.* **78**, 1330–1341. https://doi.org/10.1002/mrm.26508 (2017).
13. Ma, L. E. *et al.* Aortic 4D flow MRI in 2 minutes using compressed sensing, respiratory controlled adaptive k-space reordering, and inline reconstruction. *Magn. Reson. Med.* **81**, 3675–3690. https://doi.org/10.1002/mrm.27684 (2019).
14. Schnell, S. *et al.* K-t GRAPPA accelerated four-dimensional flow MRI in the aorta: Effect on scan time, image quality, and quantification of flow and wall shear stress. *Magn. Reson. Med.* **72**, 522–533. https://doi.org/10.1002/mrm.24925 (2014).
15. Garg, P. *et al.* Comparison of fast acquisition strategies in whole-heart four-dimensional flow cardiac MR: Two-center, 1.5 Tesla, phantom and in vivo validation study. *J. Magn. Reson. Imaging* **47**, 272–281. https://doi.org/10.1002/jmri.25746 (2018).
16. Loecher, M., Magrath, P., Aliotta, E. & Ennis, D. B. Time-optimized 4D phase contrast MRI with real-time convex optimization of gradient waveforms and fast excitation methods. *Magn. Reson. Med.* **82**, 213–224. https://doi.org/10.1002/mrm.27716 (2019).
17. Dillinger, H., Walheim, J. & Kozerke, S. On the limitations of echo planar 4D flow MRI. *Magn. Reson. Med.* **84**, 1806–16. https://doi.org/10.1002/mrm.28236 (2020).
18. Lorenz, R. *et al.* Closed circuit MR compatible pulsatile pump system using a ventricular assist device and pressure control unit. *Magn. Reson. Med.* **67**, 258–268. https://doi.org/10.1002/mrm.22983 (2012).
19. Canstein, C. *et al.* 3D MR flow analysis in realistic rapid-prototyping model systems of the thoracic aorta: comparison with in vivo data and computational fluid dynamics in identical vessel geometries. *Magn. Reson. Med.* **59**, 535–546. https://doi.org/10.1002/mrm.21331 (2008).
20. Wen, C. Y., Yang, A. S., Tseng, L. Y. & Chai, J. W. Investigation of pulsatile flowfield in healthy thoracic aorta models. *Ann. Biomed. Eng.* **38**, 391–402. https://doi.org/10.1007/s10439-009-9835-6 (2010).
21. Urbina, J. *et al.* Realistic aortic phantom to study hemodynamics using MRI and cardiac catheterization in normal and aortic coarctation conditions. *J. Magn. Reson. Imaging* **44**, 683–697. https://doi.org/10.1002/jmri.25208 (2016).
22. Jung, B. *et al.* Investigation of hemodynamics in an in vitro system simulating left ventricular support through the right subclavian artery using 4-dimensional flow magnetic resonance imaging. *J. Thorac. Cardiovasc. Surg.* **150**, 200–207. https://doi.org/10.1016/j.jtcvs.2015.02.048 (2015).
23. Rosero, E. B. *et al.* Sex, race, and age distributions of mean aortic wall thickness in a multiethnic population-based sample. *J. Vasc. Surg.* **53**, 950–957. https://doi.org/10.1016/j.jvs.2010.10.073 (2011).
24. Updegrove, A. *et al.* SimVascular: an Open Source Pipeline for Cardiovascular Simulation. *Ann. Biomed. Eng.* **45**, 525–541. https://doi.org/10.1007/s10439-016-1762-8 (2017).
25. Markl, M. *et al.* Generalized reconstruction of phase contrast MRI: Analysis and correction of the effect of gradient field distortions. *Magn. Reson. Med.* **50**, 791–801. https://doi.org/10.1002/mrm.10582 (2003).
26. Ritter, F. *et al.* Medical image analysis. *IEEE Pulse* **2**, 60–70. https://doi.org/10.1109/MPUL.2011.942929 (2011).
27. Tautz, L., Hennemuth, A. & Peitgen, H. O. Motion analysis with quadrature filter based registration of tagged MRI sequences. *Stat. Atlases Comput. Models Heart Lect. Notes Comput. Sci.* **7085**, 78–87. https://doi.org/10.1007/978-3-642-28326-0_8 (2012).
28. Selle, D., Preim, B., Schenk, A. & Peitgen, H.-O. Analysis of vasculature for liver surgical planning. *IEEE Trans. Med. Imaging* **21**, 1344–57. https://doi.org/10.1109/TMI.2002.801166 (2002).
29. Markl, M. *et al.* Estimation of global aortic pulse wave velocity by flow-sensitive 4D MRI. *Magn. Reson. Med.* **63**, 1575–1582. https://doi.org/10.1002/mrm.22353 (2010).
30. Learoyd, B. M. & Taylor, M. G. Alterations with age in the viscoelastic properties of human arterial walls. *Circ. Res.* **18**, 278–292. https://doi.org/10.1161/01.RES.18.3.278 (1966).
31. Gallarello, A. *et al.* Patient-specific aortic phantom with tunable compliance. *J. Eng. Sci. Med. Diagn. Ther.* **2**, 041005. https://doi.org/10.1115/1.4044611 (2019).
32. Birjiniuk, J. *et al.* Pulsatile flow leads to intimal flap motion and flow reversal in an in vitro model of type B aortic dissection. *Cardiovasc. Eng. Technol.* **8**, 378–389. https://doi.org/10.1007/s13239-017-0312-3 (2017).
33. Markl, M. *et al.* Analysis of pulse wave velocity in the thoracic aorta by flow-sensitive four-dimensional MRI: reproducibility and correlation with characteristics in patients with aortic atherosclerosis. *J. Magn. Reson. Imaging* **35**, 1162–1168. https://doi.org/10.1002/jmri.22856 (2012).
34. Wentland, A. L. *et al.* Aortic pulse wave velocity measurements with undersampled 4D flow-sensitive MRI: comparison with 2D and algorithm determination. *J. Magn. Reson. Imaging* **37**, 853–859. https://doi.org/10.1002/jmri.23877 (2013).
35. Fielden, S. W. *et al.* A new method for the determination of aortic pulse wave velocity using cross-correlation on 2D PCMR velocity data. *J. Magn. Reson. Imaging* **27**, 1382–1387. https://doi.org/10.1002/jmri.21387 (2008).
36. Roes, S. D. *et al.* Aortic vessel wall magnetic resonance imaging at 3.0 tesla: a reproducibility study of respiratory navigator gated free-breathing 3D black blood magnetic resonance imaging. *Magn. Reson. Med.* **61**, 35–44. https://doi.org/10.1002/mrm.21798 (2009).
37. Tan, I., Butlin, M., Liu, Y. Y., Ng, K. & Avolio, A. P. Heart rate dependence of aortic pulse wave velocity at different arterial pressures in rats. *Hypertension* **60**, 528–533. https://doi.org/10.1161/HYPERTENSIONAHA.112.194225 (2012).
38. Haesler, E., Lyon, X., Pruvot, E., Kappenberger, L. & Hayoz, D. Confounding effects of heart rate on pulse wave velocity in paced patients with a low degree of atherosclerosis. *J. Hypertens.* **22**, 1317–1322. https://doi.org/10.1097/01.hjh.0000125447.28861.18 (2004).
39. Albaladejo, P. *et al.* Heart rate, arterial stiffness, and wave reflections in paced patients. *Hypertension* **38**, 949–952. https://doi.org/10.1161/hy1001.096210 (2001).
40. Lantelme, P., Mestre, C., Lievre, M., Gressard, A. & Milon, H. Heart rate: an important confounder of pulse wave velocity assessment. *Hypertension* **39**, 1083–1087. https://doi.org/10.1161/01.HYP.0000019132.41066.95 (2002).
41. Liang, Y. L. *et al.* Effects of heart rate on arterial compliance in men. *Clin. Exp. Pharmacol. Physiol.* **26**, 342–346. https://doi.org/10.1046/j.1440-1681.1999.03039.x (1999).
42. Wilkinson, I. B. *et al.* Heart rate dependency of pulse pressure amplification and arterial stiffness. *Am. J. Hypertens.* **15**, 24–30. https://doi.org/10.1016/S0895-7061(01)02252-X (2002).
43. Albaladejo, P. *et al.* Influence of sex on the relation between heart rate and aortic stiffness. *J. Hypertens.* **21**, 555–562. https://doi.org/10.1097/00004872-200303000-00021 (2003).

Acknowledgements
We thank Nicole Schiavone, Tyler Cork, and Tabitha Bandy-Vizcaino for their technical advice and Anja Hennemuth for making available software tools. J.Z. receives personal funds through DAAD doctoral candidate scholarship grant. This project was funded, in part, by NIH R01 HL131823 to D.B.E.

Author contributions
J.Z. conceptualized the study, engineered the flow circuit setup, defined and led imaging experiments, performed image analysis and data interpretation, and wrote the manuscript. M.Lo. defined the imaging protocol and developed image pre-processing software. F.K. performed tensile testing and supported imaging experiments. K.B. and K.G. developed and manufactured the aorta model. S.A.D. supported imaging experiments. M.Le. and A.M. supervised and advised the research work. D.B.E. conceptualized the study and provided overall supervision and advice to the research. All authors reviewed and approved the manuscript.

Competing interests
The authors declare no competing interests.

Additional information
Supplementary Information The online version contains supplementary material available at https://doi.org/10.1038/s41598-021-86174-6.

Correspondence and requests for materials should be addressed to J.Z.

Reprints and permissions information is available at www.nature.com/reprints.

Publisher's note Springer Nature remains neutral with regard to jurisdictional claims in published maps and institutional affiliations.

5

QUANTITATIVE HEMODYNAMICS IN AORTIC DISSECTION: COMPARING IN VITRO MRI WITH FSI SIMULATION IN A COMPLIANT MODEL

Authors: **Judith Zimmermann**, Kathrin Baeumler, Michael Loecher, Tyler E. Cork, Fikunwa O. Kolawole, Kyle Gifford, Alison L. Marsden, Dominik Fleischmann, Daniel B. Ennis

In: Functional Imaging and Modeling of the Heart. Lecture Notes in Computer Science 2021, vol. 12738 [155]

Abstract: The analysis of quantitative hemodynamics and luminal pressure may add valuable information to aid treatment strategies and prognosis for aortic dissections. This work directly compared *in vitro* 4D-flow magnetic resonance imaging (MRI), catheter-based pressure measurements, and computational fluid dynamics that integrated fluid-structure interaction (CFD FSI). Experimental data was acquired with a compliant 3D-printed model of a type-B aortic dissection (TBAD) that was embedded into a flow circuit with tunable boundary conditions. *In vitro* flow and relative pressure information were used to tune the CFD FSI Windkessel boundary conditions. Results showed overall agreement of complex flow patterns, true to false lumen flow splits, and pressure distribution. This work demonstrates feasibility of a tunable experimental setup that integrates a patient-specific compliant model and provides a test bed for exploring critical imaging and modeling parameters that ultimately may improve the prognosis for patients with aortic dissections.

Contributions of J.Z.: study conceptualization, design and engineering of experimental setup, image acquisition, image analysis and data comparison to FSI simulation, writing and editing of manuscript.

Quantitative Hemodynamics in Aortic Dissection: Comparing *in Vitro* MRI with FSI Simulation in a Compliant Model

Judith Zimmermann[1,2(✉)], Kathrin Bäumler[1], Michael Loecher[1,3], Tyler E. Cork[1], Fikunwa O. Kolawole[5], Kyle Gifford[1], Alison L. Marsden[4], Dominik Fleischmann[1], and Daniel B. Ennis[1,3]

[1] Department of Radiology, Stanford University, Stanford, USA
judith.zimmermann@tum.de
[2] Department of Computer Science, Technical University of Munich, Munich, Germany
[3] Division of Radiology, VA Palo Alto Health Care System, Palo Alto, USA
[4] Department of Pediatrics, Stanford University, Stanford, USA
[5] Department of Mechanical Engineering, Stanford University, Stanford, USA

Abstract. The analysis of quantitative hemodynamics and luminal pressure may add valuable information to aid treatment strategies and prognosis for aortic dissections. This work directly compared *in vitro* 4D-flow magnetic resonance imaging (MRI), catheter-based pressure measurements, and computational fluid dynamics that integrated fluid-structure interaction (CFD FSI). Experimental data was acquired with a compliant 3D-printed model of a type-B aortic dissection (TBAD) that was embedded into a flow circuit with tunable boundary conditions. *In vitro* flow and relative pressure information were used to tune the CFD FSI Windkessel boundary conditions. Results showed overall agreement of complex flow patterns, true to false lumen flow splits, and pressure distribution. This work demonstrates feasibility of a tunable experimental setup that integrates a patient-specific compliant model and provides a test bed for exploring critical imaging and modeling parameters that ultimately may improve the prognosis for patients with aortic dissections.

Keywords: Aortic dissection · CFD FSI · 4D-flow MRI

1 Introduction

An aortic dissection is a life-threatening vascular disorder in which a focal tear develops within the inner aortic wall layer. This leads to subsequent formation of a secondary channel ('false lumen', FL) that is separated from the primary channel ('true lumen', TL) by a dissection flap. [13] Patients with type-B aortic dissection (TBAD, i.e. without involvement of the ascending aorta) often receive pharmacologic treatment and frequent monitoring is used in an attempt to predict late adverse events. Prognosis of late adverse events is largely informed by

D. B. Ennis et al. (Eds.): FIMH 2021, LNCS 12738, pp. 575–586, 2021.
https://doi.org/10.1007/978-3-030-78710-3_55

morphologic imaging features, but conflicting results have been reported among several predictors [17].

To improve prognosis several hemodynamic quantities are of potential interest and may confer added sensitivity of individual risk. Recent studies have suggested high FL outflow [15] as strong predictor for late adverse events, and FL ejection fraction [5] as indicator for false lumen growth rate.

To retrieve these hemodynamic markers, computational fluid dynamics (CFD) frameworks provide simulated patient-specific flow fields at high spatio-temporal resolution [11]; and those that integrate fluid-structure interaction (FSI) at deformable walls are expected to amplify the realism of patient-specific modeling even further. If simulations were able to reliably replicate hemodynamics, it would further enable non-invasive prediction of risk related to pathological changes (e.g. tear size).

While CFD FSI approaches show great potential, a direct validation with measured data in highly controlled, but realistic environments is missing. Previous comparisons between simulations and *in vivo* 4D-flow MRI [1,6,14] are challenged by: the assumption of a rigid aortic wall and dissection flap; a lack of information on accurate patient-specific hemodynamic conditions; and/or an unknown patient-specific aortic wall and dissection flap compliance.

Herein, we compare qualitative and quantitative TBAD hemodynamics based on: (1) simulations that use a recently proposed FSI framework [1], and (2) *in vitro* MRI including catheter-based pressure mapping. We utilized a patient-specific, compliant TBAD model embedded into a highly-controlled flow circuit. Uniaxial tensile testing of the compliant material, image-based flow splits and catheter-based pressure recordings informed simulation tuning.

2 Methods

2.1 Patient-Specific Aortic Dissection Model

A 3D computed tomography angiogram (CTA) of a patient (31 y/o, female) with TBAD was selected from our institution's database. A proximal intimal 'entry' tear was present distal to the left subclavian artery and an 'exit' tear was located proximal to the celiac trunk. Each tear measured 2.3 cm^2 in area size. The CTA study was approved by the institutional review board and written consent was obtained prior to imaging.

The lumen of the thoracic aorta was segmented using the active contour algorithm with manual refinements (itk-SNAP v3.4, Fig. 1a). Two tetrahedral meshes were generated (Fig. 1b): the 'fluid domain' representing the full aortic lumen; and the 'wall domain' (as extruded fluid domain) representing the outer aortic wall and dissection flap that separates TL and FL with uniform thickness ($h = 2$ mm). The wall domain mesh was further refined with (i) cylindrical caps that facilitated tubing connections, and (ii) visual landmarks to define image analysis planes. Meshing and refinements were done using SimVascular (release 2020-04) [19] and Meshmixer (v3.5, Autodesk). Further details on model generation are given in [1].

The wall model was 3D-printed using a novel photopolymer technique (PolyJet J735, Stratasys Inc.), as shown in Fig. 1d. The print material underwent uniaxial tensile testing as described in [21] and proved to be comparable to *in vivo* aortic wall compliance (tangent Young's modulus $E_{y,t} = 1.3$ MPa).

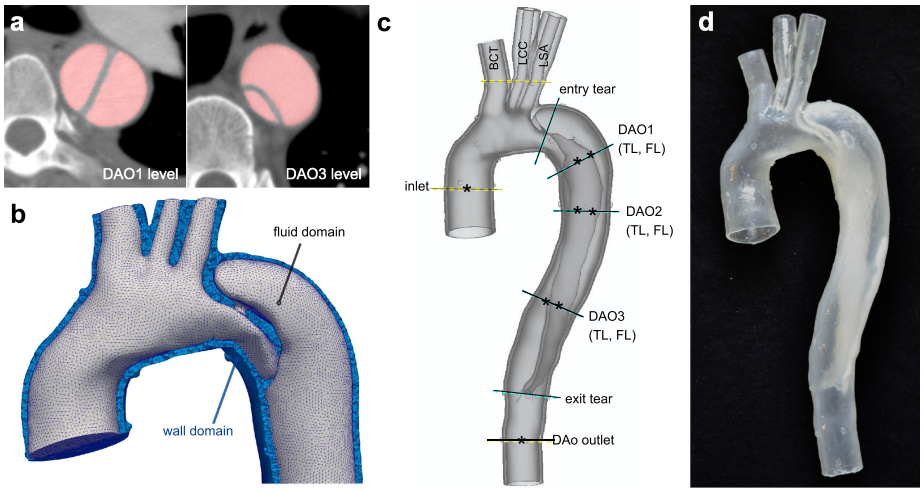

Fig. 1. (a) CTA images with lumen segmentation. (b) Tetrahedral meshes of fluid (gray) and wall domains with dissection flap (blue). (c) Cross-sectional landmarks and pressure mapping points (*). 'Entry' and 'exit' tear cover sections with combined TL and FL flow. Landmarks DAO1, DAO2, and DAO3 consist of a TL and FL cross-section. (d) Photograph of finished 3D-printed model. (Color figure online)

2.2 MRI Experiments

Imaging was performed on a 3 T MRI machine (Skyra, Siemens). An MRI-compatible flow circuit that includes a programmable pump (CardioFlow 5000 MR, Shelley) was engineered to provide controllable flow and pressure conditions similar with target values within the physiological range (Fig. 2a). Details were recently published in [21]. Glycerol-water (ratio = 40%/60%) with contrast (ferumoxytol) was used as a blood-mimicking fluid; and a typical aortic flow waveform (Fig. 2b) was applied (heart rate = 60/min, stroke volume = 74.1 mL/s, total flow = 4.45 L/min).

The circuit was tuned on the scanner table prior to image acquisition, targeting a flow split of 70%/30% (DAo outlet vs. arch branches), and luminal systolic pressure (at model inlet) of 120 mmHg. The pulse pressure was controlled via capacitance elements—designed as sealed air compression chambers—at the DAo outlet ($C1$) and at the merged arch branches ($C2$). A pressure transducer (SPR-350S, Millar) was inserted through ports at the model inlet and DAo outlet, and luminal pressures were recorded at eight points (Fig. 1c). Ultrasonic flow and pressure signals were fed into PowerLab (ADInstruments) for analysis.

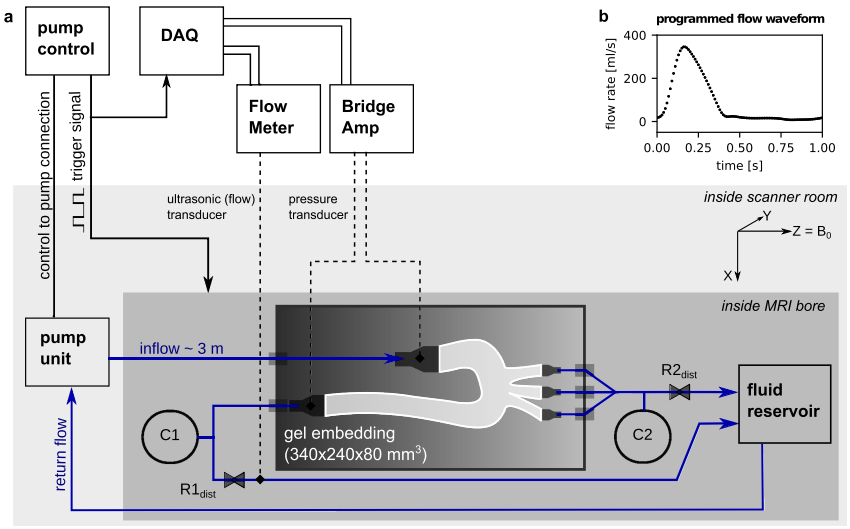

Fig. 2. (a) Schematic of the flow circuit setup. Pressure transducers were inserted through ports at the model inlet and DAo outlet. (b) Flow rate waveform that was programmed into the pump. $C1, C2$: 'capacitance' air-compression chambers, $R1, R2$: 'resistance' flow clamps. (Color figure online)

2D-Cine and 2D-PC MRI. Two-dimensional (2D) acquisitions at landmarks (Fig. 1c) included: (1) 2D cine gradient echo (2D-cine) with pixel size = 0.9 × 0.9 mm^2, slice thickness = 6 mm, T_E/T_R = 3/4.75 ms, flip angle = 7°, avg. = 2, retro. gating (40 frames); and (2) 2D phase-contrast (2D-PC) with pixel size = 1.1 × 1.1 mm^2, slice thickness = 6 mm, T_E/T_R = 3/5.25 ms, flip angle = 25°, avg. = 2, V_{enc} = 90 − 120 cm s^1, retro. gating (40 frames).

4D-Flow MRI. A four-point encoded Cartesian 4D-flow sequence was acquired as follows: FoV = 340 × 236 × 84 mm^3, matrix = 220 × 156 × 56, voxel size = 1.5 × 1.5 × 1.5 mm^3, T_E/T_R = 2.7/5.6 ms, flip angle = 15°, parallel imaging (GRAPPA, R = 2), V_{enc} = 120 cm s^{-1}, lines/seg. = 2, retro. gating (20 frames).

Image Analysis. Lumen contours were automatically tracked through time based on 2D-cine data via image-based deformable registration, which provided values of cross-sectional area and served as the boundary for net flow calculation. 2D-PC images were corrected for phase offsets (via planar 2^{nd} order fitting) and then processed to retrieve the inlet flow and net flow splits across outlets.

4D-flow MRI data was corrected for (i) Maxwell terms, (ii) gradient non-linearity distortion [10], and (iii) phase offsets (via 3^{rd} order fitting). Five landmarks along the dissected region were used for analysis (Fig. 1c). 4D-flow MRI offset correction, flow calculations, and streamline visualization were done using MEVISFlow (v11.2, Fraunhofer Institute) and ParaView (v5.7); quantitative results were exported as numeric files for comparison with simulation results.

2.3 CFD FSI Simulations

Governing Equations. The governing equations for fluid flow and structural mechanics were solved in the fluid and wall domain, respectively. In the fluid domain, the working fluid was considered incompressible and Newtonian ($\varrho_f = 1100$ kg m^{-3}, $\mu_f = 0.00392$ Pa s). Momentum and mass balance were described by the Navier-Stokes Equations in arbitrary Lagrangian Eulerian formulation to account for motion. The structural material was modeled with a Neo-Hookean model for homogeneous, isotropic hyperelastic materials ($E_y = 1.3$ MPa, $\varrho_s = 1450$ kg/m^3). Both domains were coupled at the interface via kinetic and dynamic interface conditions. A detailed mathematical description can be found in [1].

CFD FSI Boundary Conditions. The 2D-PC derived flow waveform was prescribed at the model inlet as a Dirichlet boundary condition, assuming a parabolic velocity profile. Three-element Windkessel boundary conditions were applied at fluid outlets and coupled to the 3D domain with the coupled multidomain method [7]. The catheter-based pressure values at the inlet of the model used as simulation tuning targets were: 119 mmHg, 42 mmHg, and 77 mmHg for the systolic (P_s), diastolic (P_d) and pulse pressure ($\triangle P$), respectively. Additionally, the 2D-PC derived flow splits informed the Windkessel parameter tuning, and were measured as 78.4%, 12.3%, 3.0%, and 5.2% for the DAo outlet, BCT, LCC, and LSA, respectively. The tuning of the Windkessel parameters (a distal and proximal resistance and capacitance at each of the model outlets) was then carried out in an iterative and manual process, by which a total resistance R_T and total capacitance C_T are distributed across all model outlets according to the measured flowsplits and a pre-prescribed ratio of distal to proximal resistance ($k_d = 0.9$). Details of the tuning process can be found in [1].

Wall domain outlets were fixed in space via a homogeneous Dirichlet condition for the displacement and a homogeneous Neumann boundary condition was prescribed at the outer wall of the vessel domain. This is in contrast to patient-specific simulations where a non-homogeneous Robin type boundary condition can be prescribed to account for external tissue support of the vessel. Likewise, the outer wall of the vessel domain was assumed to not be under prestress, contrary to a typical *in vivo* environment.

Numerical Formulation. The numerical simulations were performed with the SVFSI finite element solver, as implemented in SimVascular [19]. SVFSI features linear elements for velocity and pressure and is based on the "Residual Based Variational Multiscale" method. The fluid and wall domain were solved in a monolithic approach and backflow stabilization was applied at the fluid outlets. To avoid mesh degeneration, a nodal mesh smoothing was performed after each time step. Details of the numerical formulation are given in [1]. For details about the numerical discretization we refer to [2,3,8,18].

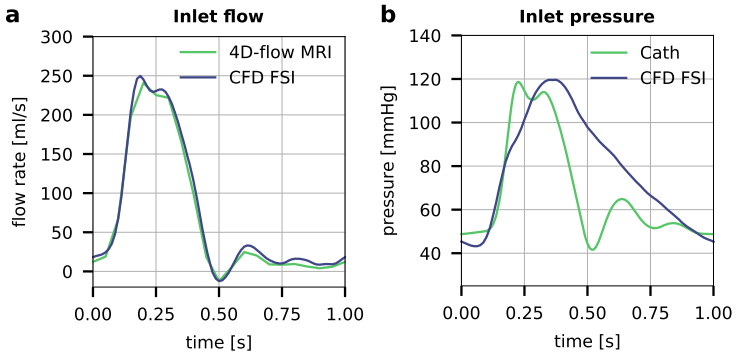

Fig. 3. CFD FSI (blue) tuning conditions, showing (a) flow rate and (b) pressure waveform at TBAD model inlet, in comparison to 4D-flow and catheter measurements (green). While the inlet flow rate waveforms match well, CFD FSI shows a slower diastolic pressure decay without oscillations. (Color figure online)

Discretization and Simulation Setup. Tetrahedral meshes of fluid and wall domain were sampled with a spatial resolution of $\triangle h = 1.3$ mm (1.6×10^6 tetrahedral elements) which was found to be a sufficiently fine resolution [1]. The temporal resolution was set to 4×10^3 timesteps per cardiac cycle ($\triangle t = 0.25$ ms). The simulation achieved cycle-to-cycle periodicity within 5 iterative runs. Compute time was 12 h per cycle on a high performance computing cluster.

CFD FSI Analysis. Time-resolved parameters were extracted from the last simulation cycle: (i) flow rate, (ii) area change, and (iii) pressure. We extracted data from every 50th simulated time step, which totaled 80 incremental results with an effective temporal resolution $\triangle t = 12.5$ ms. Quantitative metrics were analyzed at cross-sectional landmarks (Fig. 1c) using ParaView (v5.7) and exported as numeric files for direct 4D-Flow MRI comparison.

3 Results

Boundary Conditions. Inlet flow (Fig. 3a) for CFD FSI was directly prescribed based on 2D-PC results and agreed well with 4D-flow MRI. CFD-FSI flow splits across model outlets 78.7%, 12.7%, 3.2%, and 5.5% for DAo outlet, BCT, LCC, and LSA, respectively) aligned well with 2D-PC splits (78.4%, 12.1%, 3.0%, and 5.2%). After tuning, CFD FSI pressure (Fig. 3b) matched catheter measurements within the pre-defined 10% error margin (119.6 mmHg, 43.2 mmHg, and 76.4 mmHg for simulated P_s, P_d and $\triangle P$, corresponding to a relative error of $\leq$4%). While catheter-based measurements showed oscillations and a fast pressure drop at end-systole ($t = 0.4$ s), CFD FSI pressure decayed slower and without oscillation. As a results, mean pressure differed by 15.8% (78 mmHg for CFD FSI compared to 68 mmHg for catheter-based measurements).

Flow Patterns and Velocities. Qualitative flow visualizations (Fig. 4) showed well-matched flow patterns between CFD FSI and 4D-flow MRI. Particularly, streamlines depicted helical flow in FL aneurysm during systole and distal FL during diastole, as well as increased velocities through the proximal FL entry tear and along the distal TL. Overall, velocities were higher in CFD FSI, but the intra-model spatial distribution of velocities matched well.

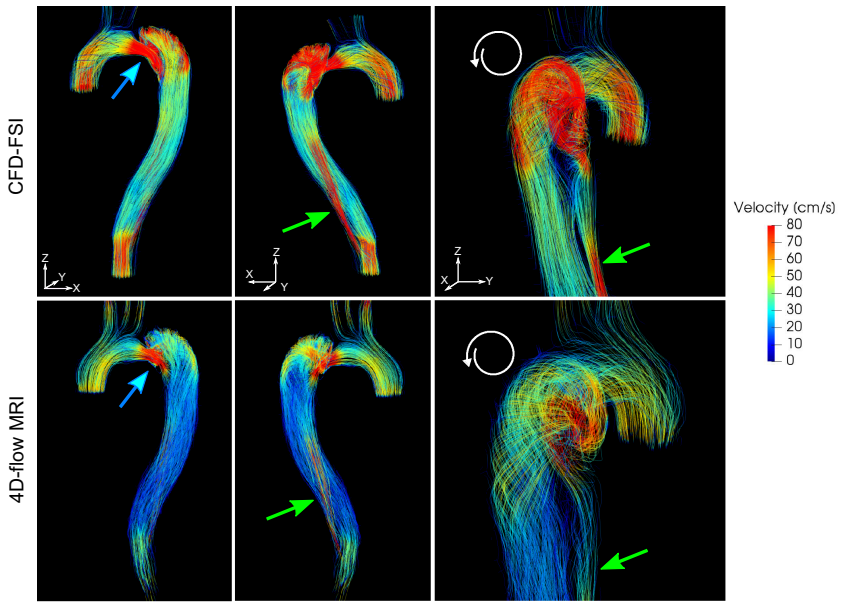

Fig. 4. Streamline visualization at systole ($t = 0.2$ s) for CFD FSI (top) and 4D-flow MRI (bottom) data. CFD FSI shows higher velocities, but intra-modality flow patterns and velocity distribution is consistent. Increased velocities through entry tear (blue arrows) and true lumen (green arrows). A helical flow pattern is visible in the false lumen aneurysm (white arrows). (Color figure online)

Pressure, Area, and Flow. Systolic TL pressure exceeded FL pressure (Fig. 5a) for both simulation and catheter measurements. At peak systole, the TL-FL presure difference was greater for CFD FSI data at landmarks DAO1 and DAO2, but matched well at DAO3. During diastole, the TL-FL difference was close to zero for CFD FSI, but was 1 to 2 mmHg for the catheter measurements. Cross-sectional area (Fig. 6, dashed lines) expanded most in FL cross-sections with up to 11% based on CFD FSI and up to 5% based on 2D-cine MRI.

Net flow volumes (Fig. 6) revealed a FL to TL flow split of 78%/22% for CFD FSI and 73%/27% for 4D-flow MRI measurements. Flow waveform shapes (Fig. 6, solid lines) aligned well, particularly regarding the peak flow timepoint, systolic upslope ($t = 0.1$ s), and oscillatory lobes in diastole. CFD FSI flow rates were higher in systole and lower in diastole when compared to 4D-flow values.

Pressure-area loops showed a steeper slope for *in vitro* data (Fig. 5b). FL peak flow preceded peaks of pressure and area change. This temporal delay was longer for CFD FSI, which was consistent for all DAO landmarks (Fig. 5c).

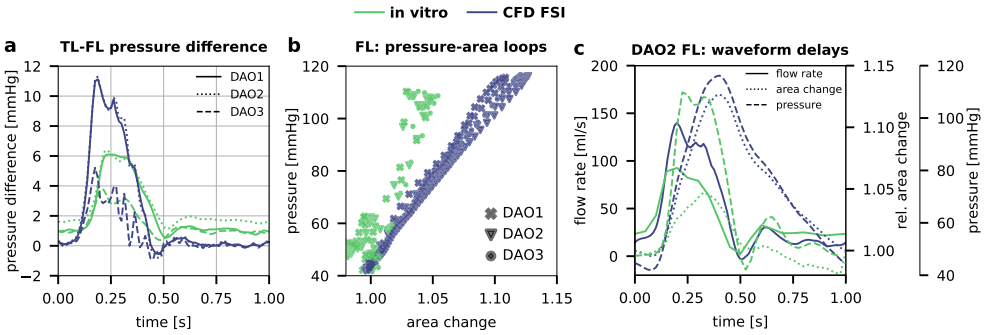

Fig. 5. (a) The TL-FL pressure difference was higher in proximal and lower in distal region. (b) FL pressure-area loops. (c) Flow rate peaks preceding both pressure and area peaks, with greater delay times for CFD FSI. (Color figure online)

4 Discussion

This study leveraged compliant 3D-printing as well as a highly-controlled MRI-compatible flow circuit setup to directly compare CFD FSI and MRI results with regards to flow and pressure dynamics in a patient-specific TBAD model. The aorta's secondary lumen and proximal FL aneurysm presented complex flow patterns with a large velocity range. These characteristics were well captured by both modalities and streamline visualizations were in very good agreement.

Our approach links measured luminal pressure with CFD FSI boundary conditions, which presents a major advantage over previous comparisons with *in vivo* data that usually lack invasive pressure measurements. During simulation tuning, pressure targets (P_s, P_d) were met, but pressure waveform shapes differed—i.e. faster and oscillatory pressure decay in catheter measurements versus slower and steady decline in CFD FSI. We note that a slower and steady pressure decline in diastole is desirable and would resemble *in vivo* pressure shapes of the arterial system [12].

To further investigate this mis-match, additional exploratory pressure data were recorded on the benchtop. Moreover, additional CFD FSI simulations with varying configurations of boundary conditions were computed. We identified three aspects to better match the measured and simulated pressure conditions. First, increasing the ratio between the distal and proximal resistance—described by parameter k_d in the three-element Windkessel model—is the key factor to improve the pressure shape towards a slower diastolic decline with its minimum at end-diastole (Fig. 7a). In practice, we increased k_d by decreasing proximal

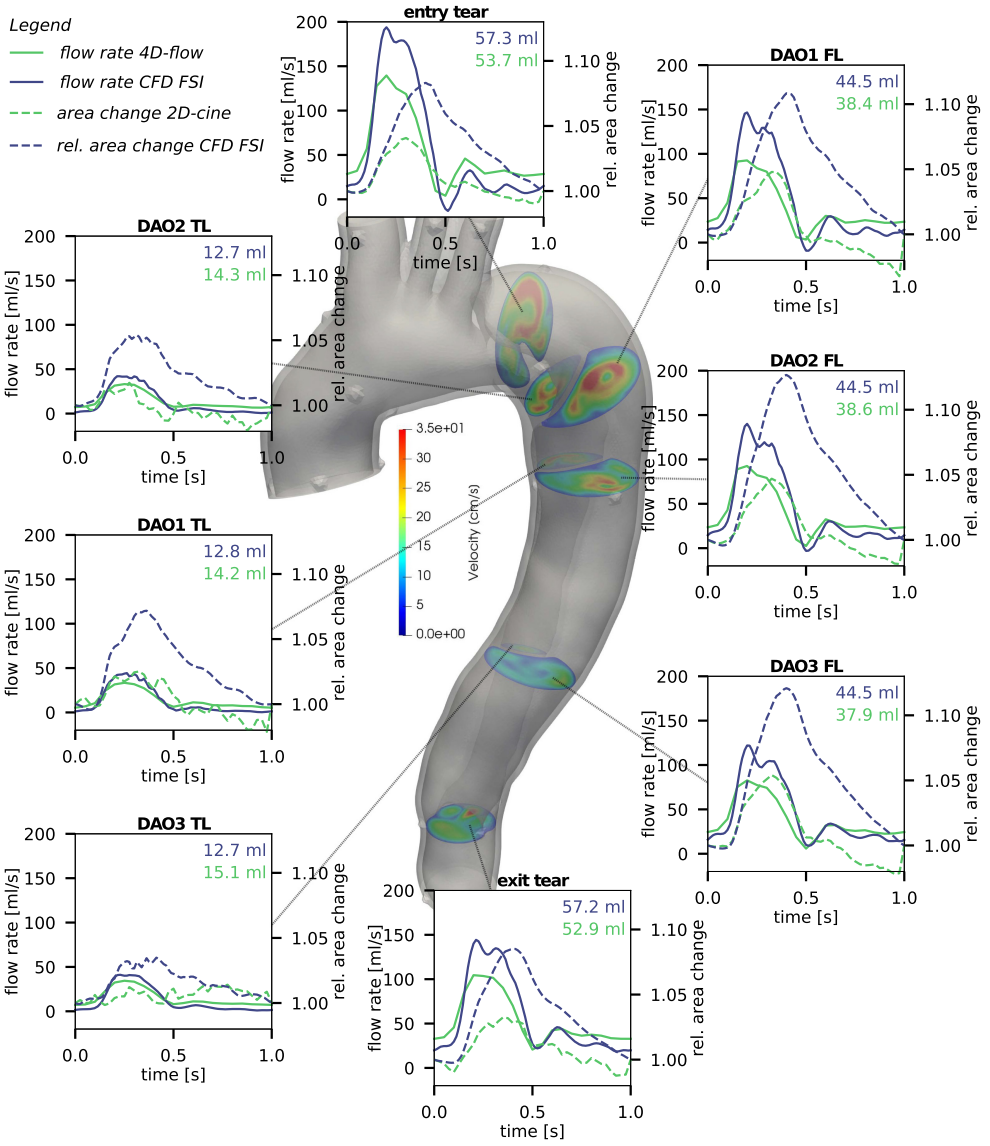

Fig. 6. Flow rate and area change (w.r.t area of first frame) at eight landmarks. Net flow values for CFD FSI (blue) and 4D-flow MRI (green) are given. CFD-FSI showed increased FL flow (78%) compared to 4D-flow (73%); and increased maximum area expansion (11% for CFD FSI vs. 5% for 4D-flow). (Color figure online)

resistance, and thus also decreased total system resistance which led to reduced $\triangle P$. Second, exploratory benchtop experiments also suggested that the characteristic pressure oscillations originate from wave reflections at multiple branching points. Other previous works that deployed flow circuits in model-based studies reported similar pressure waveform shapes [4,9,16,20]. Further engineering efforts should be made to minimize wave reflections at non-smooth boundaries

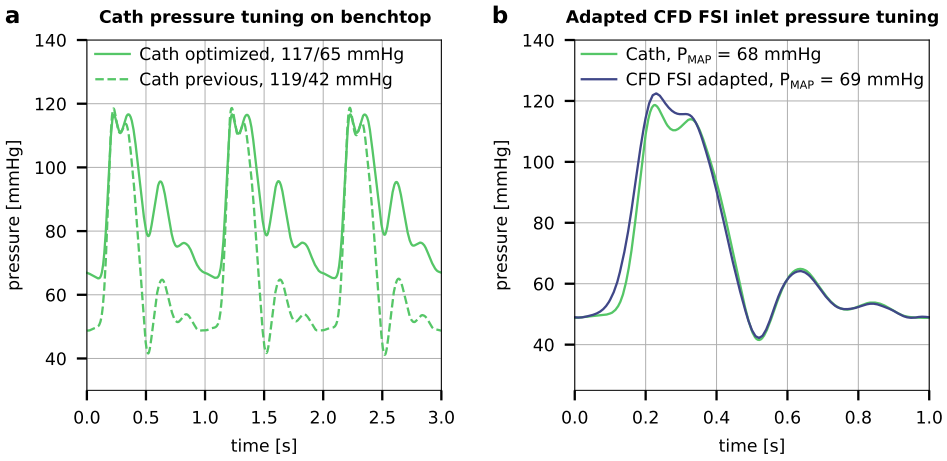

Fig. 7. (a) Exploratory benchtop data showing improvements for the setup's pressure condition. By drastically reducing proximal resistance, pulse pressure is reduced from 78 to 52 mmHg, and—if wave reflections were to be neglected—diastolic pressure declines steadily towards its minimum at end-diastole. (b) CFD FSI (blue) vs catheter-based (green) pressure at the inlet face in an adapted simulation with rigid walls and inhomogeneous pressure boundary condition at the BCT outlet. By tuning the simulation using the full pressure waveform, inlet pressure conditions closely resemble measured values, including wave reflections. (Color figure online)

as much as possible. Third, additional exploratory simulation runs suggested that the measured pressure conditions can be closely approximated by directly prescribing pressure data as inhomogeneous Neumann boundary condition at one of the outlets. To do so, we prescribed the catheter-based pressure data that was measured at the model inlet as pressure boundary condition at the brachiocephalic trunk outlet. Resulting well-matched pressure waveforms are shown in Fig. 7b. We seek to adapt both our experimental and simulation setup in future studies regarding these three aspects.

Overall, our presented results showed similar tendencies of flow and pressure parameters in the dissected region between MRI, catheter measurements, and FSI simulation. TL-FL pressure differences were comparable such that they were almost consistently positive, and that the most distal landmark (DAO3) showed a smaller difference compared to the two proximal points (DAO1, DAO2). Interestingly, CFD FSI TL-FL pressure difference briefly dropped to negative ($t = 0.4$ s) and then to zero ($t > 0.65$ s), while catheter measurements showed preserved positive TL-FL differences at all locations and times. Moreover, with only 5% difference between modalities, results suggest a well-matched TL-FL flow split.

Multiple results indicate that the performed tensile testing underestimated $E_{y,t}$: a steeper slope of the pressure-area loop for *in vitro* data, shorter flow-pressure-area waveform delays, and consistently lower outer wall expansion. To address this mis-match, future CFD FSI experiments should iteratively

increase the value for $E_{y,t}$ until *in vitro* wall deformations are sufficiently replicated.

Moving toward clinical deployment of simulation-based treatment decision support, future work should also investigate uncertainties of pressure and flow conditions and their impact on hemodynamic quantities. In particular, if pressure data are unavailable, it should be investigated how approximations of pressure boundary conditions (e.g. two-point systolic to diastolic cuff pressure) propagate errors into hemodynamic quantities. The presented highly-controlled *in vitro* setup is well suited to investigate these effects.

In conclusion, this work presents valuable information on hemodynamic similarities and differences as retrieved from CFD FSI, *in vitro* MRI, and catheter-based pressure measurements in a patient-specific aortic dissection model.

Acknowledgements. We thank the Stanford Research Computing Center for computational resources (Sherlock HPC cluster), Dr. Anja Hennemuth for making available software tools, and Nicole Schiavone for technical advice. Funding was received from DAAD scholarship program (to J.Z.) and NIH R01 HL131823 (to D.B.E).

References

1. Bäumler, K., et al.: Fluid-structure interaction simulations of patient-specific aortic dissection. Biomech. Model. Mechanobiol. **19**, 1607–1628 (2020)
2. Bazilevs, Y., Calo, V.M., Cottrell, J.A., Hughes, T.J., Reali, A., Scovazzi, G.: Variational multiscale residual-based turbulence modeling for large eddy simulation of incompressible flows. Comput. Meth. Appl. Mech. Eng. **197**(1–4), 173–201 (2007)
3. Bazilevs, Y., Calo, V.M., Hughes, T.J., Zhang, Y.: Isogeometric fluid-structure interaction: theory, algorithms, and computations. Comput. Mech. **43**(1), 3–37 (2008)
4. Birjiniuk, J., et al.: Pulsatile flow leads to intimal flap motion and flow reversal in an in vitro model of type B aortic dissection. Cardiovasc. Eng. Techn. **8**(3), 378–389 (2017)
5. Burris, N.S., et al.: False lumen ejection fraction predicts growth in type B aortic dissection: preliminary results. Eur. J. Cardio-thoracic Surg. **57**(5), 896–903 (2020)
6. Dillon-Murphy, D., Noorani, A., Nordsletten, D., Figueroa, C.A.: Multi-modality image-based computational analysis of haemodynamics in aortic dissection. Biomech. Model. Mechanobiol. **15**(4), 857–876 (2015). https://doi.org/10.1007/s10237-015-0729-2
7. Esmaily-Moghadam, M., Bazilevs, Y., Marsden, A.L.: A new preconditioning technique for implicitly coupled multidomain simulations with applications to hemodynamics. Comput. Mech. **52**(5), 1141–1152 (2013). https://doi.org/10.1007/s00466-013-0868-1
8. Esmaily-Moghadam, M., Bazilevs, Y., Marsden, A.L.: A bi-partitioned iterative algorithm for solving linear systems arising from incompressible flow problems. Comput. Meth. Appl. Mech. Eng. **286**, 40–62 (2015)
9. Gallarello, A., et al.: Patient-specific aortic phantom with tunable compliance. J. Eng. Science Med. Diagn. Therapy **2**(4), 041005 (2019)
10. Markl, M., et al.: Generalized reconstruction of phase contrast MRI: analysis and correction of the effect of gradient field distortions. Magn. Reson. Med. **50**(4), 791–801 (2003)

11. Marsden, A.L.: Simulation based planning of surgical interventions in pediatric cardiology. Phys. Fluids **25**, 101303 (2013)
12. Mills, C.J., et al.: Pressure-flow relationships and vascular impedance in man. Cardiovasc. Res. **4**(4), 405–417 (1970)
13. Nienaber, C.A., et al.: Aortic dissection. Nat. Rev. Dis. Primers. **2**, 16053 (2016)
14. Pirola, S., et al.: 4D flow MRI-based computational analysis of blood flow in patient-specific aortic dissection. IEEE Trans. Biomed. Eng. **66**(12), 3411–3419 (2019)
15. Sailer, A.M., et al.: Computed tomography imaging features in acute uncomplicated stanford type-B aortic dissection predict late adverse events. Circ. Cardiovasc. Imaging **10**(4), e005709 (2017)
16. Schiavone, N.K., Elkins, C.J., McElhinney, D.B., Eaton, J.K., Marsden, A.L.: In vitro assessment of right ventricular outflow tract anatomy and valve orientation effects on bioprosthetic pulmonary valve hemodynamics. Cardiovasc. Eng. Technol. **12**(2), 215–231 (2021). https://doi.org/10.1007/s13239-020-00507-6
17. Spinelli, D., et al.: Current evidence in predictors of aortic growth and events in acute type B aortic dissection. J. Vasc. Surg. **68**(6), 1925–1935 (2018)
18. Tezduyar, T.E., Mittal, S., Ray, S.E., Shih, R.: Incompressible flow computations with stabilized bilinear and linear equal-order-interpolation velocity-pressure elements. Comput. Meth. Appl. Mech. Eng. **95**(2), 221–242 (1992)
19. Updegrove, A., Wilson, N.M., Merkow, J., Lan, H., Marsden, A.L., Shadden, S.C.: SimVascular: an open source pipeline for cardiovascular simulation. Ann. Biomed. Eng. **45**(3), 525–541 (2016). https://doi.org/10.1007/s10439-016-1762-8
20. Urbina, J., et al.: Realistic aortic phantom to study hemodynamics using MRI and cardiac catheterization in normal and aortic coarctation conditions. J. Magn. Reson. Imaging **44**(3), 683–697 (2016)
21. Zimmermann, J., et al.: On the impact of vessel wall stiffness on quantitative flow dynamics in a synthetic model of the thoracic aorta. Sci. Rep. **11**, 6703 (2021)

Part III

DISCUSSION AND OUTLOOK

6 DISCUSSION OF THE PRESENTED WORKS

The core of this research sought to elucidate potentials and limitations of 4D flow MRI, in particular with regards to retrieving parameters that quantitatively characterize cardiovascular flow mechanics. Specifically, this dissertation focused on the quantification of hemodynamics in vascular disorders of the human thoracic aorta.

The conducted studies investigated image-derived metrics with (1) *in vivo* 4D flow MRI data from healthy subjects and patients who presented aortic diseases, and (2) *in vitro* data that were acquired with a custom-build MRI-compatible flow circuit setup and 3D printed aorta models during comprehensive experiments. Additionally, simulated data were integrated for proof-of-principle, comparison, and validation tasks at multiple points.

Though a plethora of previous studies described the use of quantitative 4D flow MRI to assess aortic diseases, the reliability and robustness of image-derived hemodynamic markers are yet to be fully understood. We may categorize these uncertainties into (1) errors originating from perturbations in the given PC MR image data and (2) errors originating from imperfect image post-processing algorithms.

As per (1), imperfections in the measured PC MR image data arise from: the fact that 4D flow MRI always warrants a trade-off between spatio-temporal resolution, SNR, and sequence run time; the always present cardiac and respiratory motion, which we need to compensate for using motion-controlling techniques; and different types of phase offsets as introduced in sec. 2.2.2. In particular, the effect of phase offsets induced by eddy currents shall not be underestimated [24]. Here, methods for mitigating eddy currents and/or reliable correction during post-processing present an active area of research. Novel developments such as DL-based offset correction [143] suggest promising results, but warrant rigorous multi-center and multi-sequence validation.

As per (2), image post-processing comprises multiple tasks that may introduce errors. These computational tasks include: segmenting the vessel of interest, registering image frames for landmark tracking, applying denoising filters, interpolating velocity vector fields, computing spatial derivatives, and others. All of which can potentially propagate errors that lead to uncertainties in the final flow metric.

Therefore, in order to implement 4D flow MRI as a standard method for quantitative analysis of blood flow dynamics, it is crucial to understand to what extent errors propagate and how they consequently affect the quantitative metric. The individual contributions presented

in Chap. 3, 4, 5 addressed this important research question. Their key findings are discussed in the following.

The first study [148] investigated the influences of spatial resolution, phase data noise, and aortic wall motion on wall shear stress estimation. The study was motivated by a lack of knowledge regarding the influences of assuming a static rather than moving aortic wall on WSS estimates. The majority of prior research articles that had introduced WSS as descriptive biomarker had used a time-averaged definition of the lumen boundary. In our work, we implemented a registration-based algorithm to propagate an initial single-frame lumen contour through all cardiac frames. We further extended the numerical computation of the WSS vectors by adapting the computation of the vessel inward normal, as presented in [147]. Our results suggested motion-dependent WSS perturbations to be as considerable as the effects of increased phase noise and low spatial resolution. The results emphasized that a precise definition of the structural boundary is crucial for reliable estimation of wall parameters.

However, limitations of this work should be discussed. First, we only evaluated *in vivo* data of the ascending aorta and only included two groups (BAV patients and healthy volunteers). Extending the study population by other cohorts should be part of future works.

Second, assessing the performance of the registration-based wall contour propagation algorithm was not the focus of this study. We note that PC MRI magnitude image quality is inferior to state-of-the-art cardiac cine MRI sequences (e.g. bSSFP), which challenges contour propagation performance. However, it often is the only available 3D+t data for defining moving vessel boundaries in arbitrarily reformatted planes. Preliminary results in a small number of datasets (N=6) showed acceptable performance, as presented in [145, 146], but further investigation on a diverse set of PC MRI data is warranted. Moreover, we extended the implementation for contour tracking from 2D+t to 3D+t to allow for fully dimensional tracking of vascular structures [150]. As with contour tracking in 2D, 3D surface tracking demonstrated acceptable performance in a small-sized cohort of healthy volunteers (N=11), but more comprehensive validation studies are needed.

Third, the image-based WSS estimation algorithm used here is based on the notation described by Stalder et al. [125], but alternative methods have been proposed [30, 108, 109, 123] by others. Benchmarking all of these methods on a comprehensive dataset with available ground truth would be an important next step to determine the role of 4D flow-based WSS as hemodynamic marker.

In the context of WSS uncertainty quantification, Castagna et al. [27] recently suggested a system based on laser doppler velocimetry as reliable basis for WSS validation; and Ko et al. [70] proposed a criterion termed 'Reynolds resolution' as a metric for WSS uncertainty.

While the first contribution to this dissertation exclusively considered *in vivo* 4D flow MRI acquisitions, the following works leveraged *in vitro* experiments. In contrast to *in vivo* MRI acquisitions, in particular those that are being added to routine clinical exams, *in vitro* approaches allow for prolonged imaging, thereby providing excellent image quality. Furthermore, *in vitro* experiments enable studying flow dynamics under controllable hemodynamic states (e.g. pressure).

We designed and engineered a closed-loop flow circuit that meets the following requirements: (i) generic layout that integrates models of the thoracic aorta, which can be swapped out during experiments, (ii) pulsatile and programmable flow conditions, (iii) flow volumes and luminal pressure at physiological range, and (iv) MRI-compatible such that it reliably and safely performs inside the scanner bore.

Regarding the aortic wall model, the aim was to develop subject-specific models that mimic wall properties of the human aorta. This is in contrast to the majority of previous works, which simplify their setup with rigid vessel models [25, 80, 137]. Depending on the specific research question, a rigid model may be a totally legitimate solution. However, with our study design, we sought to investigate influences of wall properties on flow mechanics, as well as generating image data for simulations that incorporate fluid-structure interaction. A compliant model was therefore inevitable.

The second study [154] demonstrated the feasibility of engineering a flow circuit that fulfills all requirements as stated above, and showed promising results regarding the use of novel photopolymer-based 3D printing technologies to manufacture compliant and subject-specific models of the thoracic aorta. Moreover, this work showed the impact of aortic wall compliance on 4D flow-derived pulse wave velocity, peak flow rate, and peak velocity, and analyzed the confounding effects of temporal sampling rates. Using compliant rather than rigid vascular models is essential to reproduce realistic quantitative hemodynamics that recapitulate *in vivo* conditions.

This study did not assess the linkage between HR and/or pressure variations and PWV, which appears to be a controversial topic as suggested by a number of pre-clinical [129] and clinical studies [1, 2, 57, 73, 75, 139]. In this regard, we showed preliminary results of two HR modes (60 and 100 min^{-1}) and three aorta models at ISMRM 2020 [151]. A comprehensive study is to follow, but we suggest that the developed setup is of high value to investigate this research question.

The third study [155] used the emerging advanced capabilities of 3D printing and integrated a complex type B aortic dissection (TBAD) model into the flow circuit. An aortic dissection is a life-threatening vascular disorder and to this date treatment strategies are largely informed by morphological features such as false lumen diameter and growth rate. The analysis of the complex interplay between flow

and pressure in TBAD is expected to add valuable knowledge that helps to better risk-stratify an individual's condition. In our work, the objective was to compare quantitative flow metrics as obtained via 4D flow MRI with simulated CFD FSI data. An advanced framework for CFD FSI had recently been described by Bäumler et al. [8]. However, previous comparisons with measured flow data were challenged by low *in vivo* image quality and by incomplete data for tuning boundary conditions. With the developed flow circuit, we were able to provide 4D flow MRI data of highest quality owing to prolonged imaging. Moreover, we directly measure pressure and flow to inform the tuning of boundary conditions in the simulations. Lastly, tensile testing of the compliant printing material directly provided the model's stress-strain data curve and elasticity modulus.

The results of this work suggested good agreement between MRI and CFD FSI data with respect to complex flow patterns, velocity distribution, TL-FL flow splits, and relative TL-FL pressure differences. However, the mismatch of aortic wall and dissection flap motion will require further assessment in future studies. Also, the published data demonstrated the challenges of matching pressure boundary conditions. In particular, the catheter-based pressure measurements showed an oscillatory behavior, which we were only able to replicate after directly prescribing the measured pressure waveform to one of the model outlets (see chap. 5, Fig. 7b). The influences of matched/non-matched boundary flow and pressure boundary condition should be investigated in future work.

With the gained expertise in *in vitro* flow imaging studies, we shall emphasize the unique role of such experimental setups. In particular, we identify the following key advantages: (1) controlled physiological conditions with a programmable pump and tunable downstream periphery such that flow and pressure conditions can be set as desired (and kept constant throughout an imaging experiment); (2) prolonged imaging time that is not restricted by patient compliance or clinical schedules, contrary to *in vivo* studies; (3) diverse possibilities with novel 3D printing techniques to manufacture patient-specific models with varying mechanical properties (e.g. aortic wall elasticity) and varying local morphologies (e.g. pre/post vascular repair); (4) a test bed for MRI reproducibility studies; and (5) generation of high-quality flow data with directly measured boundary conditions for CFD validation studies.

In conclusion, this dissertation contributed to the field of quantitative hemodynamics and 4D flow MRI by performing robustness and sensitivity analyses and by pushing novel applications, as demonstrated in our comprehensive *in vitro* studies with an advanced experimental setup.

7

ONGOING AND FUTURE WORK

In addition to addressing limitations of the presented studies in follow-up work, other exciting ongoing and future directions are outlined below.

AORTIC DISSECTION MORPHOLOGY. Regarding the assessment of flow dynamics in TBAD, ongoing work considers multiple modified versions of the TBAD model presented in Chap. 5 to investigate the influence of tear morphology (i.e. size) on flow dynamics in the true and false lumen. Fig. 7.1 shows preliminary results of flow streamlines — retrieved from *in vitro* 4D flow MRI — at peak systole for three TBAD models: (a) native morphology, (b) smaller-sized primary intimal tear (PIT), and (c) smaller-sized re-entry tear in distal DAo. As per qualitative assessment, we can appreciate the different flow patterns and velocity distribution. In particular, decreased PIT size resulted in a strong flow jet that impinges on the false lumen vessel wall. Several local helical flow patterns can be observed surrounding the PIT. As per quantitative assessment, pressure catheter data showed considerable absolute pressure changes and changes in TL vs. FL pressure differentials between models. The ongoing study runs detailed evaluation of the influences of tear size on multiple flow parameters. Moreover, the results are being compared against CFD FSI simulations.

ADVANCED 3D-PRINTED MODELS. The field of 3D printing has emerged considerably over the past decade. Cutting-edge technologies open up an entire new field of research methods and experimental research in cardiovascular flow mechanics can benefit hugely from these developments. While this dissertation only considers two aortic geometries (healthy and dissected) there are plenty of other complex pathologies, e.g. aortic coarctation, valvular defects such as BAV, or aortic dilation (aneurysm). Further, a big portion of 3D printing research is concerned with the development of new polymers as print material. Multi-material printed models (e.g. with local variations in stiffness) or materials with MRI properties (i.e. signal) would certainly level up the use of 3D printed phantoms in MRI studies.

REPRODUCIBILITY Reproducibility in MRI is a key component to its integrity, in particular when it comes to quantitative MRI methods. Talks and discussions among the MRI community at the ISMRM 2021 member-initiated symposium 'Reproducible MRI all across the world'

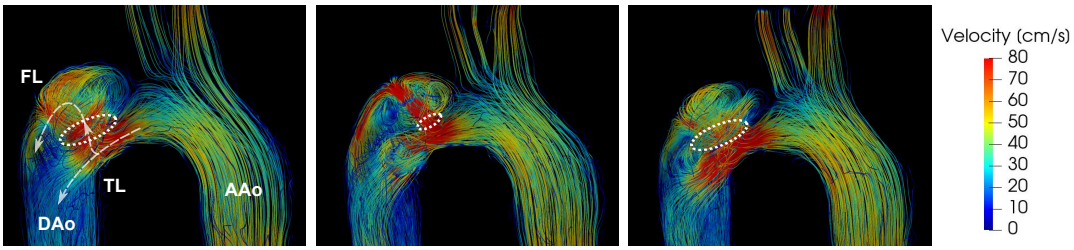

(a) native model (b) smaller PIT, native re-entry tear (c) native PIT, smaller re-entry tear

Figure 7.1: Varying morphology of aortic dissection tear size. Visualizations show streamlines through the aortic arch and primary intimal tear (PIT, dashed ellipsoid) in the model with (a) native morphology, (b) smaller PIT, and (c) smaller re-entry tear (in DAo, not shown). Tear size influence flow patterns, jet profiles, and TL/FL flow volume ratio. (unpublished data)

once more emphasized the continued need for infrastructure that enables rigorous reproducibility studies.

A recently published 'travelling volunteer' study by Demir et al. [32] investigated 4D flow-based aortic hemodynamic parameters in healthy volunteers (N=9) at three sites regarding inter-vendor comparability and reproducibility, scan-rescan reproducibility, and intra- and inter-observer agreement. A concluding statement of this study was that 'hemodynamic parameters [...] are not equivalent'. *In vivo* reproducibility studies such as this one are challenging due to possibly varying hemodynamic states for each volunteer at multiple MRI sites.

In this regard, *in vitro* studies with highly-controlled (and reproducible) physiological flow circuits that integrate realistic models will play an important role. As an example, Williams et al. [140] demonstrated the use of a 'travelling phantom' to assess reproducibility and repeatability of CSF flow dynamics in a realistic 3D printed patient model of the spinal cord.

DATA FOR ML METHODS Another application of *in vitro* phantom studies is the generation of large datasets to assist the development of machine learning methods. For example, DL-based super-resolution of 4D flow MRI datasets acquired at low spatio-temporal resolution would enable us to perform quick scans without sacrificing image resolution. Here, ongoing work (unpublished) considers a convolutional neural network that learns the inter-scale relationship of the velocity maps. Related work combining DL and CFD ('4DFlowNet') was presented by Ferdian et al. [46] and demonstrated noise-free images with upsampling factor 2. To validate such methods, studies which apply prospectively under-sampled (i.e. low resolution) and fully sampled (i.e. high resolution) data are preferred over approaches that retrospectively downs-sample data for validation purposes. A controlled experimental setup that is used to generate multiple datasets with varying sampling schemes opens up new possibilities for validation.

Part IV

APPENDIX

A

TOWARDS WALL SHEAR STRESS COMPUTATION IN THE MOVING AORTA: APPLICATION OF DIFFERENT TRACKING ALGORITHMS

Authors: **Judith Zimmermann**, Lennart Tautz, Naira Mkrtchyan, Heiko Stern, Christian Meierhofer, Anja Hennemuth.

In: Proc. ISMRM Workshop on Quantitative Flow 2016, San Francisco, CA, USA. [145]

BACKGROUND 4D flow MRI allows the image-based estimation of advanced quantitative measures such as wall shear stress (WSS) distribution in vascular structures surrounding the heart. Computation of three-dimensional WSS requires a surface mesh representation of the vessel boundary of interest (e.g. arterial wall). To enable the assessment of change in WSS (e. g.for the calculation of the oscillating shear index, OSI) in the moving aorta during the cardiac cycle, surface points have to be tracked in all cardiac phases. Accurate segmentation is crucial for the reliability of WSS [110]. Manual tracking of the aorta is extremely time-consuming and observer-dependent [13]. Our objective was to study the performance of different automatic propagation algorithms applied to the aorta. In the future, the implemented methodology for tracking should facilitate the generation of time-resolved vessel surface meshes to ultimately allow for a patient study to assess time-dependent WSS in the entire aorta.

METHODS After obtaining written consent, six subjects underwent a cardiac MRI exam (Avanto, Siemens, 1.5 T) to obtain 4D flow MRI data covering the aorta from bulb through the descending part. Acquisition parameters were: $T_E = 2.6\,\text{ms}$; $T_R = 5\,\text{ms}$; FOV $= 400 \times 300 \times 60\,\text{mm}^3$; voxel resolution = $2.3 \times 2.3 \times 2.3\,\text{mm}^3$; $V_{enc} = 150\,\text{cm/s}$. The acquisition was navigator-gated and ECG-triggered (prospectively). To reformat the time-resolved 3D magnitude data into 2D image planes on which the contour tracking is applied, a processing pipeline as shown in figure 1 was performed for each dataset. Three image registration approaches were adapted to compute vector deformation fields between neighboring time frames: Morphon [69, 131], Normalized Gradient Fields (NGF), and Mutual Information (MI). All approaches use local similarity measures for registration optimization: the Morphon is guided by local phase difference between the images, NGF is guided by similarity between image gradients, and MI is guided by the entropy which is calculated based on the joint histogram of the two images [49, 97]. All data analysis was implemented using

the MevisLab framework. Manual contours were obtained from two independent clinical experts. For performance evaluation, the Dice similarity index and the Hausdorff distance were computed.

RESULTS Comparison of manual contours from two independent observers resulted in mean $\pm$ SD for Dice (HD, in mm) of $0.88 \pm 0.04 (5.61 \pm 1.01)$, $0.89 \pm 0.04 (5.22 \pm 1.28)$, and $0.89 \pm 0.03 (4.87 \pm 1.04)$ for the three reformatted image planes at aAo, arch, and dAo respectively. Comparatively, Morphon contour tracking performed best with Dice/HD (in mm) values of $0.89 \pm 0.04 (5.01 \pm 1.05)$, $0.92 \pm 0.03 (4.74 \pm 0.85)$, and $0.92 \pm 0.02 (4.62 \pm 0.75)$ for the same three locations. For all MPRs, NGF and MI presented lower Dice/higher HD with higher standard deviations (Fig. A.3).

DISCUSSION AND CONCLUSION Out of the three evaluated algorithms, Morphon-based tracking is most suitable to replace manual tracking without loss in accuracy. NGF and MI fall behind where poor image quality (e.g. missing edges in diastole frames) is present. Future processing steps are necessary to integrate contour tracking into the pipeline for generating "moving" surface meshes. Ultimately, the implemented framework will facilitate the computation of time-resolved arterial WSS and OSI.

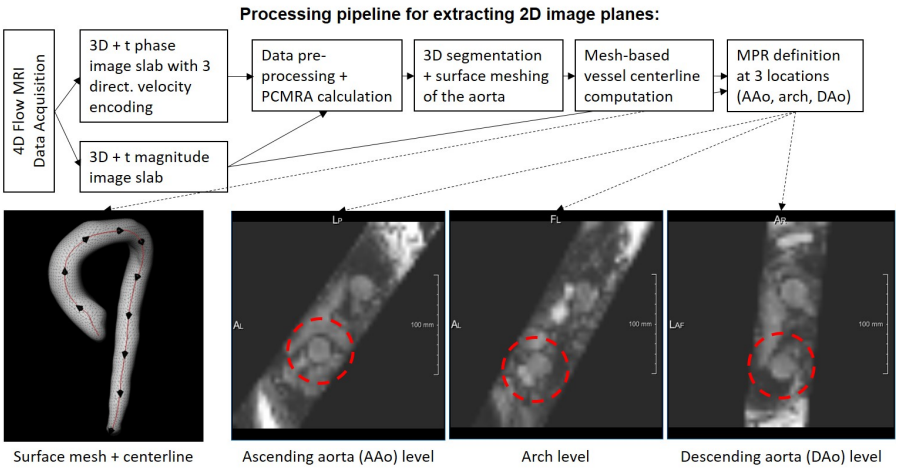

Figure A.1: Processing pipeline for definition of multi-planar-reformatted (MPR) images.

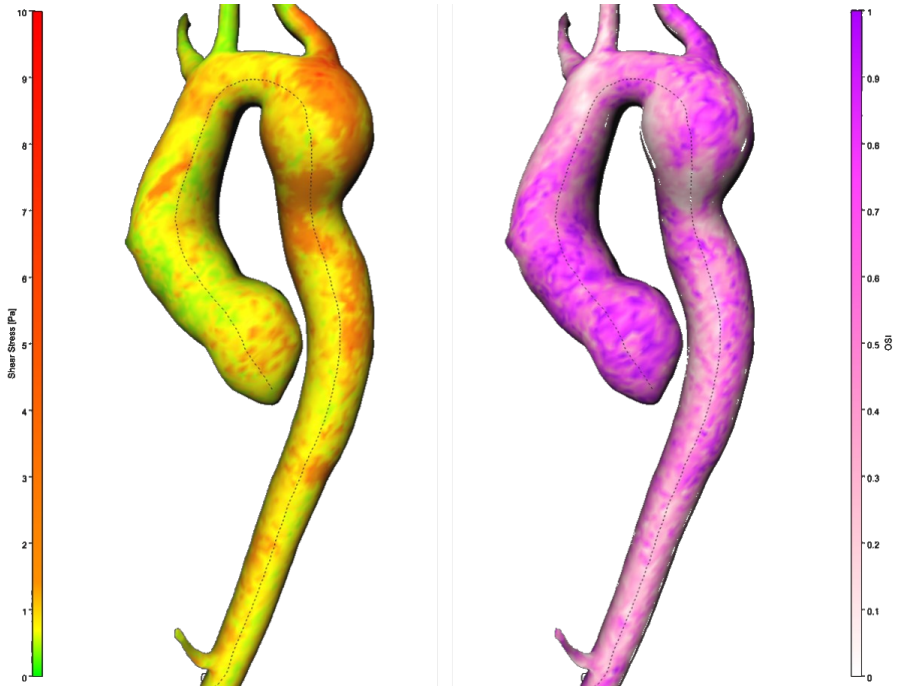

Figure A.2: 3D WSS visualization at single timepoint. A time-independent and static surface mesh was used.

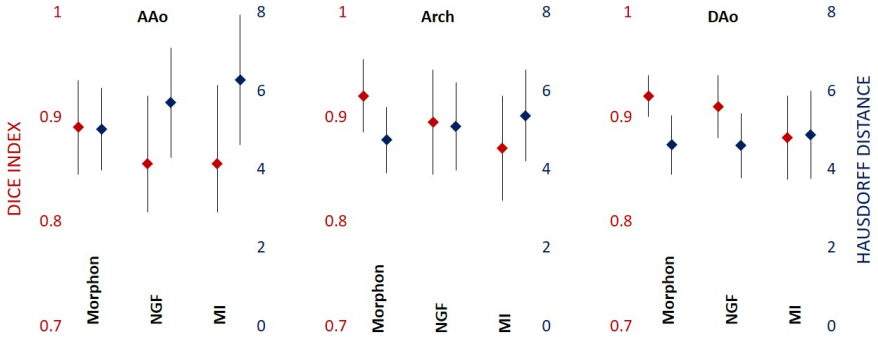

Figure A.3: Mean/SD Dice (red) and HD (blue, in mm) values for different algorithms.

B

ADVANCING QUANTITATIVE 4D FLOW MRI: ASSESSMENT OF MANUAL VERSUS AUTOMATIC BOUNDARY DEFINITION IN THE AORTA.

Authors: **Judith Zimmermann**, Lennart Tautz, Naira Mkrtchyan, Heiko Stern, Christian Meierhofer, Anja Hennemuth.

In: Proc. SCMR Scientific Sessions 2017, Washington D.C., USA. [144]

BACKGROUND 4D flow MRI enables the assessment of various quantitative hemodynamic parameters (e.g. velocity profiles) in the heart and surrounding vessel [43]. However, calculation of these parameters relies on a pre-computed lumen boundary, which should be defined individually at all cardiac phases. In contrast, if vessel movement throughout the cardiac cycle is not taken into account, velocities originating from outside the vessel of interest will contribute. Our objective was to study the performance of automatic contour propagation in the aorta based on an image registration approach using quadrature filters (*Morphon* registration) [69, 131].

METHODS Six subjects underwent a 4D flow MRI exam (Avanto, Siemens, 1.5 T) to acquire a parasagittal slab of the aorta. Acquisition parameters were: $T_E = 2.6\,\text{ms}$; $T_R = 5\,\text{ms}$; FOV = $400 \times 300 \times 60\,\text{mm}^3$; voxel resolution = $2.3 \times 2.3 \times 2.3\,\text{mm}^3$; $V_{enc} = 150\,\text{cm}\,\text{s}^{-1}$. Prospective ECG-triggering and navigator gating was employed. All data processing was performed using application tailored software implemented with the MevisLab framework [114]. 3D+t magnitude image data was reformatted to obtain image planes (MPR) orthogonal to the aortic centerline at three locations: ascending aorta (aAo), arch, and descending aorta (dAo). Manual vessel contours were obtained from two independent experts for all datasets, for all defined MPRs and for all given cardiac phases. Accordingly, automatic contour propagation of a single manually defined contour at systole and diastole throughout the cardiac cycle was performed based on the suggested image registration approach [69, 131]. Dice indices and Hausdorff distance (HD, in mm) were computed to evaluate inter-expert variability as well as algorithm performance given the corresponding manual contours as ground truth.

RESULTS Inter-observer variability resulted in acceptable scores for Dice (median = 0.88) and HD (median = 5.23 mm), with max/min outliers of 0.99/0.72 and 12.6/1.27 for Dice index and HD (in mm), respectively (Fig. B.1 A). Similarly, performance of the automatic

propagation was consistently decent when compared to the manual contours: 0.92/0.98/0.72 and 4.86 mm/13.8 mm/1.46 mm (median/-max/min) for Dice index and HD, respectively (Fig. B.1 B). Different initializations (i.e. manual starting contours) did not impact propagation results, showing acceptable agreement in overall Dice (median = 0.91) and HD (median = 4.97 mm) with small deviations (Fig. B.1 C).

CONCLUSION Automatic propagation is feasible and shows consistent results when compared to manual contours. Inter-observer median similarity scores are acceptable, however, outliers are present and would negatively influence subsequent quantitative flow data analysis. Here, propagation offers results with increased reproducibility. In addition, automation will speed up the workflow where a time-variant volumetric surface mesh is required for quantitative 4D flow analysis.

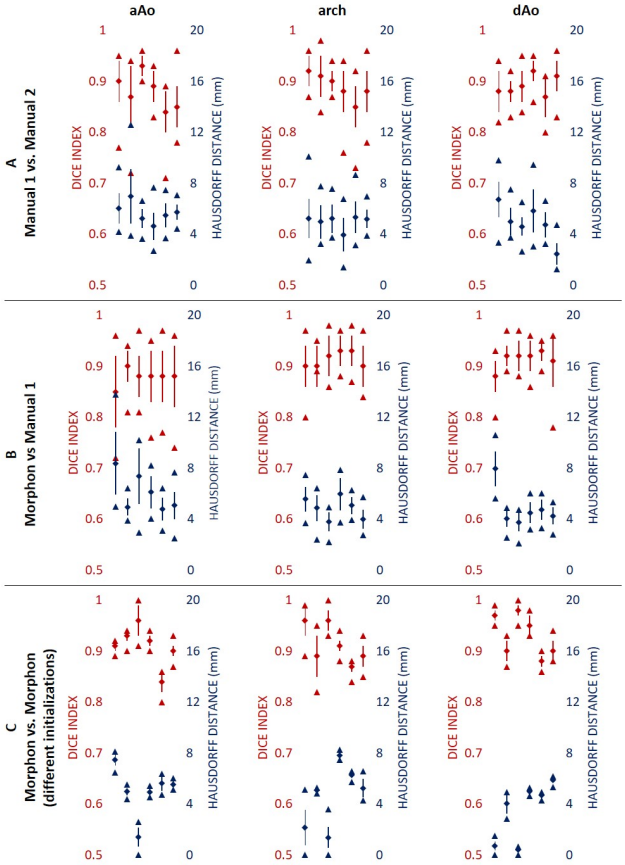

Figure B.1: Dice indices (red) and Hausdorff distance (blue) for inter-observer variability (A), Morphon performance when compared to manual contours (B), and Morphon reproducibility when different manual contours are used for initialization (C). Different MPR locations (aAo: left, arch: middle, dAo: left) are plotted separately, with better overall scores for dAo. Each subplot shows results from six datasets with mean (dot), standard deviation (bar), and min/max (triangles) values.

C

SOFTWARE FLOW PHANTOMS FOR ASSESSING IMAGE-BASED COMPUTATION OF HEMODYNAMIC PARAMETERS

Authors: **Judith Zimmermann**, Hanieh Mirzaee, Anja Hennemuth.

In: Eurographics Workshop Visual Comput. Biol. Med. 2017, Bremen, Germany. [144]

BACKGROUND 4D flow magnetic resonance imaging (MRI) outputs three-dimensional, time-resolved velocity vector fields, which depict blood flow dynamics in the vascular system. This information can be exploited by applying post-processing techniques to compute image-based hemodynamic parameters [54]. However, the accuracy of all image post-processing depends on the image characteristics such as noise level, temporal and spatial resolution, velocity encoding number (V_{enc}), and image artifacts. Therefore, understanding how these characteristics impact the computed hemodynamic parameter is crucial. The aim of this work was to implement a software tool for generating various software blood flow phantoms mimicking 4D flow MRI data. The tool's output may then be used for evaluating the computation of hemodynamic parameters.

METHODS Flow through the aorta was simulated using the Lattice-Boltzmann method [96] and 3D+t phase images (PH) were derived. A 3D phantom image of the thorax served as the initial magnitude image (MAG). We then used the artificial PH and MAG data as the input to the software toolbox. It comprises the following steps to manipulate the input images: spatial resampling with linear interpolation (PH, MAG); adjusting signal intensity and standard deviation (MAG); temporal resampling via cubic B-spline image function and subsequent sampling at discrete time points (PH); adding V_{enc}-depending phase wraps (PH); adding V_{enc}-depending velocity noise (PH); adding phase offsets (PH). The tool was implemented using the MevisLab framework.

RESULTS Fig. C.1 shows a sample phase image result of a cross section of the aorta. Here, we applied different V_{enc} values and otherwise identical parameters. Noise in the velocity images clearly increases with increasing V_{enc}.

CONCLUSION In this work we present a software tool to generate artificial 4D flow MRI phase and magnitude images. The tool allows

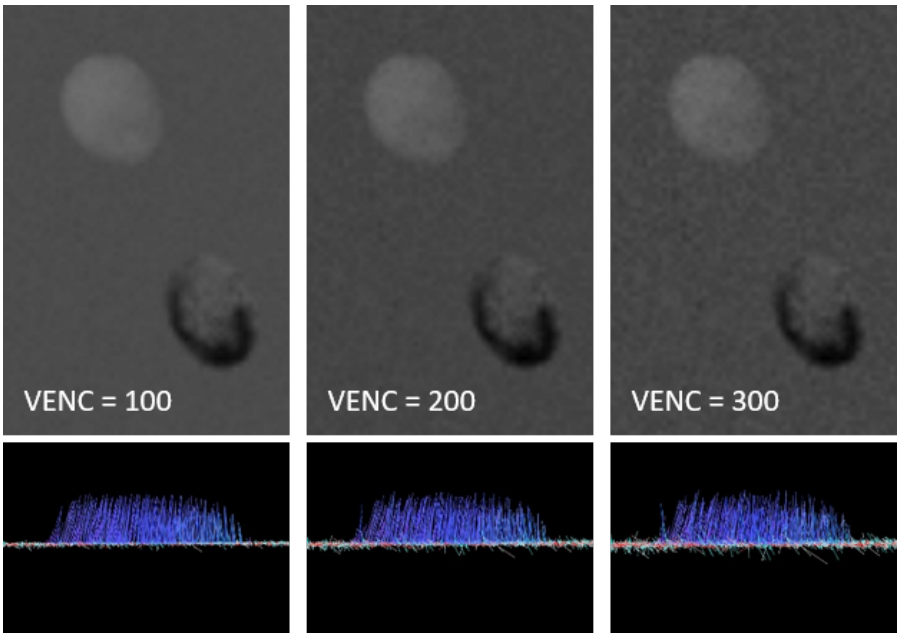

Figure C.1: Velocity images with different V_{enc} and otherwise identical parameters. Top: A cross section at aortic arch level with ascending (top circle) and descending (lower circle). Bottom: Corresponding side view of 3D velocity vector field. Left/middle/right images were generated with V_{enc} = 100, 200 and 300 cm/s.

to create phantom data of various image characteristics. It is therefore suitable when assessing the impact of noise, resolution, and artifact errors on the image-based computation of hemodynamic parameters.

D

EXPLORING VESSEL INWARD NORMAL COMPUTATION FOR 4D FLOW BASED WALL SHEAR STRESS ESTIMATION IN COMPLEX VESSEL GEOMETRIES

Authors: **Judith Zimmermann**, Daniel Demedts, Michael Markl, Christian Meierhofer, Heiko Stern, Anja Hennemuth.

In: Proc. ISMRM 26th Annual Meeting 2018, Paris, France. [147]

INTRODUCTION 4D flow MRI allows the image-based estimation of quantitative wall shear stress (WSS) in vascular structures. WSS ($\vec{\tau}$) at any vessel wall point is defined as

$$\vec{\tau} = 2\eta\dot{\epsilon} \cdot \vec{n}, \tag{D.1}$$

with $\vec{n}$: vessel surface inward normal, η: dynamic viscosity, and $\dot{\epsilon}$: velocity deformation tensor. Furthermore, the oscillatory shear index (OSI) is defined as

$$OSI = \frac{1}{2}\left(1 - \frac{|\int_0^T \vec{\tau} \cdot dt|}{\int_0^T |\vec{\tau}| \cdot dt}\right). \tag{D.2}$$

Previous works studied the impact of MRI acquisition parameters on WSS estimation [108], though the burden of inaccurate inward normal definition is unknown. Most commonly, WSS and OSI are estimated by analyzing 2D analysis planes [6, 63, 90] and the inward normal at each wall point is only comprised of the vector component lying on the respective plane. However, in case of complex vessel geometries (e.g. stenosis, dilatation) the inward normal may deviate from the analysis plane.

The aim of this work was to (1) introduce a method to accurately compute surface inward normals in cone-shaped vessel regions given the typical 4D flow MRI image data, and to (2) study the influence of deviating inward normal vectors on WSS and OSI estimates.

METHODS *Synthetic data.* Steady flow was simulated through a pipe with narrowing on a high resolution grid (Fig. D.1) using Comsol Multiphysics (resolution = $0.7 \times 0.7 \times 0.7\,\mathrm{mm}^3$; min/max vessel diameter = 10.3/33.5mm; mean velocity at inlet = $3.89\,\mathrm{cm\,s}^{-1}$).

In-vivo data. Six 4D flow MRI data sets of patients with stenotic or dilated vessel geometry were included. Scans were performed on a 1.5 T Avanto (N=3) or 3 T Trio (N=3) system (both Siemens) with: $T_E = 2.6\,\mathrm{ms}$; $T_R = 5.1\,\mathrm{ms}$; FOV = $400 \times 300 \times 60\,\mathrm{mm}^3$; voxel

dimension = 1.7–2.5 x 1.7–2.5 x 2.0–2.5 mm^3; V_{enc} = 150–300cm s^{-1}; parallel imaging with R = 5; prospective ECG triggering covering the full cycle; navigator gating.

Data pre-processing included phase offset correction (via polynomial function fitting), background noise masking, and automatic phase unwrapping if needed. WSS computation. Vessels were segmented from the generated PC-MRA image using watershed-based algorithm. For each case, one analysis plane was placed in the dilated/stenotic vessel region and vessel contours were tracked through all time frames (Fig. D.3).

Inward normals. The binary vessel mask was used to derive a Gauss gradient field ($\boldsymbol{G}$) to advance the computation of the vessel inward normal at each sampled contour point $\boldsymbol{x}$

$$\vec{n}_{\boldsymbol{x}} = \vec{a}_{\boldsymbol{x}} + \vec{g}_{\boldsymbol{x},p} \tag{D.3}$$

where $\vec{g}_{\boldsymbol{x},p} = (\boldsymbol{G}_{\boldsymbol{x}} \cdot \vec{p})\,\vec{p}$ is the projection of $\boldsymbol{G}_{\boldsymbol{x}}$ (local Gauss gradient) onto the unit plane normal, and $\vec{a}_{\boldsymbol{x}}$ is the conventional inward normal lying on the analysis plane.

WSS. WSS was then estimated at each contour point using a B-spline image function based approach [125] with $\mu = 0.0032$ Pa s. Regarding synthetic data, we analyzed single timepoint WSS (WSS_{single}); regarding *in vivo* data, we analyzed WSS at peak velocity (WSS_{peak}) and OSI. Estimates were binned into twelve angular segments to compute mean $\pm$ SD per segment. All image analysis was implemented using the MevisLab framework [114].

Evaluation. WSS_{single}, WSS_{peak}, and OSI were assessed segment-wise regarding absolute and relative differences of estimates based on conventional vs. adapted inward normal. Angle deviations between conventional ($\vec{a}_{\boldsymbol{x}}$) and adapted ($\vec{n}_{\boldsymbol{x}}$) inward normals were computed.

RESULTS Both synthetic data (Fig. D.1) and *in vivo* data (D.3) results show noticeably deviated inward normals when the Gauss gradient field is incorporated with angle deviations ranging from 0.00-0.70 rad for in-vivo data and 0.41-0.43 rad for the pipe phantom. With adapted inward normals, synthetic data results show an increase in WSS_{single} by (45.9 ± 49.6) % (Fig. D.2). Regarding in-vivo data results, we observe differences in WSS_{peak} of (8.5 ± 7.5) %, (24.4 ± 15.5) %, (18.1 ± 12.1) %, (21.6 ± 18.2) %, (25.8 ± 23.9) %, and (10.9 ± 9.7) % (Fig. D.4); and in OSI of (15.8 ± 13.3) %, (10.5 ± 10.8) %, (23.1 ± 23.2) %, (7.2 ± 8.0) %, (4.6 ± 6.0) %, and (3.0 ± 3.2) % for cases 1-6, respectively (Fig. D.5). All numbers indicated above are given as mean±SD over all twelve segments.

DISCUSSION Synthetic data results show a clear underestimation when inward normal vectors are not adapted to the local vessel geometry. Here, an outlier is present due to a very subtle flow profile and

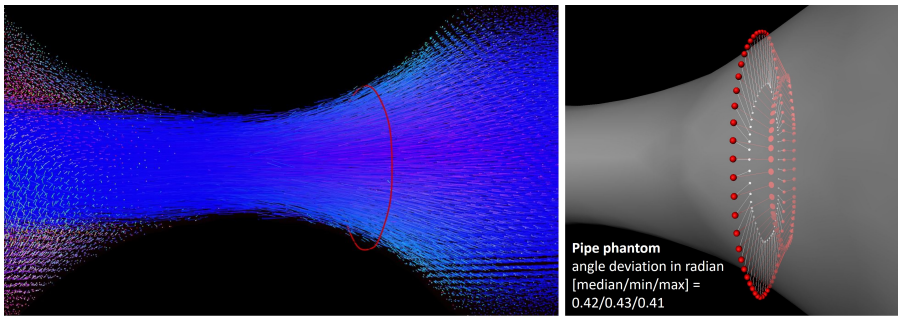

Figure D.1: Synthetic data representing steady flow through a pipe with narrow. Left: vector visualization (color coding = direction) of velocity field with simulated flow from right to left and delineated vessel wall contour at the region of interest (red). Right: Contour point samples of the vessel wall contour (red dots) and inward normal vectors defined by the conventional method (white arrows) and by integrating the gauss gradient field of the vessel mask to adapt to the vessel course (red arrows).

thus comparably small WSS values, which challenges the assessment in terms of relative differences. Synthetic data should be optimized to better represent flow velocities as given in the in-vivo data. *In vivo* data results clearly show that adapted inward normal vectors result in strong deviations of WSS and OSI, which should not be neglected when using these parameters in a clinical study. Particularly, differences are very pronounced for high angular deviations. This study did not assess differences in WSS/OSI contour-point-wise (only segment-wise) and thus did not correlate each contour point WSS/OSI value with the angular deviation of the conventional and adapted inward normal at this point.

CONCLUSION The proposed method may be used to more precisely define vessel inward normal vectors for increased WSS and OSI estimation. Particularly, this is crucial where the vessel wall depicts a cone-shaped course.

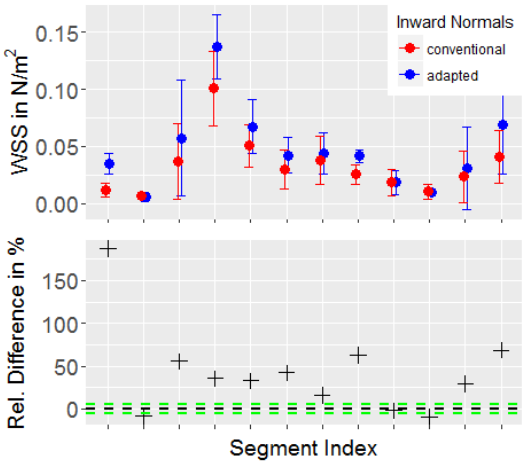

Figure D.2: Synthetic data WSS_{single} estimates. Top: Absolute differences of WSS_{single} estimates comparing the conventional (red) with the adapted (blue) inward normal vector computation. Bottom: Relative differences of WSS_{single} estimates with the conventional method considered a reference. Green bars depict a $\pm 5\,\%$ margin. Here, results show that adapted inward normals effect an increase in WSS. Note that absolute WSS_{single} values are very low compared to *in vivo* results, which is due to low overall flow velocities in the pipe phantom. This may also cause outliers as seen for the first segment.

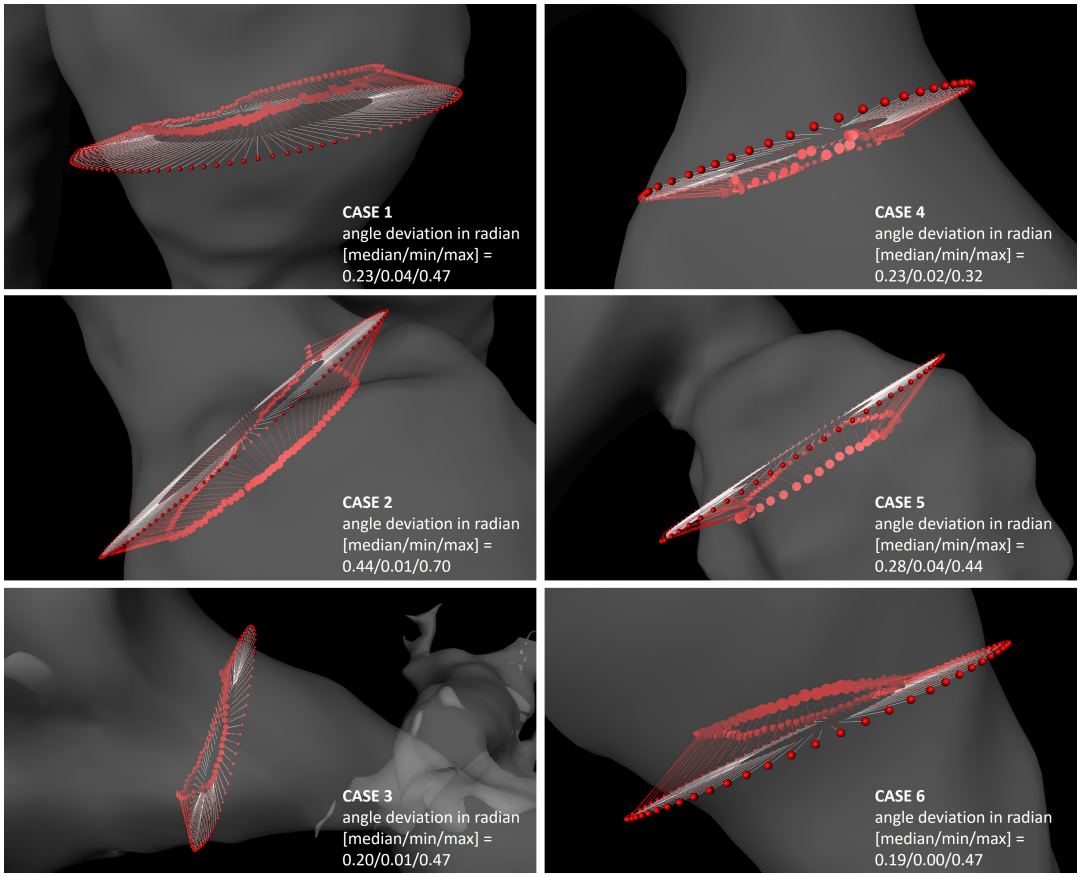

Figure D.3: Close-up view of in-vivo data vessel surface rendering (grey) with vessel wall inward normal vectors at contour points (red dots). For each case, white arrows and red arrows represent the normal vectors defined by the conventional method and by our approach, respectively. Angle deviations between white and red vectors (computed at each contour point) are given in median/min/max radian for each case.

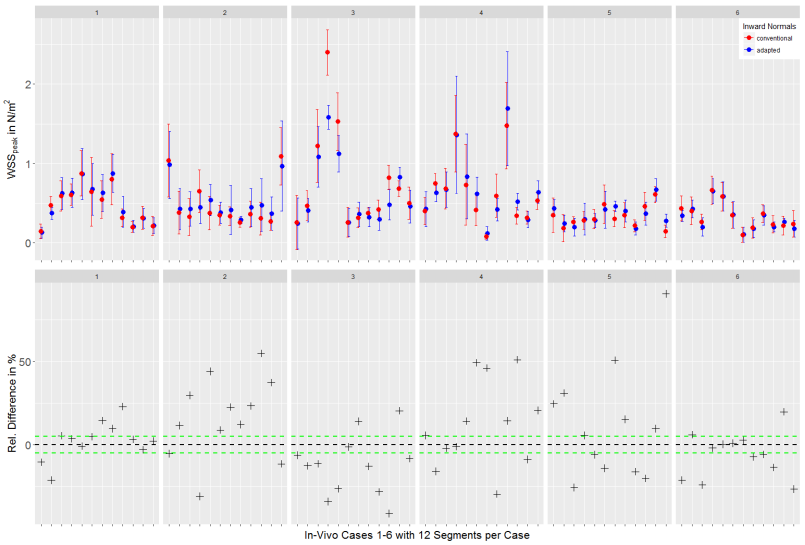

Figure D.4: In-vivo data WSS_{peak} estimates for six cases. Top: Absolute differences of WSS_{peak} estimates comparing the conventional (red) with the adapted (blue) inward normal vector computation. Bottom: Relative differences of WSS_{peak} estimates with the conventional method considered a reference. Green dashed lines depict a $\pm 5\,\%$ margin. Here, results show that adapted inward normals effect an increase/decrease in WSS_{peak} - depending on the specific case but also on the evaluated segment within one particular case. This is mainly due to the inhomogeneous flow profile observed in the in-vivo (patient) data.

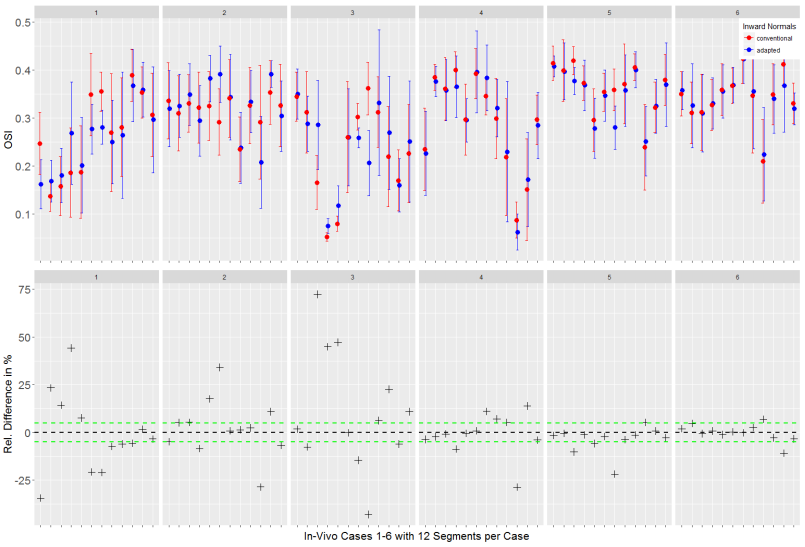

Figure D.5: In-vivo data OSI estimates for six cases. Top: Absolute differences of OSI estimates comparing the conventional (red) with the adapted (blue) inward normal vector computation. Bottom: Relative differences of OSI estimates with the conventional method considered a reference. Green dashed lines depict a $\pm 5\,\%$ margin.

E

FULLY DIMENSIONAL VESSEL SEGMENTATION IN NON-CONTRAST-ENHANCED 3D PC-MRI DATA.

Authors: **Judith Zimmermann**, Lennart Tautz, Christian Meierhofer, Heiko Stern, Bjoern Menze, Anja Hennemuth.

In: Proc. ISMRM 27th Annual Meeting 2019, Montreal, Canada. [150]

INTRODUCTION Fully dimensional (spatial + temporal) segmentation is a crucial step for accurate 3D PC-MRI based hemodynamic quantification in all moving vessels of interest. Throughout the cardiac cycle the aortic wall moves in the range of 5–10 mm which encompasses several voxels. [148] However, most flow characterization studies employ a static definition of vessel boundaries [3, 7] and approaches exploring suitable algorithms for 3D PC-MRI based 4D vessel segmentation are lacking. The objective of this work is to show feasibility of a deformable-registration-based algorithm for 4D segmentation of the aorta in non-contrast enhanced 3D PC-MRI data.

METHODS *Data.* After obtaining written consent, 11 healthy volunteers were examined using a 1.5 T MRI scanner (Avanto, Siemens) without the administration of signal-to-noise (SNR)-enhancing contrast agent. Two datasets were generated:

1. whole heart 3D PC-MRI (MAG): $T_E = 2.54\,\text{ms}$; $T_R = 5\,\text{ms}$; flip angle = 7°; FOV = $270 \times 360\,\text{mm}^3$; slices/slab = 50–64; spatial resolution = $2.25 \times 2.25 \times 2.3\,\text{mm}^3$; temporal resolution = 40 ms; V_{enc} = $150\,\text{cm}\,\text{s}^{-1}$; PEAK-GRAPPA factor = 5; prospective ECG triggering (18–22 frames).

2. whole heart 3D (3DWH) balanced steady-state GRE (TrueFISP): $T_E = 1.35\,\text{ms}$; $T_R = 269\,\text{ms}$; flip angle = 90°; FOV = $500 \times 500\,\text{mm}^3$; slices/slab = 96; spatial resolution = $2 \times 2 \times 1.3\,\text{mm}^3$; prospective ECG triggering to capture single cardiac frame in diastole.

4D segmentation. We use a registration-based segmentation approach to generate a time-resolved 3D surface mesh of the aorta. Algorithm steps are (Fig. E.1): (1) Initial shape definition by watershed-based segmentation of the aorta in static 3D whole heart (3DWH) data with subsequent surface mesh generation (marching cubes with $1\,\text{mm}^3 \times 1\,\text{mm}^3 \times 1\,\text{mm}^3$ voxelization) and Laplacian smoothing (passes = 20, factor = 0.2). (2) Iterative computation of N deformation fields between 3DWH and MAG(t) (with $t = [1, N-1]$), using local 2D quadrature

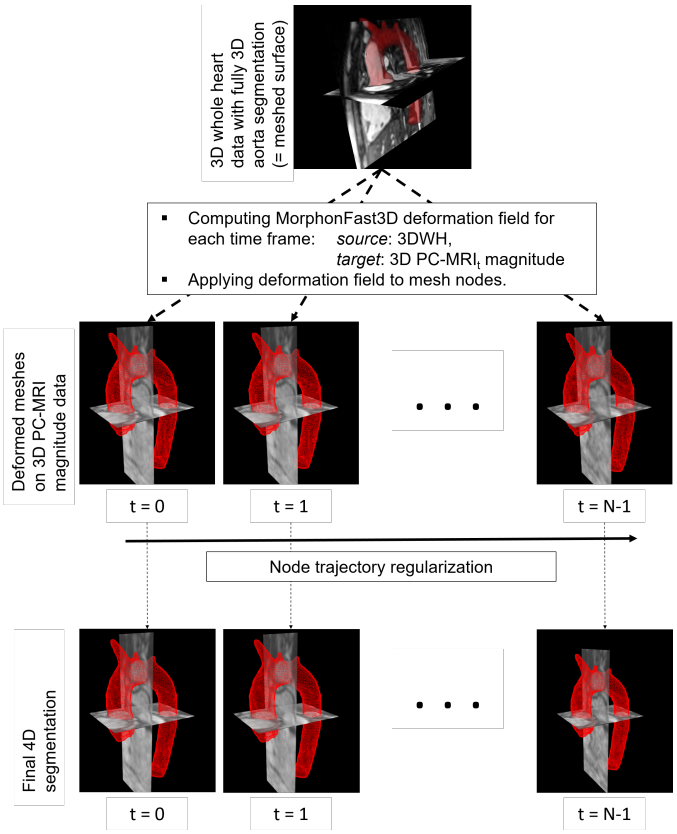

Figure E.1: Workflow for 4D vessel segmentation using high-resolution 3D whole heart data to define an initial shape via watershed based 3D segmentation and marching-cubes meshing (top row) and 3D PC-MRI magnitude data for computation of N 3D deformation fields (middle row). In the last step, we regularize each node's trajectory through spatial smoothing of the node position through time to generate our final 4D segmentation (bottom row).

filters in scale space [69, 130]. The algorithm runs on $S = 2$ down sampled scale-spaces, with $I = 5$ iterations per scale, and employs a Gaussian filter ($\sigma = 4$) for spatial regularization. For fast computation of the 3D deformation field, we reformat both target and source 3D image into 2D stacks along x, y, and y dimension, for which we compute 2D deformation fields separately and then assemble our final 3D deformation field in the last step. (3) Applying deformation field to initial shape's nodes to generate N target meshes. (4) Temporal node trajectory regularization by smoothing each node's position through time (kernel $= [0.25, 0.5, 0.25]$, passes $= 2$).

Evaluation Expert annotations of the ascending through descending aorta (2D manual contours at 8 sample locations at each time frame) were obtained and defined as ground truth (Fig. E.2). Dice index and Hausdorff distance (HD) similarity metrics were used for comparison.

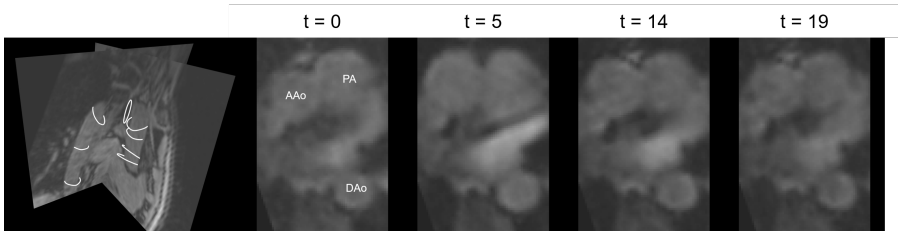

Figure E.2: (Left) Typical distribution of manual contours in 3D PC-MRI magnitude data. Eight evaluation points from ascending aorta through descending aorta were defined for evaluating algorithm performance. (Right) Sample 2D reformatted slice at five time points to show image quality given with low contrast between AAo and PA. AAo = ascending aorta; DAo = descending aorta. PA = pulmonary artery.

RESULTS Qualitative results for three exemplary cases are shown in Fig. E.3. Overall quantitative similarity (mean $\pm$ SD) is 0.86 ± 0.04 (with min/median/max = 0.74/0.87/0.93) for Dice and 3.63 ± 0.75 mm (with min/median/max = 2.27/3.56/6.24 mm) for HD (Fig. E.4b). Without applying temporal node regularization, we achieve scores of 0.87 ± 0.04 (with min/median/max = 0.75/0.87/0.93) for Dice and (3.69 ± 0.77) mm (with min/median/max = 2.34/3.60/6.31 mm) for HD (Fig. E.4a). Time-resolved evaluation does not show any preferred phase (both in systole and diastole) which performs consistently better over other phases (Fig. E.4c). Although quantitative results do not show any impact of temporal smoothing on our output, we note that qualitative visualization improved enormously, eliminating flickering of the mesh.

DISCUSSION Based on the quantitative comparison results, we found our proposed 4D segmentation workflow suitable for fully dimensional vessel wall definition in non-contrast-enhanced 3D PC-MRI data. Bustamente et al. [22] proposed an atlas-based method for time-resolved angiographic segmentation of the heart cavities and vascular structures. In contrast, our method is based on patient-specific vessel shape, which may be obtained from any 3D whole heart sequence output. We note that PC-MRI magnitude data exhibits extremely low contrast between blood pool and surrounding tissue, particularly when imaged without the administration of SNR-enhancing contrast agent, which is preferred in the clinical routine. Manual vessel wall contouring is therefore challenging and may not always present the true wall position and in turn ground truth for evaluating an algorithm's performance. The presented workflow faces two limitations, which we seek to tackle in the future: (1) registration parameters (number of iterations, size of scale-space) need to be tuned based on a-priori information (range of movement); (2) no automated segmentation of

initial 3D shape in 3DWH data, restricting the pipeline from being fully automated.

CONCLUSION This work evaluates an algorithm which proves to be suitable for accurate fully dimensional segmentation of the aorta in noisy 3D PC-MRI image data.

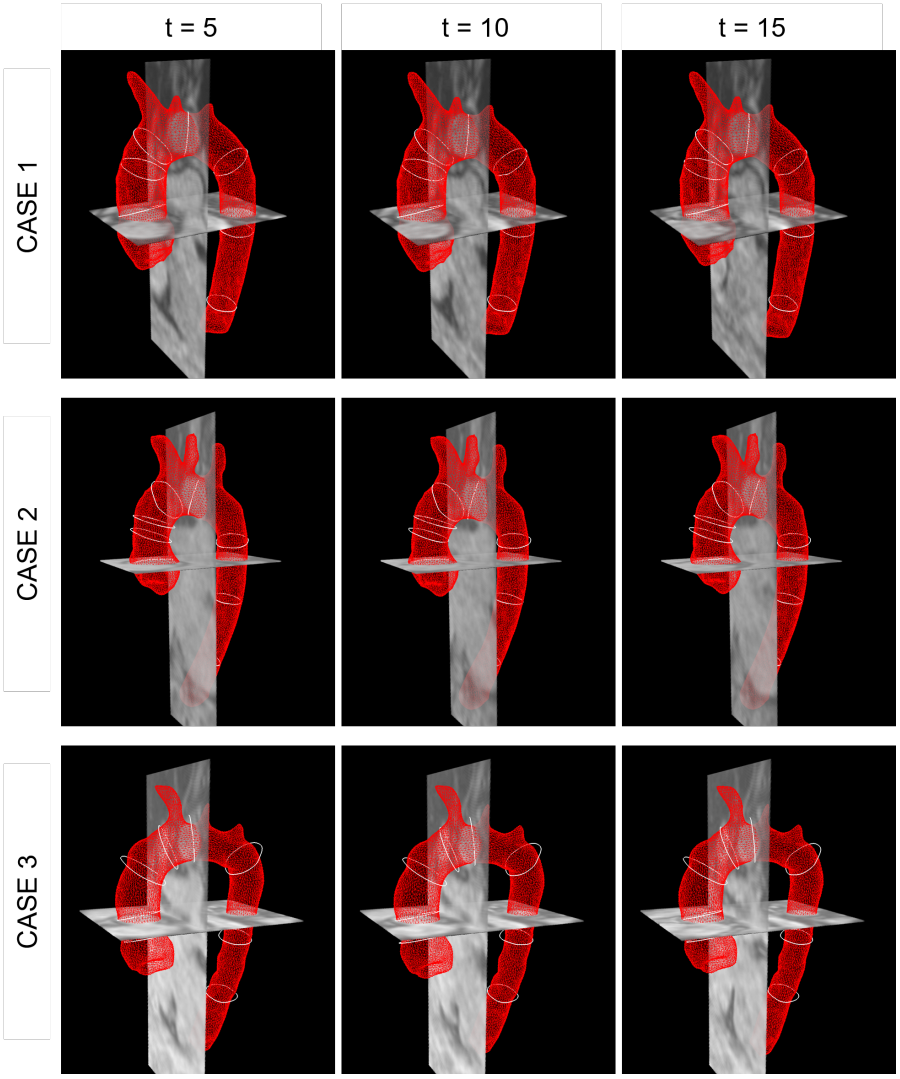

Figure E.3: Final segmentation results for three in-vivo cases at three time points (systole, early diastole, late diastole) with manual contours at 8 sample points along the aorta (white contours). Case 1 (top row) delivered best quantitative segmentation results, whereas case 3 (bottom row) delivered lowest quantitative segmentation results when compared to manual annotations.

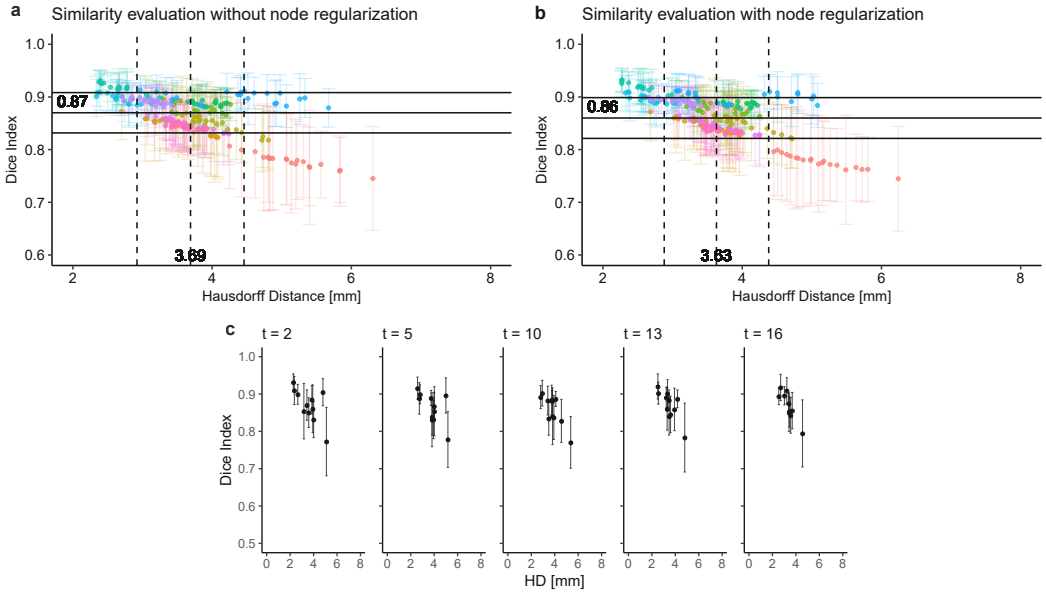

Figure E.4: Statistical evaluation of 4D segmentation output when compared to manual contours. (a, b): Dice and Hausdorff distance (HD) for each dataset (color-coded) at each available time frame prior (a) and post (b) node regularization. Solid and dashed lines depict overall mean $\pm$ SD of Dice index and HD, respectively. (c): Time-resolved analysis of similarity at five distinct time points. All points (error bars) depict mean (SD) over eight evaluation points.

F

COMPUTATIONAL METRICS FOR REPRODUCIBLE CHARACTERIZATION OF COHERENT FLOW PATTERNS IN 3D PC-MRI DATA.

Authors: **Judith Zimmermann**, Johann Drexl, Sarah Nordmeyer, Anja Hennemuth.

In: Proc. ISMRM 27th Annual Meeting 2019, Montreal, Canada. [149]

INTRODUCTION Vortices and helices are crucial features of hemodynamic flow [4, 52, 119]. Such structures may define new clinically relevant biomarkers when assessing cardiovascular pathologies mediated by abnormal flow patterns (e.g. aneurysm formation). Thus, retrieving such structures in time-resolved and velocity-encoded 3D PC-MRI image data is of tremendous interest. However, prior studies only focused on a voxel-wise identification, and are lacking meaningful quantitative metrics which characterize the full vortical flow pattern [81, 124, 136]. The objective of this work is to propose metrics for fully automated detection and quantitative characterization of vortical flow patterns in the aorta.

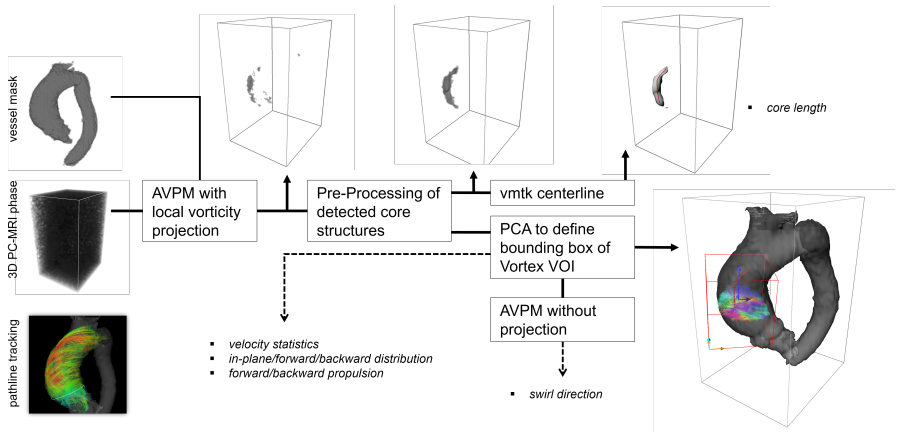

Figure F.1: Workflow for quantitative vortical pattern characterization. Visualization at the bottom right shows the final output with detected Vortex VOI (red box), curved centerline (red line), and vortex core PCA axes (dark blue). AVPM = adaptive vector pattern matching; vmtk = vascular modeling toolkit; PCA = principle component analysis.

METHODS *Vortex volume of interest (VOI) exploration.* The proposed pipeline builds upon the adaptive vector pattern matching (AVPM) algorithm proposed by Drexl et al. [36]. AVPM combines template

vector pattern matching, initially proposed by Heiberg et al. [58], with robust orientation estimation by projecting the local velocity field $\vec{v}$ onto the local vortical structure orientation n, estimated by the integral curl of $\vec{v}$. We run AVPM on each time frame t of the 3D PC-MRI phase data to generate $T[0, T-1]$ binary 3D vortex core masks. Each 3D vortex core mask is then processed using morphological operations (to retrieve a well-defined core), connected-component-analysis (to distinguish between multiple cores per volume), thresholding (to filter out small cores with number of voxels in core < 20). Subsequently, each detected core is used to define a Vortex VOI bounding box via principle component analysis (PCA), and to compute the core length via the VMTK centerline algorithm. We further propose quantitative metrics to characterize the flow pattern within each Vortex VOI (Fig. F.1):

1. mean $\pm$ SD velocity (m/s) over all voxels within bounding box.
2. in-plane/forward/backward flow distribution (% of voxels with respect to all voxels). Forward is defined as the primary flow direction in the vessel.
3. mean $\pm$ SD forward/backward propulsion index $p[0, 1]$. For each voxel labeled forward (backward), we compute

$$p = \frac{|v_{tp}|}{|v_{tp}| + |v_{ip}|} \tag{F.1}$$

   with $|v_{tp}|$ = forward (backward)-component, and $|v_{ip}|$ = in-plane-component.
4. swirl direction (left/right) with respect to the primary flow direction.

Synthetic data. We generated a synthetic velocity vector field on a $64 \times 64 \times 64$ image grid using the Burgers-Rott vortex model with varying Gaussian noise ($\sigma = [0, 0.01, 0.05, 0.1]$) and circulation strength ($\Gamma = [75, 150, 300, 500]$).

In vivo patient data. To show feasibility on clinical datasets, we analyzed six 3D PC-MRI aorta datasets of patients with aortic valve stenosis, scanned on a 1.5 T Tesla MRI machine (Philips Achieva) before (N=3) and after (N=3) valve replacement. Acquisition parameters were: $T_E = 2.1$ ms; $T_R = 3.34$ ms; flip angle = 5°; slices = 38; spatial resolution = $2.0 \times 2.0 \times 2.8\,\text{mm}^3$; temporal resolution = 40; V_{enc} = 300–600 cm/s; PAT = SENSE (factor = 2); prospective ECG triggering; respiratory navigator gating. Aortic segmentation was performed on static 3D whole heart datasets that were acquired in the same session.

RESULTS Evaluation of synthetic data showed acceptable detection and quantification of the vortical structure in 15 out of 16 tested models. All computed metrics were consistent through different levels of noise with negligible differences (Fig. F.2). The algorithm failed for subtle circulation strength ($\Gamma = 75$) and highest noise perturbation ($\sigma = 0.1$). In-vivo data results show that core detection was positive in five out of six datasets and were in line with qualitative particle tracing (Fig. F.3). In case 1, no core was detected in one dataset post-treatment, for which particle tracing did not exhibit any vortical/helical pattern. In case 3 and 4, quantitative metrics differed for pre- and post-treatment, assuring the use of the proposed markers in a future studies which seek to evaluate pre- and post-treatment flow.

DISCUSSION We present a fully automated way for a quantitative description of vortical/helical blood flow in tubular vessels. In particular, we propose reproducible metrics based on 3D PC-MRI data. As shown for synthetic velocity data, the algorithm proves to be robust towards noise, which is of great importance when considering its deployment in an in-vivo patient study. A remaining limitation of the proposed pipeline is the bounding box which we expect to generate uncertainties in the quantitative metrics for curved cores. Future efforts must include a full evaluation of the algorithm using a bigger in-vivo data patient cohort and a pre-clinical study to discover which metric may define a valuable hemodynamic biomarker.

CONCLUSION This work proposes a pipeline for characterizing vortical flow in tubular structures using a fully automated vector pattern matching and computed quantitative metrics. We seek to optimize this tool with respect to the current limitations and subsequently deploy it in a clinical study.

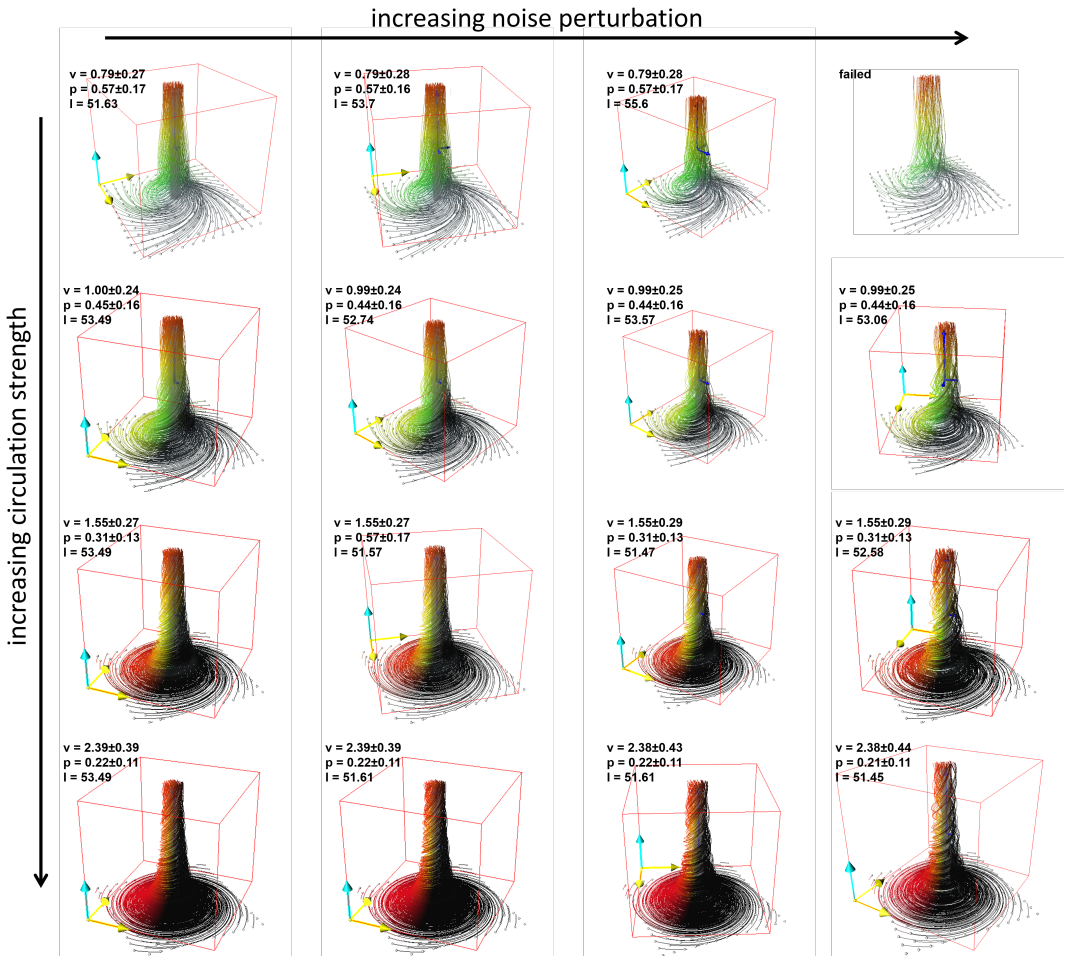

Figure F.2: Synthetic data with various circulation strength numbers (rows) and Gaussian noise levels (columns). Streamlines originating from a down-sampled 16x16 grid with color-coded velocity values. Vortex cores are visualized as grey structures, with principle component axes in dark blue. Vortex VOIs are depicted by red bounding boxes with local in-plane axes (yellow) and through plane axis (light blue, i.e. forward flow axis). Successful detection in 15/16 cases. v = velocity [m/s]; p = forward propulsion index; l = length of detected core [mm].

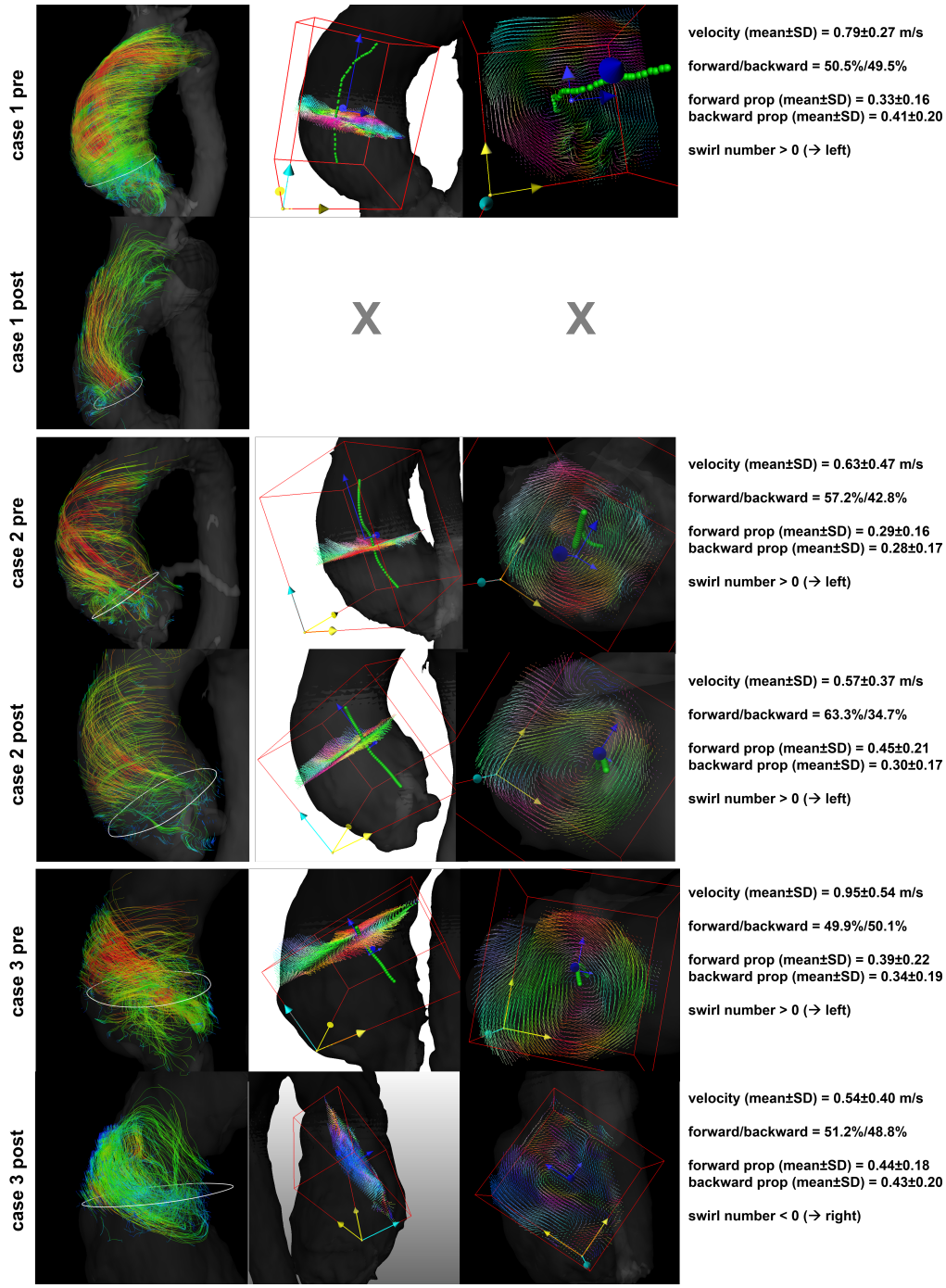

Figure F.3: Vortex quantification in three patients with aortic valve stenosis, both prior (pre) and after (post) valve replacement. Column 1: particle tracing in the ascending aorta (color-coding = velocity). Column 2: detected vortex cores (green path) and derived VortexVOI bounding boxes (red) with single velocity vector slice (color-coding = 3D-direction). Column 3: top view of VortexVOI with single velocity vector slice. Column 4: Quantitative results. Our algorithm did not detect any vortex core in the case 1 post dataset.

G

IMPACT OF AORTIC WALL STIFFNESS AND THICKNESS ON QUANTITATIVE 4D FLOW DYNAMICS IN 3D-PRINTED THORACIC AORTA MODELS.

Authors: **Judith Zimmermann**, Kathrin Baeumler, Michael Loecher, Alison L. Marsden, Daniel B. Ennis.

In: Proc. ISMRM 28th Annual Meeting 2020, Virtual Conference [151].

INTRODUCTION Pulse wave velocity (PWV) is recognized as a metric of aortic wall stiffness and may inform the diagnosis and disease management of several vascular pathologies [65, 72, 141]. 4D-flow MRI outputs velocity maps from which PWV can be estimated [31, 92]. The sensitivity of PWV to true changes in stiffness and wall thickening, however, remains uncertain and is impacted by the 4D-flow image quality which – in the clinical setting – has modest spatiotemporal resolution and signal-to-noise-ratio (SNR). This work utilizes a novel approach to subject-specific 3D-printing of compliant thoracic aorta models. The objectives of this work were: (1) to demonstrate feasibility of an in vitro flow circuit setup using a subject specific healthy thoracic aorta model; and (2) to analyze the impact of vessel wall characteristics (thickness, stiffness) and heart rate (HR) variability on quantitative flow dynamics.

METHODS *Models.* A 4D-flow MRI dataset of a healthy subject was used to generate a polygon mesh model of the thoracic aorta wall (Fig. G.1 A). The model was printed (scale 1:1) using 3D additive manufacturing (J735 PolyJet, Stratasys) and a compliant photopolymer material (Agilus, Stratasys) in three configurations (Fig. G.1 B):

- M1_1.6_soft with 1.6 mm wall thickness and Young's modulus = 0.7 MPa (Agilus30, Stratasys),
- M2_2.0_soft with 2.0 mm wall thickness and Young's modulus = 0.7 MPa (Agilus30, Stratasys), and
- M3_2.0_hardened with 2.0 mm wall thickness and Young's modulus = 3.5 MPa (Agilus30 + VeroClear, both Stratasys).

M1_1.6_soft and M2_2.0_soft closely resemble the healthy aortic stiffness; M3_2.0_hardened resembles extreme aortic hardening.

4D-flow. Each model was embedded into a pulsatile flow circuit that includes an MRI-compatible and programmable pump system (CardioFlow 5000, Shelley Medical). Six liters of glycerol-water fluid

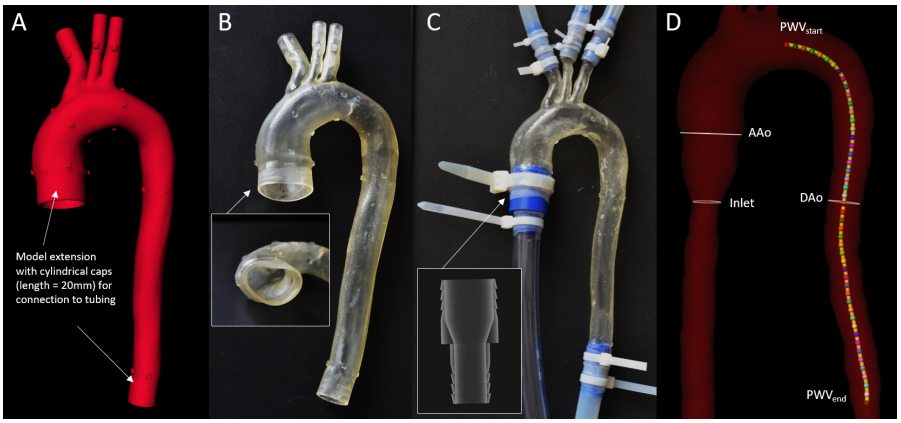

Figure G.1: (A) Subject-specific polygon mesh model with prescribed wall thickness of 2 mm. (B) Finished 3D-printed result (M2_2.0_soft). (C) Model connected to tubing with customized transition connectors (blue), and double-secured with sealing tape and cable ties. (D) Analysis landmarks shown in the acquired in vitro 4D-flow data (fluid domain mask in red), cross-sectional regions of interest at inlet, AAo, and DAo (white), and equidistantly spaced landmarks (colored path) used for PWV analysis. AAo = ascending aorta; DAo = descending aorta; PWV = pulse wave velocity.

(ratio = 2/3) infused with T_1-shortening contrast agent (Ferumoxytol, 0.75 mL per liter of fluid) was used to mimic blood viscosity with increased SNR. Six 4D-flow MRI datasets were acquired with: T_E = 2.6 ms; T_R = 5.2 ms; flip angle = 12°; spatial resolution = 2.5 × 2.5 × 2.5 mm^3; FOV = 320 × 320 mm^2; matrix = 128 × 128; num. slices = 36; temporal resolution = 20.6 ms; averages = 1; V_{enc} = 150 cm s^{-1}; GRAPPA (R = 2, ref. lines = 24); and prospective external triggering. For each model, we applied the subject-specific flow rate waveform — derived from in vivo 4D-flow MRI data, scaled to meet 300 mL/s peak flow rate pump limit —, and acquired data with two heart rates: (1) HR = 60 min^{-1} (RR = 1008 ms, frames = 48); and (2) HR = 100 min^{-1} (RR = 594 ms, frames = 28). Both HR settings led to a total flow volume of 4.38 L/min.

Analysis. Image data was pre-processed as follows: (1) image background noise filtering to improve performance of automated analysis; (2) fully-automated phase unwrapping based on PRELUDE [66]; (3) 3D watershed segmentation of the aortic lumen; and (4) lumen centerline detection [120]. PWV was measured as follows: (1) definition of descending aorta (DAo) centerline (distal to left subclavian artery to end of model, length = 240 mm); (2) computation of flow rate curves at equidistant cross-sectional DAo planes (N = 48, spacing = 5 mm); (3) computation of temporal shifts for each flow curve via cross-correlation; ("travelling-time-for-fixed-distance" approach) (4) PWV was defined as the slope of the fitted linear regression line. In addition, we analyzed flow rate curves and absolute velocity maps

at the model inlet and at mid DAo. Refer to Fig. G.1 D for landmark definition.

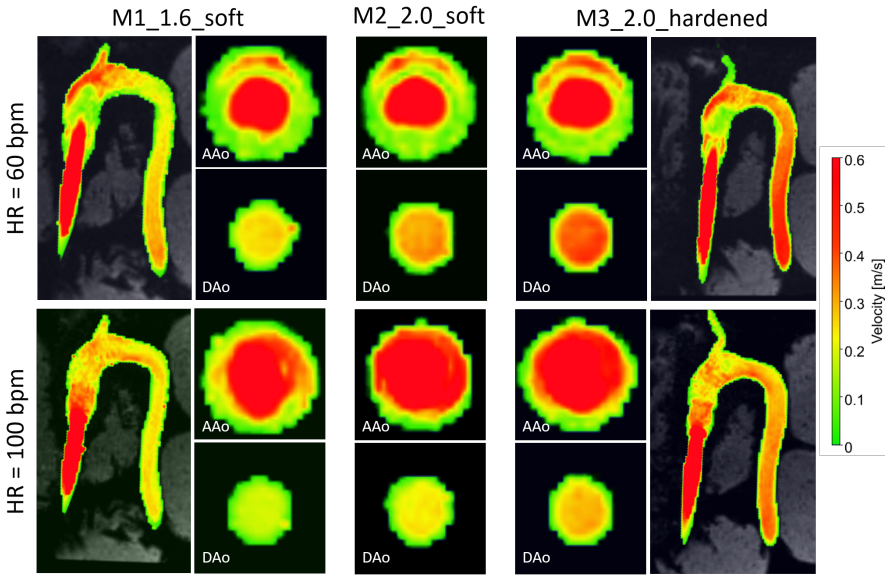

Figure G.2: Absolute velocity maps at mid-systole. AAo cross-sectional velocity maps are in good agreement for all models, but vary at the DAo landmark. Mid-systole was defined as 0.33 × cycle length (i.e. $t = 300\,\text{ms}$ for HR = $60\,\text{min}^{-1}$, and $t = 180\,\text{ms}$ for HR = $100\,\text{min}^{-1}$). Progressive flow dampening is apparent in the softer 3D-printed models.

RESULTS Absolute velocity maps qualitatively demonstrated the impact of wall characteristics. Compliant wall recoiling effects was present in all models and overall higher velocities were measured in the hardened model (Fig. G.2). Measured inlet flow waveforms were consistent with programmed flow waveforms and in good agreement between all models (Fig. G.4 A). For all models, peak flow rate was dampened through the inflow tubing (firm, length = 3 m) from $300\,\text{mL}\,\text{s}^{-1}$ (programmed) to 258–$265\,\text{mL}\,\text{s}^{-1}$ (HR = $60\,\text{min}^{-1}$) and 278–$284\,\text{mL}\,\text{s}^{-1}$ (HR = 100 1/min) at the inlet landmark (Fig. G.4 B). Measured peak flow rate through the models was further dampened at the DAo landmark, with the strongest dampening effect in the most compliant model. PWV (Fig. G.3) was lowest in M1_1.6_soft (2.22, $2.56\,\text{m}\,\text{s}^{-1}$ for HR = 60, $100\,\text{min}^{-1}$) and increased by a factor of 2.5 (HR = $60\,\text{min}^{-1}$) and 3.5 (HR = $100\,\text{min}^{-1}$) for the hardened model.

DISCUSSION Embedding compliant aorta models into the described experimental setup is technically feasible and allows acquiring high-quality 4D-flow MRI data. Measured PWV numbers are within a plausible range when compared to prior in vivo studies.5 Results suggest that waveform dampening and PWV in the 3D-printed thoracic aorta model are influenced by vessel wall thickness and stiffness. Therefore,

choosing a material that resembles in vivo aortic wall characteristics best is important as it impacts flow dynamics, thus impacting any quantitation. Changes in HR influence the quantitation of flow dynamics. Therefore, HR variations need to be considered for large-scale clinical studies. The presented experimental setup is valuable for assessing 4D-flow MRI sampling requirements, generating high-quality ground truth data for CFD/FSI validation, as well as studying flow dynamics in different vascular pathologies under controlled conditions (e. g.atherosclerosis, dissections, aneurysms). This work is limited by not incorporating pressure measurements to tune the setup toward optimal boundary conditions, which will be approached next.

CONCLUSION This work demonstrates the feasibility of in vitro flow measurements in subject-specific and compliant 3D-printed aorta models and emphasizes the importance of choosing compliant materials of appropriate stiffness and thickness for vessel models in quantitative 4D-flow studies.

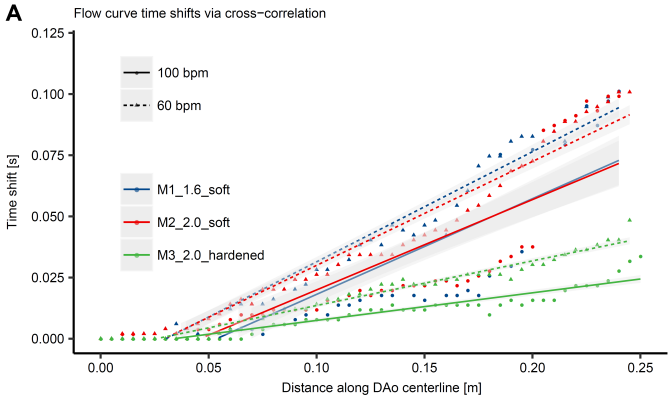

B

PWV [m/s]

	HR = 60/min	HR = 100/min
M1_1.6_soft	2.22	2.56
M2_2.0_soft	2.35	2.7
M3_2.0_hardened	5.48	8.86

Figure G.3: PWV estimation along the descending aorta centerline. (A) Measured time-shift over distance points and linear regression of the time-shift over distance along the centerline for three models at two heart rates (triangles and dashed lines for 60 min^{-1}, dots and solid lines for 100 min^{-1}). (B) Derived PWV values, i.e. inverse slope values for each fitted linear regression line, increase with increasing stiffness, increasing wall thickness, and higher heart rate.

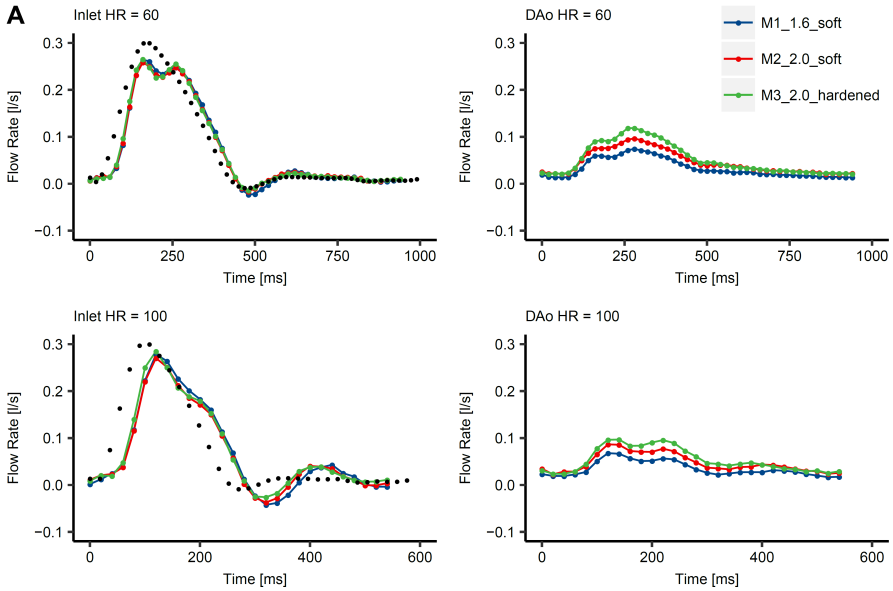

B

Measured peak flow rates [ml/s]

	HR = 60/min		HR = 100/min	
	inlet	*DAo*	*inlet*	*DAo*
M1_1.6_soft	264	74	278	57
M2_2.0_soft	258	96	270	77
M3_2.0_hardened	265	119	284	95

Figure G.4: (A) Flow rate curves at inlet and DAo landmarks under HR = 60 min^{-1} and HR = 100 min^{-1}. The black dotted curve represents the programmed flow rate curve with a constant update time of 18 ms (i.e. 56, 33 sampling points at HR = 60, 100 min^{-1}). Note that prospective ECG triggering missed the last $\approx$ 30 ms of the programmed cycle. (B) Results show consistency of flow rates at the inlet, and model-specific dampening effects at the DAo landmark. Stronger dampening at DAo occurs for the higher heart rate.

H

IN VITRO 4D-FLOW AND PRESSURE MAPPING IN THE TRUE AND FALSE LUMEN OF A TYPE-B AORTIC DISSECTION MODEL.

Authors: **Judith Zimmermann**, Michael Loecher, Kathrin Baeumler, Tyler E. Cork, Kyle Gifford, Alison L. Marsden, Dominik Fleischmann, Daniel B. Ennis.

In: Proc. SCMR Scientific Sessions 2021, Virtual Conference [153].

BACKGROUND The treatment and prognosis of patients with type-B aortic dissection (TBAD) is strongly informed by morphologic imaging findings [102, 116]. However, flow-based factors and pressure distribution may be better markers of individual risk [9, 35, 103], but the complex interplay between morphology and function is poorly understood. 4D-flow MRI excels at mapping flow, but in vivo evaluation is challenged by the balance of image quality and clinically efficient scan times [34, 108, 148]. Computational fluid dynamics (CFD) with deformable walls, i. e.integrating fluid structure interaction (FSI), is missing validation against high-quality measured data [8]. Our objective was to (1) to engineer an MRI-compatible setup that embeds a compliant, 3D-printed TBAD model under physiological flow and pressure conditions; and (2) to report flow parameters and catheter-based absolute pressure waveforms in the true and false lumen (TL, FL).

METHODS A TBAD model was constructed from a CT angiogram of a 31 year old woman with TBAD and FL aneurysm (Fig. H.1 A, B). The model was 3D-printed (Fig. H.1 C) using a photopolymer material with aortic compliance (E=0.58 MPa) and was embedded into a bio-mimicking flow loop with HR=60 min^{-1} and stroke volume = 71 mL (Fig. H.1 D). Prior to image acquisition, the system was tuned to 124/68 mmHg at the ascending aorta (AAo), and 75/25 flow volume split (DAo outlet vs arch branches). Additionally, pressures were directly recorded at TL, FL, and DAo outlet. Imaging (3T, Skyra, Siemens) included:

- 4D-flow 6-point high-moment encoding acquisition [78]: voxel size = $1.5 \times 1.5 \times 1.5\,\mathrm{mm}^3$, FOV = $360 \times 360 \times 84\,\mathrm{mm}^3$, V_{enc} = $80\,\mathrm{cm\,s}^{-1}$, V_{max} (reconstructed) = $80\,\mathrm{cm\,s}^{-1}$; temporal resolution = 50 ms; $T_E = 3.3$ ms; $T_R = 6.2$ ms.
- 2D-CINE (pixel size = $0.9 \times 0.9\,\mathrm{mm}^3$, temporal resolution = 50 ms) at specific cross-sectional landmarks (Fig. H.1 B);

- 2D-PC (pixel size = $1.4 \times 1.4\,mm^3$, temporal resolution = 50 ms) at identical cross-sectional landmarks.

4D-flow datutza was visualized using MEVISFlow [114], and 2D-CINE and PC data was processed to retrieve flow rate, velocity, and wall expansion curves.

RESULTS 4D-flow path line tracing showed increased velocities through the entry tear and in the distal, narrow FL, as well as dominant helical flow in the FL aneurysm and FL flow residence over two cardiac cycles (Fig. H.2 A, B). Absolute velocity maps (Fig. H.2 C) showed a large range of velocities in systole, confirming that selection of velocity encoding range to accurately capture velocities in both TL and FL is challenging. 2D cross-sectional analysis (Fig. H.3) showed TL/FL flow volume splits of 30/70%. Instantaneous TL pressure was >8 mmHg higher than FL pressure in peak systole.

CONCLUSIONS We demonstrated an advanced setup to study TBAD flow and pressure conditions, displaying valuable information of flow patterns, flow volume, velocity and TL/FL pressure. Future studies will (1) exploit options to vary flow (i. e.programmed inlet waveform) and pressure conditions (i. e.lowering pressure) to evaluate impacts on flow and pressure dynamics; and (2) provide high-quality 4D-flow data for verifying novel CFD simulation approaches that integrate deformable aortic walls.

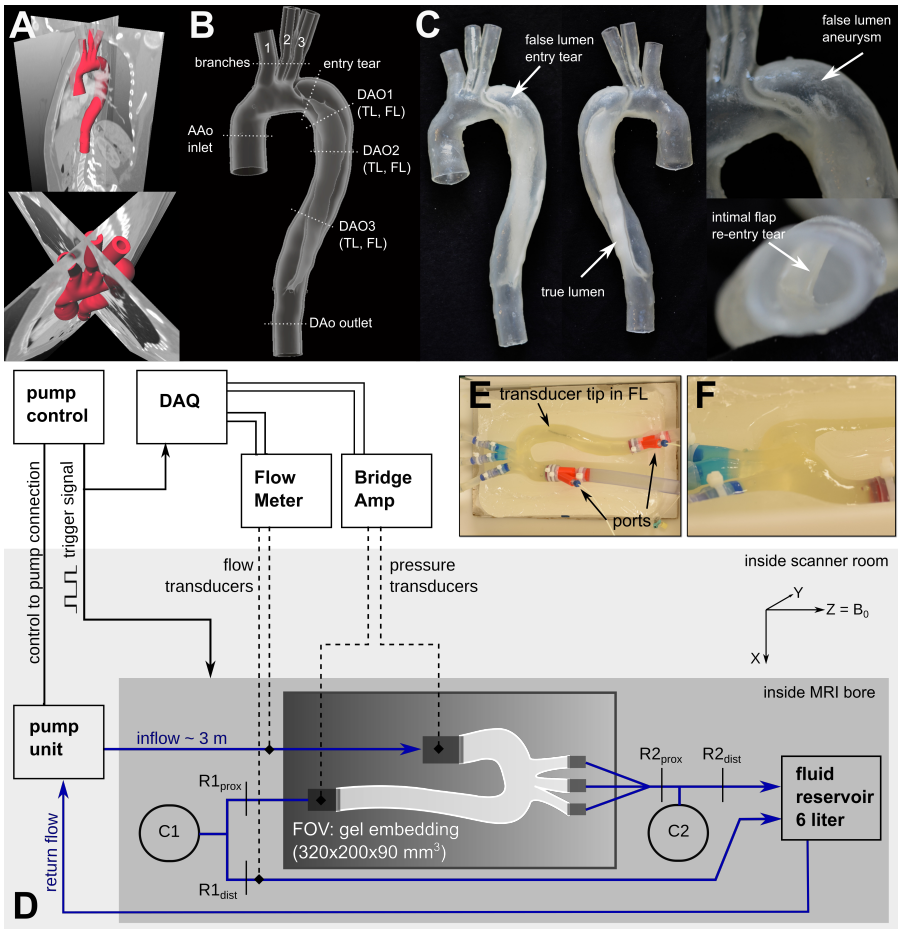

Figure H.1: (A) TBAD model construction based on 3D computed tomography data using semi-automated wall and flap segmentation and subsequent surface meshing. Entry tear is distal to the left subclavian artery and the re-entry tear is just proximal to the origin of the celiac trunk. (B) Aortic wall and intimal flap model with wall thickness = 2 mm, depicting location of the primary entry and re-entry tear, as well cross-sections used for 2D-CINE and 2D-PC acquisitions. (C) Photographs of finished 3D-printed model. (D) Schematic drawing of experimental setup. (E) TL/FL pressures were mapped at landmark DAO2 via catheterization through the DAO outlet port. (F) TBAD model fully embedded into a gel block to mimic static tissue to ensure eddy current phase offset correction of the entire volume of interest.

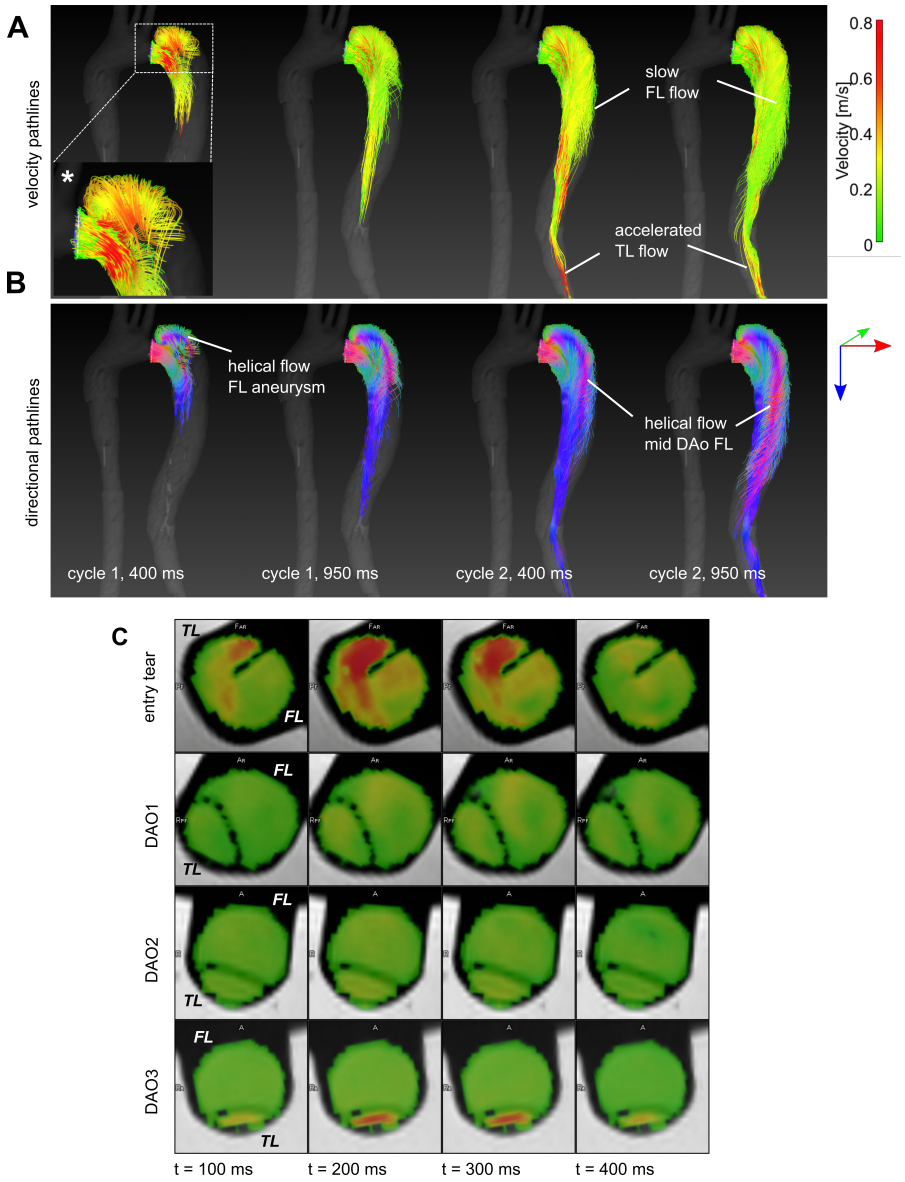

Figure H.2: 4D-flow based path line tracing (emitter plane distal to left subclavian artery, proximal to entry tear) with (A) velocity color-coding and (B) 3D-direction color-coding over two cardiac cycles. Snapshots are shown at end-systole (t = 400 ms) and end-diastole (t = 950 ms). Increased velocities at the entry tear (close-up view marked *) and in the distal TL region. Straight flow patterns in TL (blue direction) vs. helical flow patterns in FL (red lines). Path lines in the FL take two cycles to arrive at the entry tear. (C) Cross-sectional absolute velocity overlays at four systolic timepoints show a large velocity range between the TL (high velocities) and the FL (low velocities).

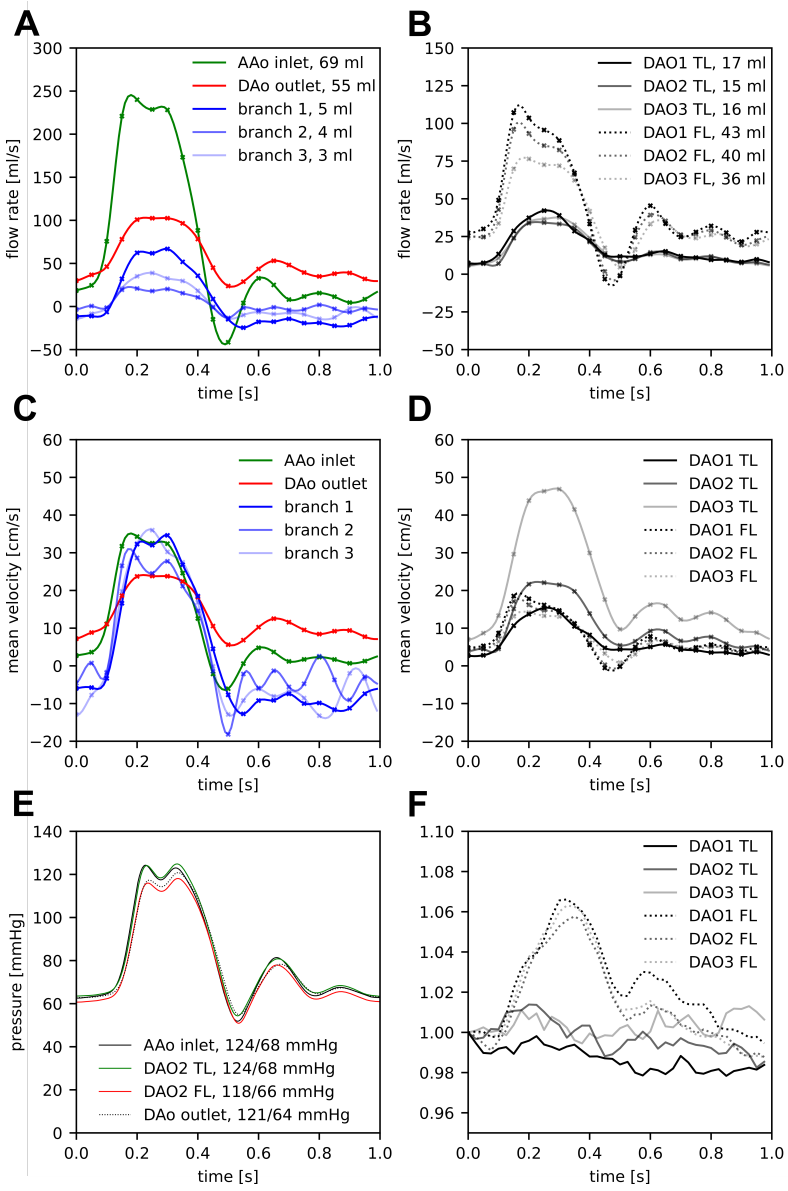

Figure H.3: 2D analysis at cross-sectional landmarks (see Fig. H.1 B for definition) and TL, FL pressure recording. (A, B) Flow splits between the DAo outlet and arch branch vessel confirm pre-scan mapping with ultrasonic probe ($\approx$ 75/25). Smaller DAo flow volume (total = 55 mL) through TL (15–16 mL, $\approx$ 30 %), and more flow through FL (36–43 mL, $\approx$ 70 %). (C) Mean cross-section velocities in peak systole are highest at the AAo inlet and branch vessels, and lower at the DAo outlet, but diastolic flow is most pronounced at the DAo outlet. (D) Mean cross-section velocities in peak systole are higher in the TL (due to much smaller cross-sectional area, particularly at the DAo3). (E) Luminal pressure mapping at four points prior to image acquisition shows a TL (green) to FL (red) pressure gradient of >8 mmHg at peak systole, and mean arterial pressures of 80, 81, 77 and 79 mmHg for the AAo inlet, TL, FL, and DAo outlet, respectively. (F) Relative cross-sectional lumen area change (w.r.t. lumen area at start-systole) shows expansion of $\approx$ 6 % in FL, and non-detectable area change of TL lumen. Note that accuracy of TL area change curves may be impacted by the small absolute TL area.

I

EVALUATING ICOSA6 4D-FLOW IN A COMPLIANT AORTIC DISSECTION MODEL WITH LARGE VELOCITY RANGE AND COMPLEX FLOW PATTERNS.

Authors: **Judith Zimmermann**, Michael Loecher, Tyler E. Cork, Kathrin Baeumler, Alison L. Marsden, Dominik Fleischmann, Daniel B. Ennis.

In: Proc. ISMRM 29th Annual Meeting 2021, Virtual Conference. [152]

INTRODUCTION The treatment and prognosis of patients with type-B aortic dissection (TBAD) is largely based on morphologic imaging findings [102]. However, flow parameters in the true and false lumen (TL, FL) may confer added sensitivity of individual risk. 4D-flow MRI [88] can be used to estimate several flow parameters in TBAD cases [9, 35, 77]. Typical TBAD flow, however, presents substantial flow pattern complexity including a large velocity range. Therefore, careful consideration should be made regarding 4D-flow acquisition parameters and the trade-offs that balance flow measurement accuracy and precision against exam time. The objective of this work was to use an accelerated high spatial resolution multi-directional (ICOSA6) high-moment stack-of-stars 4D-flow sequence in a TBAD model to determine the maximum acceleration factor that minimized errors in net flow and peak velocity within 5 %.

METHODS A patient-specific TBAD model with two aortic wall tears (entry and exit) was constructed and 3D-printed using a photopolymer material with wall elasticity similar to the human aortic wall [153]. The model was embedded into a bio-mimicking pulsatile flow loop (Fig. I.1) with HR = 60 min^{-1}, stroke volume = 74.1 mL, and systolic/diastolic pressure = 124/68mmHg.

4D-flow data was acquired (3 T Skyra, Siemens) using a multi-directional (ICOSA6) high-moment encoding scheme [156] with a stack-of-stars k-space trajectory: FOV = $360 \times 360 \times 90\,\mathrm{mm}^3$; voxel size = $1.5 \times 1.5 \times 1.5\,\mathrm{mm}^3$; $T_E = 3.3$ ms; $T_R = 6.2$ ms; 92 000 radial spokes per flow encode (corresponding to R = 5 acceleration); $V_{enc} = \pm 80\,\mathrm{cm\,s}^{-1}$; and retrospective binning with 20 frames/cycle. ICOSA6 datasets were reconstructed with parallel imaging and compressed sensing (using JSENSE coil maps [142]) as well as total variation regularizations in space and time, which were increased with under-sampling to keep similar image quality and apparent aliasing. Images were reconstructed to $\pm 160\,\mathrm{cm\,s}^{-1}$ using a weighted non-convex velocity solver [78]. ICOSA6 data corresponded to the following

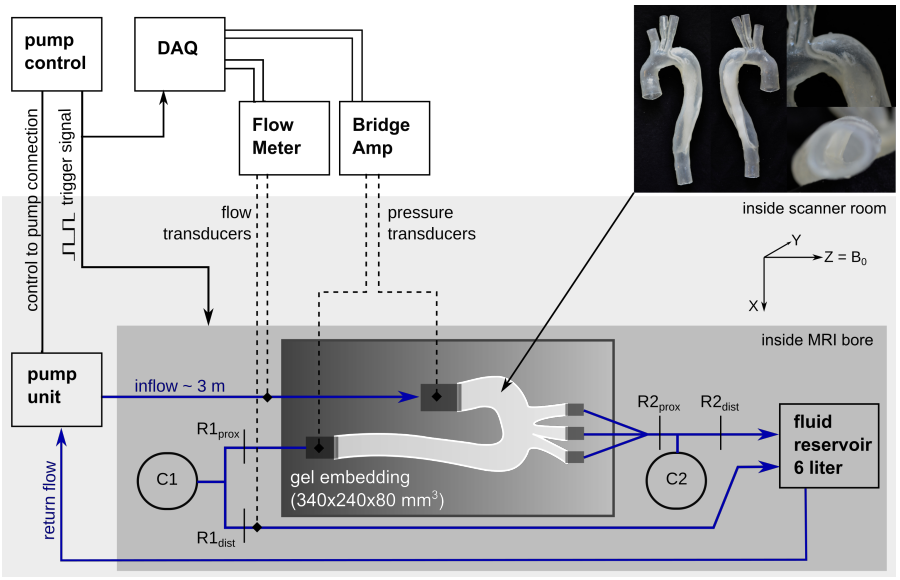

Figure I.1: Schematic diagram of the engineered MRI-compatible flow circuit setup. The pump unit is positioned at the end of the patient table, leading to an inflow tubing length of 3 meter. The pump control provides an external trigger for triggering image acquisition and data acquisition system (DAQ) for synchronizing the sampling flow and pressure signals. Ultrasonic flow transducers and pressure transducers were disconnected after tuning and prior to moving the setup to bore iso-center amid their lacking MRI compatibility. The gel embedding defines the 3D imaging volume with slab orientation along the y-direction. The top right photograph shows the 3D-printed TBAD model used in this study.

scan times (in minutes): 67 min (using 100 % of radial spokes, R = 5), 33 min (50 %, R = 10), 17 min (25 %, R = 20), 8 min (12 %, R = 40), and 5 min (7.5 %, R = 65). The latter two were each reconstructed with two different space-time regularization weighting pairs, leading to a total of seven ICOSA6 datasets. Regularization weighting pairs ($\lambda_{space}/\lambda_{time}$) were: $1 \times 10^{-3}/1 \times 10^{-3}$, $2 \times 10^{-3}/2 \times 10^{-3}$, $2.5 \times 10^{-3}/5 \times 10^{-3}$, $5 \times 10^{-3}/1 \times 10^{-2}$, $7.5 \times 10^{-3}/1.25 \times 10^{-2}$ (Reg1, Reg2, Reg3, Reg4, and Reg5).

RESULTS Multi-directional (ICOSA6) high-moment encoding was reconstructed with very limited residual phase wrapping, but velocity data displayed some smoothing effects (over the entire FOV) and visible radial sampling artifacts (at FOV boundaries) when compared to four-point Cartesian data (Fig. I.2). Overall, flow patterns in the TBAD model recapitulated in vivo patterns. Pathline tracing revealed helical flow patterns for all ICOSA6 data, but pathline travelling-range at end-diastole was decreased for ICOSA6 12 % and 7.5 % data.

Fig. I.3 displays flow volume (b, c) and peak velocity (d, e) errors for different under-sampling factors. When compared to four-point Cartesian for a range of slice locations, ICOSA6 net flow volumes

(reported as mean $\pm$ SD %) differed by 2.0 ± 8.1, 0.3 ± 4.5, -3.0 ± 5.6, -2.5 ± 5.3, -2.4 ± 5.3, -10.5 ± 10.7, and -12.8 ± 12.8 for 100 % (Reg1), 50 %(Reg2), 25 % (Reg2), 12 % (Reg2), 12 % (Reg3), 7.5 % (Reg4), and 7.5 % (Reg5) of radial spokes used. Likewise, peak flow velocities (i.e. maximum velocity through cross-section at peak-systole, reported as mean $\pm$ SD %) differed by -18.1 ± 14.6, -26.0 ± 11.9, -25.3 ± 15.4, 4.7 ± 47.9, -6.3 ± 35.9, -18.3 ± 54.4, and -15.8 ± 93.5.

Flow rate waveforms evaluated at three landmarks (Fig. I.3f, I.3g, I.3h) showed an overall decrease in peak flow rates with increasing under-sampling. ICOSA6 100 % (Reg1) and 50 % (Reg2) were within the ± 5 % margin when compared to peak flow rates of four-point Cartesian data, and values were dampened by up to 49.1 %for ICOSA6 7.5 %.

DISCUSSION This work demonstrates the successful deployment of a 3D-printed patient-specific TBAD model with complex flow pattern in an in vitro setup to evaluate the effect of ICOSA6 under-sampling and how flow quantitation compares to four-point Cartesian data. Under-sampling down to 12 % (R=40) of the acquired radial spokes measured average net flow volumes within the ± 5 % margin when compared to four-point Cartesian data. However, net flow standard deviations among all evaluated cross-sections showed larger disagreements in complex flow zones (e.g. 'entry tear'). This emphasizes the importance of performing acceleration analyses using 'patient-specific' flow phantoms that include large velocity ranges and complex flow patterns, rather than simple tube phantoms. We note that sampling requirements — and thus scan time — were much higher compared to standard 4D-flow exams because of the high spatial resolution (1.5 mm^3), and the ICOSA6 velocity encoding, which requires seven velocity encodes instead of four. Regularization schemes and parameter tuning both require further investigation. The 4D-flow Cartesian references scan was very long (42 min) and accelerated schemes also need to be evaluated and compared.

CONCLUSION Multi-directional high-moment 4D-flow compares well to Cartesian 4D-flow if performed with adequate sampling. Highly under-sampled ($<$12 % of spokes, R$>$40) ICOSA6 4D-flow underestimates net flow and results in inaccurate peak velocity measurements.

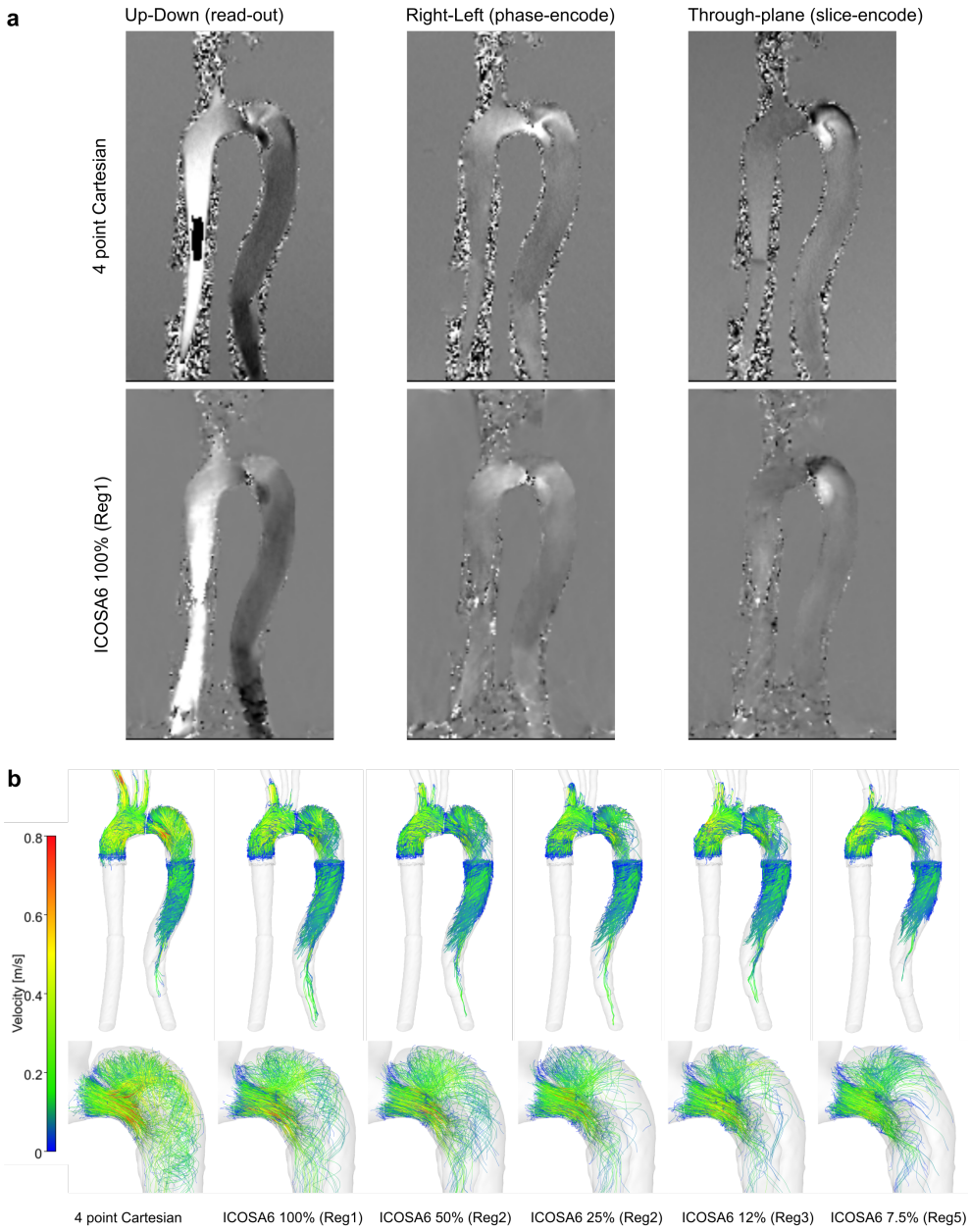

Figure I.2: (a) Phase data for four-point Cartesian and ICOSA6 100 %. Smoothing effects were observed in ICOSA6 data, particularly in the entry tear region, where helical flow with a large velocity range is present. Four-point Cartesian included aliased pixels prior to the model inlet, which was not present in ICOSA6 data. (b) End-diastolic pathlines based on four-point Cartesian and ICOSA6 data. With increased under-sampling, the pathline travelling range decreased, the detection of helical flow in the proximal FL becomes more challenging, and jet flow velocities (entry tear) become smaller.

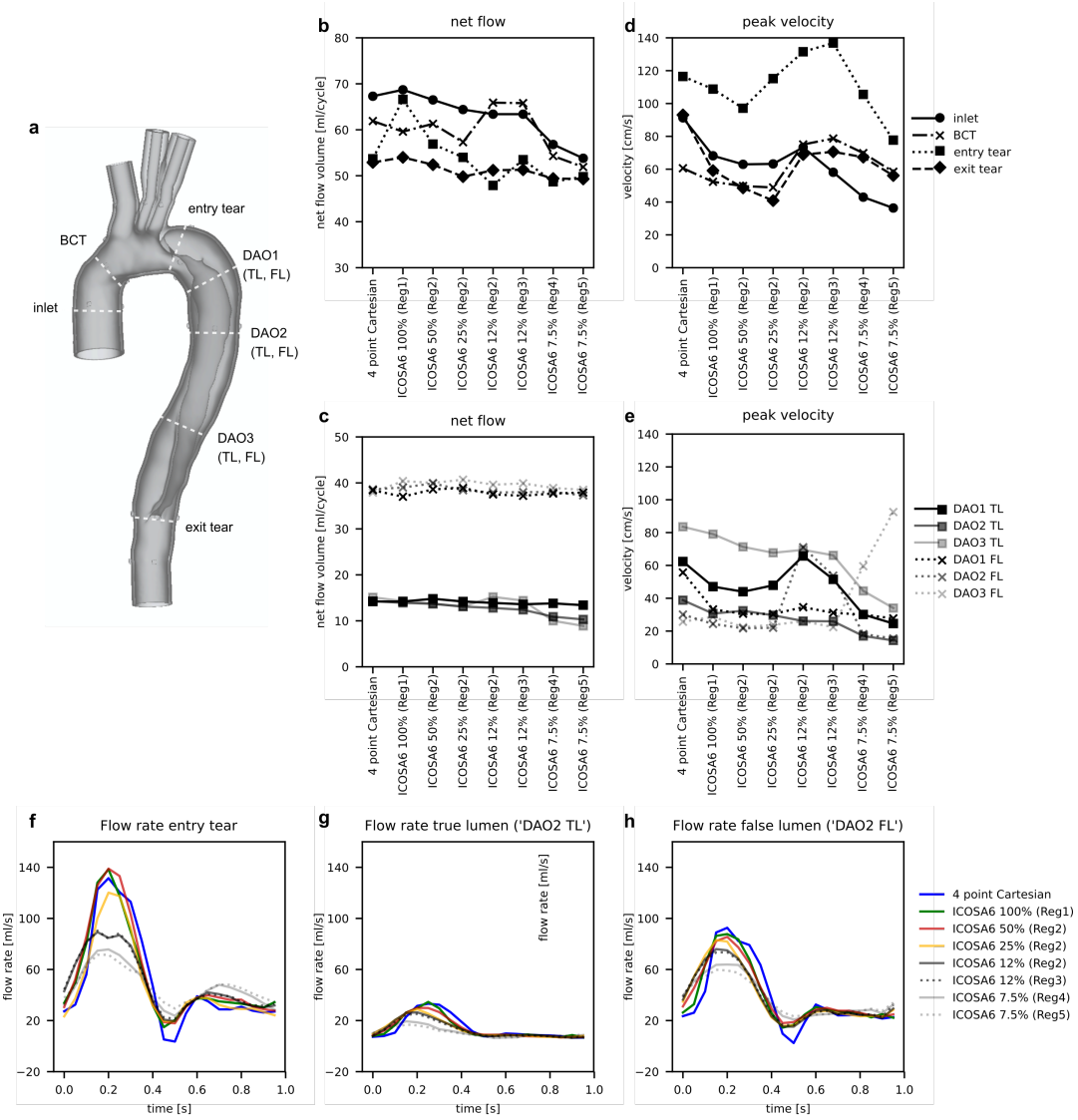

Figure I.3: (a) TBAD cross-sections. (b, c) Calculated net flow and (d, e) peak velocity for four-point Cartesian and ICSOA6. Conservation of mass dictates that net flow through 'inlet' versus 'BCT, 'entry tear' versus 'exit tear', all TL sections, as well as all FL sections should be equal. Flow waveforms shown for the entry tear (f), true lumen (g), and false lumen (h). Overall, flow waveforms between the four-point Cartesian (blue) and ICOSA6 100 % (green) as well as 50 % (red) correspond well. With increased under-sampling of ICOSA6 reconstructions, peak flow rates decrease by up to 49.1 %.

BIBLIOGRAPHY

[1] P. Albaladejo et al. "Heart Rate, Arterial Stiffness, and Wave Reflections in Paced Patients." In: *Hypertension* 38.4 (2001), pp. 949–952. DOI: 10.1161/hy1001.096210.

[2] P. Albaladejo et al. "Influence of sex on the relation between heart rate and aortic stiffness." In: *J. Hypertension* 21.3 (2003), pp. 555–562. DOI: 10.1097/00004872-200303000-00021.

[3] B. D. Allen et al. "Thoracic aorta 3D hemodynamics in pediatric and young adult patients with bicuspid aortic valve." In: *J. Magn. Reson. Imaging* 42.4 (2015), pp. 954–963. DOI: 10.1002/jmri.24847.

[4] P. M. Arvidsson et al. "Vortex ring behavior provides the epigenetic blueprint for the human heart." In: *Scientific Reports* 6 (2016). DOI: 10.1038/srep22021.

[5] C. Baltes et al. "Accelerating cine phase-contrast flow measurements using k-t BLAST and k-t SENSE." In: *Magn Reson Med* 54.6 (2005), pp. 1430–1438. DOI: 10.1002/mrm.20730.

[6] A. J. Barker et al. "Bicuspid Aortic Valve Is Associated With Altered Wall Shear Stress in the Ascending Aorta." In: *Circ. Cardiovasc. Imaging* 5.4 (2012), pp. 457–466. DOI: 10.1161/CIRCIMAGING.112.973370.

[7] A. J. Barker et al. "Viscous energy loss in the presence of abnormal aortic flow." In: *Magn. Reson. Med.* 72.3 (2014), pp. 620–628. DOI: 10.1002/mrm.24962.

[8] K. Bäumler et al. "Fluid–structure interaction simulations of patient-specific aortic dissection." In: *Biomech. Model. Mechanobiol.* 19.5 (2020), pp. 1607–1628. DOI: 10.1007/s10237-020-01294-8.

[9] H. W. de Beaufort et al. "Four-dimensional flow cardiovascular magnetic resonance in aortic dissection: Assessment in an ex vivo model and preliminary clinical experience." In: *J Thorac Cardiovasc Surg* 157.2 (2019), pp. 467–476. DOI: 10.1016/j.jtcvs.2018.06.022.

[10] M. A. Bernstein and Y. Ikezaki. "Comparison of phase-difference and complex-difference processing in phase-contrast MR angiography." In: *J Magn Reson Imaging* 1.6 (1991), pp. 725–729. DOI: 10.1002/jmri.1880010620.

[11] M. A. Bernstein, K. King, and X. Zhou. *Handbook of MRI Pulse Sequences*. Burlington, London, San Diego: Elsevier Academic Press, 2004, p. 1040. ISBN: 9780120928613.

[12] M. A. Bernstein et al. "Concomitant gradient terms in phase contrast MR: Analysis and correction." In: *Magn Reson Med* 39.2 (1998), pp. 300–308. DOI: 10.1002/mrm.1910390218.

[13] E. T. Bieging et al. "In vivo three-dimensional mr wall shear stress estimation in ascending aortic dilatation." In: *J. Magn. Reson. Imaging* 33.3 (2011), pp. 589–597. DOI: 10.1002/jmri.22485.

[14] C. Binter et al. "Turbulent Kinetic Energy Assessed by Multipoint 4-Dimensional Flow Magnetic Resonance Imaging Provides Additional Information Relative to Echocardiography for the Determination of Aortic Stenosis Severity." In: *Circ. Cardiovasc. Imaging* 10.6 (2017). DOI: 10.1161/CIRCIMAGING.116.005486.

[15] M. M. Bissell et al. "Aortic dilation in bicuspid aortic valve disease: Flow pattern is a major contributor and differs with valve fusion type." In: *Circulation: Cardiovasc Imaging* 6.4 (2013), pp. 499–507. DOI: 10.1161/CIRCIMAGING.113.000528.

[16] J. Bock et al. "In vivo noninvasive 4D pressure difference mapping in the human aorta: Phantom comparison and application in healthy volunteers and patients." In: *Magn Reson Med* 66.4 (2011), pp. 1079–1088. DOI: 10.1002/mrm.22907.

[17] E. Bollache et al. "k-t accelerated aortic 4D flow MRI in under two minutes: Feasibility and impact of resolution, k-space sampling patterns, and respiratory navigator gating on hemodynamic measurements." In: *Magn Reson Med* 79.1 (2018), pp. 195–207. DOI: 10.1002/mrm.26661.

[18] R. W. Brown et al. *Magnetic Resonance Imaging: Physical Principles and Sequence Design, Second Edition*. Hoboken, New Jersey: Wiley Blackwell, 2014, p. 976. DOI: 10.1002/9781118633953.

[19] D. J. Bryant et al. "Measurement of flow with nmr imaging using a gradient pulse and phase difference technique." In: *J Comp Assisted Tomography* 8.4 (1984), pp. 588–593. DOI: 10.1097/00004728-198408000-00002.

[20] N. S. Burris and M. D. Hope. "4D flow MRI applications for aortic disease." In: *Magn Reson Imaging Clin N Am* 23.1 (2015), pp. 15–23. DOI: 10.1016/J.MRIC.2014.08.006.

[21] J. Busch, D. Giese, and S. Kozerke. "Image-based background phase error correction in 4D flow MRI revisited." In: *J Magn Reson Imaging* 46.5 (2017), pp. 1516–1525. DOI: 10.1002/jmri.25668.

[22] M. Bustamante et al. "Atlas-based analysis of 4D flow CMR: Automated vessel segmentation and flow quantification." In: *J. Cardiovasc. Magn. Reson.* 17 (2015), p. 87. DOI: 10.1186/s12968-015-0190-5.

[23] E. E. Calkoen et al. "Characterization and quantification of dynamic eccentric regurgitation of the left atrioventricular valve after atrioventricular septal defect correction with 4D Flow cardiovascular magnetic resonance and retrospective valve tracking." In: *J Cardiovasc Magn Reson* 17.1 (2015). DOI: 10.1186/s12968-015-0122-4.

[24] F. M. Callaghan et al. "Flow quantification dependency on background phase correction techniques in 4D-flow MRI." In: *Magn. Reson. Med.* 83.6 (2020), pp. 2264–2275. DOI: 10.1002/mrm.28085.

[25] C. Canstein et al. "3D MR flow analysis in realistic rapid-prototyping model systems of the thoracic aorta: Comparison with in vivo data and computational fluid dynamics in identical vessel geometries." In: *Magn. Reson. Med.* 59.3 (2008), pp. 535–546. DOI: 10.1002/mrm.21331.

[26] C. G. Caro et al. *The Mechanics of the Circulation: Second Edition*. New York: Cambridge University Press, 2012. ISBN: 9780521151771. DOI: 10.1115/1.3138216.

[27] M. Castagna et al. "An LDV based method to quantify the error of PC-MRI derived Wall Shear Stress measurement." In: *Scientific Reports* 11 (2021), p. 4112. DOI: 10.1038/s41598-021-83633-y.

[28] A. Chernobelsky et al. "Baseline correction of phase contrast images improves quantification of blood flow in the great vessels." In: *J Cardiovasc Magn Reson* 9.4 (2007), pp. 681–685. DOI: 10.1080/10976640601187588.

[29] T. E. Contur and B. H. Robinson. "Analysis of encoding efficiency in MR imaging of velocity magnitude and direction." In: *Magn Reson Med* 25.2 (1992), pp. 233–247. DOI: 10.1002/mrm.1910250203.

[30] P. Corso et al. "Toward an accurate estimation of wall shear stress from 4D flow magnetic resonance downstream of a severe stenosis." In: *Magn Reson Med* 86.3 (2021), pp. 1531–1543. DOI: 10.1002/mrm.28795.

[31] A. R. Damughatla et al. "Quantification of aortic stiffness using MR Elastography and its comparison to MRI-based pulse wave velocity." In: *J. Magn. Reson. Imaging* 41.1 (2015), pp. 44–51. DOI: 10.1002/jmri.24506.

[32] A. Demir et al. "Traveling Volunteers: A Multi-Vendor, Multi-Center Study on Reproducibility and Comparability of 4D Flow Derived Aortic Hemodynamics in Cardiovascular Magnetic Resonance." In: *J Magn Reson Imaging* (2021). DOI: 10.1002/jmri.27804.

[33] A. Deshmane et al. "Parallel MR imaging." In: *J. Magn. Reson. Imaging* 36 (2012), pp. 55–72. DOI: 10.1002/jmri.23639.

[34] H. Dillinger, J. Walheim, and S. Kozerke. "On the limitations of echo planar 4D flow MRI." In: *Magn. Reson. Med.* 84.4 (2020), pp. 1806–16. DOI: 10.1002/mrm.28236.

[35] D. Dillon-Murphy et al. "Multi-modality image-based computational analysis of haemodynamics in aortic dissection." In: *Biomech. Model. Mechanobiol.* 15.4 (2016), pp. 857–76.

[36] J Drexl et al. "A Software Tool for the Computation of Arterial Pulse Wave Velocity from Flow-sensitive 4D MRI Data." In: *Comput. Cardiol.* 40 (2013), pp. 559–562. ISSN: 23258861.

[37] J. Drexl et al. "Detection of Vortical Structures in 4D Velocity Encoded Phase Contrast MRI Data Using Vector Template Matching." In: *Func. Imaging Model. Heart. FIMH 2013. Lect. Notes Comput. Science*. Springer Berlin Heidelberg, 2013, pp. 276–283. DOI: 10.1007/978-3-642-38899-6_33.

[38] M. M. Driessen et al. "Tricuspid flow and regurgitation in congenital heart disease and pulmonary hypertension: Comparison of 4D flow cardiovascular magnetic resonance and echocardiography." In: *J Cardiovasc Magn Reson* 20 (2018), p. 5. DOI: 10.1186/s12968-017-0426-7.

[39] C. L. Dumoulin et al. "Simultaneous acquisition of phase-contrast angiograms and stationary-tissue images with Hadamard encoding of flow-induced phase shifts." In: *J Magn Reson Imaging* 1.4 (1991), pp. 399–404. DOI: 10.1002/jmri.1880010403.

[40] P. Dyverfeldt, T. Ebbers, and T. Länne. "Pulse wave velocity with 4D flow MRI: Systematic differences and age-related regional vascular stiffness." In: *Magn. Reson. Med.* 32.10 (2014), pp. 1266–1271. DOI: 10.1016/j.mri.2014.08.021.

[41] P. Dyverfeldt et al. "Quantification of intravoxel velocity standard deviation and turbulence intensity by generalizing phase-contrast MRI." In: *Magn Reson Med* 56.4 (2006), pp. 850–858. DOI: 10.1002/mrm.21022.

[42] P. Dyverfeldt et al. "Magnetic resonance measurement of turbulent kinetic energy for the estimation of irreversible pressure loss in aortic stenosis." In: *JACC Cardiovasc. Imaging* 6.1 (2013), pp. 64–71. DOI: 10.1016/j.jcmg.2012.07.017.

[43] P. Dyverfeldt et al. "4D flow cardiovascular magnetic resonance consensus statement." In: *J. Cardiovasc. Magn. Reson.* 17 (2015), p. 72. DOI: 10.1186/s12968-015-0174-5.

[44] M. S. Elbaz et al. "Assessment of viscous energy loss and the association with three-dimensional vortex ring formation in left ventricular inflow: In vivo evaluation using four-dimensional flow MRI." In: *Magn Reson Med* 77.2 (2017), pp. 794–805. DOI: 10.1002/mrm.26129.

[45] R. Erbel et al. "2014 ESC guidelines on the diagnosis and treatment of aortic diseases." In: *Eur Heart J* 35 (2014), pp. 2873–2926. DOI: 10.1093/eurheartj/ehu281.

[46] E. Ferdian et al. "4DFlowNet: Super-Resolution 4D Flow MRI Using Deep Learning and Computational Fluid Dynamics." In: *Front Phys* 8 (2020), p. 138. DOI: 10.3389/fphy.2020.00138.

[47] J. F. Fernandes et al. "CMR-Based and Time-Shift Corrected Pressure Gradients Provide Good Agreement to Invasive Measurements in Aortic Coarctation." In: *JACC: Cardiovascular Imaging* 11.11 (2018), pp. 1725–1727. DOI: 10.1016/J.JCMG.2018.03.013.

[48] S. W. Fielden et al. "A new method for the determination of aortic pulse wave velocity using cross-correlation on 2D PCMR velocity data." In: *J. Magn. Reson. Imaging* 27.6 (2008), pp. 1382–1387. DOI: 10.1002/jmri.21387.

[49] D. Forsberg. "Robust Image Registration for Improved Clinical Efficiency : Using Local Structure Analysis and Model-Based Processing." PhD thesis. Linköping University, 2013, p. 120. ISBN: 978-91-7519-637-4.

[50] A. Frydrychowicz, C. J. François, and P. A. Turski. "Four-dimensional phase contrast magnetic resonance angiography: potential clinical applications." In: *Eur J Radiology* 80.1 (2011), pp. 24–35. DOI: 10.1016/J.EJRAD.2011.01.094.

[51] A. Frydrychowicz et al. "Three-dimensional analysis of segmental wall shear stress in the aorta by flow-sensitive four-dimensional-MRI." In: *J Magn Reson Imaging* 30.1 (2009), pp. 77–84. DOI: 10.1002/jmri.21790.

[52] A. Frydrychowicz et al. "Interdependencies of aortic arch secondary flow patterns, geometry, and age analysed by 4-dimensional phase contrast magnetic resonance imaging at 3 Tesla." In: *Eur. Radiol.* 22.5 (2012), pp. 1122–1130. DOI: 10.1007/s00330-011-2353-6.

[53] P. Gatehouse et al. "Flow measurement by cardiovascular magnetic resonance: A multi-centre multi-vendor study of background phase offset errors that can compromise the accuracy of derived regurgitant or shunt flow measurements." In: *J Cardiovasc Magn Reson* 12 (2010), p. 5. DOI: 10.1186/1532-429X-12-5.

[54] R. J. van der Geest and P. Garg. "Advanced Analysis Techniques for Intra-cardiac Flow Evaluation from 4D Flow MRI." In: *Curr. Radiol. Rep.* 4 (2016), p. 38. DOI: 10.1007/s40134-016-0167-7.

[55] M. A. Griswold et al. "Generalized Autocalibrating Partially Parallel Acquisitions (GRAPPA)." In: *Magn Reson Med* 47.6 (2002), pp. 1202–1210. DOI: 10.1002/mrm.10171.

[56] T. Gu et al. "PC VIPR: A high-speed 3D phase-contrast method for flow quantification and high-resolution angiography." In: *Am J Neuroradiol* 26.4 (2005), pp. 743–749.

[57] E. Haesler et al. "Confounding effects of heart rate on pulse wave velocity in paced patients with a low degree of atherosclerosis." In: *J. Hypertension* 22.7 (2004), pp. 1317–1322. DOI: 10.1097/01.hjh.0000125447.28861.18.

[58] E. Heiberg et al. "Three-dimensional flow characterization using vector pattern matching." In: *IEEE Trans. Vis. Comp. Graph.* 9.3 (2003), pp. 313–319. DOI: 10.1109/TVCG.2003.1207439.

[59] B. Holland, B. Printz, and W. Lai. "Baseline correction of phase-contrast images in congenital cardiovascular magnetic resonance." In: *J Cardiovasc Magn Reson* 12 (2010), p. 11. DOI: 10.1186/1532-429X-12-11.

[60] M. D. Hope, T. Sedic, and P. Dyverfeldt. "Cardiothoracic magnetic resonance flow imaging." In: *J Thorac Imaging* 28.4 (2013), pp. 217–230. DOI: 10.1097/RTI.0B013E31829192A1.

[61] M. D. Hope et al. "Evaluation of bicuspid aortic valve and aortic coarctation with 4D flow magnetic resonance imaging." In: *Circulation* 117.21 (2008), pp. 2818–2819. DOI: 10.1161/CIRCULATIONAHA.107.760124.

[62] M. D. Hope et al. "4D flow CMR in assessment of valve-related ascending aortic disease." In: *JACC Cardiovasc. Imaging* 4.7 (2011), pp. 781–787. DOI: 10.1016/j.jcmg.2011.05.004.

[63] M. D. Hope et al. "MRI hemodynamic markers of progressive bicuspid aortic valve-related aortic disease." In: *J. Magn. Reson. Imaging* 40.1 (2014), pp. 140–145. DOI: 10.1002/jmri.24362. arXiv: NIHMS150003.

[64] J. JEong and F. Hussain. "On the identification of a vortex." In: *J Fluid Mech* 285 (1995), pp. 69–94. DOI: 10.1017/S0022112095000462.

[65] K. B. Jarvis et al. "Longitudinal Study of Aortic Stiffness and Flow Reversal in Patients with Cryptogenic Stroke." In: *Proc. ISMRM 27th Annual Meeting*. Montreal, 2019, P450.

[66] M. Jenkinson. "Fast, automated, N-dimensional phase-unwrapping algorithm." In: *Magn Reson Med* 49.1 (2003), pp. 193–197. DOI: 10.1002/mrm.10354.

[67] K. M. Johnson and M. Markl. "Improved SNR in phase contrast velocimetry with five-point balanced flow encoding." In: *Magn Reson Med* 63.2 (2010), pp. 349–355. DOI: 10.1002/mrm.22202.

[68] B. Jung et al. "Parallel MRI with extended and averaged GRAPPA kernels (PEAK-GRAPPA): Optimized spatiotemporal dynamic imaging." In: *J. Magn. Reson. Imaging* 28.5 (2008), pp. 1226–1232. DOI: 10.1002/jmri.21561.

[69] H. Knutsson and M. Andersson. "Morphons: Paint on Priors and Elastic Canvas for Segmentation and Registration." In: *Scandinavian Conf. Image Analysis. SCIA 2005. Lect. Notes Comput. Science*. Vol. 3540. Springer, Berlin, Heidelberg, 2005, pp. 292–301. ISBN: 1424407796. DOI: 10.1007/11499145.

[70] S. Ko et al. "Novel and facile criterion to assess the accuracy of WSS estimation by 4D flow MRI." In: *Medical Image Analysis* 53 (2019), pp. 95–103. DOI: 10.1016/j.media.2019.01.009.

[71] B. Köhler et al. "A Survey of Cardiac 4D PC-MRI Data Processing." In: *Comput. Graphics Forum* 36.6 (2017), pp. 5–35. DOI: 10.1111/cgf.12803.

[72] A. Kolipaka et al. "Quantification of abdominal aortic aneurysm stiffness using magnetic resonance elastography and its comparison to aneurysm diameter." In: *J. Vasc. Surg.* 64.4 (2016), pp. 966–974. DOI: 10.1016/j.jvs.2016.03.426.

[73] P. Lantelme et al. "Heart rate: An important confounder of pulse wave velocity assessment." In: *Hypertension* 39.6 (2002), pp. 1083–1087. DOI: 10.1161/01.HYP.0000019132.41066.95.

[74] P. C. Lauterbur. "Image formation by induced local interactions: Examples employing nuclear magnetic resonance." In: *Nature* 242.5394 (1973), pp. 190–191. DOI: 10.1038/242190a0.

[75] Y. L. Liang et al. "Effects of heart rate on arterial compliance in men." In: *Clin. Exp. Pharmacol. Physiol.* 26.4 (1999), pp. 342–346. DOI: 10.1046/j.1440-1681.1999.03039.x.

[76] B. R. Lindman et al. "Calcific aortic stenosis." In: *Nat. Rev. Dis. Primers* 2 (2016), p. 16006. DOI: 10.1038/nrdp.2016.6.

[77] D. Liu et al. "Quantitative Study of Abdominal Blood Flow Patterns in Patients with Aortic Dissection by 4-Dimensional Flow MRI." In: *Scientific Reports* 8 (2018), p. 9111. DOI: 10.1038/s41598-018-27249-9.

[78] M. Loecher and D. B. Ennis. "Velocity reconstruction with non-convex optimization for low-velocity-encoding phase-contrast MRI." In: *Magn. Reson. Med.* 80.1 (2018), pp. 42–52. DOI: 10.1002/mrm.26997.

[79] M. Loecher et al. "Phase unwrapping in 4D MR flow with a 4D single-step laplacian algorithm." In: *J Magn Reson Imaging* 43.4 (2016), pp. 833–842. DOI: 10.1002/jmri.25045.

[80] R. Lorenz et al. "Closed circuit MR compatible pulsatile pump system using a ventricular assist device and pressure control unit." In: *Magn. Reson. Med.* 67.1 (2012), pp. 258–268. DOI: 10.1002/mrm.22983.

[81] R. Lorenz et al. "4D flow magnetic resonance imaging in bicuspid aortic valve disease demonstrates altered distribution of aortic blood flow helicity." In: *Magn. Reson. Med.* 71.4 (2014), pp. 1542–1553. DOI: 10.1002/mrm.24802.

[82] D. P. Lum et al. "Transstenotic pressure gradients: Measurement in swine - Retrospectively ECG-gated 3D phase-contrast MR angiography versus endovascular pressure-sensing guidewires." In: *Radiology* 245.3 (2007), pp. 751–760. DOI: 10.1148/radiol.2453061946.

[83] M. Lustig, D. Donoho, and J. M. Pauly. "Sparse MRI: The application of compressed sensing for rapid MR imaging." In: *Magn Reson Med* 58.6 (2007), pp. 1182–1195. DOI: 10.1002/mrm.21391.

[84] M. Lustig et al. "Compressed sensing MRI." In: *IEEE Signal Proc Mag* 25.2 (2008), pp. 72–82. DOI: 10.1109/MSP.2007.914728.

[85] L. E. Ma et al. "Aortic 4D flow MRI in 2 minutes using compressed sensing, respiratory controlled adaptive k-space reordering, and inline reconstruction." In: *Magn. Reson. Med.* 81.6 (2019), pp. 3675–3690. DOI: 10.1002/mrm.27684.

[86] P. Mansfield and A. A. Maudsley. "Medical imaging by NMR." In: *British J Radiol* 50 (1977), pp. 188–194. DOI: 10.1259/0007-1285-50-591-188.

[87] M. Markl et al. "Generalized reconstruction of phase contrast MRI: Analysis and correction of the effect of gradient field distortions." In: *Magn Reson Med* 50.4 (2003), pp. 791–801. DOI: 10.1002/MRM.10582.

[88] M. Markl et al. "Time-resolved three-dimensional phase-contrast MRI." In: *J. Magn. Reson. Imaging* 17.4 (2003), pp. 499–506. DOI: 10.1002/jmri.10272.

[89] M. Markl et al. "Estimation of global aortic pulse wave velocity by flow-sensitive 4D MRI." In: *Magn. Reson. Med.* 63.6 (2010), pp. 1575–1582. DOI: 10.1002/mrm.22353.

[90] M. Markl et al. "In vivo wall shear stress distribution in the carotid artery: effect of bifurcation geometry, internal carotid artery stenosis, and recanalization therapy." In: *Circ. Cardiovasc. Imaging* 3.6 (2010), pp. 647–655. DOI: 10.1161/circimaging.110.958504.

[91] M. Markl et al. "4D flow MRI." In: *J. Magn. Reson. Imaging* 36.5 (2012), pp. 1015–36. DOI: 10.1002/jmri.23632.

[92] M. Markl et al. "Analysis of pulse wave velocity in the thoracic aorta by flow-sensitive four-dimensional MRI: Reproducibility and correlation with characteristics in patients with aortic atherosclerosis." In: *J. Magn. Reson. Imaging* 35.5 (2012), pp. 1162–1168. DOI: 10.1002/jmri.22856.

[93] M. Markl et al. "Co-registration of the distribution of wall shear stress and 140 complex plaques of the aorta." In: *Magn Reson Imaging* 31.7 (2013), pp. 1156–1162. DOI: 10.1016/j.mri.2013.05.001.

[94] M. Markl et al. "Advanced flow MRI: emerging techniques and applications." In: *Clin. Radiol.* 71.8 (2016), pp. 779–795. DOI: 10.1016/j.crad.2016.01.011.

[95] S. Meier et al. "A Fast and Noise-Robust Method for Computation of Intravascular Pressure Difference Maps from 4D PC-MRI Data." In: *Stat. Atlases Comput. Model. Heart. STACOM 2012. Lect. Notes Comput. Science*. Vol. 7746. Springer, Berlin, Heidelberg, 2012, pp. 215–224. DOI: 10.1007/978-3-642-36961-2_25.

[96] H. Mirzaee et al. "MRI-based computational hemodynamics in patients with aortic coarctation using the lattice Boltzmann methods: Clinical validation study." In: *J. Magn. Reson. Imaging* 45.1 (2017), pp. 139–146. ISSN: 15222586. DOI: 10.1002/jmri.25366.

[97] J. Modersitzki. *FAIR*. Society for Industrial and Applied Mathematics, 2009. ISBN: 089871690X.

[98] R. Moftakhar et al. "Noninvasive measurement of intra-aneurysmal pressure and flow pattern using phase contrast with vastly undersampled isotropic projection imaging." In: *Am J Neuroradiol* 28.9 (2007), pp. 1710–1714. ISSN: 01956108. DOI: 10.3174/ajnr.A0648.

[99] P. R. Moran, R. A. Moran, and N. Karstaedt. "Verification and evaluation of internal flow and motion. True magnetic resonance imaging by the phase gradient modulation method." In: *Radiology* 154.2 (1985), pp. 433–441. DOI: 10.1148/radiology.154.2.3966130.

[100] P. R. Moran. "A flow velocity zeugmatographic interlace for NMR imaging in humans." In: *Magn Reson Imaging* 1.4 (1982), pp. 197–203. DOI: 10.1016/0730-725X(82)90170-9.

[101] G. L. Nayler, D. N. Firmin, and D. B. Longmore. "Blood flow imaging by cine magnetic resonance." In: *J Comp Assisted Tomography* 10.5 (1986), pp. 715–722. DOI: 10.1097/00004728-198609000-00001.

[102] C. A. Nienaber et al. "Aortic dissection." In: *Nat. Rev. Dis. Primers* 2.16053 (2016). ISSN: 2056-676X.

[103] A Osswald et al. "Elevated Wall Shear Stress in Aortic Type B Dissection May Relate to Retrograde Aortic Type A Dissection: A Computational Fluid Dynamics Pilot Study." In: *Eur. J. Vasc. Endovasc. Surg.* 54.3 (2017), pp. 324–330. DOI: 10.1016/j.ejvs.2017.06.012.

[104] A. Pathrose et al. "Highly accelerated aortic 4D flow MRI using compressed sensing: Performance at different acceleration factors in patients with aortic disease." In: *Magn Reson Med* 85.4 (2021), pp. 2174–2187. DOI: 10.1002/mrm.28561.

[105] N. J. Pelc et al. "Encoding strategies for three-direction phase-contrast MR imaging of flow." In: *J Magn Reson Imaging* 1.4 (1991), pp. 405–413. DOI: 10.1002/jmri.1880010404.

[106] N. J. Pelc et al. "Phase Contrast Cine Magnetic Resonance Imaging." In: *Magn. Reson. Quaterly* 7.4 (1991), pp. 229–254.

[107] N. J. Pelc et al. "Quantitative magnetic resonance flow imaging." In: *Magnetic resonance quarterly* 10.3 (1994), pp. 125–147. ISSN: 08999422.

[108] S. Petersson, P. Dyverfeldt, and T. Ebbers. "Assessment of the accuracy of MRI wall shear stress estimation using numerical simulations." In: *J. Magn. Reson. Imaging* 36.1 (2012), pp. 128–138. ISSN: 1522-2586. DOI: 10.1002/jmri.23610.

[109] F Piatti et al. "Towards the improved quantification of in vivo abnormal wall shear stresses in BAV-affected patients from 4D-flow imaging: Benchmarking and application to real data." In: *J. Biomech.* 50 (2017), pp. 93–101. DOI: 10.1016/j.jbiomech.2016.11.044.

[110] W. V. Potters et al. "Volumetric arterial wall shear stress calculation based on cine phase contrast MRI." In: *J. Magn. Reson. Imaging* 41.2 (2015), pp. 505–516. DOI: 10.1002/jmri.24560.

[111] K. P. Pruessmann et al. "Advances in sensitivity encoding with arbitrary k-space trajectories." In: *Magn Reson Med* 46.4 (2001), pp. 638–651. DOI: 10.1002/mrm.1241.

[112] Y. Richter and E. R. Edelman. "Cardiology is flow." In: *Circulation* 113.23 (2006), pp. 2679–82. DOI: 10.1161/CIRCULATIONAHA.106.632687.

[113] E. Riesenkampff et al. "Pressure fields by flow-sensitive, 4D, velocity-encoded CMR in patients with aortic coarctation." In: *JACC Cardiovasc. Imaging* 7.9 (2014), pp. 920–926. DOI: 10.1016/j.jcmg.2014.03.017.

[114] F. Ritter et al. "Medical image analysis." In: *IEEE Pulse* 2.6 (2011), pp. 60–70. DOI: 10.1109/MPUL.2011.942929.

[115] F. Robicsek et al. "The congenitally bicuspid aortic valve: How does it function? Why does it fail?" In: *Ann Thorac Surg* 77.1 (2004), pp. 177–185. DOI: 10.1016/S0003-4975(03)01249-9.

[116] A. M. Sailer et al. "Computed Tomography Imaging Features in Acute Uncomplicated Stanford Type-B Aortic Dissection Predict Late Adverse Events." In: *Circ. Cardiovasc. Imaging* 10.4 (2017), e005709.

[117] S. Schmitter et al. "Towards high-resolution 4D flow MRI in the human aorta using kt-GRAPPA and B1+ shimming at 7T." In: *J Magn Reson Imaging* 44.2 (2016), pp. 486–499. DOI: 10.1002/jmri.25164.

[118] S. Schnell et al. "K-t GRAPPA accelerated four-dimensional flow MRI in the aorta: Effect on scan time, image quality, and quantification of flow and wall shear stress." In: *Magn. Reson. Med.* 72.2 (2014), pp. 522–533. DOI: 10.1002/mrm.24925.

[119] S. Schnell et al. "Altered aortic shape in bicuspid aortic valve relatives influences blood flow patterns." In: *Eur. Heart J. Cardiovasc. Imaging* 17.11 (2016), pp. 1239–1247. DOI: 10.1093/ehjci/jew149.

[120] D. Selle et al. "Analysis of vasculature for liver surgical planning." In: *IEEE Trans. Med. Imaging* 21.11 (2002), pp. 1344–57. DOI: 10.1109/TMI.2002.801166.

[121] L. M. Sierra-Galan and C. J. François. "Clinical Applications of MRA 4D-Flow." In: *Curr Treat Options Cardio Med* 21.10 (2019), pp. 1–18. DOI: 10.1007/s11936-019-0758-8.

[122] M. Sigovan et al. "Comparison of four-dimensional flow parameters for quantification of flow eccentricity in the ascending aorta." In: *J. Magn. Reson. Imaging* 34.5 (2011), pp. 1226–1230. DOI: 10.1002/jmri.22800.

[123] J. Sotelo et al. "3D Quantification of Wall Shear Stress and Oscillatory Shear Index Using a Finite-Element Method in 3D CINE PC-MRI Data of the Thoracic Aorta." In: *IEEE Trans. Med. Imaging* 35.6 (2016), pp. 1475 –1487. DOI: 10.1109/TMI.2016.2517406.

[124] J. Sotelo et al. "Three-dimensional quantification of vorticity and helicity from 3D cine PC-MRI using finite-element interpolations." In: *Magn. Reson. Med.* 79.1 (2018), pp. 541–553. DOI: 10.1002/mrm.26687.

[125] A. F. Stalder et al. "Quantitative 2D and 3D phase contrast MRI: Optimized analysis of blood flow and vessel wall parameters." In: *Magn. Reson. Med.* 60.5 (2008), pp. 1218–1231. DOI: 10.1002/mrm.21778.

[126] Z. Stankovic et al. "4D flow imaging with MRI." In: *Cardiovasc. Diagn. Therapy* 4.2 (2014), pp. 173–92. DOI: 10.3978/j.issn.2223-3652.2014.01.02.

[127] Z. Stankovic et al. "K-t GRAPPA-accelerated 4D flow MRI of liver hemodynamics: influence of different acceleration factors on qualitative and quantitative assessment of blood flow." In: *MAGMA* 28.2 (2015), pp. 149–159. DOI: 10.1007/s10334-014-0456-1.

[128] M. K. Stehling, R. Turner, and P. Mansfield. "Echo-planar imaging: Magnetic resonance imaging in a fraction of a second." In: *Science* 254.5028 (1991), pp. 43–50. DOI: 10.1126/science.1925560.

[129] I. Tan et al. "Heart rate dependence of aortic pulse wave velocity at different arterial pressures in rats." In: *Hypertension* 60.2 (2012), pp. 528–533. DOI: 10.1161/HYPERTENSIONAHA.112.194225.

[130] L. Tautz, A. Hennemuth, and H.-O. Peitgen. "Motion Analysis with Quadrature Filter Based Registration of Tagged MRI Sequences." In: *Stat. Atlases Comput. Model. Heart. STACOM 2011. Lect. Notes Comput. Science*. Vol. 7085. Springer, Berlin, Heidelberg, 2012, pp. 78–87. ISBN: 9783642283253. DOI: 10.1007/978-3-642-28326-0_8.

[131] L. Tautz et al. "Phase-based non-rigid registration of myocardial perfusion MRI image sequences." In: *IEEE Intl Symposium Biomed Imaging*. IEEE, 2010, pp. 516–519. DOI: 10.1109/ISBI.2010.5490297.

[132] J. Tu, K. Inthavong, and K. K. L. Wong. "Fundamentals of Haemodynamics." In: *Computational Hemodynamics – Theory, Modelling and Applications*. Springer, Dordrecht, 2015, pp. 67–94. DOI: 10.1007/978-94-017-9594-4_4.

[133] J. M. Tyszka et al. "Three-Dimensional, Time-Resolved (4D) Relative Pressure Mapping Using Magnetic Resonance Imaging." In: *J Magn Reson Imaging* 12 (2000), pp. 321–329. DOI: 10.1002/1522-2586.

[134] G. Valvano et al. "Accelerating 4D flow MRI by exploiting low-rank matrix structure and hadamard sparsity." In: *Magn. Reson. Med.* 78.4 (2017), pp. 1330–1341. DOI: 10.1002/mrm.26508.

[135] S. S. Vasanawala et al. "Congenital heart disease assessment with 4D flow MRI." In: *J. Magn. Reson. Imaging* 42.4 (2015), pp. 870–886. DOI: 10.1002/jmri.24856.

[136] J. Von Spiczak et al. "Quantitative analysis of vortical blood flow in the thoracic aorta using 4D phase contrast MRI." In: *PLoS ONE* 10.9 (2015), pp. 1–19. DOI: 10.1371/journal.pone.0139025.

[137] C. Y. Wen et al. "Investigation of pulsatile flowfield in healthy thoracic aorta models." In: *Ann. Biomed. Eng.* 38.2 (2010), pp. 391–402. DOI: 10.1007/s10439-009-9835-6.

[138] A. L. Wentland et al. "Aortic pulse wave velocity measurements with undersampled 4D flow-sensitive MRI: Comparison with 2D and algorithm determination." In: *J. Magn. Reson. Imaging* 37.4 (2013), pp. 853–859. DOI: 10.1002/jmri.23877.

[139] I. B. Wilkinson et al. "Heart rate dependency of pulse pressure amplification and arterial stiffness." In: *Am. J. Hypertension* 15.1 (2002), pp. 24–30. DOI: 10.1016/S0895-7061(01)02252-X.

[140] G. Williams et al. "In vitro evaluation of cerebrospinal fluid velocity measurement in type I Chiari malformation: repeatability, reproducibility, and agreement using 2D phase contrast and 4D flow MRI." In: *Fluids Barriers CNS* 18 (2021), p. 12. DOI: 10.1186/s12987-021-00246-3.

[141] D. A. Woodrum et al. "Phase-contrast MRI-based elastography technique detects early hypertensive changes in ex vivo porcine aortic wall." In: *J. Magn. Reson. Imaging* 29.3 (2009), pp. 583–587. DOI: 10.1002/jmri.21702.

[142] L. Ying and J. Sheng. "Joint image reconstruction and sensitivity estimation in SENSE (JSENSE)." In: *Magn. Reson. Med.* 57.6 (2007), pp. 1196–1202. DOI: 10.1002/mrm.21245.

[143] S. You et al. "Fully-Automated Deep Learning-Based Background Phase Error Correction for Abdominopelvic 4D Flow MRI." In: *Proc. ISMRM 29th Annual Meeting*. Virtual, 2021, p. 2413.

[144] J. Zimmermann, H. Mirzaee, and A. Hennemuth. "Software Flow Phantoms for Assessing the Image-Based Computation of Hemodynamic Parameters." In: *Eurographics Workshop Visual Comput. Biol. Med.* Bremen, 2017.

[145] J. Zimmermann et al. "Towards wall shear stress computation in the moving aorta: Application of different tracking algorithms." In: *Proc. ISMRM Workshop on Quantitative MR Flow*. San Francisco, CA, 2016.

[146] J. Zimmermann et al. "Advancing quantitative 4D flow MRI: Assessment of manual versus automatic boundary definition in the aorta." In: *Proc. SCMR 20th Scientific Sessions*. Washington D.C., 2017, P99.

[147] J. Zimmermann et al. "Exploring vessel inward normal computation for 4D flow based wall shear stress estimation in complex vessel geometries." In: *Proc. ISMRM 26th Annual Meeting*. Paris, 2018, P3435.

[148] J. Zimmermann et al. "Wall shear stress estimation in the aorta: Impact of wall motion, spatiotemporal resolution, and phase noise." In: *J. Magn. Reson. Imaging* 48.3 (2018), pp. 718–728. DOI: 10.1002/jmri.26007.

[149] J. Zimmermann et al. "Computational metrics for quantitative characterization of vortical flow patterns based on 3D PC-MRI data." In: *Proc. ISMRM 27th Annual Meeting*. Montreal, 2019, P1967.

[150] J. Zimmermann et al. "Fully dimensional vessel segmentation in non-contrast-enhanced 3D PC-MRI image data." In: *Proc. ISMRM 27th Annual Meeting*. Montreal, 2019, P1966.

[151] J. Zimmermann et al. "Impact of Vessel Wall Characteristics on Quantitative 4D-Flow Dynamics in Compliant 3D-Printed Thoracic Aorta Models." In: *Proc. ISMRM 28th Annual Meeting*. Virtual, 2020, P2280.

[152] J. Zimmermann et al. "Evaluating ICOSA6 4D-Flow in a Compliant Aortic Dissection Model with Large Velocity Range and Complex Flow Patterns." In: *Proc. ISMRM 29th Annual Meeting*. Virtual, 2021, P2093.

[153] J. Zimmermann et al. "In Vitro 4D-Flow and Pressure Mapping in the True and False Lumen of a Type-B Aortic Dissection Model." In: *Proc. SCMR 24th Scientific Sessions*. Virtual, 2021.

[154] J. Zimmermann et al. "On the impact of vessel wall stiffness on quantitative flow dynamics in a synthetic model of the thoracic aorta." In: *Scientific Reports* 11 (2021), p. 6703. DOI: 10.1038/s41598-021-86174-6.

[155] J. Zimmermann et al. "Quantitative Hemodynamics in Aortic Dissection: Comparing in Vitro MRI with FSI Simulation in a Compliant Model." In: *Funct. Imaging Model. Heart. FIMH 2021. Lecture Notes Comput. Science*. Vol. 12738. Springer, Cham, 2021, pp. 575–586. DOI: 10.1007/978-3-030-78710-3_55.

[156] N. R. Zwart and J. G. Pipe. "Multidirectional high-moment encoding in phase contrast MRI." In: *Magn. Reson. Med.* 69.6 (2013), pp. 1553–1563. DOI: 10.1002/mrm.24390.